DOCTORAL SCHOOL IN ENGINEERING

XXIV CYCLE

Dissertation

Neuroanatomical and Functional Magnetic Resonance Imaging Studies for Pediatric Applications

Dr. **Federico Nocchi**

SUPERVISOR: Prof. **Tommaso D'Alessio**

CO-SUPERVISOR: Dr. **Vittorio Cannatà**

CO-SUPERVISOR: Dr. **Carlo Capussotto**

COORDINATOR: Prof. **Lucio Vegni**

ACADEMIC YEAR 2010-2011

Acknowledgments

This work is the result of the cooperation between the Department of Applied Electronics of the University Roma Tre and the Clinical Technology Innovations Research Area (Scientific Direction) of Bambino Gesù Children's Hospital.

I would like to thank Professor Tommaso D'Alessio and his staff at the BioLab^3 Laboratory for the support and advice they have provided throughout the duration of my Ph.D. I am indebted to Dr. Vittorio Cannatà for teaching me the basis of MRI and to Dr. Carlo Capussotto and Dr. Pietro Derrico for providing the impetus for much of my work. I would also like to thank all the researchers of the Imaging, Neurorehabilitation and Robotics, and Health Technology Assessment Research Units, together with the physicians and technicians of Bambino Gesù Children's Hospital with whom I have worked over the past years.

Finally, my research work would not have been possible without the countless sacrifices that I asked to my family. I hope to be able, from now on, to devote adequate time to my family, confident that I'll be given the strength to help preserve its values.

SUMMARY

INTRODUCTION

Magnetic resonance imaging (MRI) is considered the most important medical imaging advance since the introduction of X-rays and has assumed a role of unparalleled importance in diagnostic medicine and in basic research. MRI provides a good spatial resolution and high contrast between soft tissues of the body, which makes it especially useful in imaging the brain. A variety of properties may be used to generate different types of MR images by varying the scanning parameters. Therefore, a collection of techniques exist that enable many aspects of the structure, biochemistry, and function of the human brain to be investigated.

The present work is focused on the application of two MR neuroimaging techniques in children and adolescent patients and in healthy adult subjects. Voxel-based morphometry (VBM) was used to investigate the anatomical correlates of pathologic conditions, while functional magnetic resonance imaging (fMRI) was applied to study brain function.

VBM is an objective morphometric technique used to study neuroanatomical differences between groups of subjects, without a priori hypotheses about their localisation. It allows answering the question whether a group of subjects shows specific structural features that could be related to a pathologic condition or to a common characteristic of the group. VBM has been successful in characterising structural brain abnormalities in a variety of diseases. Furthermore, several VBM studies in groups of healthy subjects have shown structural changes at the macroscopic level, thus challenging the traditional view that the acquisition of new skills only impacts on brain function.

Following these results, recent studies provided evidence of structural neuroplasticity in patients after a rehabilitative training.

fMRI allows non-invasively observing the human brain at work and linking brain structure and function. During the last two decades, it has had a major impact in cognitive neuroscience and has been used in research studies on a number of diseases and disorders and on the recovery of brain function. Despite still in the earliest stages of translation from research laboratories to clinical applications, fMRI has also a growing role in clinical neuroimaging. A drawback of this technique is that it does not directly detect the electrical activity of neurons, nor does it measure the rapid increase in metabolism. Instead, fMRI indirectly estimates neuronal activity by recording an MR signal related to brain haemodynamics. However, fMRI opens an array of opportunities to advance understanding of the organisation of brain functions in healthy subjects and in those in disease states.

The research projects in which both VBM and fMRI were applied also involved the combined use of further approaches and technologies, notably electroencephalography (EEG) for EEG-fMRI coregistration and robotic devices for robot-mediated therapy (RMT).

Research involving pediatric populations, both with VBM and fMRI, is less common than studies in adults, but it represents a growing field of inquiry that is generating a rapidly expanding body of knowledge about the development of brain structure and cognitive processes in children. The non-invasive nature of MRI allows performing longitudinal analyses, which are useful in studies on brain recovery and on the development of cognitive functions in child populations. However, there are many specific issues to consider when MRI is applied in children. Some aspects of brain development continue to progress in childhood. Many physical changes are associated with the process of brain maturation, including synaptogenesis and pruning, alterations in grey matter thickness, and increases in white matter volume,

which can cause regional and global variation in brain structure across children of different ages and with various neurologic and developmental disorders. This process of development has many important implications. In addition to these physical changes, normal patterns for cognitive processes associated with specific tasks may change depending on the developmental level of the child. For example, some cognitive studies show that the extent of functional activation for a given task is often larger for younger children and becomes more focal as development progresses. fMRI requires subject cooperation and depends on patient's attention which may affect the haemodynamic response, thus producing a relevant variability of activations between subjects and in repeated exams in the same subject. Therefore, patient sedation in case of anxiety or claustrophobia, which are more frequent in young children than in adults, is not possible. This may result in subject's movement, which in turn reduces signal-to-noise ratio in fMRI images and, if it is stimulus-correlated, can introduce artefacts in the activation maps. Data processing methods can remove some movement artefact; however studies with children are sometimes compromised by excessive movement. Designing appropriate tasks for a child's developmental level is also critical. Paradigms that are too easy may result in little activation. Tasks that are too hard may cause a child to give up. Therefore, the age and condition of the child to be scanned is an important consideration for successful fMRI task completion. However, by gearing paradigms to each child's developmental level, it becomes difficult to make group generalisations and comparisons across these graded tasks.

The present work is divided into 4 Chapters.

Chapter 1 presents the principles of MRI. The mechanisms of data acquisition are described, together with basic imaging sequences. An overview of neuroimaging technologies and techniques is also provided in this Chapter. Computational neuroanatomy approaches for exploring brain structure in cross-sectional and longitudinal studies are briefly introduced. A summary

description is also given of the differences between the physiological principles on which invasive and non-invasive functional techniques are based, together with the strengths and weaknesses of each technique.

Principles and applications of VBM are examined in Chapter 2, where details are provided on the processing of structural data (including segmentation, normalisation and use of customised templates) and on mass-univariate analyses for statistical parametric mapping.

Recruiting large groups of patients in pediatric trials can take several months or years, depending on the pathology under investigation. The issue of the number of subjects that should be included for VBM studies to provide reliable results is addressed and a simulation study intended to provide guidelines for recruiting subjects is presented. The simulation study also assesses the effects of including outliers in VBM analyses, i.e. subjects that have different anatomical characteristics from the group in which they are included.

In close collaboration with a team of neuropsychiatrists and neuroradiologists of Bambino Gesù Children's Hospital, VBM was applied to a clinical study in a group of adolescent patients with anorexia nervosa. The characteristics of the subjects included in the study allowed searching for brain areas possibly involved in the early stages of the illness. Results of this study showed a significant global reduction of grey matter in anorexia nervosa patients, compared to control subjects. Furthermore, a region-specific reduction of grey matter was found in brain areas known to participate in mental processes related to the pathology. The latter result may indicate a greater vulnerability of these regions that could play a role in the pathophysiology of the disease and may explain the presence of a distorted body image in anorexia nervosa patients.

Chapter 3 discusses principles and applications of fMRI. This technique depends on several factors. Exam paradigm (i.e. the stimulus sequence), data processing pipeline (i.e., the sequential combination of spatio-temporal image

processing steps) and statistical analysis of data are all relevant aspects for the outcome, both for single subject and group studies. Strategies for controlling movement artefacts and for coregistering images from different acquisition modalities are examined, together with the general linear model for the statistical analysis of pre-processed data. Overviews are also provided of MR-compatible stimuli-delivery systems and of the fMRI experimental setting of the Imaging Department of Palidoro at Bambino Gesù Children's Hospital. Paradigms for preliminary studies on motor planning implemented with this experimental setting are presented as example applications of fMRI.

The cumulative incidence of epilepsy in children is approximately 1% and in 30÷40% of cases drug-resistant forms are present, often eligible to be surgically treated. Indeed, neurosurgery can prevent the deleterious effects on cognitive development that are evident in some forms of childhood epilepsy. The pre-surgical mapping of brain functions allows predicting the likelihood of post-surgical deficits and to spare tissue that, if injured, would cause new clinical deficits or limit good recovery. fMRI may represent a helpful tool to localise cerebral functions in tissue within or near regions intended for neurosurgical resection of epileptic foci. Furthermore, fMRI can be used to non-invasively investigate lateralisation, which has proven useful to study organisation of cognitive functions in children and for pre-surgical evaluation of patients with medically intractable epilepsy. For such reasons, an experimental protocol for the localisation of language and motor functions and the assessment of functional lateralisation was designed. The protocol consists in a set of tasks that are likely to be easy to perform for children and impaired subjects. Furthermore, a tool was designed and implemented both to determine the dominant hemisphere and to provide the lateralisation of brain functions in specific regions of interest. A preliminary study was carried out on healthy adult subjects with the aim of providing a set of reference values for the analysis of lateralisation in children with drug-resistant epilepsy.

In recent years there has been an increase of interest in the multimodal approach to the study of neuroscience due to the advantages provided by the combined use of non-invasive functional imaging tools and traditional neurophysiological techniques. In particular, simultaneous EEG and fMRI recording has overcome the inherent limitations of individual techniques, allowing localisation of the generators of functional changes that underlie specific events. The interest in this tool is supported by its potential clinical applications for the pre-surgical localisation of ictal foci. The goal is to identify regions of the brain that show signal changes immediately following epileptic spikes. However, despite the promising results from leading centres, several aspects of the combined approach are still being investigated. A preliminary study was carried out, in collaboration with a team of neurologists at Bambino Gesù Children's Hospital, to set up the simultaneous EEG-fMRI recording technique. A substantial reduction of the MR-induced artefacts on the EEG was obtained and the quality of fMRI images was fully preserved. However, wearing conventional EEG caps used in EEG-fMRI recordings may be particularly problematic in children. Therefore, the use of a reduced set of electrodes was also explored, by testing a prototype. The results obtained showed that when the interest is in detecting when an event happens, and in localising the corresponding neuronal activations with fMRI, a reduced set of electrodes could be preferred to standard EEG caps.

An issue dominating the current debate in the field of rehabilitation concerns with the nature of functional recovery after brain injury. The recovery of motor function has been partly attributed to adaptive functional reorganisation within the central nervous system. Therefore, current rehabilitation models seek to stimulate functional recovery by capitalising on the inherent potential of the brain for positive reorganisation. Studies suggest the potential modulative effects of focused, intensive rehabilitative training in facilitating the use-dependent reorganisation. With the use of fMRI,

rehabilitation therapy-induced adaptive reorganisation has been investigated. Nevertheless, the correlates between motor functional gains and changes in brain organisation are still a matter of debate. VBM studies investigated the impact of learning and practice on brain structure and studies on healthy subjects with this technique have challenged the traditional view that the acquisition of new skills only changes the way the brain functions, by showing structural changes at the macroscopic level. Recently, evidence was also provided of structural neuroplasticity resulting from rehabilitative therapy. New technologies such as robotics and virtual reality are increasingly placing side by side traditional rehabilitation treatments to assist, enhance and assess motor training. The role of these technologies within therapeutic treatment programs has been a very active area of research in recent years and is currently under debate. However, the potential of RMT and virtual reality in rehabilitation has not been extensively investigated with neuroimaging tools yet. Moreover, few studies on RMT have been conducted with patients in developmental age, when there is a bigger window for neuronal plasticity and the expected functional recovery could be better. The Movement Analysis and Robotics Laboratory (MARLab) of Bambino Gesù Children's Hospital is the first organisation worldwide using robotic instrumentation in clinical protocols.

Chapter 4 is focused on a project developed in collaboration with a team of neurorehabilitators and neuropshycologists of the MARLab. The research is aimed at applying neuroimaging techniques to explore the effectiveness of motor RMT protocols on the recovery of upper limb deficits in children affected by congenital or acquired hemiparesis. Furthermore, it aims at comparing RMT to traditional rehabilitation techniques. VBM and fMRI are used to detect potential anatomical and functional cerebral plasticity induced by rehabilitation and underlying the recovery of upper limb motor performance. This would provide an objective means for proving or refuting the greater effectiveness of RMT, when compared to traditional therapy. The final goal is to obtain specific

indications on the most effective rehabilitation protocols for children with hemiparesis based on clinical evidence. The results of the research could also expand our knowledge on how the human brain recovers or improves impaired motor skills after brain damage in developmental age. Pediatric patients with mild to moderate upper extremity hemiparesis, clinically stable and able to participate in a RMT program, are taking part in this longitudinal study. Clinical evaluations based on standard functional scales, neuropsychological assessment, robot-based measurements, and MRI exams (fMRI tasks implemented for this study and T1 sequences for VBM analyses) are performed at the enrolment and completion of the rehabilitative training. Children are randomly assigned to receive a traditional rehabilitation therapy or a treatment with the two degrees-of-freedom planar InMotion2 robot used at the MARLab for upper limb rehabilitation. However, owing to the effort required by the training protocol (lasting 4 weeks for each subject), only very preliminary results are presented for this study.

In preparation for the application to hemiplegic children, a preliminary study was carried out on healthy adult subjects. A visual fMRI protocol was set up, able to detect a neuronal network associated with upper limb robotic training with the InMotion2 robot. The fMRI task was designed to identify the neuronal activation patterns associated with processing (observation, analysis, and representation) of human and abstract object movements similar to those executed and observed during robotic training. The subsequent aim was to verify commonalities and differences in the brain networks able to process upper limb gestures and abstract object movements, i.e. to assess the brain's ability to assimilate abstract movements to human motor gestures. This analysis is useful to test the effectiveness of the non-biological visual feedback provided to patients during robotic rehabilitation, with respect to human movement observation, in activating brain networks for motor processing.

CHAPTER 1: Principles of Magnetic Resonance Imaging

1.1 Basic principles of MRI

Nuclear magnetic resonance (NMR) is a physical phenomenon in which magnetic nuclei in a magnetic field absorb and re-emit electromagnetic radiation. This energy is at a specific frequency which depends on the strength of the magnetic field and the magnetic properties of the material that is being examined. This property can be used to record the signals emitted when the nuclei are excited at the resonance frequency.

Magnetic resonance imaging (MRI) makes use of the property of NMR to image nuclei of atoms inside the body. It is a medical imaging technique used in radiology to visualize detailed internal structures and to distinguish pathologic tissue from normal one. Any nucleus with a net nuclear spin could potentially be imaged with MRI. Such nuclei include ^{3}He, ^{13}C, ^{19}F, ^{17}O, ^{23}Na, ^{31}P and ^{129}Xe. However, hydrogen is the most frequently imaged nucleus in MRI because it is present in biological tissues in great abundance (in water molecules, as well as in proteins and lipids), and because its high gyromagnetic ratio gives a strong signal. Therefore, most MR techniques are based on the acquisition of the radio frequency (RF) energy from hydrogen protons, while ^{13}C, ^{19}F, ^{23}Na, and ^{31}P are currently used in research studies more than for clinical purposes. As the result of a combination of the naturally occurring proportions of these nuclei in the body and the lower intrinsic NMR sensitivity, studies with these latter species suffer from relatively low levels of signal to noise ratio (SNR) and resolution. However, they can provide important information about biochemical and metabolic processes.

MRI is a relatively new technology. In the 1950s, Herman Carr reported on the creation of a one-dimensional NMR image. In 1971 Raymond Damadian reported that tumours and normal tissue can be distinguished *in vivo* by NMR and suggested that these differences could be used to diagnose cancer. While

researching the analytical properties of NMR, in 1972 he discovered the NMR tissue relaxation differences and described the concept of whole-body NMR scanning. However, he did not describe a method for generating pictures from such a scan or precisely the characteristics that such a scan should have. Paul Lauterbur expanded on Carr's technique and developed a way to generate the first two-dimensional (2D) and three-dimensional (3D) MRI images using gradients. In 1973, Lauterbur published the first NMR image and the first cross-sectional image of a living mouse was published in 1974. Subsequently Peter Mansfield developed a mathematical technique that would allow scans to take seconds rather than hours and produce clearer images than Lauterbur had. Damadian, along with Larry Minkoff and Michael Goldsmith, subsequently went on to perform the first MRI body scan of a human being in 1977. Paul Lauterbur and Sir Peter Mansfield were awarded the 2003 Nobel Prize in Physiology or Medicine for their discoveries concerning magnetic resonance imaging (the award was vigorously protested by Raymond Damadian). The Nobel citation acknowledged Lauterbur's insight of using magnetic field gradients to determine spatial localisation, a discovery that allowed rapid acquisition of 2D images. Mansfield was credited with introducing the mathematical formalism and developing techniques for efficient gradient utilisation and fast imaging.

MRI is considered the most important imaging advance since the introduction of X-rays by Conrad Röntgen in 1895. Since its introduction in the clinic in the 1980s, it has assumed a role of unparalleled importance in diagnostic medicine and more recently in basic research (Logothetis, 2008). It provides a good spatial resolution and high contrast between the different soft tissues of the body, which makes it especially useful in imaging the brain compared with other medical imaging techniques such as Computed Tomography (CT). Unlike CT scans, MRI uses non-ionizing radiation and is

harmless to the patient. Therefore, this technique is currently widely used in medical imaging.

Unlike other imaging modalities, MRI is a collection of techniques that enable many aspects of the structure, biochemistry, and function of the brain to be identified (Kuzniecky and Jackson, 2005). There are a number of choices that have to be made by the operator in order to acquire the most relevant information. Today, several MRI techniques are being used in the field of medical imaging. Examples include MR spectroscopy, diffusion MRI, MR angiography, arterial spin labelling, and functional magnetic resonance imaging, to mention only some of the most frequently used. MRI scanners are among the most complex and expensive medical technologies: the acquisition cost for a 1.5 T or 3 T scanner for medical diagnosis is currently 10^6> €.

1.1.1 Principles of data acquisition

1.1.1.1 Static magnetic field

The basis of MRI is the directional magnetic field associated with nuclei containing an odd number of protons and/or neutrons. Because nuclei are charged particles with a precession motion, they produce a small magnetic moment. When no external magnetic field is applied, the magnetic moments of the particles are oriented in a random manner. However, when a human body is placed in a large magnetic field, many of the free hydrogen nuclei align themselves with the direction of the magnetic field and precess about this direction like gyroscopes. This behaviour is termed Larmor precession. The frequency of precession of magnetic moments around the axis of an external magnetic field (called the Larmor frequency, ω_0) is proportional to strength of the applied magnetic field, as stated by the Larmor equation:

$$\omega_0 = \gamma B_0 \quad (1.1)$$

where γ is the gyromagnetic ratio and B_0 is the strength of the magnetic field. The gyromagnetic ratio is nuclei specific (for hydrogen, γ=42.6 MHz/T), however, it is influenced by the molecular environment surrounding the nuclei. That is, the effects of the local environment of the molecule act to alter the effect of the applied magnetic field at the nucleus (e.g. hydrogen protons in fat molecules have different γ values from those in water molecules). Given a certain B_0 static field, the frequency variation determined by a different γ value is called the chemical shift.

Two discrete possibilities exist for the direction of precession: one for the nucleus aligned along the direction of the external magnetic field and another one in the opposite direction (anti-aligned). These two states are referred to as parallel and anti-parallel states. The parallel state is slightly lower in energy than the anti-parallel state. More nuclei occupy the lower energy than the higher energy state, thus producing a net magnetisation vector. Clinical MRI scanners use powerful magnetic fields, with field strengths between 0.1 and 3 T and even more, depending on the application (while the strength of the earth's magnetic field is about 50 μT, i.e. about 2,000 to 60,000 times smaller). However, even with these strong fields, the excess of protons in the parallel state is only a few parts per million. Although the magnetisation effect is small, the natural abundance of protons makes the cumulative magnetisation sufficiently large to be measurable. The parameter describing the contribution of protons to the net magnetisation vector is proton density (ρ), which is one of the 3 main parameters used to contrast between different tissues (the remaining 2 parameters are the relaxation times, which will be described later).

The stronger is the B_0 field, the larger will be the density of protons contributing to the net magnetisation vector and subsequently to the MRI signal.

Therefore, ever stronger static magnetic fields are being produced for MRI scanners. The static magnetic field can be obtained with permanent magnets, electromagnets, or superconducting magnets. Currently, most scanners use a large coil of superconducting wire, to produce homogeneous static magnetic fields of 1> T (i.e. 10,000> Gauss). These scanners are far less power consuming than electromagnets, while the operating expenses of a superconducting magnet come from maintenance of the cooling agents, or cryogens (newer systems use liquid helium and a cold-head compressor). The superconducting magnet consists of a solenoid of wire, typically made of niobium-titanium, tightly wound to form a solenoid or cylinder around the bore of the magnet. When a constant current flows through the wire, a static, relatively uniform magnetic field is generated within the bore of the magnet, aligned in the direction of the bore. At room temperature, niobium-titanium has normal resistance. However, when it is cooled to less than 9.5 K, it becomes superconducting. Once a superconducting magnet is ramped up and fully installed, it is always on. It is essential that the main magnetic field is as homogeneous as possible, as small variations in the magnetic field are used to encode spatial position. For this reason, inhomogeneities (e.g., caused by metal) will grossly interfere with image quality. The inhomogeneity of a field is typically described in parts per million. Additional coils (known as shim coils) are used to improve the field homogeneity over the area of imaging. Shimming is particularly important after a subject is introduced into the magnet bore because the presence of the body distorts the magnetic field.

The magnetic field directed along the main axis, or bore, of the magnet usually defines the *z* axis. Magnetisation along the bore is referred to as longitudinal magnetisation, while that perpendicular to the bore is called transverse magnetisation. Because of the symmetry of magnetisation in the transverse plane, the *x* and *y* directions are interchangeable. By convention, 3D magnetisation vectors *M* are therefore considered in terms of their longitudinal

(M_z) and transverse (M_{xy}) components. The angle of the vector *M* with respect to the *z* axis, α, is referred to as the flip angle.

1.1.1.2 Radiofrequency excitation

The longitudinal magnetisation of protons in a given tissue is very small when compared to the static magnetic field B_0 of the MRI scanner, so the net magnetisation vector cannot be measured at steady state. It is therefore necessary to modify this equilibrium condition. The steady state can be perturbed by exciting protons with a brief application of a RF pulse generated by a transmitting coil, i.e. with a pulse of oscillating magnetic field that is itself precessing at the fundamental precessional frequency of the nuclei.

The energy difference between parallel and anti-parallel energy state is directly related to the precessional frequency through the following equation:

$$\Delta E_0 = hf \tag{1.2}$$

where *h* is the Planck's constant and *f* is the precessional frequency, related to the Larmor frequency, ω, through:

$$\omega = 2\pi f \tag{1.3}$$

Thus, transitions from the parallel to the anti-parallel state can be induced in the sample when it is excited with electromagnetic radiation of energy ΔE. This energy is about 1.75×10^{-7} eV for a proton in a 1 T field, a tiny amount of energy compared with electron binding energies. The energy difference between the nuclear spin states corresponds to a RF photon, i.e. the energy of electromagnetic radiation in the RF region of the electromagnetic spectrum. So,

if a tissue sample was placed in a magnetic field of 1 T and RF waves at 42.58 MHz were beamed into it, protons would be excited from the parallel to the anti-parallel state. The RF pulse represents a weak magnetic field, called B_1, which needs to be oriented perpendicular to B_0 for the energy to be efficiently absorbed. B_1 tilts the net magnetisation away from the direction of the bore of the magnet. Two processes occur simultaneously during absorption of the radiant energy:

1. reduction in longitudinal magnetisation (M_z): some of the protons resonate and move to the anti-parallel state, resulting in a reduction in the longitudinal magnetisation;
2. phase coherence: the vectors align with each other in phase.

The outcome of phase coherence is the establishment of a net magnetic vector in the transverse plane, called the transverse magnetisation (before the RF pulse, the phases of spins were random and the magnetisation vector in the transverse plane was null). So, once longitudinal magnetisation is established by placing a patient in the magnet of an MRI scanner and radio waves at the resonant frequency are generated, we establish a transverse magnetisation while reducing the longitudinal magnetisation.

Once the RF pulse has excited the protons, tipping their magnetisation toward the transverse plane, the transmitting coil is turned off. The magnetic moments are exposed again only to the static B_0 magnetic field and the magnetisation vector will tend to relax back to its equilibrium state, becoming realigned with B_0. This phenomenon is referred to as relaxation. Transitions back to the parallel state occur spontaneously over a time period which is characteristic of individual tissues and their various pathological conditions. The recovery of longitudinal magnetisation is called longitudinal or T1 relaxation and occurs exponentially with a time constant T1. The loss of phase coherence in the transverse plane is called transverse or T2 relaxation. T1 is thus associated with the enthalpy of the spin system (the number of nuclei with parallel versus

anti-parallel spin) while T2 is associated with its entropy (the number of nuclei in phase). Therefore, transverse and longitudinal magnetisation are components of a vector with time-varying module and represent different relaxation processes.

The rotating transverse component of net magnetisation produces an oscillating magnetic field which induces a small current in the receiver coil (frequently, the same coil is used to detect the resulting signal after the excitation stage has been terminated: the coil is then called a combined transmitter-receiver coil). It should be noted that signals cannot be detected in the longitudinal plane, while the transverse magnetisation component can be measured because it is orthogonal to the B_0 field. The current collected by the receiving coil is amplified and measured as MR signal. The detected emissions produce an exponential signal called Free Induction Decay (FID). In an idealized NMR experiment, the FID decays approximately exponentially with a time constant T2, but in practical MRI small differences in the static magnetic field at different spatial locations (inhomogeneities) cause the Larmor frequency to vary across the body creating destructive interference which shortens the FID. The time constant for the observed decay of the FID is called the T2* relaxation time, and is always shorter than T2.

Typically in soft tissues T1 is around one second while T2 and T2* are a few tens of milliseconds, but these values vary widely between different tissues (and different external magnetic fields), giving MRI its high soft tissue contrast (Table 1.1). Relaxation times depend on the efficiency of energy transfer between protons and the surrounding environment, which in turn depends on the freedom of movement of the molecules. Together with proton density ρ, relaxation times allow to contrast different tissues.

	T1 (ms)	T2 (ms)
Grey Matter	920	100
White Matter	790	92
CSF	2.400	160

Table 1.1 - T1 and T2 values of brain tissues at 1.5 Tesla.

As stated above, the time required for protons to recover the steady state longitudinal magnetisation is expressed as the time constant T1 which, at a given magnetic field strength, is a property of the examined tissue and depends on the energy transfer with the surrounding environment. Following RF excitation, it is interactions with the local environment which cause protons to lose their excess energy and return to the lower energy state with the emission of RF radiation. This is the origin of the re-establishment of longitudinal magnetisation during relaxation. This phenomenon is called spin-lattice relaxation (spin referring to the spinning proton and lattice to its local environment). The rate at which molecules can move within their environment is related to their size and hence small molecules have a low probability for interaction. This is why fluids such as cerebrospinal fluid (CSF) have long T1 values, for instance. Medium-sized molecules (e.g. lipids), in contrast, have a greater probability for interaction and exhibit relatively short T1 values. The recovery of the longitudinal magnetisation is governed by the Bloch equation for M_z, which has the solution:

$$M_z(t) = M_{z,eq}\left(1 - e^{-t/T_1}\right) \tag{1.4}$$

The decay of the transverse magnetisation is governed by:

$$M_{xy}(t) = M_{xy}(0)e^{-t/T_2} \tag{1.5}$$

The so-called spin-spin interactions are interactions where two nearby protons can cause each other to flip so that one changes from anti-parallel to parallel alignment, while the other changes from parallel to anti-parallel, i.e. one gains the excitation energy from the other. Phase coherence with other excited protons is lost during this exchange and the end result is a relaxation of the transverse magnetisation. This spin-spin interaction is also called T2 relaxation. Since T2 arises mainly from neighbouring protons, a higher interaction probability exists with larger than with smaller molecules. Macromolecular environments will therefore display shorter T2 values than water-based fluids, e.g. CSF. Transverse relaxation tends to happen much more rapidly than longitudinal relaxation and T2 values are therefore generally smaller than T1 values.

Paramagnetic and ferromagnetic materials have a high magnetic susceptibility. When the field strength is raised around these materials, the magnetic field distortions raise in turn. This phenomenon produces a local variation of relaxation times. Moreover, inhomogeneities are present in the main magnetic field due to scanner non-idealities. As a consequence, neighbouring protons experience different field strengths and vary their frequency of precession, thus dephasing. Thus, differently from T2, the T2* time constant takes into account the compounding effect of imperfections in the external magnetic field and of spin-spin interactions.

1.1.1.3 Spatial localisation: magnetic field gradients

To locate the sources of MR signal, spatial encoding is required. This relies on applying strong magnetic field gradients, i.e. fields that are superimposed to the static field B_0 and that vary in given directions. The magnetic field gradient set is located between the main magnet and the bore of

the scanner (Figure 1.1). Magnetic field intensity varies in a linear manner along the gradient application axis. By applying a magnetic field gradient along a given direction, precessional frequencies can be deliberately made to vary with position in the magnetic field. Therefore, 3D spatial information can be obtained by providing gradients along each axis:

$$\omega(r) = \gamma B(r) = \gamma(B_0 + iG) = \omega_0 + \gamma i G_i, G_i = \left(\frac{dB_i}{di}\right), (i = x, y, z) \quad (1.6)$$

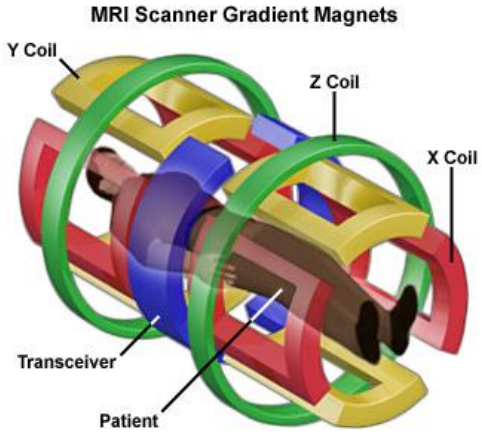

Figure 1.1 – The magnetic field gradient set (source: www.magnet.fsu.edu).

Each gradient is characterised by its strength (greater or lesser field variation for the same unit of distance), direction and the moment and time of application. First of all, a slice selection gradient is used to select the anatomical plane of interest. Within this plane, the position of each point will be encoded by applying a phase encoding gradient, and a frequency-encoding gradient. The different gradients have identical properties but are applied at distinct moments and in different directions. Gradient equivalence in the three axes means that slices can be selected on any spatial plane.

The first step of spatial encoding consists in selecting the slice plane. To do this, the slice selection gradient is applied perpendicular to the desired slice plane (let's say along the *z* axis). This is added to B_0, and the protons present a

resonance frequency variation proportionate to the field strength variation that they experience (see Eq. 1.1). An RF wave is simultaneously applied, with the same frequency as that of the protons in the desired slice plane. This causes a shift in the magnetisation of only the protons on this plane. As none of the hydrogen nuclei located outside the slice plane are excited, they will not emit a signal. The RF wave associated with the slice selection gradient and the adapted resonance frequency is called the selective pulse. The thickness of the slice can be varied by adjusting the bandwidth of the selective pulse and the amplitude of the slice selection gradient. Moreover, the shape of the RF pulse in time will also determine the bandwidth profile in frequency, and thus the slice profile.

The second step in spatial encoding consists in applying a phase encoding gradient (e.g., along the *y* axis). The phase encoding gradient intervenes for a limited time period. While it is applied, it modifies the spin resonance frequencies, inducing dephasing which persists after the gradient is interrupted and until the signal is recorded. This results in all the protons precessing at the same frequency but with different phases. The protons in the same row, perpendicular to the gradient direction, will all have the same phase. To carry out the different phase encoding steps, the gradient is applied with different, regularly incremented values.

The final step in spatial encoding consists in applying a frequency encoding gradient in the last direction (e.g. *x* axis), when the signal is received. This modifies the Larmor frequencies in the *x* direction throughout the time it is applied. It thus creates proton columns, which all have an identical Larmor frequency. When the frequency-encoding gradient is applied, the signal is digitized at regular intervals in time. Each signal sample corresponds to a given accumulation of the gradient effect: the longer the time, the longer the effect of the gradient on the spins, and the greater their phase modification.

Frequency-encoding and phase-encoding are applied so that data are spatially encoded by differences in frequency and phase. Each frequency-phase

couple represents a *xy* coordinate in a given slice and the corresponding signal intensity is proportional to the chosen weighting (ρ, T1, T2). The frequency-phase space (spectral map) obtained this way is called the k-space. To go from k-space data to an image requires using a 2D inverse Fourier Transform. Assuming a proton density weighting has been adopted, the Fourier relationship between signal and spin density can be written as:

$$S(k) = \iiint \rho\,(r) e^{ik \cdot r} dr$$
$$\rho(k) = \iiint S\,(k) e^{-ik \cdot r} dk \tag{1.7}$$

The easier way to fill the k-space is to use a line-by-line rectilinear trajectory. One line of k-space is fully acquired at each excitation, containing low (contrast) and high resolution information in a given direction (e.g., along the k_x axis). Between each repetition, there is a change in phase-encoding-gradient strength, corresponding to a change along the k_y axis. This allows filling of all the lines of k-space from top to bottom. During the filling of k-space, the resulting image is containing at the beginning the edge information with low contrast, then the general shape and contrast with a blur in the k_y direction that will disappear as high spatial-frequency information in the k_y direction is completed.

1.1.2 Basic acquisition sequences

The basis of MRI ability to provide an excellent contrast and resolution and/or a fast signal acquisition is the complex library of pulse sequences that medical MRI scanners include. The essential components for any imaging sequence are: 1) an RF excitation pulse, required for the phenomenon of

magnetic resonance; 2) gradients for spatial encoding, whose arrangement will determine how the k-space is filled; 3) a signal reading, combining one or a number of echo types determining the type of contrast. The ideal MR sequence should have high spatial resolution, high SNR, no artefacts (e.g. partial volume, motion), short acquisition time, high contrast between normal tissues and between pathologic and normal tissue, and quiet pulse sequences.

The in-plane resolution is determined by the field of view and the matrix size in the frequency encoding and phase encoding directions, that is how many picture elements (pixels) we divide the area we are imaging into. A typical matrix in clinical practice is 256x256, which means that the whole image is divided, in two dimensions, into an array of this many pixels. The actual size of the pixels will depend on the field of view. The basic volume element (voxel) of MRI images is given by the product of the slice thickness and the in-plane resolution. Therefore, the voxel is the volume of tissue from which the signal in each element arises.

Usually, more than one excitation is needed to improve the SNR. For a given pulse sequence and for given pulse parameters, the SNR is directly proportional to the voxel size and the square root of the number of data acquisitions (N_{ex}). As the noise does not add coherently (it increases by the square root of N_{ex}) we have:

$$SNR \propto slice\ thickness \cdot \sqrt{\frac{N_{ex} \cdot FOV^2}{NF_x \cdot NP_y}} \tag{1.8}$$

with NP_y number of phase encoding steps and NF_x number of frequency encoding steps. It can be seen from Eq. 1.8 that tradeoffs between certain desired aspects of the scanning procedure have to be made. For example, thinner slices improve the signal resolution in the through-slice direction but will have a lower SNR.

Another important issue when deciding on the optimal in-plane and though-plane resolution is that of partial volumes, i.e. the mixing of signals from different tissue types within the same voxel, which leads to a blurring of the signal intensities. The smaller the voxel size, the better will be the suppression of partial volume effects. However, this will be at the cost of SNR and acquisition time.

Motion is a major problem in standard MRI pulse sequences, in which the image is acquired one phase-encoding step at a time rather than in a "single shot". The effect of motion is significant not just because of gross head movements but also because of pulsations from blood vessels and respiration, which are intrinsic to the biologic system being imaged and may cause image ghosting.

Contrast is a direct consequence of the relative signal intensities from different tissue types. The most important contrast factors in MRI are proton density (ρ) and relaxation times (T1, T2 and T2*). For example, with particular values of the echo time (TE) and the repetition time (TR), which are basic parameters of image acquisition, a sequence takes on the property of T2-weighting. On a T2-weighted scan, water- and fluid-containing tissues are bright and fat-containing tissues are dark. The reverse is true for T1-weighted images. Other intrinsic components of the signal that can generate contrast include diffusion contrast, chemical shift, and perfusion contrast.

There is over a hundred different types of sequences, most of which may be classified in two main families, depending on the type of echo recorded: spin echo (SE) sequences (characterised by the presence of a 180° rephasing RF pulse) and gradient echo (GRE) sequences (Figure 1.2). Numerous variations have been developed within each of these families, mainly to increase acquisition speed (e.g.: fast SE, single shot fast SE, spoiled GRE, ultrafast GRE, steady state GRE, echoplanar. Some sequences are hybrid, mixing SE and GE

(GRASE, SE-EPI). Specific sequences have been developed for MR angiography, perfusion imaging, diffusion imaging and MR spectroscopy.

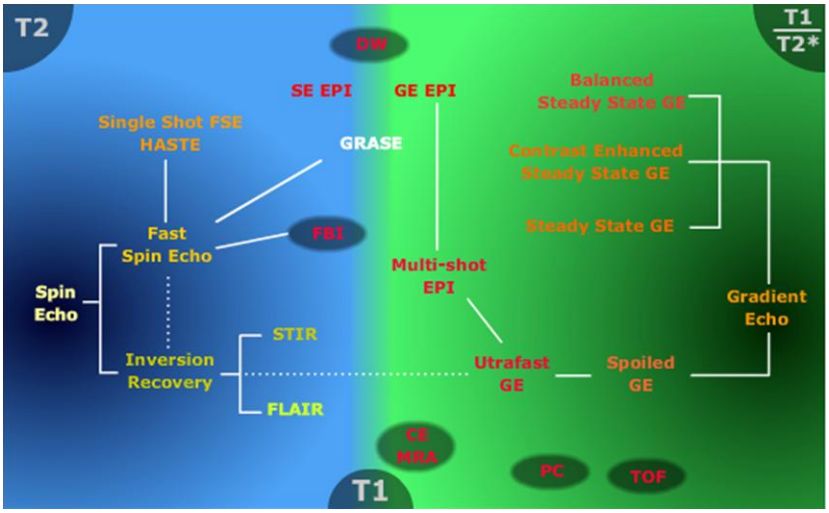

Figure 1.2 – Families of spin echo and gradient-echo sequences (source: www.imaios.com).

1.1.2.1 Spin echo sequences

The SE sequence is made up of a series of events: 1) 90° pulse; 2) 180° rephasing pulse at TE/2; 3) signal reading at TE (Figure 1.3). Historically, SE was the first sequence to be used. The 90° RF pulse rotates the net magnetisation vector from the *z* axis to the *xy* plane. After the 90° pulse, the net magnetisation vector precesses on the *xy* plane, however, due to field inhomogeneities, single protons precess with different frequencies leading to an irreversible loss of magnetisation. This dephasing can be reversed by applying a 180° or inversion pulse that inverts the magnetisation vectors (in fact, a 180° pulse can be used to either invert the magnetisation in the *z*-direction or to reverse the direction of the magnetisation when it is already in the *xy*-plane). If the inversion pulse is applied after a period TE/2 of dephasing, protons will rephase to form an echo at time TE. The intensity of the echo relative to the initial signal is given by $e^{-TE/T2}$ where T2 is the time constant for spin-spin relaxation. Therefore, the 180°

rephasing pulse compensates for the constant field inhomogeneities to obtain an echo that is weighted in T2.

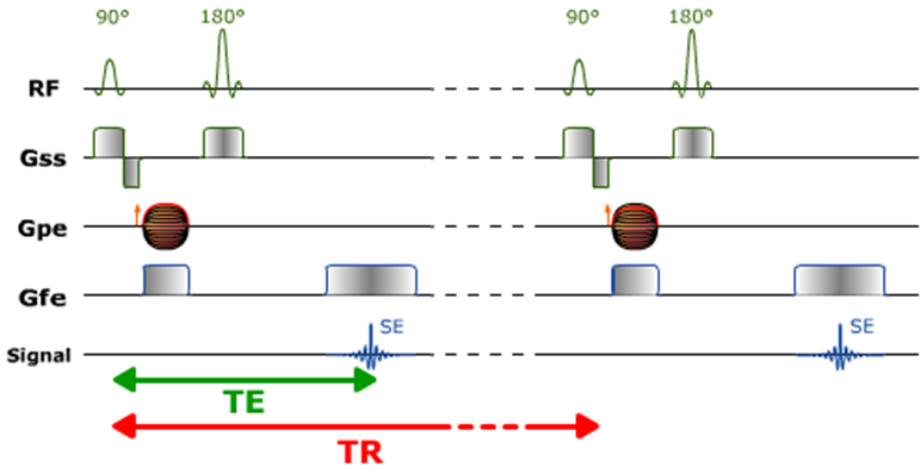

Figure 1.3 – Spin echo sequence time diagram (source: www.imaios.com).

In the classical SE sequence, this series is repeated at each time interval TR. With each repetition, a k-space line is filled, thanks to a different phase encoding, so that for a SE sequence with NP_y rows, we make NP_y acquisitions. Therefore, the duration of the classical SE sequence is:

$$T = TR \cdot NP_y \cdot N_{ex} \tag{1.9}$$

It is of no use to acquire an image that does not have any contrast between grey and white matter, even if there is strong signal from both of them, so shortening the TR of a sequence (i.e. the time interval between two successive 90° RF waves) to reduce imaging time needs to be considered carefully.

A SE sequence has two essential parameters: TR and TE. TR conditions the longitudinal relaxation of the explored tissues (depending on T1). The longer the TR, the more complete the longitudinal magnetisation regrowth (M_z tends to its steady state value). Reducing TR to 300÷600 ms weights the image in T1 as the differences between the longitudinal relaxations of the tissues' magnetisation

will be highlighted. In the T2-weighted SE sequence the TR and TE parameters are optimised to reflect T2 relaxation. When the TR is long (over 1,600÷2,000 ms), longitudinal magnetisation recovery is complete and the influence of T1 on signal magnitude will be minimised. Associated with long TE (60÷140 ms), the different tissues are better highlighted according to their T2. Long T2 tissues will appear as a hypersignal, as opposed to short T2 structures, which will appear as a hyposignal. A long TR (over 2,000 ms), associated with a short TE (10 to 20 ms) will relatively suppress both the influence of T1 and the effect of T2 on signal magnitude and the contrast obtained will depend on the proton density ρ. The major disadvantage with T2 weighted SE sequences is linked to long TR resulting in prohibitive acquisition times. While SE sequences can be used in clinical practice to obtain good quality anatomical T1-weighted images, faster types of sequence are preferred to obtain T2-weighted images.

In the classical SE sequence, the time interval between reading the echo and the new RF excitation pulse is usefulness. In fast SE sequences, multiple 180° pulses are applied to obtain a SE train. After each echo, the phase-encoding is cancelled and a different phase-encoding is applied to the following echo. This enables to use the time interval after the first echo to receive the echo train in order to fill the other k-space lines in the same slice. Because of the reduced number of repetitions (TR) required, the k-space is filled faster and slice acquisition time is reduced.

Multi-echo SE sequences allow several images of the same slice position without increasing overall acquisition time. The advantage is that the images are obtained with a different contrast, which is useful in characterising certain lesions. After the first echo is obtained, there is a free interval until the next TR. By applying a new 180° pulse, a new echo is received, with the same phase encoding, to build the second image. The echo time of the two images differs and the second image will be more T2-weighted than the first. Typically, these sequences are used to obtain simultaneously ρ- and T2-weighted images.

Finally, in multi-section acquisition, another slice is excited during this time interval with a RF pulse at a slightly different frequency and the corresponding echo is measured. Therefore, for each TR multiple slices can be excited. Slices are usually excited in an interleaved manner to avoid cross-talk effects that could occur in case two adjacent slices were excited.

1.1.2.2 Inversion recovery

Inversion-recovery (IR) is a magnetisation preparation technique followed by an imaging sequence of the SE type. The sequence starts with a 180° RF inversion wave which flips longitudinal magnetisation M_z in the opposite direction. Due to relaxation, longitudinal magnetisation will increase to return to its initial value, passing through null value. After an inversion time (TI), a further 90° RF pulse tilts some or all of the *z*-magnetisation into the *xy*-plane to obtain transverse magnetisation, where the signal is usually rephased with a 180° pulse as in the SE sequence. If a TI is chosen such that when the 90° pulse is applied the longitudinal magnetisation of a tissue is null, the latter cannot emit a signal (absence of transverse magnetisation due to the absence of longitudinal magnetisation). The IR technique thus allows the signal of a given tissue to be suppressed by selecting a TI adapted to the T1 of this tissue.

As longitudinal regrowth speed is characterised by relaxation time T1, IR sequences are weighted in T1. This sequence has the advantage that it can provide very strong contrast between tissues having different T1 relaxation times. IR can also be combined with sequence types other than the standard SE. In particular, it can be combined with fast SE sequences to save considerable time. However, a disadvantage of this technique is that the additional inversion RF pulse makes it less time efficient than the other pulse sequences.

IR can be used to suppress tissues like fluid or fat. In particular, fluid attenuated inversion recovery (FLAIR) is an IR pulse sequence utilised to null signal from fluids that can be used in brain imaging to suppress CSF so as to bring out the periventricular hyperintense lesions, such as multiple sclerosis plaques.

1.1.2.3 Gradient echo sequences

The gradient echo (GRE) sequence differs from the SE sequence in regard to the absence of a 180° RF rephasing pulse and to the excitation pulse (termed the α pulse) which tilts the magnetisation by a partial flip angle between 0° and 90° (Figure 1.4).

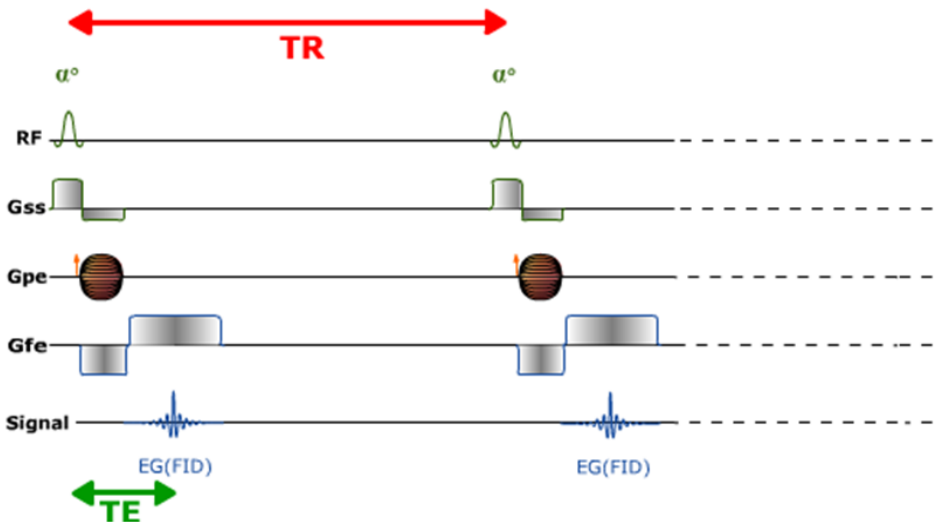

Figure 1.4 – Gradient echo sequence time diagram (source: www.imaios.com).

As there is no 180° RF pulse, a bipolar readout gradient (which is the same as the frequency-encoding gradient) is required to create an echo. The gradient echo formation results from applying a dephasing gradient before the frequency-encoding or readout gradient. The goal of this dephasing gradient is to obtain an echo when the readout gradient is applied and the data are acquired.

The dephasing stage of the readout gradient is in the inverse sign of the readout gradient during data acquisition. Moreover, its dephasing effect is designed so that it corresponds to half of the dephasing effect of the readout gradient during data acquisition. Consequently, during data acquisition, the readout gradient will rephase the spins in the first half of the readout (by reversing the dephasing effect of the dephasing lobe), and the spins will dephase in the second half (due to the dephasing effect of the readout gradient). Data are not acquired in a steady state, where *z*-magnetisation recovery and destruction by α-pulses are balanced. The *z*-magnetisation is used up by tilting a little more of the remaining *z*-magnetisation into the *xy*-plane for each acquired imaging line. The consequence of a low-flip angle excitation is a faster recovery of longitudinal magnetisation that allows shorter TR and TE and decreases scan time. On the other hand, the result of a lower flip angle excitation is a lower tipped magnetisation. As GE techniques use a single RF pulse and no 180° rephasing pulse, the relaxation due to fixed causes is not reversed and the loss of signal results from T2* effects. The signal obtained is thus T2*-weighted rather than T2-weighted. These sequences are thus more sensitive to magnetic susceptibility artefacts than are SE sequences. T2* weighting can be minimised by keeping the TE as short as possible, but pure T2 weighting is not achievable. Gradient echoes have a reduced crosstalk, so that a small or no slice gap can be used.

Proton density-weighted images can be obtained by applying a small flip angle, a long TR and a short TE; to obtain T1-weighted images a large flip angle (>70°), a short TR (less than 50 ms) and a short TE must be applied; finally, for T2*-weighted images a small flip angle, a longer TR (100 ms) and a long TE (>20 ms) are required.

1.1.2.4 Echo Planar Imaging sequences

Echo planar imaging (EPI) is a fast acquisition sequence (tens to hundreds of ms/slice), introduced by Peter Mansfield in 1977. It is used in applications like diffusion, perfusion, and functional magnetic resonance imaging. The EPI sequence is based on: 1) an excitation pulse, possibly preceded by magnetisation preparation; 2) a continuous signal acquisition in the form of a gradient echo train, to acquire total or partial k-space (single shot or segmented acquisition, respectively); 3) readout and phase-encoding gradients adapted to spatial image encoding. In single shot EPI, the complete image is formed from a single data sample (i.e., all k-space lines are filled in one repetition time) of a GRE or SE sequence. The major drawback of EPI is the limited spatial resolution. Moreover, EPI is relatively demanding on the scanner performance, in particular on gradient strengths, gradient switching times, and receiver bandwidth (the scan time is dependent on the spatial resolution required, the strength of the applied gradient fields and the time the machine needs to ramp the gradients). In addition, EPI is extremely sensitive to image artefacts and distortions.

Contrast possibilities include GRE EPI (a single RF excitation pulse is used, with no preparation, and a T2* weighting is obtained), SE EPI (where a pair of 90°-180° pulses is used and a T2 weighting is obtained), and IR EPI (with a 180° inversion pulse to prepare magnetisation, followed by an RF excitation pulse to obtain T1 weighting). The time diagram for SE and GRE EPI sequences is shown in Figure 1.5. By periodically fast reversing the readout or frequency encoding gradient, a train of echoes is generated.

Several trajectories can be used to fill the k-space. As stated above, a readout gradient is continuously applied to constitute the echo train (a GRE train in Figure 1.6), with positive and negative alternations.

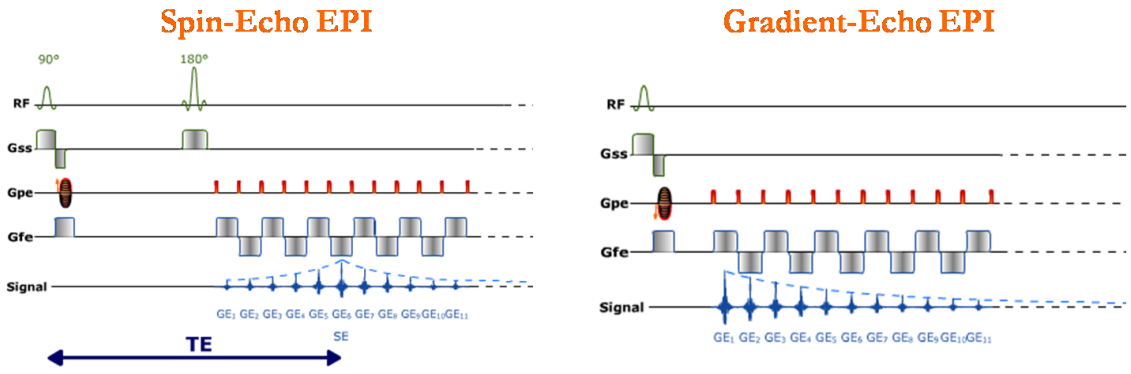

Figure 1.5 – Spin echo and gradient echo EPI sequences time diagrams (source: www.imaios.com).

The k-space will be scanned from left to right and back, with each echo. At the same time, the phase encoding gradient may be permanent and constant (nonblipped EPI) giving a "zigzag" global trajectory, or intermittent (blipped EPI) at each echo onset, giving a rectilinear trajectory. In the case of spiral k-space filling, phase encoding and readout gradients will have a sinusoidal growing envelope.

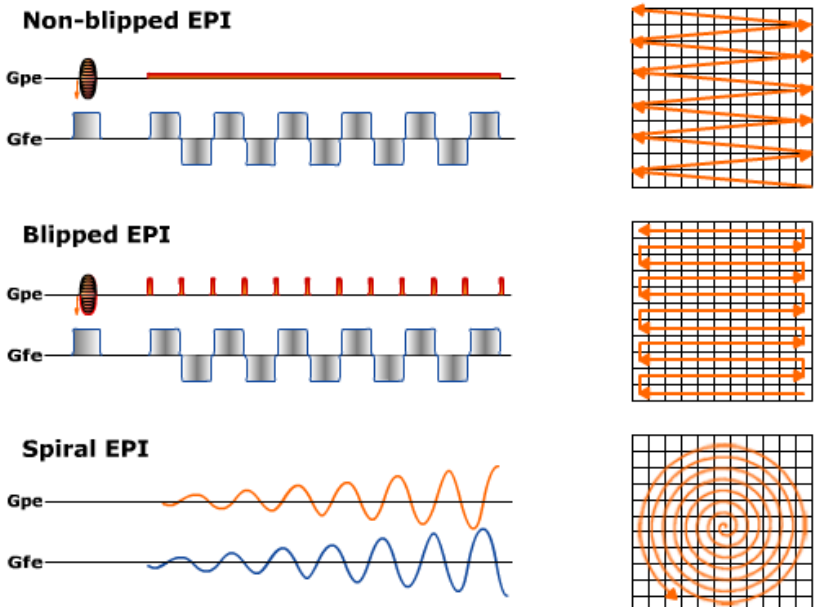

Figure 1.6 – Examples of EPI sequences and corresponding trajectories in the k-space (source: www.imaios.com).

1.1.2.5 3D imaging sequences

In 3D acquisition sequences, a complete volume (or a thick slice, or slab), rather than a single slice, is excited at each repetition. Therefore more signal (coming from the whole volume) is recorded, with less noise. Spatial encoding is achieved by adding phase encoding in the third dimension in relation to the phase and frequency encodings used in 2D imaging (Figure 1.7). Phase encoding is followed by a readout gradient during which the FID is sampled. The assembled FIDs are then subject to a 3D Fourier transform yielding the volume image. To fill all the 3D k-space, the number of repetitions must be multiplied of a factor equal to the number of partitions in the third dimension. Given the large amount of data needed to fill the 3D k-space, either very short TR sequences (gradient echo type) are used, or faster k-space filling methods. The duration of the sequence is given by:

$$TR = NP_y \cdot NP_z \cdot N_{ex} \tag{1.10}$$

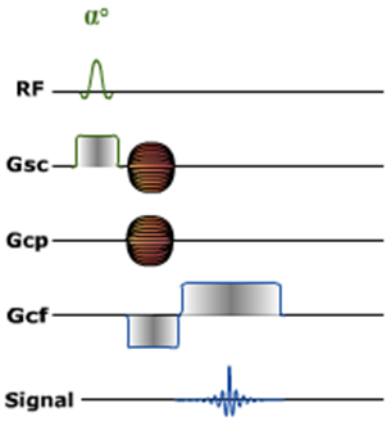

Figure 1.7 – 3D MRI sequence time diagram (source: www.imaios.com).

1.2 Overview of neuroimaging techniques

Neuroimaging falls into the two broad categories of structural and functional imaging. Structural neuroimaging deals with the structure of the brain and the diagnosis of intracranial diseases and injuries. Functional imaging allows diagnosing metabolic diseases and lesions on a finer scale. Furthermore, functional neuroimaging is used to visualise the relationship between activity in certain brain areas and specific mental functions for neurological and cognitive science research and for building brain-computer interfaces.

Several approaches exist, based on different physical principles and technologies, to directly or indirectly image the structure and function of the brain, with each technique being designed to convey distinct types of information, depending on the scientific or medical question at hand. Technologies employed in neuroimaging include, among others, MRI, CT, nuclear medicine imaging techniques such as positron-emission tomography (PET) and single-photon-emission computed tomography (SPECT), diffuse optical imaging (DOI), event-related optical signal (EROS), magnetoencefalography (MEG).

1.2.1 Techniques for studying brain structure

The most common approaches to study brain structure are CT and MRI. CT scanning uses a series of X-rays, i.e. an ionizing radiation, to acquire images of the head taken from many different directions. X-ray images stem from the interaction between the X-rays themselves and the electron cloud of the atoms. This is a diffraction technique and the resolution that can be obtained is therefore related to the wavelength of the radiation. In CT, a numerical integral

calculation (the inverse Radon transform) is performed on the measured X-ray series to estimate how much of an X-ray beam is absorbed in a small volume of tissue. CT can produce high resolution images and is frequently used for quickly imaging brain injuries. It is more widely available than MRI, less expensive, faster (thus suffering less from motion artefacts), and may be less likely to require the patient to be sedated or anaesthetised as a result of being less enclosed and noisy, and therefore less psychologically intimidating. In the past, CT was limited to acquiring images in the axial (or near axial) plane (the scans used to be called computed axial tomography scans). However, the development of multi-detector CT scanners with near-isotropic resolution allows the CT scanner to produce data that can be retrospectively reconstructed in any plane with minimal loss of image quality.

Similarly to CT, also MRI scanners are able to generate multiple 2D slices of tissue in any plane (including oblique planes) and 3D reconstructions. Contrast in CT images is generated purely by X-ray attenuation, while a variety of properties may be used to generate contrast in MR images. By variation of scanning parameters, tissue contrast can be altered to enhance different features in an image. MRI is best suited for soft tissue than CT and for purposes of tumour detection and identification in the brain it is generally superior. Both CT and MR images may be enhanced by the use of contrast agents. Contrast agents for CT (e.g., iodine or barium) contain elements of a high atomic number, relative to tissue, while contrast agents for MRI (e.g., gadolinium and manganese) have paramagnetic properties, used to alter tissue relaxation times. MRI uses non-ionizing RF signals. As compared to both X-rays (as in CT) and radioisotopes (as in PET and SPECT), the energy used in MRI is nine orders of magnitude less. It is known to be largely the high energy of the radiation that causes biologic damage to cells (particularly to their DNA) and therefore the extremely low energy of the RF electromagnetic radiation employed in MRI (when compared to X-rays) is far less likely to cause significant biologic

damage. As a consequence, MRI is also best suited for cases when a patient is to undergo the exam several times successively in the short term.

Recent advances in structural MRI techniques include semi-quantitative and quantitative imaging, offering insight into specific tissue properties. These techniques include T1-weighted imaging, diffusion-weighted imaging (DWI), and quantitative relaxometry.

T1-weighted images are widely used in brain morphometry, providing sufficient contrast between grey and white matter in most cortical areas. The main limitation of T1-weighted imaging is the contrast decrease in subcortical structures with high iron content, reducing the reliability of automated tissue classification algorithms.

DWI is sensitive to Brownian motion of molecules, thus utilising proton behaviour in brain tissue water. In an isotropic medium, water molecules naturally move randomly according to turbulence and Brownian motion. In biological tissues however, where the Reynolds number is low enough for flows to be laminar, the diffusion may be anisotropic. A molecule inside the axon of a neuron has a low probability of crossing the myelin membrane. Therefore the molecule moves principally along the axis of the neural fiber. If it is known that molecules in a particular voxel diffuse principally in one direction, the assumption can be made that the majority of the fibers in this area are going parallel to that direction. The recent development of diffusion tensor imaging (DTI) enables to describe the brain tissue water diffusion properties in three ways: by predominant diffusion directions, by degree of anisotropy or by magnitude of diffusion (Basser and Pierpaoli, 1996; Le Bihan et al., 2001; Mori and Zhang, 2006). Tissue loss is commonly associated with mean diffusivity increases owing to enlarged extracellular spaces. Fractional anisotropy decreases are caused by reduction in cellular boundaries hindering diffusion. Fractional anisotropy and mean diffusivity estimates in grey matter are thought to represent variable densities of myelinated axons because directional coherence in grey

matter is almost negligible. DTI also enables to make brain maps of fiber directions to examine the anatomical connectivity of different regions in the brain by using tractography. It has been used to demonstrate subtle abnormalities in a variety of diseases (including stroke, multiple sclerosis, dyslexia, and schizophrenia) and is becoming part of many routine clinical protocols. Figure 1.8 shows examples of fractional anisotropy and fiber tracking images obtained from applying DTI.

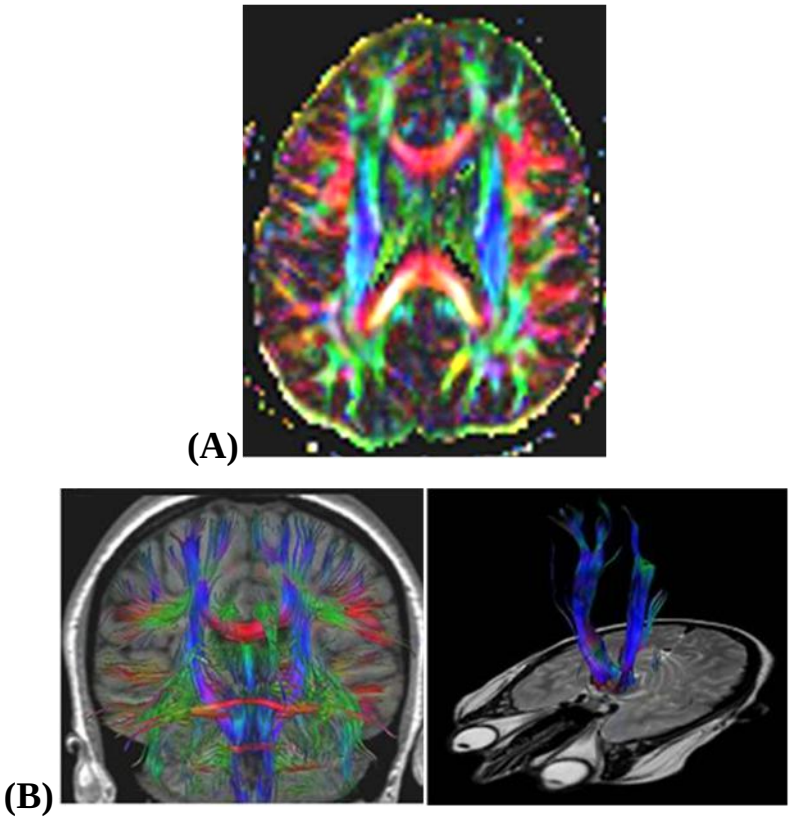

Figure 1.8 – Diffusion tensor imaging. (A) Fractional anisotropy. (B) Fiber tracking. Colours represent the direction of fibers. Images were acquired with the 1.5 T scanner of the Imaging Department of Palidoro at Bambino Gesù Children's Hospital.

Finally, relaxometry comprises advances in quantitative mapping of magnetisation transfer, T1 and T2* relaxation based on well-defined biophysical models. Magnetisation transfer is considered a direct measurement of myelin (and other macromolecules), T1 relaxation shows robust sensitivity to tissue water, whereas T2* depends on ferritin content. Using magnetisation transfer

maps for tissue classification in basal ganglia and thalamus may be useful owing to superior grey matter vs. white matter contrast.

Computational neuroanatomy comprises numerous automated or semiautomated volume-based, surface-based and shape-based techniques developed for exploring brain structure in cross-sectional and longitudinal study designs (Draganski and Bhatiad, 2010).

Manual and semiautomated region-of-interest (ROI) approaches dominated the field of volumetry until computational neuroanatomy offered feasible and unbiased ways for performing whole-brain analyses. Although widely accepted in the medical community, manual 2D or 3D ROI measurements are labour consuming, subject to inter-rater variability and potentially insensitive to concomitant changes in other brain regions.

Voxel-based morphometry (VBM) in the framework of statistical parametric mapping represents a fully automated approach for general analysis of structural MRI images and volume assessment within and between cohorts. This technique will be described in detail in Chapter 2.

Finally, in surface-based methods, following a segmentation step with computation of tissue class surfaces, surface deformation algorithms are applied to obtain close matching of grey matter and white matter boundaries, such that cortical thickness can be calculated on the basis of the distance between surfaces. Image registration can be performed either in a canonical manner or using “inflated” spherical representations of the brain and surface-based coordinate systems. Subsequently, cortical thickness data are smoothed for statistical analysis (Dale et al., 1999).

1.2.2 Techniques for studying brain function

The idea of functional localisation within the brain has only been accepted for the last century and a half. It was first developed from the mid 19th century by clinicians such as Pierre Paul Broca, who discovered the speech production centre of the brain located in the ventroposterior region of the frontal lobes, and Angelo Mosso, who created the first crude neuroimaging technique by recording the pulsation of the human cortex in patients with skull defects following neurosurgical procedures, and inferred that during mental activities blood flow increases to the brain. Most of the information available on the human brain came from subjects who had sustained major head wounds, or who suffered from various mental disorders. By determining the extent of brain damage, and the nature of the loss of function, it was possible to infer which regions of the brain were responsible for which function. At mid 20th century, the neurosurgeon Wilder G. Penfield stimulated the brain of patients suffering from severe epilepsy with electrical probes while the patients were conscious on the operating table (under only local anaesthesia), and observed their responses. In this way he could more accurately target the responsible areas of the brain, reducing the side-effects of the surgery. This technique also allowed him to create maps of the sensory and motor cortices of the brain showing their connections to the limbs and organs of the body (Figure 1.9).

With the development of the imaging techniques of CT and MRI it was possible to be more specific as to the location of damage in brain injured patients. Electroencephalography (EEG) opened up new possibilities in studying brain function in normal subjects. However, it was the advent of the functional imaging modalities of PET, SPECT, functional magnetic resonance imaging (fMRI), and MEG that led to a new era in the study of brain function.

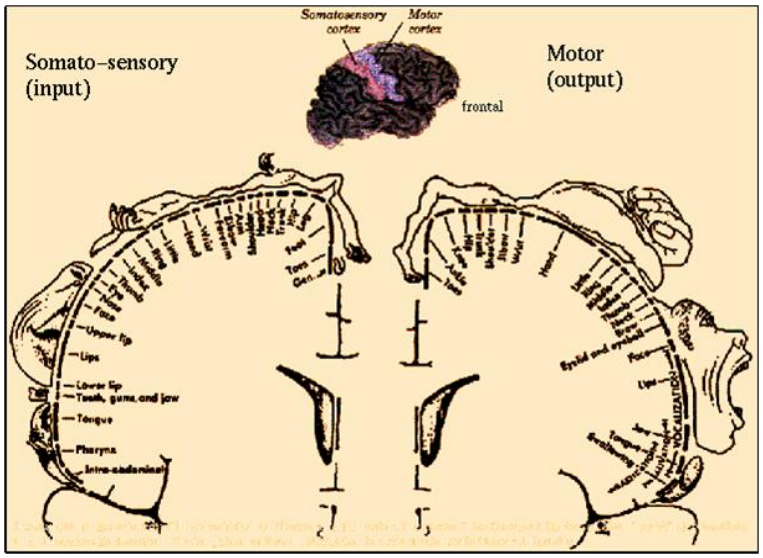

Figure 1.9 – Cortical homunculus: representation of the anatomical divisions of the primary motor cortex and the primary somatosensory cortex.

Table 1.2 shows the brain properties exploited by different neuroimaging techniques together with the classification of these techniques with respect to their invasiveness. It is interesting to note how techniques for brain function may be split between those utilising single-neuron or multi-unit recordings and those mapping the brain as subjects perform various high-level tasks (Figure 1.10).

Method	Brain property used	Invasiveness
Single-cell / multi-unit recordings	Electrical	Invasive
EEG/ERP	Electrical	Non-invasive
TMS	Electromagnetic	Non-invasive
MEG	Magnetic	Non-invasive
PET	Haemodynamic	Invasive
fMRI	Haemodynamic	Non-invasive

Table 1.2 - Invasiveness of neuroimaging techniques and brain property exploited.

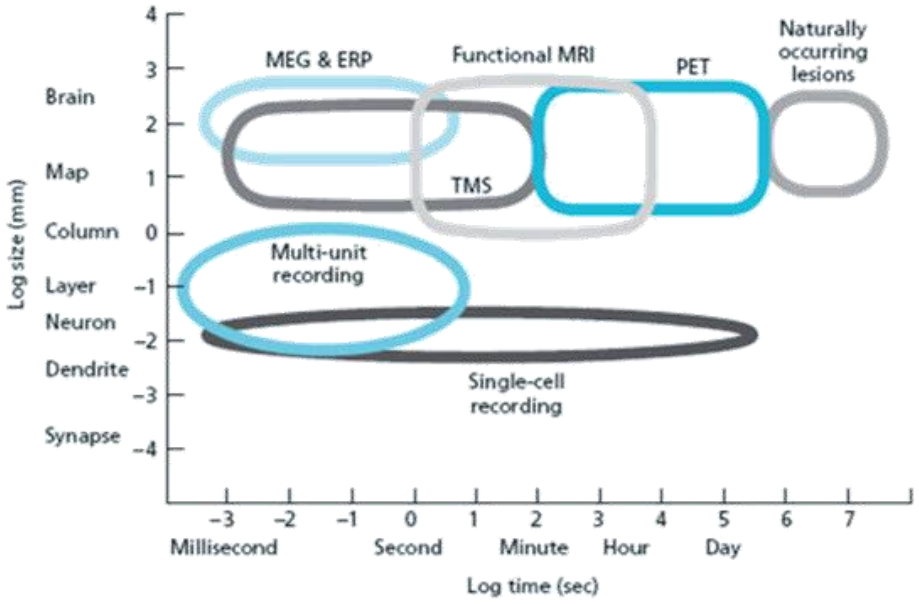

Figure 1.10 – Spatial and temporal resolution of techniques for studying brain function.

Single- and multi-unit recording are invasive techniques which make use of tiny tungsten or platinum-iridium alloys electrodes inserted into the brain for the purpose of measuring the action potentials (firing) from a single neuron or a small group of neurons. These techniques have been applied in animal studies and have shed a light on basic emotional and motivational processes.

The goal of studies in higher-level activities is to determine how a network of brain areas collaborates to perform each task.

Multichannel EEG records the electrical activity of the brain, arising from the synchronous firing of the neurons, via electrodes placed on the scalp. EEG works by recognising changes and measuring differences in voltage between different parts of the brain and looks for abnormalities in the patterns of activity. In particular, event-related potentials (ERPs) are used to measure the response of EEG signals to specific stimuli. In fact, because of its extremely high temporal resolution, EEG was the first neuroimaging tool to depict the working of the human brain in near real time. EEG has been used routinely for many years, and is a widely-accepted technique featured in a great deal of medical literature.

Currently, EEG is used to distinguish between different types of seizures, to diagnose sleep disorders, to examine head injuries, tumours, infections and neurodegenerative diseases, and to confirm brain death. Much of the benefit of EEG is that it is non-invasive, safe, and low-cost. However, it has limited spatial resolution compared to other techniques and the inverse problem of accurately finding out the originating location of the brain waves is very difficult to solve.

Similarly to EEG, MEG is a non invasive technique that gathers data through electrodes placed on the scalp. However, rather than measuring electrical voltage, MEG measures the magnetic fields produced by electrical currents in the brain. While the skull and the tissue surrounding the brain affect the electrical impulses measured by EEG, they interfere much less in the magnetic fields measured by MEG. This difference allows for greater accuracy when trying to identify the locations of brain functions. Clinically, MEG can be very useful in locating brain tumours and the sources of epileptic seizures, as well as accurately pinpointing defects in primary auditory, somatosensory, and motor areas. However, MEG alone is not an efficient diagnostic tool when used during complex cognitive tasks. In these instances, it is often used in combination with other imaging techniques, particularly fMRI. In these cases, MEG is used to measure the time courses of brain activity.

Transcranial magnetic stimulation (TMS) is a relatively recent innovation in brain imaging. In TMS, a coil is held near a subject’s head to generate magnetic field impulses that stimulate underlying brain cells to make the subject perform a specific action. Using this technique in combination with MRI, maps of the brain performing very specific functions can be generated. In addition to fMRI, the activation of TMS can be measured using EEG or near infrared spectroscopy (NIRS).

Nuclear medicine (NM) imaging techniques provide 3D *in vivo* information about biodistribution of tracer molecules labelled with radioactive isotopes. NM methods are often referred to as molecular imaging because they

are able to localise molecular receptor sites, study biological markers expressed by diseased cells, and image the presence and extent of specific disease processes. Their strength is in the fact that they can be used in tracer studies where a radiopharmaceutical is selectively absorbed in a region of the brain. Furthermore, NM techniques have an excellent sensitivity, which is several orders of magnitude better than MRI and CT for *in vivo* detection of metabolic changes.

SPECT uses gamma rays to directly measure regional cerebral blood flow (rCBF) and indirectly measure metabolic activity in the brain. It has been used to look at psychiatric and neurological diseases, including dementia, stroke and seizures disorders. There are a range of radiotracers that can be injected into the bloodstream and bind to specific receptors in the brain. Detection is carried out using a gamma camera (a scintillation detector consisting of a collimator, a crystal of Sodium Iodide, and a set of photomultiplier tubes). By rotating the gamma camera around the head, a 3D image of the distribution of the radiotracer can be obtained by employing filtered back projection. Data can actually be reconstructed from almost any angle. Advantages of SPECT include speed and portability. Over time, this technology has improved vastly to show high resolution images from deeper within the brain. The radioisotopes used in SPECT have relatively long half lives (a few hours to a few days) making them easy to produce and relatively cheap. This represents the major advantage of SPECT as a brain imaging technique, since it is significantly cheaper than either PET or fMRI. However it lacks good spatial and temporal resolution, and there are safety aspects concerning the administration of radioisotopes to the subject, especially for serial studies.

Similarly to SPECT, PET makes use of radioactive markers injected into the bloodstream or inhaled by the subject. The marker substances can be pharmacologically designed to participate in certain metabolic reactions. PET scans differ from other imaging technology because they can measure metabolic

changes at the cellular level, which usually occur long before any structural changes detected by a CT scan or an MRI. PET has two major advantages over SPECT, namely better spatial resolution and greater sensitivity. This comes from using positron emitters, such as ^{15}O and ^{18}F as the radionuclide. When such nuclei decay they emit a positron, that is a particle with the same rest mass as an electron but with a positive charge. Once the positron is emitted, it travels a short distance before colliding with an electron. The annihilation of the two particles creates two photons each with energy 511 keV. In order to conserve momentum, the two photons are emitted at virtually 180° to each other, and it is these photons that are detected in a ring of scintillators and photomultiplier tubes surrounding the head. Opposite pairs of detectors are linked so as to register only coincident photons, thus defining a set of coincidence lines. Reconstruction of these lines by filtered back projection gives an image of the source of the annihilation. Since the detectors only record the site of the annihilation, resolution in a PET scanner is limited by the distance travelled by the positron through the tissue before it meets an electron. This fundamentally restricts the resolution of the scanner to a few millimetres at best. The positron emitters used in PET have short half lives, of the order of 2'÷100'. This means that the beta-decaying isotopes must usually be produced at the site of the scanner, using an expensive cyclotron. Furthermore, their rapid decaying makes their usage difficult. However, this short half life means that dynamic studies of brain function can be carried out using this technique. Usually two cognitive states are imaged in functional studies with PET (one active and one resting) and by subtracting these two states a map of the regions of the brain responsible for performing the task can be obtained. The fast decaying improves the image contrast, but the temporal resolution is not very good due to the slowness of the metabolic changes. Additionally, injecting radioactive substances into the body is invasive and potentially harmful. Thus, PET is mostly used in studying severe illnesses.

fMRI is a method for measuring activation of brain areas based on the magnetic properties of haemoglobin, which in turn depend on the amount of oxygen carried by the haemoglobin molecules. Therefore, the contrast mechanism used in fMRI is endogenous, which makes fMRI a non-invasive technique. This contrast mechanism, discovered in 1990 by Seiji Ogawa (Ogawa et al., 1990), is known as blood oxygen level dependent (BOLD) contrast (actually, the first successful fMRI experiment, performed by John W. Belliveau in 1991, made use of gadolinium as an exogenous contrast: Belliveau et al., 1991). To study brain function using fMRI, it is necessary to repeatedly image the brain, whilst the subject is presented with a stimulus or required to carry out some task. The success of the experiment is dependent on the scanning sequence used, the design of the stimulus paradigm, and the way acquired data are analysed. The imaging sequence must produce T2*-weighted images. This means that a GRE sequence is most commonly used. Most research is carried out using EPI since its fast acquisition rate allows the activation response to short stimuli to be detected. EPI also has the benefit of reduced artefacts from subject motion. The magnitude of the static field used is critical to the percentage signal change obtained on activation. This is because susceptibility differences have a greater signal dephasing effect at higher fields. The non-invasive nature of fMRI and the high spatial resolution of MRI have led to many advances in the investigation of several aspects of brain function, both in normal states and in pathologic conditions.

Advantages of fMRI over PET include the relatively short duration of the total scan time and the in-plane resolution. PET studies require multiple acquisitions, and, therefore, extended imaging times. Furthermore, the expected resolution of PET images is much larger than the usual fMRI voxel size. Additionally, PET usually requires that multiple individual brain images are combined in order to obtain a reliable signal. Table 1.3 compares the

characteristics of fMRI and PET. More in-depth on fMRI principles will be given in Chapter 3.

	fMRI	PET
Contrast agent	Endogenous	Exogenous (radiotracer)
Temporal resolution	Low	Lower than fMRI
Spatial resolution	Higher than PET	High (identification of specific receptors)
Sensitivity	Low	High

Table 1.3 – Comparison of fMRI and PET characteristics.

The physiological principles on which NM techniques and fMRI are based deserve a further consideration. Measurement of metabolic processes and rCBF is useful in studying brain function because these parameters are closely related to neural activity. Following an endogenous or exogenous stimulus, variations are elicited in the electric activity of neurons and subsequently in the haemodynamic processes. However, metabolic and haemodynamic variations follow the neuronal electrical activity with a time delay. Furthermore, haemodynamic processes may be partially misplaced with respect to the location of the electrical activity. Therefore, techniques such as SPECT, PET and fMRI, which do not directly measure the electrical activity of neurons, should be considered as indirect method to study neuronal activity (Table 1.4).

	Measurement of electrical parameters	Measurement of metabolic / haemodynamic parameters
Measurement of neuronal activity	Direct	Indirect
Temporal resolution	Excellent	Low
Spatial resolution	Low (unless invasive)	Excellent

Table 1.4 – Comparison of neuroimaging techniques measuring electrical and metabolic/haemodynamic parameters.

CHAPTER 2: Voxel-Based Morphometry

2.1 Principles of VBM

Since the introduction of MRI in research and clinical practice, several semiautomated and automated computational neuroanatomy methods have been developed (Draganski and Bhatiad, 2010). During the last two decades, the study of neuroanatomic differences between groups of subjects has been developed by means of objective morphometric techniques, such as Voxel-based morphometry (VBM). VBM is a technique consisting in processing and analysing MRI data of groups of subjects to allow a voxel-by-voxel assessment of differences in structures of the brain (Good et al., 2001). The experimental question that VBM seeks to answer is whether a group of subjects shows specific structural features that could be related to a pathology or to a common characteristic of the subjects in the group. VBM has been applied to study a number of pathological conditions as well as to groups of healthy subjects (Mechelli et al., 2005). This automated technique allows evaluating regional volumetric alterations without *a priori* hypotheses about their localisation. This approach is minimally operator-dependent, in that it avoids the potential confounds and challenges associated with ROI hand-tracing methods and enables us to make a more reliable evaluation of alterations in cerebral tissues.

VBM enables to reveal statistically significant local "concentration" and volume morphological differences between samples, while discounting macroscopic individual anatomic differences (Ashburner and Friston, 2000). The original aim of VBM was to study so-called mesoscopic anatomical differences, by modelling macroscopic differences by deformation fields that warp individual brains to a common reference space. However, the precise definition of what constitutes mesoscopic and what constitutes macroscopic is unclear (Bookstein, 2001). Another view would be that the analysis of mesoscopic differences could be considered an examination of registration

errors. If image registration were exact, then there would be no differences to examine. The original aim was then modified by starting to investigate volume rather than concentration differences. Pre-processed data were scaled such that the total volume of tissue in each structure is preserved after warping the data to a standard reference space. This correction is by scaling by the Jacobian determinant of the deformation and is known as "modulation". The result is that the pre-processed data represent a quantitative measure, i.e. tissue volume per unit volume of spatially normalized image (Ashburner, 2009).

2.1.1 Applications of VBM

VBM studies have been successful in characterising structural brain differences in a variety of diseases including developmental and congenital disorders, schizophrenia, autism, bipolar disorders, cluster headache, temporal lobe epilepsy (Keller et al., 2004), supranuclear palsy, Down's syndrome (White et al., 2003), herpes simplex encephalitis, Parkinson's disease, Huntington's disease, Alzheimer's disease, multiple sclerosis, and primary progressive aphasia. These studies contributed both to the understanding of how the brain changes in these disorders and of how brain changes relate to characteristic clinical features (Mechelli et al., 2005; Whitwell, 2009). Applications of VBM to the study of anorexia nervosa will be described in detail in Section 2.3.

Although results from VBM studies are generally difficult to validate, studies have compared results of VBM analyses to manual and visual measurements of particular structures and have shown relatively good correspondence between the techniques, providing some confidence in the biological validity of VBM (Giuliani et al., 2005; Whitwell, 2009).

VBM was originally devised to examine structural abnormalities in patients. However, the technique can also be used with healthy subjects. Several

VBM studies, motivated by reports that experience-related structural changes may occur in the brain of animals, investigated the impact of learning and practice on brain structure (Draganski et al., 2004; Gaser and Schlaug, 2003; Maguire et al., 2000; Mechelli et al., 2004). These studies, which will be described in Chapter 4, have shown structural changes at the macroscopic level, thus challenging the traditional view that the acquisition of new skills only impacts on brain function. More recently, following these results, studies with VBM provided evidence of structural neuroplasticity in patients with stroke after a rehabilitative training (Gauthier et al., 2008).

2.1.2 Processing of structural data

The basic idea behind VBM is to identify a particular tissue type in the scan of each subject, to warp the tissue maps to a common anatomical space, to spatially blur the deformed tissue maps, and to statistically analyse the pre-processed data. Several variations in the implementation of the VBM pre-processing algorithm have been proposed in literature (Senjem et al., 2005). The most common strategy, however, is the so-called "optimised" VBM. This approach involves spatially normalising subjects' brain images to a standard space by matching grey matter (GM) in these images to a GM reference, or by matching white matter (WM) to a WM reference. With respect to the standard approach, optimised VBM prevents confounding effects of non-brain (e.g., scalp, skull) structural variability from compromising the morphological analysis of ROIs as a consequence of the low spatial frequency deformation field applied while normalising individual scans to a standard stereotactic space (Good et al., 2001; Mechelli et al., 2005). This is obtained by using optimised normalisation parameters for each kind of tissue, thus ensuring that highlighted statistically significant differences can be attributed to the kind of tissue being

analysed. This approach includes an iterative algorithm combining voxel-by-voxel parcellation (i.e., segmentation) of MRI data into different tissue classes with registration to a common anatomical space (i.e., normalisation). The following processing steps compose the optimised VBM algorithm (Figure 2.1):

- registration of the individual images to a reference stereotactic space;
- segmentation of the registered images in GM, WM, CSF, and non-brain voxels;
- spatial normalisation of the original structural images in native space to the GM (or WM) *a priori* probability map in the template stereotactic space;
- segmentation of the images obtained from the optimised normalisation;
- smoothing of the segmented GM (or WM) images with a Gaussian kernel.

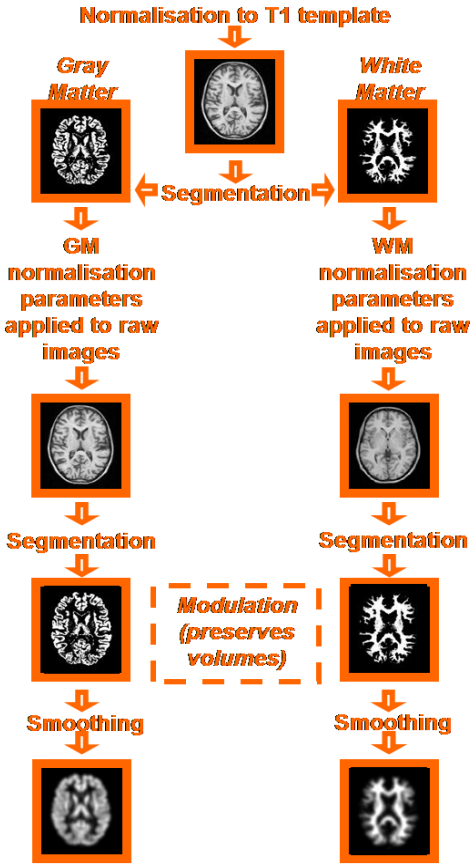

Figure 2.1 – Schematic representation of the optimised pre-processing for voxel-based morphometry.

2.1.2.1 Segmentation

Segmentation of brain images in maps of different tissues is based on classifying voxels using a mixture of Gaussians model, which represents the intensity probability density by a number of Gaussian distributions. In other words, the assumption is made that voxels intensity in each cluster (i.e., tissue) is Gaussian. This approach is constrained anatomically by tissue specific probability images, i.e. maps of *a priori* probability for GM, WM and CSF. Usually, modified versions of the tissue probabilistic atlases of the International Consortium for Brain Mapping (ICBM) are used. These atlases, in turn, are derived from 452 T1-weighted scans aligned with an atlas space, corrected for scan inhomogeneities, and classified into GM, WM and CSF (Figure 2.2).

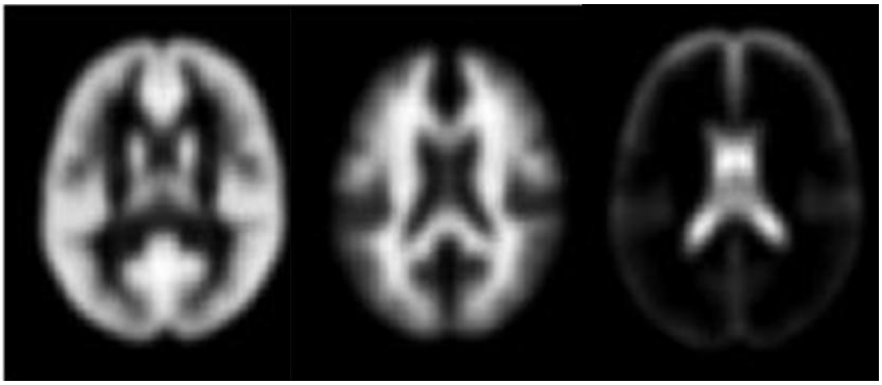

Figure 2.2 – Tissue probability maps. Axial sections of *a priori* probability maps for grey matter, white matter, and cerebro-spinal fluid are shown.

Tissue classification requires the raw images to be registered with the tissue probability maps (Ashburner et al., 1997). A nonlinear deformation field is estimated that best overlays the tissue probability maps on the individual subjects' image. After registration, these maps represent the prior probability of different tissue classes being found at each location in an image. Bayes rule can then be used to combine these priors with tissue type probabilities derived from

voxel intensities, to provide the posterior probability of each voxel to belong to a given tissue type (belonging probabilities are assigned by normalising to one).

This procedure is inherently circular, because the registration requires an initial tissue classification, and the tissue classification requires an initial registration. Moreover, several factors may negatively influence normalisation (which will be described in Section 2.1.2.2), including noise, artefacts, partial volume effects, intensity inhomogeneity and differences between sequences. Normalising segmented tissue maps is typically more robust and precise than using the original images. This is a further motivation for simultaneous segmentation and normalisation in a unified model.

This circularity is resolved in the Statistical Parametric Mapping (SPM) tool (The Wellcome Department of Imaging Neuroscience, University College, London, UK; www.fil.ion.ucl.ac.uk/spm) by combining both components into a single generative model (Ashburner and Friston, 2005). This model also includes parameters that account for image intensity non-uniformity determined by the low spatial frequency intensity variations of the magnetic field. Model parameters are iteratively estimated to obtain a maximum a posteriori solution by alternating among classification (i.e. estimate of the number of voxels, of mean and variance of voxels intensity in each cluster, and of belonging probabilities of each voxel), bias correction and registration steps. This approach provides better results than simple serial applications of each component.

MR images are usually corrupted by a smooth, spatially varying artefact that modulates the intensity of the image (the so-called bias field). These artefacts, although not usually a problem for visual inspection, can impede automated processing of the images. Bias corrected versions of images can be produced, which should have more uniform intensities within the different types of tissues. Figure 2.3 shows a 2D projection of the estimated bias field for the 1.5 T Siemens Magnetom MRI scanner of the Imaging Department at Bambino Gesù Children’s Hospital (Ritrovato et al., 2007, AIFM Congress).

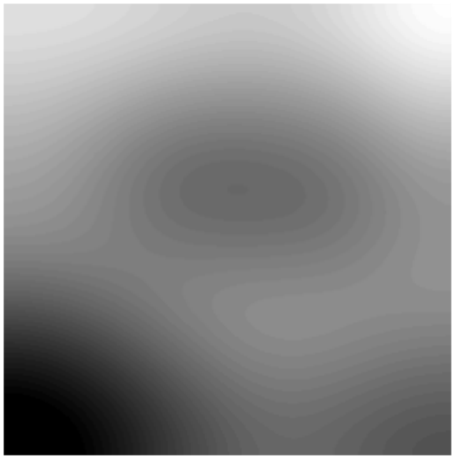

Figure 2.3 – Estimated inhomogeneity field of the 1.5 T Siemens Magnetom MRI scanner of the Imaging Department at Bambino Gesù Children's Hospital. The minimum estimated multiplicative factor of the bias field was 0.4996, with a maximum value of 2.0017, indicating that the bias field may markedly influence image intensity.

Figure 2.4 shows the effects of applying the segmentation procedure to a raw T1-weighted image.

Figure 2.4 – Axial sections of grey matter (left), white matter (centre) and cerebro-spinal fluid (right) obtained from the segmentation of the raw T1-weighted image of a control subject for the research study described in Section 2.3.

A problem with the segmentation algorithm is that of partial volume effects. Because the model assumes that all voxels contain only one tissue type,

the voxels that contain a mixture of tissues may not be modelled correctly. In particular, those voxels at the interface between WM and ventricles will often appear as GM (Ashburner and Friston, 1999). The problem of partial volume increases with the size of voxels, or after a smoothing procedure. Due to partial volume, the distributions of the intensities of the various clusters may differ from a normal distribution. To account for partial volume effects, multiple Gaussians per tissue class have been introduced in the model.

2.1.2.2 Normalisation

Individual brains differ in size and shape. Normalisation stereotactically (i.e., spatially) normalises MRI images into a standard space defined by some template image. The best known stereotactic space is that described in the atlas of Talairach and Tournoux (Figure 2.5.A). Most research groups have moved away from the Talairach and Tournoux template, based on a single brain, in favour of a population standard defined by many MRIs. There are a number of such standard templates developed by the Montréal Neurological Institute (MNI) and by the ICBM. However, coordinates from these spaces may still be converted into coordinates from the Talairach and Tournoux space. The MNI T1 template is shown in Figure 2.5.B.

Methods for image normalisation can be broadly classified in label-based and intensity-based approaches. In label-based methods, homologous features in the source and reference images (e.g., points, lines, surfaces) are labelled and then images are warped to align the landmarks. The main limits of this approach are that features must often be identified manually (which is time consuming and subjective) and that there may be few identifiable landmarks. In intensity-based methods, a spatial transformation must be identified that maximises some voxel-wise similarity measure. The drawbacks of intensity-based approaches are

that they assume correspondence in intensity between the source and reference images and that they are susceptible to poor starting estimates. Before transforming, image position should be adjusted to improve the starting estimate, thus reducing risk of local minima.

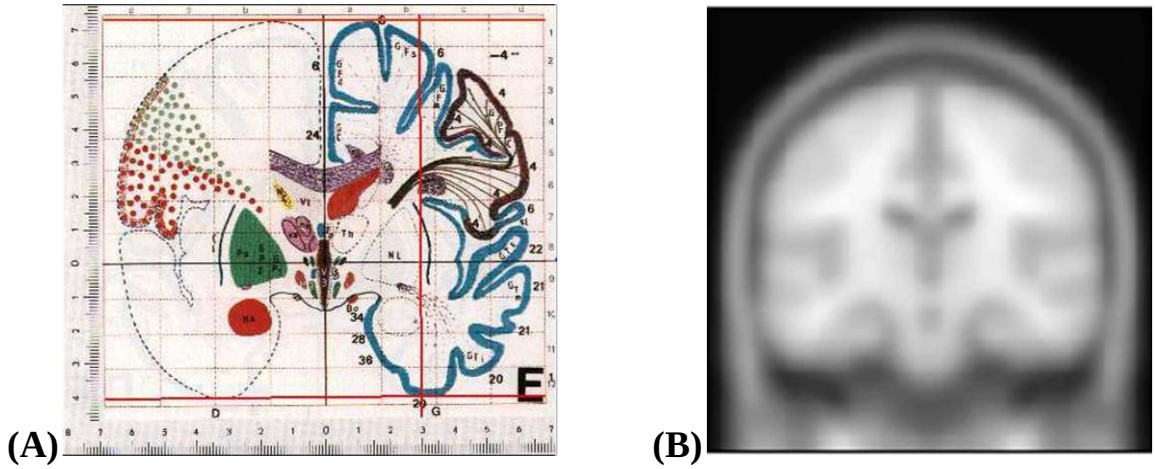

Figure 2.5 – (A) The atlas of Talairach and Tournoux is the best known stereotactic space and coordinates in published studies often still refer to this atlas. (B) The Montréal Neurological Institute (MNI) T1 template. The MNI developed a series of standard templates following the convention of Talairach and Tournoux, but these templates are obtained from a set of MRI scans on multiple subjects and don't match the particular brain of the Talairach and Tournoux atlas.

Algorithms used to match structural (or functional) MRI to a template are based on cost functions using voxel intensities. Generally, the algorithms work by minimising the sum of squares difference between the image which is to be normalised, and the template image. Affine transformations with relatively few parameters are typically used to initialize nonlinear transformations. The nonlinear transformation consist in warps with hundreds to thousands degrees of freedom from which a deformation field is obtained, i.e. a vector field where three values are associated with each location in the field (the field maps from coordinates in the normalised image back to coordinates in the original image). Affine and nonlinear registration into a standard space can be made more robust

by regularisation (penalising excessive stretching or shrinking), that is, by influencing the smoothness of the deformation fields.

Therefore, the first step of the normalisation is to determine the optimum 12-parameter affine transformation to fit the overall shape and size of the brain. The 12 parameter allow for translating, rotating, zooming and shearing. The registration searches for the solution that maximises the *a posteriori* probability of it being correct, i.e., it maximises the product of the likelihood function (derived from the residual squared difference) and the prior function (which is based on the probability of obtaining a particular set of zooms and shears).

The affine registration is followed by estimating nonlinear deformations, whereby the deformations are defined by a linear combination of 3D discrete cosine transform (DCT) basis functions (Ashburner and Friston, 1999; Friston et al., 1995). With the field of view of the MNI templates and the typical values of spatial frequency cut-off for normalisation in the SPM tool (only DCT bases of periods longer than the cut-off are used to describe the warps), the deformation field is described by over one thousand parameters for each dimension. These parameters represent the coefficients of the deformations in three orthogonal directions. The matching involves simultaneously minimising the residual mean squared difference between the source image and the template and the squared distance between deformation fields and their expected values. Without this regularisation, the nonlinear spatial normalisation can introduce unnecessary warping into the spatially normalised images. The result of the estimate step is a set of warps, which can subsequently be applied to the source image. The effects of normalisation are shown in Figure 2.6.

Spatially normalised images may preserve the total amount of signal (in which case they are referred to as “modulated” images) or the intensities of the original images (areas that are expanded during warping are correspondingly reduced in intensity; in this latter case they are referred to as “non-modulated”).

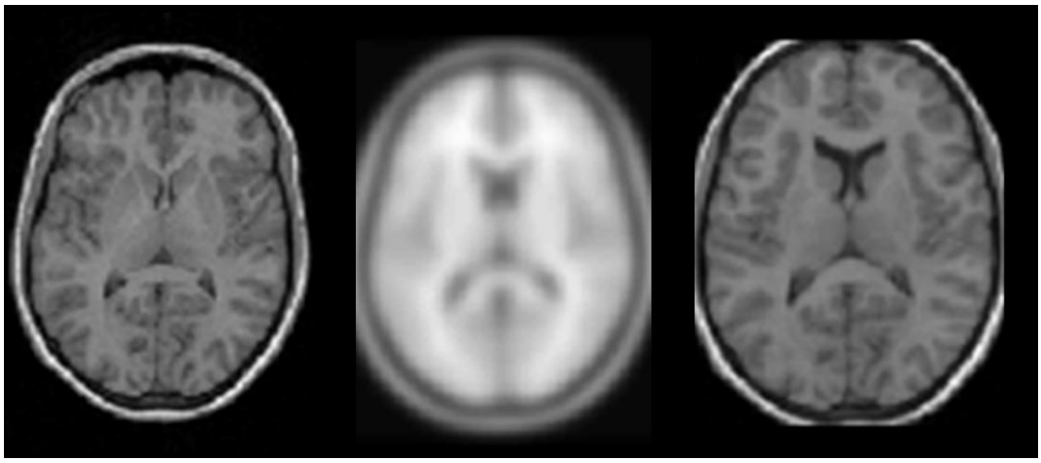

Figure 2.6 – Effects of normalisation. Left: raw T1-weighted image of a control subject for the research study described in Section 2.3; centre: MNI T1 template; right: normalised image.

Images should be inspected before normalisation. While VBM was originally devised to identify subtle neuroanatomical changes associated with neurological and psychiatric dysfunction, the method has also been used to examine gross structural abnormalities. However, the use of VBM with highly distorted brains presents special challenges, due to the difficulties that arise during spatial normalisation, and masks may be used for registering abnormal or lesioned brains. These images should contain zeros corresponding to regions of abnormal tissue. However, there is no simple metric for evaluating the validity of the normalisation and segmentation procedures. The assessment of these procedures relies on visual inspection after normalisation and segmentation, respectively.

Normalisation has some limitations. First of all, it seeks to match homologous regions of the brain, but different cortices can have different folding patterns. Furthermore, when normalisation is applied to functional images (see Chapter 3), it should be considered that there is no exact match between structure and function. Finally, the high-dimensional optimisation is challenging and there may be many local *optima*. The compromise used is that

normalisation corrects for large-scale variability, while finer-scale residual differences are subsequently smoothed.

Finally, recently a new approach, the diffeomorphic anatomical registration through exponentiated lie algebra (DARTEL), has been proposed when good quality anatomical MRI scans are available (Ashburner, 2007). With this algorithm, deformations are parameterized by a single flow field. A high dimensional warping process is applied that improves the registration between individuals, resulting in better localisation and increased sensitivity in analyses.

2.1.2.3 Customised templates

Improvements to the segmentation and normalisation procedures can be obtained by using customised prior probability maps appropriate to the subject group of interest. This has particular relevance when studying patient populations whose brain structure differs greatly from young normal subjects (Good et al., 2001). Figure 2.7 shows the schematic representation of the algorithm used for construction of custom template and priors (Senjem et al., 2005). First, an affine registration between each subject's MRI and the MNI template is performed. The registered image is then segmented using the MNI priors and the segmented GM image is normalised to the MNI GM prior. The obtained deformation field is applied to the raw T1 image which is subsequently segmented using the MNI priors. The normalized whole head, GM, WM, and CSF images from all the subjects included in the study can now be averaged together to obtain the custom template and GM, WM, and CSF priors, respectively. Finally, a Gaussian smoothing kernel should be applied both to the custom template and priors.

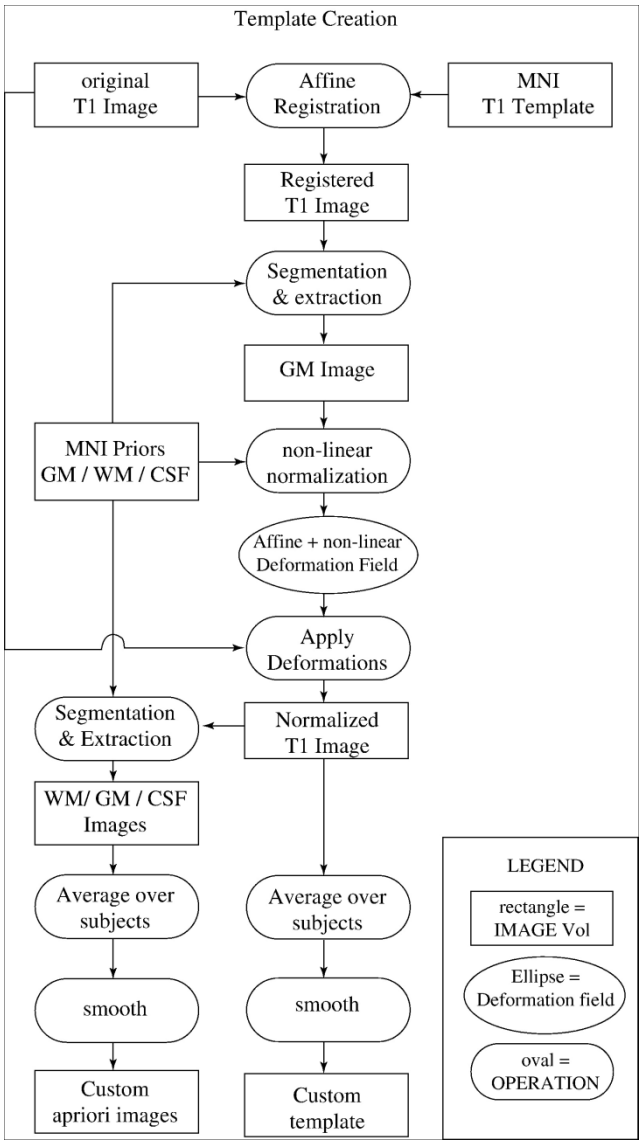

Figure 2.7 –Schematic representation of the algorithm used for construction of custom template and priors (source: Senjem et al., 2005).

2.1.2.4 Modulation

At the end of the second segmentation step in the optimised VBM pre-processing (Figure 2.1), tissue specific segments may be "modulated", i.e. corrected for volumetric differences. When warping a series of images to match a template (see Section 2.1.2.2), volumetric differences will be introduced into the warped images. For example, if one subject's temporal lobe has half the

volume of that of the template, then its volume will be doubled during spatial normalisation. This will also result in a doubling of the number of voxels classified as GM. In order to remove this confound, the spatially normalised GM (or other tissue class) is adjusted by multiplying by its relative volume before and after warping. If warping results in a region doubling its volume, then the correction will halve the intensity of the tissue label. The initial volumes are preserved by using the Jacobian determinants encoding relative volume of tissue from the registration step. This whole procedure has the effect of preserving the total amount of GM signal in the normalised partitions. Non-modulated and modulated VBM detect differences in concentration and volume respectively and, therefore, may identify significant effects in different regions. The difference between these procedures may account for some of the inconsistencies in the literature.

2.1.2.5 Smoothing

The smoothing step of the pre-processing allows for low-pass filtering of image volumes by convolving with a specified function. At a first glance it may seem counterintuitive to spatially blur images when spatial resolution is a factor of primary interest. However, averaging neighbouring voxels suppresses noise at high spatial frequencies, thus significantly improving SNR. Furthermore, smoothing is used to reduce the effects of normalisation errors, as well as residual differences in functional and gyral anatomy during inter-subject averaging. Finally, according to the central limit theorem, smoothing the dataset helps to satisfy the requirements for applying Gaussian random field theory to correct for multiple comparisons in the ensuing statistical analysis (by making the data more normally distributed) and reduces the effective number of multiple comparisons (see Section 2.1.2.6).

Smoothing is performed by convolving the volume with a 3D Gaussian kernel. Every data point is multiplied by a curve in the shape of a 3D normal distribution. The full-width at half maximum (FWHM) of the 3D smoothing curve should match the spatial shape of the signal of interest, because smoothing increases sensitivity to effects of similar scale to kernel due to the matched filter theorem. Therefore, amount of smoothing will influence the size of the areas where a significant difference in GM or WM volume can be detected (or, referring to fMRI, the size of the areas where an increase in the BOLD fMRI signal can be detected) in the statistical analysis. The effects of smoothing a segmented GM image are shown in Figure 2.8

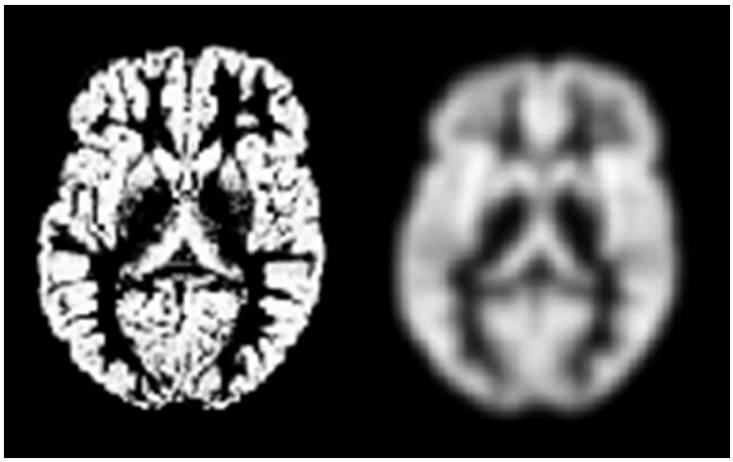

Figure 2.8 – Effects of smoothing. Left: grey matter image obtained from applying segmentation to the raw T1-weighted image of a control subject for the research study described in Section 2.3; right: image smoothed with an 8 mm isotropic Gaussian kernel.

2.1.2.6 Statistical threshold for mass-univariate analyses

The statistical analysis of data in the context of the general linear model will be described in Section 3.1.5.1. The result of this analysis is a t-score for each voxel. If the probability threshold is set at 5%, the voxel has a 5% or less probability of being activated by chance alone. However, this statistical test is

performed for each voxel separately. If twenty thousand voxels are tested at a probability threshold of 5%, a thousand voxels will show erroneous significant activation by chance (i.e. there are false positives or statistical type I errors). In other words, the probability of finding false positives for all univariate tests combined (or the family-wise error, FWE) is very high. Therefore, a different statistical threshold should be chosen in order to have a reasonable FWE.

One way to achieve this is by applying a Bonferroni correction, in which the probability threshold is divided by the number of univariate tests, with the end result that the probability threshold for all univariate tests combined is the desired 5%. However, a Bonferroni correction assumes that the different univariate tests are independent, while in VBM (as well as in fMRI) the signal in adjacent voxels is often correlated, so the amount of independent tests is actually lower than the amount of univariate tests performed. Therefore a Bonferroni correction will be too stringent a correction and will produce too many false negatives (i.e. statistical type II errors), thus dramatically reducing statistical power. There are a number of methods that aim to preserve as much statistical power as possible. These include using a minimum cluster size, utilising Gaussian random field theory, false discovery rate correction and region of interest analysis.

The first solution is using a minimum cluster size. No correction for multiple comparisons is applied; instead a reasonably strict uncorrected probability threshold is used together with setting a lower limit to the cluster size, i.e. to the minimum number of adjacent statistically significant voxels. The logic is that it is highly unlikely that many adjacent voxels would all appear significant purely by chance. The drawback of this method is that it is by definition impossible to detect small clusters of real significant signal. Furthermore, if spatial smoothing has been applied, adjacent voxels are not really independent tests: smoothing (as well as interpolation during other pre-

processing steps) results in neighbouring voxels often having similar statistical values.

The Gaussian random field theory assumes that the signal at each voxel has a normal spatial distribution, an assumption that will generally be valid when the data has been spatially smoothed with a Gaussian kernel. In this method first the number of independent observations, known as resolution elements (resels), is determined. This number of resels is calculated utilising the FWHM used during smoothing of the data (e.g., if the dataset was smoothed using an 8mm FWHM smoothing kernel, each resel will be $8mm^3$ in size). If the number of resels in a volume is known, it is possible to calculate the expected Euler characteristic given a certain Z threshold (the Euler characteristic is the number of significant clusters at a given Z threshold). The statistical threshold that will be chosen is when the expected Euler characteristic is less than 0.05. This means that the chance of one or more significant clusters being false positives is less than 0.05. This method is far less stringent than a Bonferroni correction while still resulting in an acceptable probability of false positives.

Another method is known as the false discovery rate (FDR) correction. Unlike the previously discussed methods, which strive to keep the probability of a false positive for all univariate tests combined below a certain statistical threshold (usually 5%), the FDR only attempts to keep the expected proportion of false positives amongst real positives below a certain statistical threshold. In other words, using the FDR with a statistical threshold of 5% means accepting that 5% of the significant voxels in the dataset will be false positives. The statistical threshold determined with the FDR is sensitive to the amount of signal in the dataset. The FDR is far more sensitive in detecting the real signal present in the dataset than the Gaussian random field method. However, depending on the amount of signal in the dataset, the FDR threshold will be more or less conservative.

The final method is an extension of the Gaussian random field theory. In this method, in addition to using the Gaussian random field theory, the number of multiple comparisons is reduced by only selecting a specific subset of voxels for analysis, thus increasing the statistical power. This approach is known as a ROI analysis or as small volume correction. A ROI can be defined where only the voxels in that ROI are statistically assessed. A ROI analysis can be very useful when there are precise predictions about the locations of the areas of significant signal. One way to define a ROI is by running a so-called localiser experiment. Areas of the brain where the signal is significant in this localiser experiment can then be used to create a ROI for the analysis of a subsequent experiment. Another way to define a ROI is by selection of certain anatomical coordinates (for example, based on previous literature) or landmarks.

2.2 Choice of sample size in VBM: a simulation study

An important limit to the diffusion of VBM is the need of sufficiently large groups of subjects with homogeneous characteristics (Salmond et al., 2002; Thacker, 2003). This limit is especially relevant for pediatric applications, because recruiting large pathological and control sample groups can be particularly time consuming. Hence, quite frequently the need to search for statistical significant differences between small samples arises. This could invalidate the statistical analysis and the resulting clinical assessment.

In fact, the opportunity of analysing small groups with VBM should be carefully considered. With the normalisation step included in data pre-processing, volumes representing single subjects are mapped onto the same stereotactic space by means of a low spatial frequency deformation field (Ashburner and Friston, 2000). This way, large scale differences are removed and corresponding anatomic structures are overlapped. Subsequently, local

differences are evaluated by means of a mass-univariate statistical analysis. Thus, one can think of VBM as a processing technique that enables disclosing possible statistically significant morphological differences between populations, when recognising individual alterations by means of other methods wouldn't be possible. This means that in VBM analyses one cannot control the input to the statistical tests, so that in each sample there could be one or more subjects with structural abnormalities (outliers) that are not identifiable *a priori*. Even if the clinician can state that a given patient belongs to a certain pathological category, evaluating *a priori* if that particular subject shows a local concentration or volume variation of a given cerebral tissue type could not be possible.

It follows the need to define the limits within which including a certain number of subjects with atypical anatomic characteristics in a sample can be accepted and the analysis reliably answers the experimental question, i.e. whether or not the pathology is correlated to specific structural features of the corresponding population. If the statistical analysis is carried out on relatively small samples, the occurrence of one or more subjects with atypical local anatomic characteristics can invalidate the analysis, thus leading to erroneous inferences about the anatomic characteristics correlated to the pathological population.

To assess to what extent inter-group differences highlighted from the statistical analysis of VBM pre-processed data can be considered reliable when analysing small samples, a simulation study was carried out (Nocchi et al., 2008, IFMBE Proceedings; Nocchi et al., 2008, OHBM Meeting) to provide tools for controlling the input to the statistical tests. We implemented a model consisting in sets of virtual phantoms obtained by superimposing matrices of voxels cubes with predetermined characteristics (grey level distribution, mean and variance for each group) on the pre-processed GM images of real subjects. Group mean and variance value ranges were chosen according to the results yielded by the analysis of clinical data. The ultimate purpose of this study is giving clinicians

the chance of making use of an advanced method such as VBM, while knowing the limits within which the results obtained can be considered reliable.

2.2.1 Layout of the study

Experimental data from two ongoing research projects at Bambino Gesù Children's Hospital were used to obtain group mean and variance value ranges for the models. These studies pertain to two diseases with a clinical hypothesis of GM alteration: Down's syndrome (hereinafter referred to as study "A") and anorexia nervosa (both restrictive and binge/purging subtypes, hereinafter referred to as study "B"). Twelve patients (eight males and four females, age 15.99±2.18) and twelve healthy control subjects (eight males and four females, age 16.00±2.26) were recruited for study "A", while eighteen female patients (age 15.76±1.95) and eighteen female healthy control subjects (age 15.64±2.24) were recruited for study "B".

MRI was performed on a 1.5 T Siemens Magnetom Vision scanner (Siemens, Erlangen, Germany). A 3D structural MRI was acquired on each subject using a T1-weighted 3D magnetisation prepared rapid acquisition gradient echo (MPRAGE) sequence (TR = 11.4 ms; TE = 4.40 ms; flip angle = 15°; field of view 249x249; reconstruction matrix = 256x256; pixel size = 0.97x0.97; slice thickness = 1.25 mm).

Individual structural images of each subject (for both studies, "A" and "B") were then pre-processed in the SPM2 version of SPM according to the following steps.

- Registration of the individual images to the MNI T1 template.
- Segmentation of the normalised images in GM, WM and CSF.
- Spatial normalisation of the original structural images in native space to the GM *a priori* probability map in the template stereotactic space.

- Segmentation of the images obtained from the optimized normalisation.
- Smoothing of the segmented GM images with an 8 mm Gaussian kernel.

Pre-processed data were analysed to obtain group mean and standard deviation of voxels grey levels over the whole brain for both studies, “A” and “B”. The same analysis was repeated, for each study, for the most significant cluster. Table 2.1 shows the voxels mean grey level, the standard deviation averaged over the whole brain and over the most significant cluster and the maximum standard deviation. For cluster analyses, mean and standard deviation were calculated over those voxels belonging both to the most significant cluster and to the main anatomical area of the cluster as defined according to an automatic anatomical labelling (AAL) algorithm (Tzourio-Mazoyer et al., 2002, Figure 2.9). Only voxels with a probability ≥10% of being GM were included in the analysis. Results in Table 2.1 enabled specifying value ranges for variance and group mean difference in the model.

In order to obtain controlled data for evaluating the effects of outliers, we designed and implemented sets of digital phantoms in Analyze 7.5 data format. The virtual phantoms were created using MATLAB version 7.0 (The Mathworks, Natick, Massachusetts, USA) code and the MRIcro 1.40 (www.cabiatl.com/mricro/) software.

Figure 2.9 – The Tzourio-Mazoyer digital atlas, used to obtain neuroanatomical labels, is a macroscopic anatomical parcellation of the MNI MRI Single-Subject Brain.

		Study "A"		Study "B"	
		Control group	Patients group	Control group	Patients group
Whole Brain	Mean	93.2	92.4	92.8	82.5
	Mean difference	-0.8		-10.3	
	Average Standard Deviation	14.9	16.7	14.8	15.5
	Maximum Standard Deviation	53.7	59.3	52.5	61.6
Most Significant Cluster	Mean	97.3	120.9	117.7	100.0
	Mean difference	23.6		-17.7	
	Average Standard Deviation	9.6	9.3	9.9	14.8
	Maximum Standard Deviation	14.0	17.0	19.0	24.0

Table 2.1 – Mean and standard deviation in patients and control groups (grey level of pre-processed GM images).

Groups with different numbers of subjects (7 to 20) were generated so that analysing the effects of outliers for different sample dimensions was possible. For each set of phantoms, two identical groups of subjects were created. A 3D matrix of 4x4x4 voxels cubes was superimposed on the pre-processed GM image of each subject of the two groups. Each cube has a uniform grey level, while its intensity distribution within each group is Gaussian with controlled group mean and variance. The difference between group means varies along the

anterior-posterior direction (Figure 2.10) up to 50% of a predetermined grey level (100, in the range 0÷255), with 5% steps. The reference grey level was chosen according to the values in Table 2.1. The number of outliers (subjects of the first group with the same mean values as the ones in the second group) varies along the left-right direction. This way, simulating the effect of including in a group of pathological subjects one or more patients that do not show the typical morphological characteristics of the pathology was possible. Standard deviation varies along the foot-head direction and was set to 10, 15, 20, 25, 30 and 50 for both groups.

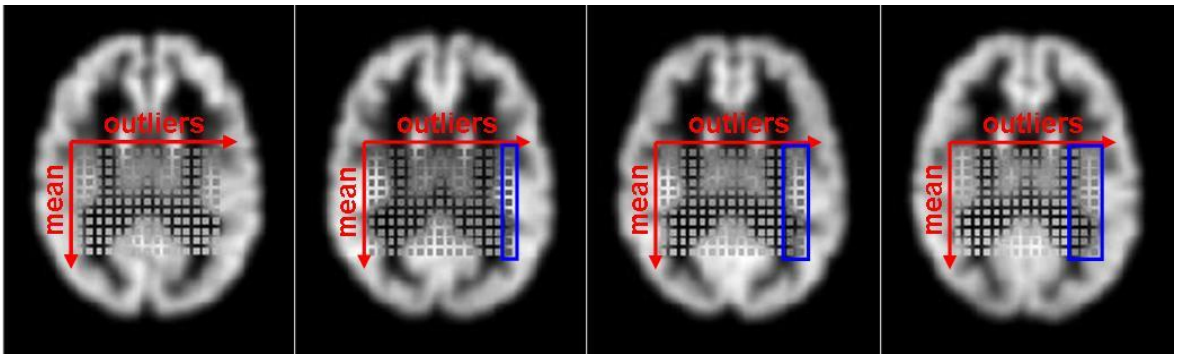

Figure 2.10 – Phantoms for evaluating the effects of outliers on the results of VBM analyses. Subjects of the first group show the following behaviour. While the first subject (left) has the typical values of its own sample in all the cubes, the cubes of the last column of the second subject have the typical distribution of the ones of the second group, the third subject behaves in the same way for the last two columns, and so on for the other subjects of the group.

2.2.2 Results of the simulation study

For each set of phantoms, a statistical parametric analysis (one-tailed t-test) for comparing the two groups of subjects was performed within SPM2. Maps representing statistically significant results for each group mean difference and group variance values were obtained. The maps also enable assessing the effects of including outliers in a sample. In Figure 2.11 an example of the results

yielded by the statistical analyses is shown. Figure 2.12 represents the minimum statistically significant group mean difference as a function of the samples dimensions, for different numbers of outliers. Based on the group mean and average standard deviation values in Table 2.1, results for standard deviation levels of 10 and 15 are represented.

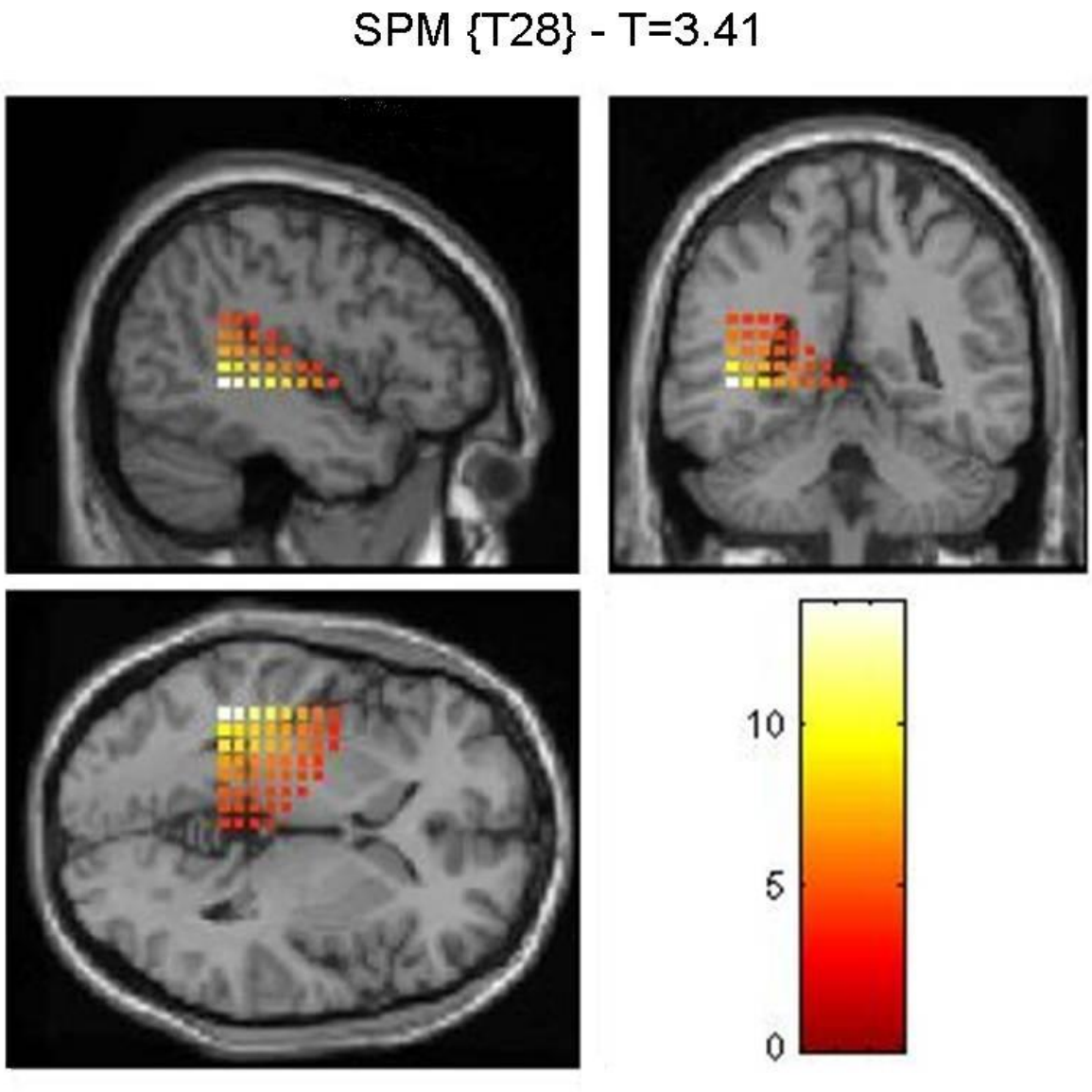

Figure 2.11 – Statistical parametric map obtained by comparing two groups of 15 subjects each, represented on the MNI single subject template (t-test without correction for multiple comparisons, $p<0.001$, $T = 3.41$).

Simulation results in Figure 2.12 show that outliers may compromise the results of VBM analyses performed on small samples, thus leading to erroneous clinical inferences. As the number of subjects increases, the effect of outliers becomes less relevant.

Results were compared to those obtained from the experimental data of studies “A” and “B”. The number of subjects for study “A” (12 subjects per group) is sufficient for reliably analysing the GM differences in the most significant cluster (group mean difference = 23.6, with standard deviation averaged over the cluster ≤10, see Table 2.1), assuming that up to 1 outlier was included in the sample. According to values in Table 2.1, 18 subjects per group are just sufficient for highlighting statistically significant differences in the most significant cluster in study “B” and a larger sample would be desirable.

To summarise, in this study a model for assessing the effects of including in VBM analyses subjects that do not have the typical anatomic characteristics of their group (outliers) is presented. Sets of digital phantoms were implemented to study these effects for different sample dimensions. The results yielded by the simulations confirm that sample dimensions are a critical aspect to consider while designing a VBM study and that outliers may lead to erroneous clinical inferences in VBM analyses performed on small groups of subjects.

The study is aimed at providing the clinician with a support tool for evaluating the conditions under which the clinical results yielded by VBM analyses can be considered acceptable and for driving the recruiting process. This is furthermore important in pediatric trials where this process is frequently particularly time consuming.

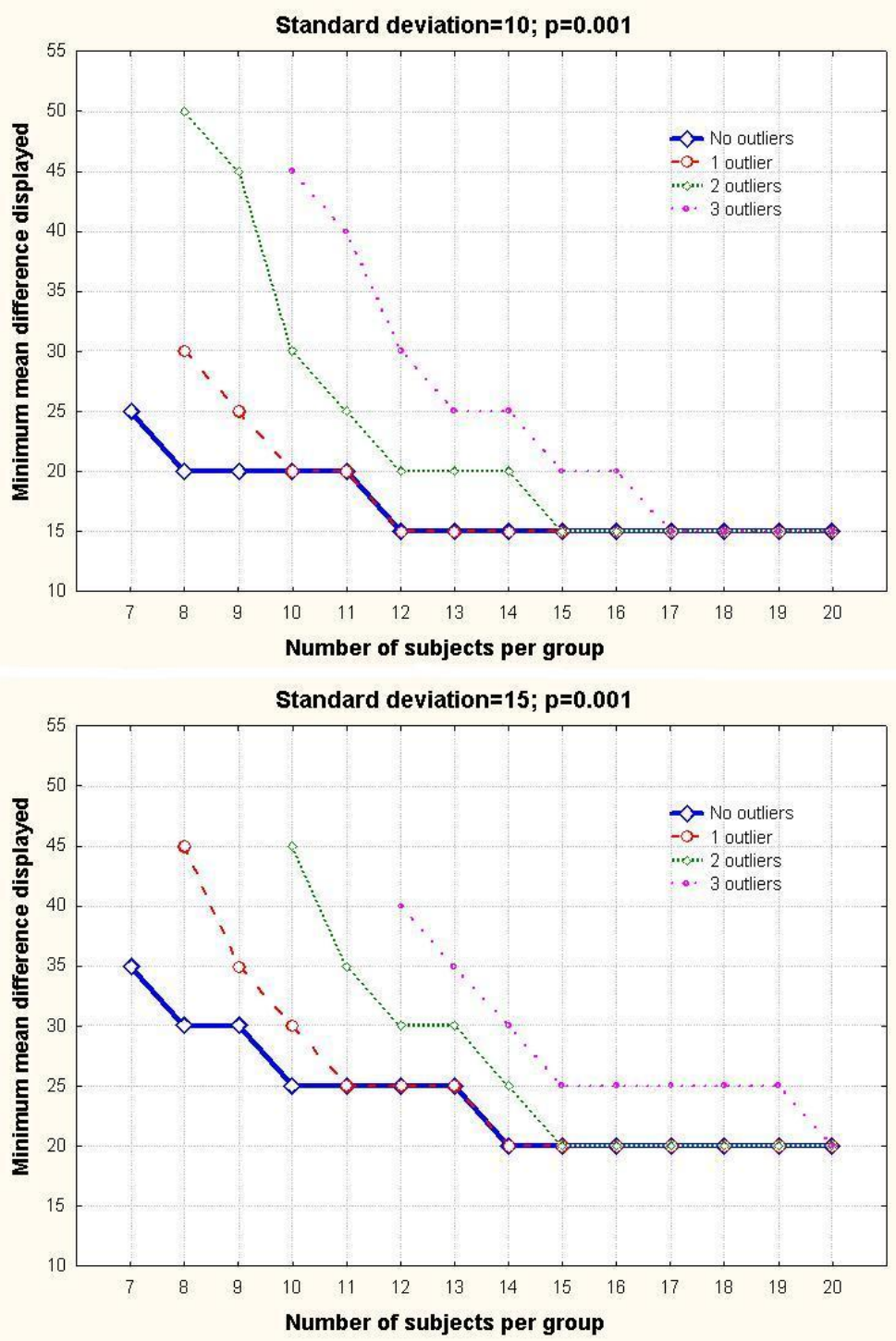

Figure 2.12 – Minimum statistically significant group mean difference as a function of the samples dimensions, for different numbers of outliers. Top: standard deviation = 10. Bottom: standard deviation = 15. According to the simulation results, with a standard deviation of 10, groups of 12 subjects are sufficient to account for up to 1 outlier when analysing the most significant cluster in study "A", while larger samples would be needed assuming that 2 or more outliers were included. 18 subjects per group are just sufficient for highlighting statistically significant differences in the most significant cluster in study "B".

2.3 Application of VBM to a clinical study: grey matter decrease in the early stages of anorexia nervosa in adolescents

Few studies have used VBM to examine brain structure in anorexia nervosa patients (Jáuregui-Lobera, 2011). The purpose of the present study (Gaudio et al., 2011; Gaudio et al., 2009, Suppl. of The World Journal of Biological Psychiatry; Gaudio et al., 2008, WCP; Longo et al., 2008, NRP Congress) was to investigate a sample of anorexia nervosa restrictive type (AN-r) adolescent patients in the early stages of the illness, using VBM in order to characterise morphometric GM changes.

Participants were 16 AN-r female patients (with no other psychiatric disorders) whose AN-r had been in progress for less than 12 months and 16 age-matched healthy female subjects. High-resolution T1-weighted MRIs were pre-processed according to the optimised VBM method, and statistically analysed.

The analyses revealed a significant global GM decrease in the AN-r patients; furthermore, a significant region-specific decrease in GM volume was found bilaterally in the middle cingulate cortex, the precuneus, and the inferior and superior parietal lobules.

The significant early GM decrease in the aforementioned regions in AN-r adolescent patients suggests that there might be a region-specific GM vulnerability that could play a role in the pathophysiology of the disease. Given that these regions are also involved in the manipulation of mental images and the mental representation of the self, this might explain the presence of a distorted body image in these patients.

2.3.1 Neuroimaging studies on Anorexia nervosa

Anorexia nervosa (AN) is a disorder which generally begins in adolescence and primarily affects female subjects. Its relevance is not only related to the increased incidence of AN over the last few decades (Lucas et al., 1999), but also to the high occurrence of medical complications which can occasionally prove fatal (Harris and Barraclough, 1998). The DSM-IV-TR classification of AN recognises two subtypes: AN restrictive type (AN-r) and AN binge/purging type (AN-b/p).

The use of advanced functional brain imaging techniques (fMRI, PET, SPECT) allowed the identification of several cerebral regions involved in AN. However, the direct involvement of these regions in the onset of AN still remains unclear and under debate (Chowdhury et al., 2003).

In neuroimaging structural studies most authors (Dolan et al., 1988; Golden et al., 1996; Kohn et al., 1997; Krieg et al., 1988) showed a global GM and WM decrease with a CSF increase, while Swayze et al. (2003) demonstrated a WM decrease and a CSF increase, with no significant GM decrease. Some authors indicated a relationship between brain mass loss and severity of AN (Golden et al., 1996; Katzman et al., 1996; Kohlmeyer et al., 1983), a full reversibility of brain mass loss (Chowdhury et al., 2003; Golden et al., 1996; Swayze et al., 1996), and persistence of GM decrease (Katzman et al., 1997; Lambe et al., 1997).

A few authors used MRI and manual volume measurement on AN patients demonstrating a significant volume reduction in the hypophysis (Doraiswamy et al., 1990) and the amygdala-hippocampus complex (Giordano et al., 2001). Compared to manual volume measurement approaches, VBM has the advantage of enabling us to evaluate regional volumetric alterations without *a priori* hypotheses about their localisation (Ashburner and Friston, 2000) and of

being minimally operator-dependent, in that it avoids the potential confounds and challenges associated with ROI hand-tracing methods (Gilbert et al., 2008). In AN patients this technique produced differing results: Wagner et al. (2006) found no GM, WM and CSF differences between 40 recovered patients with eating disorders (ED) and a healthy control group; Mülhau et al. (2007) demonstrated, in a sample of 22 recovered AN patients, a global GM loss of 1% and a region-specific GM loss of 5% in the anterior cingulate cortex; Castro-Fornieles et al. (2009) in 12 AN patients (9 AN-r and 3 AN-b/p) showed a global GM decrease which normalised at follow-up (after 7 months and weight recovery) and several regions particularly affected (temporal and parietal areas), although only left and right supplementary motor areas and middle cingulate cortex remained significantly altered at follow up.

The purpose of the present study was to perform, via VBM, a global and local GM analysis in a sample of adolescent patients whose AN-r had been in progress for less than 12 months at the time of scanning.

2.3.2 Experimental design

2.3.2.1 Subjects and clinical procedures

The clinical sample was composed of 16 adolescent patients, all fulfilling the DSM-IV-TR diagnostic criteria for AN-r, under treatment at the Unit of Child Neuropsychiatry of Bambino Gesù Children's Hospital. Informed consent was obtained from all parents and the study followed the ethical guidelines of the hospital.

The inclusion criteria for the AN-r patient sample were: 12÷18 years of age; duration of AN-r less than 12 months at the time of scanning; no other current or previous DSM-IV-TR disorders; right-handedness. The exclusion

criteria were a previous history of other EDs and concomitant medical diseases. Diagnosis of past or current EDs and diagnosis of past or current other Axis I disorders was made in accordance with DSM-IV-TR criteria by clinical interview. Structured Clinical Interview for Axis II Disorders (SCID II) (First et al., 1997) was used to assess personality disorders in patients older than 16 years of age. Moreover, the Children's Depression Inventory (CDI) (Kovacs, 1988) and the Eating Attitudes Test (EAT 26) (Garner et al., 1982) were administered to all patients. All interviews were carried out, prior to scanning, by an experienced investigator who was specifically trained to use the diagnostic tools applied. Data concerning age, body mass index (BMI), AN-r age of onset, lowest BMI and current psychopharmacological treatment were also retrieved.

The same psychopathological examination was carried out on a volunteer control group prior to scanning. The group was composed of 16 adolescent right-handed females, less than 18 years of age, with no previous nor current psychiatric disorders (DSM-IV-TR) and without any concomitant medical diseases. Informed consent was obtained from all parents.

At the time of scanning, all participants of both groups had received similar schooling and had no specific training or skills (Draganski et al., 2004).

2.3.2.2 MRI acquisition

All scans were performed on the same scanner (1.5 T Magnetom Vision, Siemens, Erlangen, Germany), equipped with a standard head coil. The imaging protocol consisted of a 3D T1-weighted MPRAGE sequence covering the entire head with the following image parameters: sagittal acquisition plane; 128 slices; slice thickness = 1.25 mm; field of view = 249x249 mm; reconstruction matrix = 256x256; pixel size = 0.97x0.97 mm; flip angle=15°; TE = 4.40 ms and TR = 1.14 ms.

2.3.2.3 Processing and statistical analyses of grey matter

Morphometric changes were investigated with the optimised VBM protocol (Good et al., 2001) using the SPM2 version of the SPM tool, running in MATLAB version 7.0.

Since subjects ranged from 12 to 18 years old, study-specific *a priori* probability maps were created and a customised T1 template was used rather than the standard MNI template as the reference stereotactic space (Mechelli et al., 2005; see Section 2.1.2.3). Data were modulated in order to account for the shrinkage or growth of brain regions following the nonlinear spatial normalisation step. As a result, volume rather than concentration changes were investigated. A Gaussian kernel of 8 mm was used for smoothing the images.

Two different analyses of covariance (ANCOVA) were performed on pre-processed GM images, both including age as a nuisance variable in order to control its potential effect. In the second ANCOVA, global volume of GM was included as a further nuisance variable, so that changes which cannot be explained by global effects can be exclusively identified. ANCOVA is a general linear model (see Chapter 3) with a continuous outcome variable and two or more predictor variables where at least one is continuous and at least one is categorical. ANCOVA is a merger of ANOVA and regression for continuous variables. It tests whether certain factors have an effect on the outcome variable after removing the variance for which covariates account. The inclusion of covariates can increase statistical power because it accounts for some of the variability.

According to Mühlau et al. (2007), we will refer to the first analysis, including only age as a nuisance variable, as “analysis for the regional distribution of GM changes”, while we will refer to the second approach as “analysis for region-specific GM changes”.

For both analyses a height (statistical) threshold of $p<0.05$ at the voxel-level, corrected for FWE, was applied. In all the aforementioned tests, an absolute threshold was set, so that only voxels with a probability greater than 20% of being GM were included in the analysis.

2.3.2.4 Global and local volume of grey matter

Total Intracranial Volume (TIV) was obtained from the sum of global volumes of GM, WM e CSF. These values were derived from the non-normalised segmented images yielded by the first segmentation in optimised VBM. One-sided independent t-tests were then performed on TIV and global volume of GM to look for significant differences between AN-r and control groups.

For local analyses, the calculation of GM volumes was performed on the most significant regions (MSRs) of GM differences as resulting from the second ANCOVA. The GM content of those voxels belonging both to a significant cluster and to the corresponding main anatomical area as defined according to the AAL algorithm from Tzourio-Mazoyer (Tzourio-Mazoyer et al., 2002) was considered. Only MSRs consisting of 1,000 voxels or more were taken into account.

2.3.2.5 Correlation analyses

An analysis of the correlations between GM and clinical parameters was performed within the AN-r group. The following parameters were taken into account: TIV; global volume of GM; GM content of the MSRs of GM

differences; age at onset; lowest BMI; duration of AN-r, age, and BMI at the time of scanning.

2.3.3 Results

2.3.3.1 Characteristics of the subjects

Table 2.2 shows the clinical features of the AN-r sample and the control group. Both groups were of a similar age distribution. AN-r patients had a significant lower BMI ($p<10^{-10}$), a higher score in the EAT 26 ($p<10^{-9}$) and a higher score in the CDI ($p<10^{-4}$) compared to the control group. However, no patients fulfilled DSM-IV-TR criteria for depression or any other Axis I or Axis II disorders. At the time of scanning all AN-r patients were under psychopharmacological treatment with antidepressants (clorimipramine or SSRIs); the mean duration of treatment was 16.4 (S.D. ±6.4) days. Ten patients were also prescribed low doses of antipsychotics (haloperidol) as combination therapy with antidepressants for AN-r. These patients received 0.5 to 2.0 mg/day of haloperidol (mean dose ± S.D.: 1.3 ± 0.5 mg/day); the mean duration of treatment was 9.2 (S.D. ±6.4) days. Analyses for the regional distribution of GM changes and for region-specific GM changes were performed to exclude the possibility that such low doses of haloperidol with such a short duration of treatment could have influenced the results. We compared non-haloperidol Vs control groups, haloperidol Vs control groups, and non-haloperidol Vs haloperidol groups. No significant influence of haloperidol was found (see Section 2.3.3.6).

	AN-r Patients (N = 16)	Control Subjects (N = 16)	One-Sided t-test		
	Mean (range) ± S.D.	Mean (range) ± S.D.	df	t Score	p-Value
Age* (years)	15.2 (11.8-17.8) ± 1.7	15.1 (12.5-17.9) ± 1.5	30	0.23	0.41
BMI*	14.2 (11.6-16.0) ± 1.4	20.2 (18.1-23.0) ± 1.6	29	11.41	$<10^{-10}$
Age at onset (years)	14.7 (11.0-17.4) ± 1.7				
Duration* (months)	5.3 (1-12) ± 3.2				
Lowest BMI	14.0 (11.6-16.0) ± 1.4				
EAT	36.8 (24-55) ± 9.5	6.7 (2-13) ± 3.2	18	12.06	$<10^{-9}$
CDI	13.1 (4-22) ± 5.7	6.1 (3-11) ± 2.2	19	4.57	$<10^{-4}$

*At the time of scanning.

Table 2.2 – Clinical variables in AN-r patients and comparison subjects.

2.3.3.2 Global volume changes

The one-sided independent t-test performed between AN-r and control groups on TIV revealed no significant difference (+0.8%, t = 0.23, p = 0.41), while the clinical sample showed a significant decrease in global volume of GM (-7.4%, t = 2.47, p<0.01) (Table 2.3). The latter result, together with the age of subjects (which spanned from 12 to 18 years old), suggested the use of a customised template.

Volumes (ml)	AN-r Patients (N = 16)	Control Subjects (N = 16)	Mean Difference	One-Sided t-test		
	Mean (range) ± S.D.	Mean (range) ± S.D.		df	t Score	p-Value
Total Intracranial Volume	1,528 (1,299-1,737) ± 144	1,516 (1,264-1,764) ± 134	+0.8%	30	0.23	0.41
Global Volume of Grey Matter	697 (587-823) ± 68	753 (628-858) ± 61	-7.4%	30	2.47	<0.01
Midcingulate Cortex (GMCC*)	5.38 (4.89-5.76) ± 0.22	5.93 (5.85-6.03) ± 0.06	-9.3%	17	9.54	$<10^{-7}$
Precuneus (GMCC*)	4.87 (4.37-5.46) ± 0.26	5.68 (5.21-5.97) ± 0.23	-14.3%	29	9.21	$<10^{-9}$
Inf. and Sup. Par. Lobules (GMCC*)	5.36 (4.81-6.35) ± 0.38	6.34 (5.84-6.70) ± 0.21	-15.5%	23	8.87	$<10^{-8}$

*GMCC = grey matter content of the cluster in the most significant region specified.

Table 2.3 – Comparison of volumetric variables between AN-r and control groups.

2.3.3.3 Regional distribution of GM changes

Applying the ANCOVA with only age as confounding covariate no GM increase was found in AN-r patients compared to control subjects, while several regions of decrease were identified, including frontal, temporal, parietal, occipital and cerebellar areas. Figure 2.13 shows the distribution of GM decrease in the AN-r sample. A statistical threshold of $p<0.001$ at the voxel-level (uncorrected) and a spatial threshold of 1,000 contiguous voxels were applied, so that only clusters larger than 1 cm^3 are displayed.

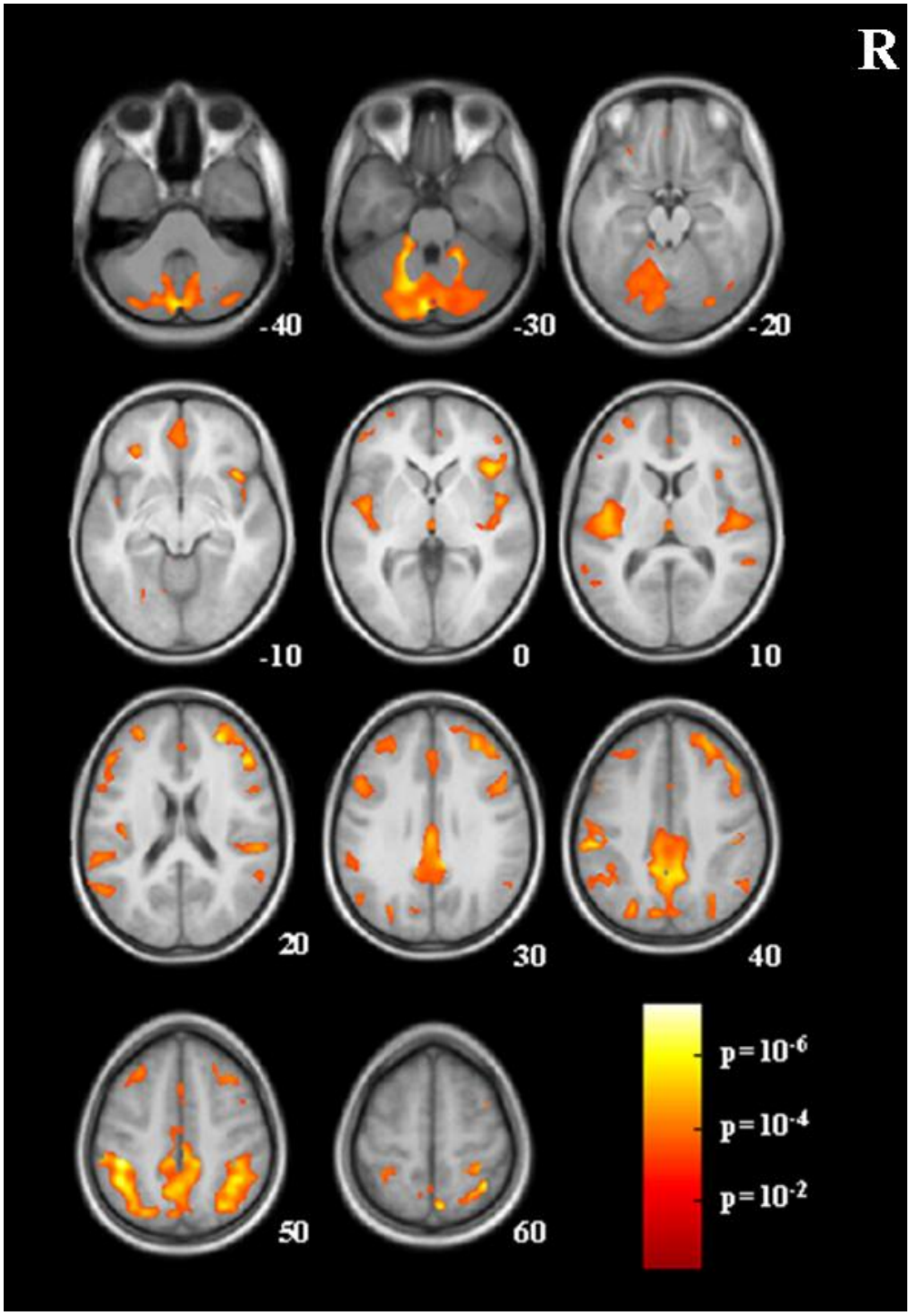

Figure 2.13 –Regional distribution throughout the whole brain of GM decrease in AN-r patients compared to control subjects. Statistical maps ($p<0.001$, uncorrected; spatial threshold = 1,000 voxels) are superimposed on the study-specific averaged T1 image. The colour scale represents the significance level (p-value) according to the colour bar in the lower right corner. The coordinates represented in the lower right corner of each axial section refer to the Talairach stereotactic space.

2.3.3.4 Region-specific GM changes

The analysis for region-specific GM changes (ANCOVA with age and global volume of GM as nuisance variables) yielded three clusters of significant voxels at $p<0.05$ corrected applying the FWE (Table 2.4). For $p<0.001$ (without FWE correction) and a spatial threshold of 1,000 contiguous voxels, these clusters included the following MSRs (Table 2.4): left and right middle cingulate cortex, left and right precuneus (cluster 1); left inferior and superior parietal lobules (cluster 2); right inferior and superior parietal lobules (cluster 3).

Cluster / Anatomical Label	% per Anatomical Region	Peak of t Score	p-Value (FWE Cluster-Level)	p-Value (FWE Voxel-Level)	N. of Voxels Within the Cluster (FWE, p<0.05)	N. of Voxels Within the Cluster (w/o FWE, p<0.001)	N. of Voxels Within the Anatomical Region
Cluster 1		7.11	$<10^{-3}$	0.003	79	17,359	
Cingulum_Mid_L	27.10						4,704
Cingulum_Mid_R	25.78						4,479
Precuneus_R	24.00						4,166
Precuneus_L	23.12						4,010
Cluster 2		6.46	$<10^{-3}$	0.012	97	7,492	
Parietal_Inf_L	61.25						4,588
Parietal_Sup_L	25.52						1,912
Postcentral_L	13.23						992
Cluster 3		6.08	$<10^{-3}$	0.028	24	6,571	
Parietal_Inf_R	47.41						3,115
Parietal_Sup_R	26.51						1,741
Angular_R	14.21						933
Postcentral_R	11.87						782

Table 2.4 – Region-specific GM decrease in AN-r patients compared to the control group.

Figure 2.14 shows the distribution of GM decrease in AN-r in the above mentioned MSRs. The statistical parametric maps represented in Figure 2.14 were obtained by masking the pre-processed images with the anatomical areas defined in the AAL atlas prior to performing the statistical analysis.

The region-specific analysis enabled us to perform a local comparison of the volumes between both groups. The GM content of the voxels of the middle cingulate cortex in the most significant cluster (cluster 1) was compared in both groups and revealed a 9.3% decrease in GM volume in AN-r patients. Similarly, the GM content of the voxels of the precuneus in cluster 1 revealed a 14.3% decrease. Finally, a 15.5% decrease was found in the volume of the region composed by those voxels belonging both to clusters 2 and 3 and to the left and right inferior and superior parietal lobules (Table 2.3).

2.3.3.5 Correlations between GM changes and clinical variables in AN-r patients

The analysis of the correlations within the AN-r group (Table 2.5) revealed no meaningful correlation between clinical variables (age at onset; lowest BMI; duration of AN-r, age, and BMI at the time of scanning) and global volumes (TIV; global volume of GM), nor between clinical variables and local GM content of the MSRs (middle cingulate cortex; precuneus; inferior and superior parietal lobules).

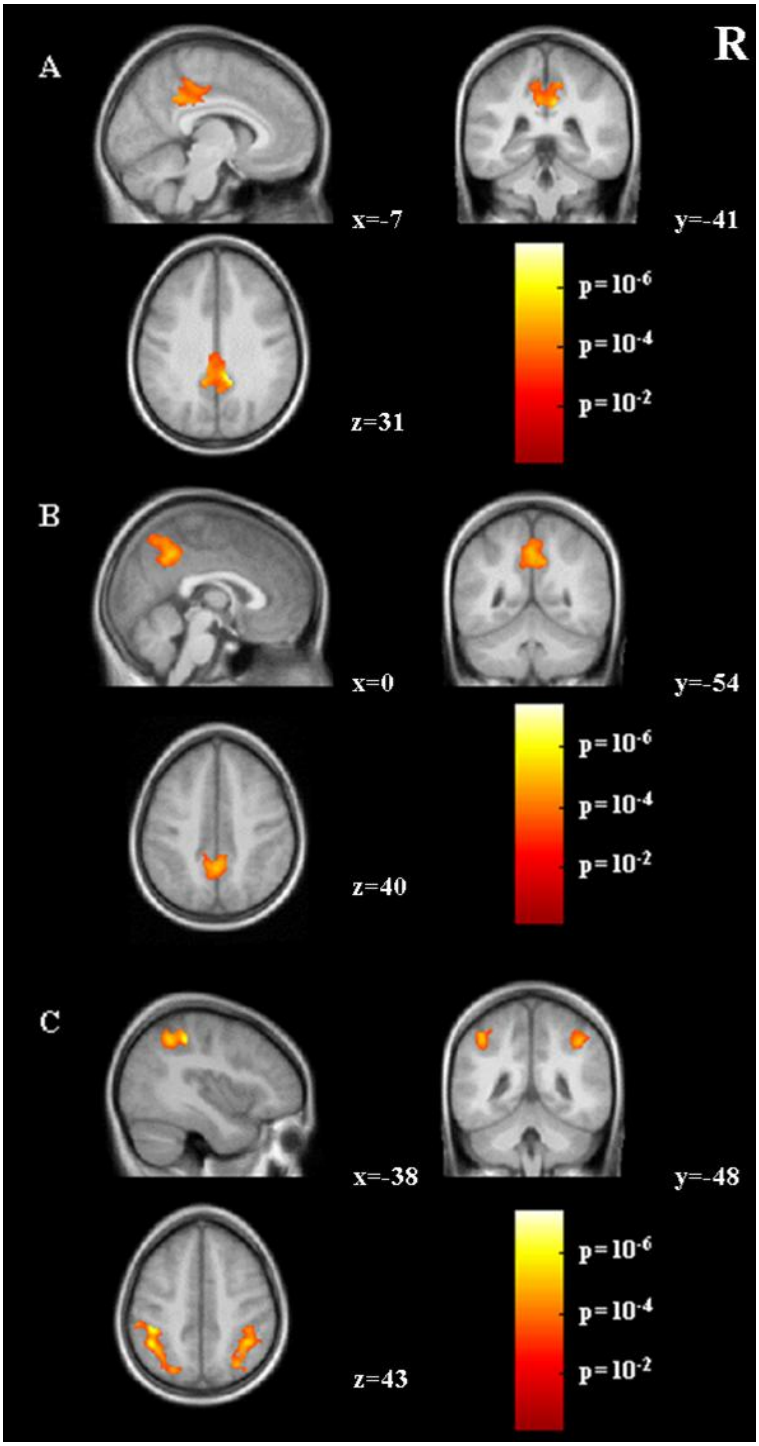

Figure 2.14 – Region-specific GM decrease in AN-r patients compared to control subjects (most significant regions): (A) middle cingulate cortex; (B) precuneus; (C) left and right inferior and superior parietal lobules. Statistical maps ($p<0.001$, uncorrected; spatial threshold=1,000 voxels) are superimposed on the study-specific averaged T1 image. The colour scale represents the significance level (p-value) according to the colour bar in the lower right corner. The coordinates refer to the Talairach stereotactic space.

	Age at Onset	Lowest BMI	Duration*	Age*	BMI*
	Pearson Correlation Coefficient				
Total Intracranial Volume	0.09 (p = 0.74)	0.30 (p = 0.26)	-0.22 (p = 0.42)	0.13 (p = 0.64)	0.21 (p = 0.43)
Global Volume of Grey Matter	0.18 (p = 0.50)	0.18 (p = 0.50)	-0.14 (p = 0.60)	0.10 (p = 0.71)	0.34 (p = 0.19)
Midcingulate Cortex (GMCC)**	0.31 (p = 0.24)	0.20 (p = 0.47)	-0.14 (p = 0.60)	0.09 (p = 0.73)	0.20 (p = 0.45)
Precuneus (GMCC)**	0.18 (p = 0.51)	0.16 (p = 0.56)	-0.11 (p = 0.69)	0.08 (p = 0.77)	0.10 (p = 0.70)
Inf. and Sup. Parietal Lobules (GMCC)**	0.01 (p = 0.96)	0.08 (p = 0.78)	-0.10 (p = 0.71)	0.36 (p = 0.17)	0.02 (p = 0.93)

*At the time of scanning.

**GMCC= grey matter content of the cluster in the most significant region specified.

Table 2.5 –Correlations of volumetric and clinical variables within the AN-r group.

2.3.3.6 Further results

To exclude the possibility that the low doses of haloperidol administered to a subgroup of 10 patients for a short time period could have influenced the results, we compared non-haloperidol Vs control groups, haloperidol Vs control groups, and non-haloperidol Vs haloperidol groups.

Table 2.6 shows the clinical features of the 10 adolescents with anorexia nervosa restrictive type (AN-r) who received low doses of haloperidol and of the 6 adolescents with AN-r who did not receive haloperidol treatment. No significant difference was found between the two subgroups for all clinical features.

	Haloperidol Patients (N = 10)		No Haloperidol Patients (N = 6)		Student's t-test		
	M	(S.D.)	M	(S.D.)	df	t Score	p-Value
Age* (years)	14.9	(1.7)	15.7	(1.5)	12	1.01	0.33
BMI*	14.1	(1.5)	14.3	(1.1)	13	0.26	0.80
Age at onset of AN-r (years)	14.4	(1.8)	15.3	(1.6)	12	1.11	0.29
Duration of AN-r* (months)	5.8	(3.5)	4.3	(2.7)	13	0.95	0.36
Lowest BMI	13.9	(1.6)	14.0	(0.9)	14	0.32	0.75
EAT	38.0	(10.2)	34.7	(8.4)	12	0.70	0.50
CDI	12.5	(5.5)	14	(5.7)	10	0.52	0.61

*At the time of scanning.

Table 2.6 – Clinical variables in AN-r patients with and without treatment with low doses of haloperidol.

We compared the 6 non-haloperidol patients (NHP) to the 16 control subjects (CS), using as nuisance variables both age (analysis for the regional distribution of GM changes) and age plus global volume of GM (analysis for region-specific GM changes).

- No GM increase was observed in the NHP compared to the CS.
- No GM decrease in NHP compared to CS survived FWE correction.
- A GM decrease in NHP was observed in the analysis for the regional distribution of GM changes in a cluster that survived the spatial thresholding (>1,000 voxels), as shown in Table 2.7 and the associated glass brain.
- No cluster survived spatial thresholding (>1,000 voxels) in the analysis for region-specific GM changes. For the sake of completeness Table 2.8 shows the results obtained when applying no multiple comparisons correction and without spatial threshold, and the associated glass brain.

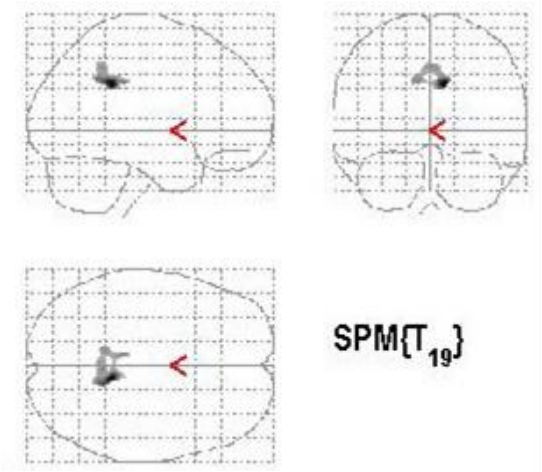

cluster-level			voxel-level					x,y,z {mm}
$p_{corrected}$	k_E	$p_{uncorrected}$	$p_{FWE-corr}$	$p_{FDR-corr}$	T	$(Z_=)$	$p_{uncorrected}$	
0.064	2089	0.010	0.144	0.121	5.86	4.37	0.000	9 -41 32
			0.721	0.121	4.62	3.73	0.000	13 -50 36
			0.856	0.121	4.37	3.59	0.000	-8 -33 34

Table 2.7 – Analysis for the regional distribution of GM changes (CS>NHP): glass brain and table (no multiple comparisons correction; spatial threshold 1,000 voxels).

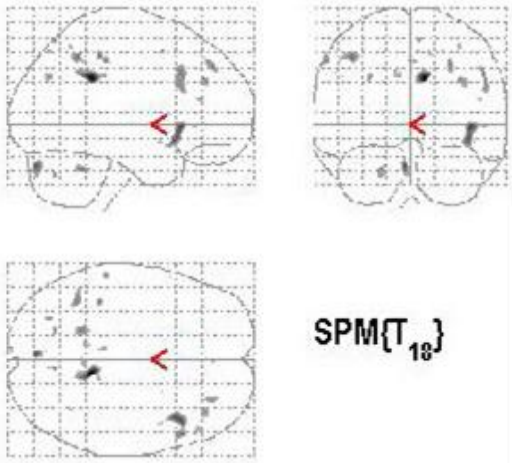

set-level		cluster-level			voxel-level					x,y,z {mm}
p	c	$p_{corrected}$	k_E	$p_{uncorrected}$	$p_{FWE-corr}$	$p_{FDR-corr}$	T	$(Z_=)$	$p_{uncorrected}$	
0.000	30	0.662	512	0.143	0.234	0.224	5.69	4.25	0.000	9 -41 32
					0.942	0.224	4.24	3.48	0.000	13 -50 36
		0.569	616	0.111	0.663	0.224	4.83	3.82	0.000	43 21 -2
		0.897	250	0.300	0.776	0.224	4.63	3.71	0.000	-4 -81 -29
		0.890	259	0.291	0.889	0.224	4.40	3.58	0.000	-41 -52 47
		0.985	85	0.556	0.916	0.224	4.32	3.53	0.000	-20 -47 -31
		0.998	13	0.846	0.922	0.224	4.31	3.52	0.000	22 7 51
		0.891	258	0.292	0.935	0.224	4.26	3.50	0.000	52 21 36
					0.975	0.224	4.07	3.38	0.000	54 20 28
		0.983	92	0.539	0.945	0.224	4.22	3.47	0.000	-40 -36 48
		0.990	67	0.606	0.949	0.224	4.21	3.47	0.000	-59 -31 45
		0.996	36	0.718	0.955	0.224	4.18	3.45	0.000	6 -67 60
		0.962	146	0.431	0.965	0.224	4.14	3.42	0.000	29 44 40
		0.970	128	0.463	0.975	0.224	4.07	3.38	0.000	36 37 31
		0.991	62	0.622	0.982	0.224	4.02	3.35	0.000	-28 -71 33
		0.994	46	0.677	0.984	0.224	4.00	3.34	0.000	-20 -68 -35
		0.997	27	0.761	0.985	0.224	3.99	3.33	0.000	-8 -33 34
		0.997	25	0.771	0.994	0.224	3.86	3.25	0.001	49 34 18
		0.997	23	0.782	0.994	0.224	3.86	3.25	0.001	14 -37 50

Table 2.8 – Analysis for region-specific GM changes (CS>NHP): glass brain and table (no multiple comparisons correction; no spatial threshold).

The 10 haloperidol patients (HP) were then compared to the 16 control subjects (CS), using as nuisance variables both age (analysis for the regional distribution of GM changes) and age plus global volume of GM (analysis for region-specific GM changes).

- No GM increase was observed in HP compared to the CS.
- A GM decrease was observed in HP in the analysis for the regional distribution of GM changes in a few (10) small clusters that survived the FWE correction (Table 2.9).
- A GM decrease was observed in HP in the analysis for region-specific GM changes in 6 small clusters that survived the FWE correction (Table 2.10).

As shown by Tables 2.11 and 2.12, the comparisons of HP Vs CS and NHP Vs CS revealed that the regions involved in the different analyses are extremely similar, even though the HP Vs CS analyses show slightly higher t-scores when compared to NHP Vs CS. The regions shown in Tables 2.11 and 2.12 are also very similar to the ones yielded by the analyses with the complete sample (16 AN-r patients Vs 16 control subjects). Furthermore, as described in Section 2.2, when comparing VBM analyses the size of samples and the unbalanced number of subjects in the groups must be taken into account (Nocchi et al., 2008, IFMBE Proceedings; Nocchi et al., 2008, OHBM).

Finally, we compared the 6 non-haloperidol patients (NHP) to the 10 haloperidol patients (HP), using as nuisance variables both age (analysis for the regional distribution of GM changes) and age plus global volume of GM (analysis for region-specific GM changes).

- When looking for decreased GM in HP compared to NHP, our analyses revealed:
  - no significant differences after FWE correction;

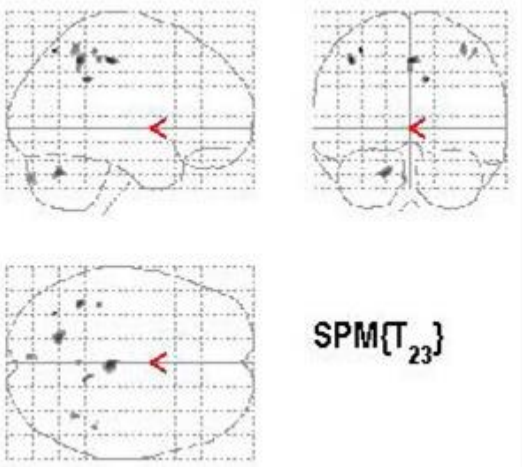

set-level		cluster-level			voxel-level					x,y,z {mm}
p	c	$p_{corrected}$	k_E	$p_{uncorrected}$	$p_{FWE-corr}$	$p_{FDR-corr}$	T	$(Z_=)$	$p_{uncorrected}$	
0.000	10	0.025	26	0.496	0.003	0.002	7.53	5.30	0.000	-34 -67
		0.002	282	0.032	0.005	0.002	7.25	5.18	0.000	1 -28
		0.003	205	0.062	0.005	0.002	7.21	5.16	0.000	-41 -50
		0.012	78	0.233	0.007	0.002	7.04	5.09	0.000	12 -45
		0.002	238	0.046	0.009	0.002	6.93	5.04	0.000	-17 -65
		0.006	147	0.108	0.016	0.002	6.63	4.91	0.000	37 -52
		0.014	67	0.268	0.016	0.002	6.61	4.90	0.000	-40 -35
		0.013	68	0.264	0.017	0.002	6.58	4.89	0.000	46 -39
		0.006	132	0.126	0.019	0.002	6.52	4.86	0.000	-4 -84
		0.009	98	0.183	0.021	0.002	6.47	4.83	0.000	0 -50

Table 2.9 – Analysis for the regional distribution of GM changes (CS>HP): glass brain and table (FWE correction).

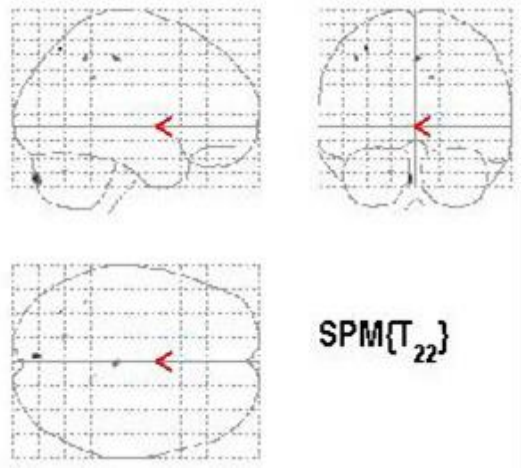

set-level		cluster-level			voxel-level					x,y,z {mm}
p	c	$p_{corrected}$	k_E	$p_{uncorrected}$	$p_{FWE-corr}$	$p_{FDR-corr}$	T	$(Z_=)$	$p_{uncorrected}$	
0.000	6	0.032	12	0.631	0.009	0.006	7.08	5.06	0.000	-34 -67
		0.005	129	0.106	0.016	0.006	6.79	4.94	0.000	-4 -84
		0.015	51	0.298	0.019	0.006	6.67	4.88	0.000	1 -28
		0.022	29	0.436	0.023	0.006	6.57	4.84	0.000	-41 -50
		0.031	13	0.615	0.028	0.006	6.47	4.79	0.000	12 -45
		0.025	22	0.501	0.034	0.006	6.36	4.74	0.000	-17 -65

Table 2.10 – Analysis for region-specific GM changes (CS>HP): glass brain and table (FWE correction).

(A)

Labels : *volume summary (labels and percentages per cluster)*

x,y,z mm	label	%
9 -41 32	Cingulum_Mid_R	35.62
	Precuneus_R	25.99
	Cingulum_Mid_L	22.69
	Precuneus_L	12.69
	Cingulum_Post_R	3.02

(B)

Labels : *volume summary (labels and percentages per cluster)*

x,y,z mm	label	%
-34 -67 55	Parietal_Inf_L	61.41
	Postcentral_L	17.41
	Parietal_Sup_L	16.70
	SupraMarginal_L	2.11
	Occipital_Sup_L	1.02
1 -28 48	Cingulum_Mid_L	23.32
	Cingulum_Mid_R	21.47
	Precuneus_L	21.46
	Precuneus_R	21.05
	Paracentral_Lobule_R	3.63
	Cingulum_Post_L	2.80
	OUTSIDE	2.39
	Paracentral_Lobule_L	1.44
	Supp_Motor_Area_R	1.03
-17 -65 -31	Cerebelum_6_L	16.21
	Cerebelum_Crus1_R	11.68
	Cerebelum_Crus1_L	10.58
	Cerebelum_Crus2_L	9.05
	Cerebelum_4_5_L	8.68
	OUTSIDE	8.34
	Cerebelum_6_R	7.02
	Cerebelum_Crus2_R	6.06
	Vermis_8	3.96
	Cerebelum_8_R	3.76
	Cerebelum_8_L	3.05
	Vermis_7	2.21
	Fusiform_L	2.11
	Vermis_6	1.61
	Cerebelum_7b_L	1.12
37 -52 57	Parietal_Inf_R	43.49
	Parietal_Sup_R	24.46
	Postcentral_R	17.35
	Angular_R	12.56
	Occipital_Sup_R	1.22
28 47 22	Frontal_Mid_R	65.86
	Frontal_Inf_Oper_R	14.00
	Frontal_Sup_R	11.77
	Frontal_Inf_Tri_R	5.82
	Precentral_R	2.45
-28 52 14	Frontal_Mid_L	89.58
	Frontal_Sup_L	10.42
46 -16 12	Rolandic_Oper_R	35.10
	Insula_R	30.53
	Temporal_Sup_R	16.21
	Heschl_R	14.99
	SupraMarginal_R	1.03

Table 2.11 – Analysis for the regional distribution of GM changes (no multiple comparisons correction; spatial threshold 1,000 voxels); (A) CS>NHP; (B) CS>HP.

(A)

Labels : *volume summary (labels and percentages per cluster)*

x,y,z mm	label	%
9 -41 32	Cingulum_Mid_R	83.40
	Precuneus_R	13.09
	Cingulum_Post_R	3.52
43 21 -2	Insula_R	85.23
	Frontal_Inf_Tri_R	13.96
-4 -81 -29	Cerebelum_Crus2_L	88.80
	Vermis_7	8.40
	Cerebelum_Crus1_L	2.80
-41 -52 47	Parietal_Inf_L	100.00
-20 -47 -31	OUTSIDE	89.41
	Cerebelum_4_5_L	7.06
	Cerebelum_6_L	3.53
22 7 51	Frontal_Sup_R	100.00
52 21 36	Frontal_Inf_Oper_R	49.22
	Frontal_Mid_R	25.97
	Frontal_Inf_Tri_R	24.81
-40 -36 48	Postcentral_L	84.78
	Parietal_Inf_L	15.22
-59 -31 45	Parietal_Inf_L	91.04
	OUTSIDE	8.96
6 -67 60	Precuneus_R	100.00
29 44 40	Frontal_Mid_R	76.71
	Frontal_Sup_R	23.29
36 37 31	Frontal_Mid_R	100.00
-28 -71 33	Occipital_Mid_L	87.10
	Occipital_Sup_L	12.90
-20 -68 -35	Cerebelum_Crus1_L	80.43
	OUTSIDE	19.57
-8 -33 34	Cingulum_Mid_L	100.00
49 34 18	Frontal_Inf_Tri_R	64.00
	Frontal_Mid_R	36.00
14 -37 50	Paracentral_Lobule_R	95.65
	Cingulum_Mid_R	4.35
1 43 40	Frontal_Sup_Medial_L	100.00
52 31 -1	Frontal_Inf_Tri_R	100.00
35 -56 54	Parietal_Sup_R	85.00
	Parietal_Inf_R	15.00
-11 -45 37	Cingulum_Mid_L	94.87
	Precuneus_L	5.13
-52 -28 37	Parietal_Inf_L	100.00
17 -48 -30	OUTSIDE	100.00
6 -71 52	Precuneus_R	100.00
1 -48 45	Precuneus_R	82.50
	Precuneus_L	15.00
	Cingulum_Mid_L	2.50

(B)

Labels : *volume summary (labels and percentages per cluster)*

x,y,z mm	label	%
-34 -67 55	Parietal_Inf_L	75.57
	Postcentral_L	16.16
	Parietal_Sup_L	6.49
	SupraMarginal_L	1.78
-4 -84 -36	Cerebelum_6_L	15.35
	Cerebelum_4_5_L	11.15
	OUTSIDE	9.49
	Cerebelum_6_R	8.30
	Cerebelum_Crus1_R	7.17
	Cerebelum_Crus1_L	7.01
	Cerebelum_Crus2_L	6.14
	Cerebelum_Crus2_R	4.93
	Vermis_8	4.59
	Cerebelum_8_R	3.97
	Cerebelum_8_L	3.49
	Vermis_6	3.17
	Cerebelum_4_5_R	3.10
	Vermis_7	2.21
	Vermis_4_5	2.08
	Fusiform_L	1.57
	Vermis_9	1.41
	Lingual_L	1.26
1 -28 48	Cingulum_Mid_L	23.83
	Precuneus_R	23.42
	Cingulum_Mid_R	21.43
	Precuneus_L	21.07
	Paracentral_Lobule_R	3.86
	OUTSIDE	2.15
	Paracentral_Lobule_L	1.44
	Cingulum_Post_L	1.25
46 -39 54	Parietal_Inf_R	51.30
	Parietal_Sup_R	23.72
	Postcentral_R	13.40
	Angular_R	10.96
28 47 22	Frontal_Mid_R	97.10
	Frontal_Sup_R	2.90
-27 51 15	Frontal_Mid_L	94.77
	Frontal_Sup_L	5.23
1 40 43	Frontal_Sup_Medial_L	78.66
	Frontal_Sup_Medial_R	15.81
	OUTSIDE	5.53
46 -16 12	Rolandic_Oper_R	38.55
	Insula_R	29.01
	Heschl_R	22.77
	Temporal_Sup_R	9.26
-46 -36 24	SupraMarginal_L	83.18
	Temporal_Sup_L	16.36

Table 2.12 – Analysis for region-specific GM changes (no multiple comparisons correction; no spatial threshold); (A) CS>NHP; (B) CS>HP.

  - no significant differences with a spatial threshold of 1,000 voxels (without FWE correction).

For the sake of completeness, the following Tables 2.13 and 2.14 and the associated glass brains show our results when comparing the two groups with no multiple comparisons correction, and without spatial threshold.

- When looking for decreased GM in NHP compared to HP, our analyses revealed:
  - no significant differences after FWE correction;
  - no significant differences with a spatial threshold of 1,000 voxels (without FWE correction).

For the sake of completeness, the following tables 2.15 and 2.16 and the associated glass brains show our results when comparing the two groups with no multiple comparisons correction, nor spatial threshold.

2.3.4 Discussion of the results of the AN-r study

The purpose of the study was to investigate, via VBM, a sample of AN-r adolescent patients whose AN-r had been in progress for less than 12 months in order to evaluate global and local structural GM alterations. The main results found in AN-r patients compared to control subjects were: 1) a significant global GM decrease; 2) a regional distribution of GM decrease throughout the whole brain; 3) a region-specific GM decrease in the left and right middle cingulate cortex, the left and right precuneus and the left and right inferior and superior parietal lobules.

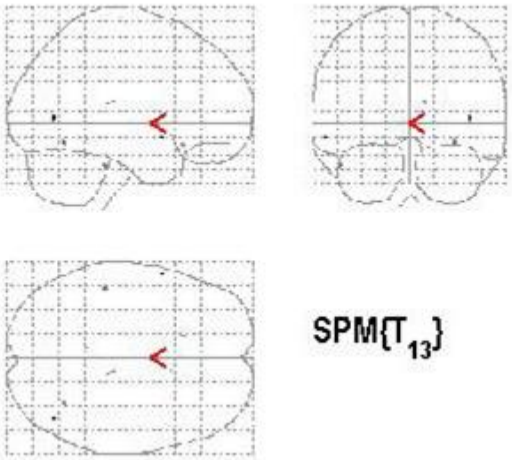

set-level		cluster-level			voxel-level					x,y,z {mm}	
p	c	$p_{corrected}$	k_E	$p_{uncorrected}$	$p_{FWE-corr}$	$p_{FDR-corr}$	T	$(Z_=)$	$p_{uncorrected}$		
0.516	9	1.000	7	0.881	0.944	0.801	4.75	3.55	0.000	-59	9
		0.998	31	0.711	0.955	0.801	4.69	3.53	0.000	42	-67
		0.998	30	0.716	0.991	0.801	4.36	3.36	0.000	-48	-31
		0.998	32	0.705	0.991	0.801	4.35	3.36	0.000	32	-60
		0.999	11	0.843	0.997	0.801	4.20	3.28	0.001	11	-28
		0.999	21	0.768	0.998	0.801	4.11	3.23	0.001	-16	23
		1.000	6	0.892	0.999	0.801	3.98	3.16	0.001	9	14
		1.000	5	0.904	0.999	0.801	3.97	3.16	0.001	-7	-44
		1.000	2	0.947	1.000	0.801	3.89	3.11	0.001	-13	-21

Table 2.13 – Analysis for the regional distribution of GM changes (NHP>HP): glass brain and table (no multiple comparisons correction; no spatial threshold).

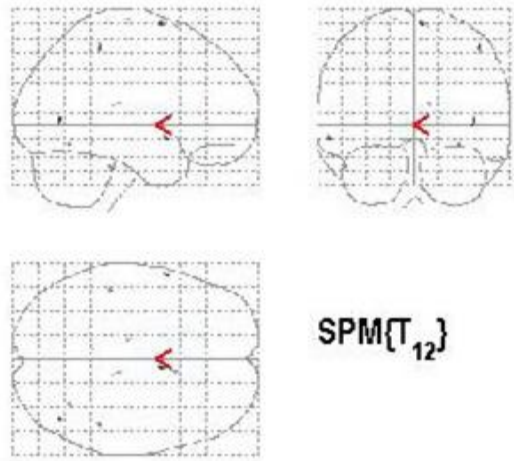

set-level		cluster-level			voxel-level					x,y,z {mm}	
p	c	$p_{corrected}$	k_E	$p_{uncorrected}$	$p_{FWE-corr}$	$p_{FDR-corr}$	T	$(Z_=)$	$p_{uncorrected}$		
0.495	11	0.999	34	0.657	0.949	0.844	5.04	3.62	0.000	41	-69
		1.000	13	0.801	0.959	0.844	4.97	3.60	0.000	-60	7
		0.998	43	0.611	0.964	0.844	4.94	3.58	0.000	6	4
		0.999	35	0.651	0.994	0.844	4.55	3.40	0.000	46	-39
		0.999	26	0.703	0.999	0.844	4.33	3.29	0.000	-48	-31
		1.000	23	0.723	0.999	0.844	4.31	3.28	0.001	32	-61
		1.000	11	0.820	0.999	0.844	4.26	3.26	0.001	11	-28
		1.000	13	0.801	1.000	0.844	4.17	3.21	0.001	9	14
		1.000	12	0.810	1.000	0.844	4.10	3.18	0.001	-13	-21
		1.000	4	0.904	1.000	0.844	4.06	3.16	0.001	-7	-44
		1.000	3	0.920	1.000	0.844	4.00	3.13	0.001	-16	23

Table 2.14 – Analysis for region-specific GM changes (NHP>HP): glass brain and table (no multiple comparisons correction; no spatial threshold).

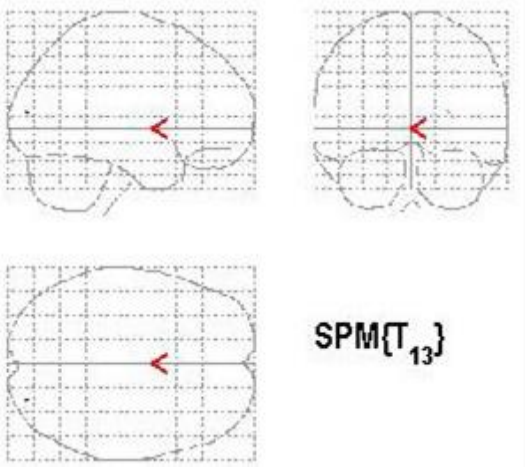

cluster-level			voxel-level					x,y,z {mm}
$p_{corrected}$	k_E	$p_{uncorrected}$	$p_{FWE-corr}$	$p_{FDR-corr}$	T	$(Z_=)$	$p_{uncorrected}$	
0.999	13	0.826	0.997	0.984	4.18	3.27	0.001	26 -87

Table 2.15 – Analysis for the regional distribution of GM changes (HP>NHP): glass brain and table (no multiple comparisons correction; no spatial threshold).

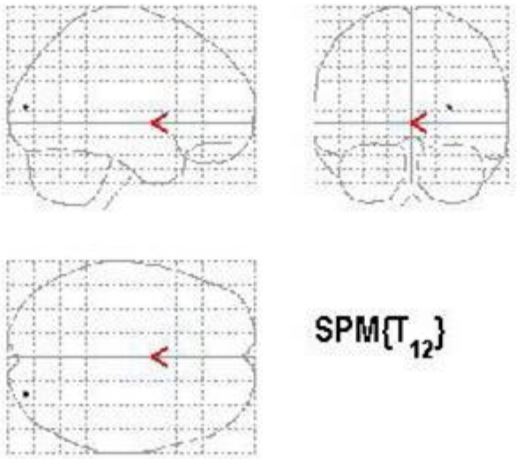

cluster-level			voxel-level					x,y,z {mm}	
$p_{corrected}$	k_E	$p_{uncorrected}$	$p_{FWE-corr}$	$p_{FDR-corr}$	T	$(Z_=)$	$p_{uncorrected}$		
0.998	50	0.580	0.919	0.988	5.18	3.69	0.000	27 -87	11

Table 2.16 – Analysis for region-specific GM changes (HP>NHP): glass brain and table (no multiple comparisons correction; no spatial threshold).

The first result confirms the findings of most other CT and MRI studies (Dolan et al., 1988; Golden et al., 1996; Katzman et al., 1996; Kohn et al., 1997; Krieg et al., 1988) and of the single other study that used VBM analysis on AN patients (Castro-Fornieles et al., 2009). Our result only contrasts with the MRI studies of Swayze et al. (1996, 2003), which indicated a WM decrease and a CSF increase without a significant GM decrease. Our sample has the shortest mean duration of AN at the time of scanning (5 months, see Table 2.2) compared to the above mentioned studies. Therefore we could suggest that a global GM decrease takes place in the early stages of AN and, as our second result highlights, uniformly regards almost all cerebral areas.

The third result, obtained by a region-specific GM analysis, is difficult to compare to the findings of other authors, in that our study is the first VBM study carried out on solely AN-r patients. There is one other VBM study on 12 AN patients but it includes both 9 AN-r and 3 AN-b/p patients (Castro-Fornieles et al., 2009). This sample has almost the same mean age and duration of AN as ours and the results partially overlap. In fact, also these authors found a significant GM decrease bilaterally in the precuneus, the middle cingulate cortex and the inferior and superior parietal lobules. In particular, they found a significant GM decrease in the left and right middle cingulate cortex at follow up (after 7 months and weight recovery). However, they found other regions involved: the right temporal lobe and, at follow up, both supplementary motor areas. We can suggest that the differences between the two studies could be due to the different composition of our sample, which only included AN-r patients.

Among the GM areas affected, the precuneus plays a central role in the modulation of conscious processes. It seems to be involved in the internally guided attention and manipulation of mental images and belongs to a neural network, which includes the parietal lobules and the medial prefrontal cortex, supporting the mental representation of the self (Cavanna and Trimble, 2006). In

this regard, despite the difficulties in comparing results from functional and morphological neuroimaging techniques, it is interesting to consider that the fMRI study of Sachdev et al. (2008) revealed, in a sample of 10 AN patients (without subtype analysis) compared to a control group, a reduced signal in the precuneus in the processing of self-images, while there was not such a reduction in the processing of non-self-images. It should also be taken into consideration that the inferior and superior parietal lobules are involved in both somato-sensorial and motor functions; the inferior parietal lobule also plays a role in several psychiatric disorders, including schizophrenia (Torrey, 2007). Finally, the middle cingulate cortex belongs to the limbic system which is involved in the processing of emotions. In particular, the anterior sub-region of the middle cingulate cortex seems to be involved in fear and avoidance behaviour and it has higher and more direct amygdala input than other cingulate regions, while the posterior sub-region seems to be primarily involved in skeletomotor orientation (Vogt et al., 1992).

We also analysed correlations between GM volume changes and clinical variables within the AN-r group, finding no significant values. However, this result can be conditioned by the sample size and the small range of duration of AN-r. Therefore, although the lack of an association between local GM decrease (precuneus, middle cingulate cortex and inferior and superior parietal lobules) and the duration of AN seems to suggest that these alterations could be independent of AN, we consider this hypothesis premature. The lack of correlation between global GM decrease and duration of AN-r would seem to strengthen our conviction.

The results yielded by our analyses lead us to hypothesize that there is an early GM decrease in the above mentioned regions, allowing for two possible interpretations. The first one is that these regions are more vulnerable than the rest of the brain to starvation, weight loss and other conditions related to AN-r. However, there is no scientific evidence of a specific vulnerability of these areas

to these conditions. The second interpretation is that the greater vulnerability of the regions highlighted by our study is related to their direct involvement in the early stages of the disorder. This hypothesis seems to be supported by the fact that some of these regions are involved in the mental representation of the self and the manipulation of mental images; a consideration which should not be undervalued considering that the central disturbance in AN is that of a distorted body image. We therefore suggest that there might be a specific GM vulnerability of these regions that could play a role in the pathophysiology of AN-r and might explain the presence of a distorted body image in the AN-r patients.

Finally, we found no significant GM decrease in the anterior cingulate cortex. This result is consistent with the VBM study conducted by Castro-Fornieles et al. (2009), whereas it is in contrast with the VBM study of Mühlau et al. (2007), who found a regional GM loss of 5% in the anterior cingulate cortex in a sample of 22 recovered AN-r patients, and it also contrasts with SPECT studies which highlighted a hypoperfusion in this region in AN-r patients (Naruo et al., 2001; Takano et al., 2001; Kojima et al., 2005). These findings might suggest that the involvement of the anterior cingulate cortex in AN could emerge later over the course of the illness.

The main limitation of the present study is that we did not examine the morphometric changes longitudinally. However, our purpose was to investigate a homogeneous sample of AN-r patients whose AN-r had been in progress for a limited time period in order to highlight global and local structural GM alterations in the early stages of AN-r.

In conclusion, the study showed a significant global GM decrease in an AN-r sample with a short illness history; furthermore, it highlighted an early region-specific GM decrease bilaterally in the middle cingulate cortex, the precuneus and the inferior and superior parietal lobules. The early GM decrease in these regions, which are also involved in the manipulation of mental images

and the mental representation of the self, might indicate their greater vulnerability and could explain the presence of a distorted body image in the AN-r patients.

CHAPTER 3: Functional Magnetic Resonance Imaging

3.1 Principles of fMRI

fMRI is an *in vivo* non-invasive imaging technique which enables to observe which structures of the brain participate in specific functions by mapping changes in brain haemodynamics corresponding to mental operations. The subject undergoes a task involving one or more sets of motor, sensorial, and/or cognitive stimuli. These stimuli elicit variations in neuronal activity and subsequently in the metabolic and haemodynamic response, thus leading to changes in the local magnetic field (deoxyhaemoglobin is the endogenous contrast agent used in fMRI). This generates the BOLD MR signal contrast. By registering this signal, the increase in blood flow to the local vasculature following neural activity in the brain can be used to obtain activation maps. These activation maps can then be superimposed on high resolution structural images to study the relations between function and anatomy of brain regions. Thus, fMRI enables to link brain structure and function by non-invasive investigations in the same subject. Studies on functional activity of the brain with fMRI have confirmed many distinct anatomically known processing areas (e.g., in the visual cortex, the motor cortex, and Broca's area of speech and language-related activities). Further, a number of evidences documents corresponding findings between fMRI and conventional electrophysiological techniques to localise specific functions of the human brain. Consequently, the number of medical and research centres with fMRI capabilities and investigational programs continues to escalate (Figure 3.1).

Unfortunately, fMRI does not directly detect the electrical activity, nor does it measure the rapid increase in metabolism. Rather, it measures the increase in rCBF in response to the increased metabolism. Therefore, fMRI is an indirect method to study neuronal activity and a complete characterisation of the neurovascular coupling is still lacking (see Section 3.1.2). Compared to other

MRI techniques, fMRI has a poor spatial resolution (typically a few millimetres). This is due to the size and delocalisation of the vasculature giving rise to the observed MR signal. Furthermore, it depends on the characteristics of the EPI sequences used to acquire data and on the image processing steps that must be subsequently applied. The brain is scanned at a rapid rate (typically once every 2÷3 seconds), but the temporal resolution is limited by the latency and duration of the haemodynamic response function.

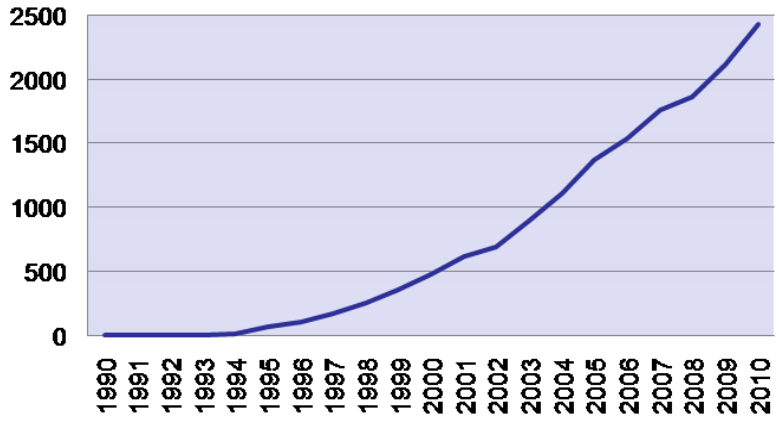

Figure 3.1 – Number of PubMed indexed publications per year containing the fMRI acronym in the title or in the abstract.

Other limits of fMRI include the need of patient interaction, which may cause movement artefacts. MRI exams often require patient sedation in case of anxiety or patients suffering from claustrophobia (this is more frequent in children). In these cases, a mild sedative may be administered prior to the examination. However, this approach is not possible in case of fMRI exams. Furthermore, patient's attention may affect his/her haemodynamic response. This may produce a relevant variability of activations between subjects and in repeated exams in the same subject, as those required by longitudinal studies.

3.1.1 Applications of fMRI

fMRI opens an array of opportunities to advance understanding of brain organisation, both in normal states and in pathologic conditions, and to assess neurological status and neurosurgical risk. The first fMRI experiments, at the beginning of 1990s, were mostly intended to prove the reliability of this technique, to study its basic mechanisms and the correlation between BOLD signal and rCBF measured with PET. Therefore, most of these studies replicated previous researches with PET. During the last two decades, BOLD fMRI has had a major impact in cognitive neuroscience and has been used in research studies on degenerative diseases (e.g., Alzheimer's disease, amyotrophic lateral sclerosis, Parkinson's disease, dementia), neurological diseases (e.g., Huntington's disease), neuropsychiatric disorders (e.g., schizophrenia, depression, eating disorders, substance dependencies), neurodevelopmental disorders (e.g., Williams syndrome, autism), vegetative or minimally conscious states, recovery of brain function following ischemia (e.g., hemiplegia, aphasia).

Despite still in the earliest stages of translation from research laboratories to clinical applications, fMRI has a growing role in clinical neuroimaging. Current clinical research has emphasized novel concepts for clinicians, such as the role of plasticity in recovery and the maintenance of brain functions in a broad range of diseases. There is a wider potential for clinical fMRI in applications ranging from pre-symptomatic diagnosis of diseases, through drug development and individualisation of therapies, to understanding functional brain disorders (Matthews et al., 2006). Potential applications of fMRI for clinical management also include the characterisation of disease risk, its use as a diagnostic marker of disease, and to predict and measure treatment response. Although still not routine, the best-established current clinical application of fMRI is for pre-surgical mapping to localise cerebral functions in tissue within

or near regions intended for neurosurgical resection of cerebral tumours or epileptic foci (see Section 3.2). This application can enhance safety in resection of tumours and foci and may be used to guide functional neurosurgical ablation or stimulation. Furthermore, multimodal approaches such as simultaneous EEG-fMRI registration may prove particularly useful in the pre-surgical localisation of epileptic foci (see Section 3.2.3).

Although fMRI was initially mostly used to study brain function in adult subjects, the number of studies in children and pediatric populations is now continuously increasing. The non-invasive nature of fMRI allows performing longitudinal analyses, which are useful in studies on the development of associative and cognitive functions in children.

Table 3.1 shows a set of brain functions that can be mapped with fMRI, together with examples of stimuli commonly used to map these functions.

Brain function/domain	Stimulus
Motor	Finger tapping, repetitive opening/closing of hands, foot extension/flexion, tongue movement, etc.
Somatosensory	Passive stimulation of hand, foot, leg, …
Language processing	Visual and auditory stimuli for word generation, reading or listening to words/non-words, object naming, semantic decision, …
Visual, auditory, emotion processing, memory, attention, pain, reward and decision making, …	Various kinds of simple or complex stimuli (e.g.: known/unknown faces, flashes, complex light stimuli, odd-balls tasks, …)

Table 3.1 – Examples of stimuli used in fMRI tasks to map brain functions.

Motor function is the most frequently explored one. This is due to the simple and reproducible tasks that can be used to map this function. No systems for patient stimulation are needed to excite neurons. Another frequently studied function is language. As stated before, fMRI can be used for the assessment of surgical risk. If a lesion is located near the inferior frontal gyrus (Broca's area), the posterior portion of the superior temporal gyrus (Wernicke area), the supramarginal gyrus or the angular gyrus, a permanent deficit in language

processing may be determined during surgical procedures. Figure 3.2 shows an example of functional activations in language areas in a verb generation task. A left lateralisation of language function can be observed in this 3D representation.

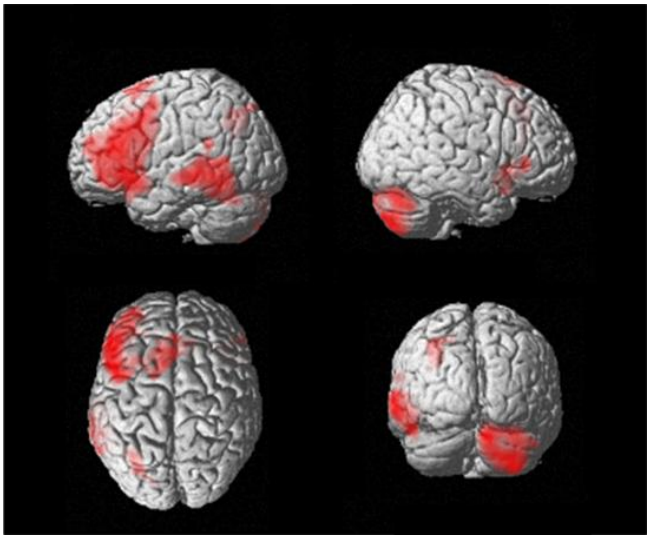

Figure 3.2 – 3D rendering of functional activations in a verb generation task (this results was obtained from the study described in Section 3.2).

3.1.2 Physiological principles

The brain requires a steady supply of oxygen in order to metabolise glucose to provide energy. To keep up with the high energy demand of the brain, oxygen delivery and blood flow to this organ is relatively large. Although the brain's weight is only 2% of the body's weight, its oxygen consumption rate is 20% of the body's, and blood flow 15%. In particular, the blood flow to the grey matter, which is a synapse rich area, is about 10 times that to the white matter per unit volume. Oxygen is supplied by the blood molecule called haemoglobin, whose magnetic properties depend on the amount of oxygen it carries. Oxygenated haemoglobin (oxyhaemoglobin) is diamagnetic and its presence doesn't produce appreciable changes in the surrounding magnetic field, whereas

non-oxygenated haemoglobin (deoxyhaemoglobin) is paramagnetic and causes a difference in magnetic susceptibility between the blood vessel and its surrounding tissue. This susceptibility difference, in turn, produces field gradients around vessels and dephases protons, leading to a reduction in the value of T2*, thus attenuating the MR signal. Therefore, T2* sequences are able to identify the presence of red blood cells containing deoxyhaemoglobin and variations in its local concentration.

When neurons fire in response to a sensory or cognitive process, the glial cells, the nerve cell bodies and the synaptic terminals of the axon perform an orchestrated sequence of events resulting in action potentials being transmitted and received. One consequence of this heightened activity is an increase in the local cerebral metabolism. Regulation of the rCBF is poorly understood and consequently the precise nature of the relationship between neural activity and the BOLD signal is still under debate, but it is known that localised neural activity results in a rapid selective increase in blood flow to that area. In fact, increased neural activity causes increased oxygen consumption. The rCBF increases to the relevant region, but for reasons that are still not completely understood, it increases far more than the expected increase in oxygen demand. This gives rise to the paradoxical situation in which the oxygenation state of the local capillary and venule beds is higher during focal brain activity than during rest. Thus, the amount of oxyhaemoglobin in the blood increases and the level of deoxyhaemoglobin decreases. In other words, upon neural activity, as well as the slight increase in oxygen extraction from the blood, there is a much larger increase in cerebral blood flow due to the vascular response and the bulk effect is a regional decrease in paramagnetic deoxyhaemoglobin concentration. The haemodynamic process is shown in a schematic way in Figure 3.3. At capillary bed level, the cerebral metabolic rate of oxygen extraction ($CMRO_2$) increases following the neural response to a stimulus. This produces an increase of the rCBF and regional cerebral blood volume (rCBV). The increase of rCBF

overcompensate the increase of $CMRO_2$. The subsequent reduction of deoxyhaemoglobin level reduces, in turn, local field inhomogeneities. The corresponding changes of MR signal are used as an indirect measure of the neural activity. Therefore, the BOLD signal is a measure of local field inhomogeneities produced by blood oxygen level. When field inhomogeneities decrease, the BOLD signal increases.

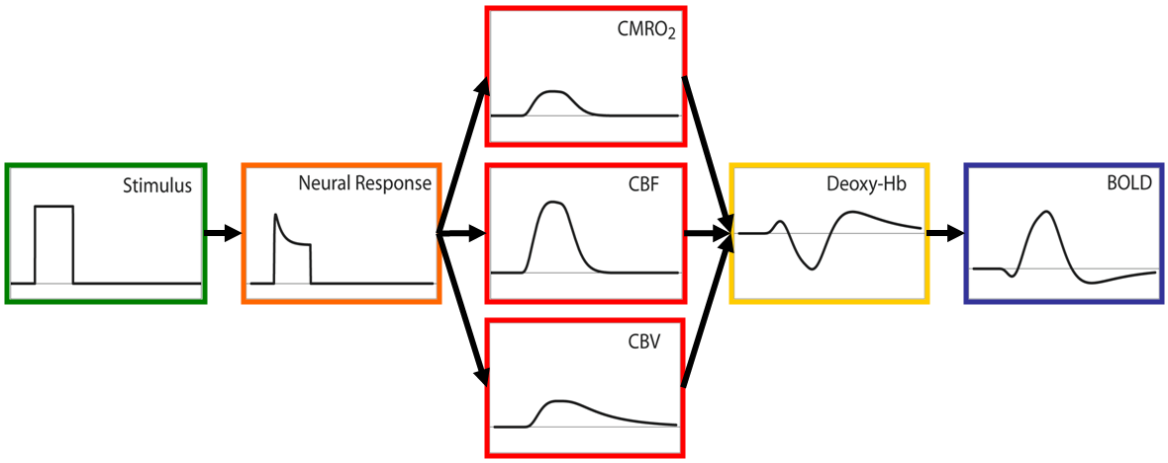

Figure 3.3 –Schematic representation of BOLD signal generation following an endogenous or exogenous stimulus.

The time course of the local haemodynamic changes following an impulsive stimulus is referred to as the haemodynamic response function (HRF). The same term is used to identify the measured MR (BOLD) signal. This time course is delayed from the onset of the corresponding neural activity by a few seconds, and is smooth (Figure 3.4). There have been observations of an initial small "dip" in signal before and after the larger increase in signal, possibly reflecting a transient imbalance between the metabolic activity and blood flow. The peak value of the HRF is reached in about 6 seconds, while the response, after a moderate undershoot, falls back to baseline in 12÷20 seconds. The temporal resolution of fMRI is limited by the time course of the HRF, whose return to baseline takes much longer than the neural activity that produced the haemodynamic response.

The relatively poor sensitivity of fMRI comes from the small percentage changes of the BOLD signal determined by the haemodynamic response. However, the magnitude of the static field B_0 is critical to the signal change obtained on activation. This is because susceptibility differences have a greater signal dephasing effect at higher fields.

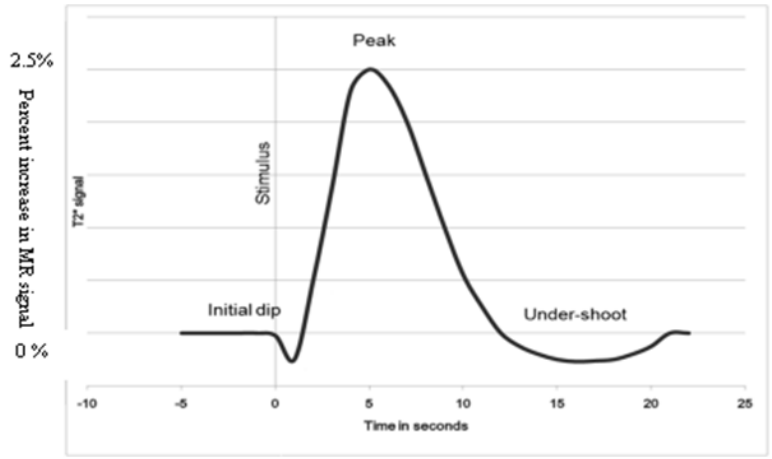

Figure 3.4 – Typical time course of the haemodynamic response function (HRF).

As stated above, although the induced rCBF increase is an accepted marker for the functional electrical activity, the mechanism of activation-related rCBF control is not yet established. Because the arterial side of the brain vasculature is essentially fully oxygenated, no BOLD changes occur on this side. The BOLD effect is manifested in the bluish capillary beds, venules and draining veins, which are only 60÷70% saturated with oxygen at rest. The size of the vasculature giving rise to the observed MRI signal changes is one of the major issues limiting reaching arbitrarily high spatial resolution in fMRI. Since gradient echo images are sensitive to vessels of diameters from micrometers to millimetres, it can be difficult to distinguish between signal coming from the capillary bed in the cortex and that from the draining veins. Signal changes in the capillary bed are more accurately co-localised with the neural site of activity,

but those in the draining veins can be centimetres away from the activation site and hence are not desirable (Figure 3.5).

Inhibition and excitation are both energy consuming processes. The principle of excitation–inhibition balance implies that microcircuits are capable of large changes in activity while maintaining proportionality in their excitatory and inhibitory synaptic conductances (Logothetis, 2008). Therefore, it is not clear whether they can be differentiated using the fMRI response in any single region. Similarly, we do not know what relative contribution spiking and subthreshold action potentials make to the fMRI measurements of a region. Ultimately this may also be important for spatial localisation, because subthreshold activity often extends further in space than the active spiking.

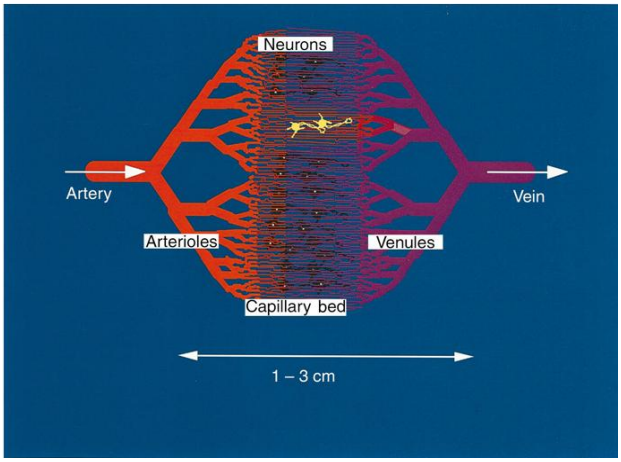

Figure 3.5 – Vasculature in the brain. The various sizes of cerebral vessels and the neuronal network within the capillary bed are shown.

During the scanning there are a number of physiological effects that can affect results. Physiological noise arises from cardiac-linked brain pulsations (0.8 ÷ 1.3 Hz) and bulk susceptibility variations of the chest with respiration that propagate as small magnetic field variations in the brain (0.1 ÷ 0.3 Hz). Another source of artefacts is general subject movement. Movement can reduce SNR in fMRI images, and introduce artefacts in the activation maps if it is stimulus correlated. All these problems can be dealt with in two ways, either at the time

of scanning (with cardiac or respiratory gating) or in image processing (which is the most commonly used way to deal with this problem). Movement can also be reduced by restraining the head of the subject.

Figure 3.6 summarises the physiological principles of fMRI by showing the sequence of events from stimulus presentation to BOLD signal recording.

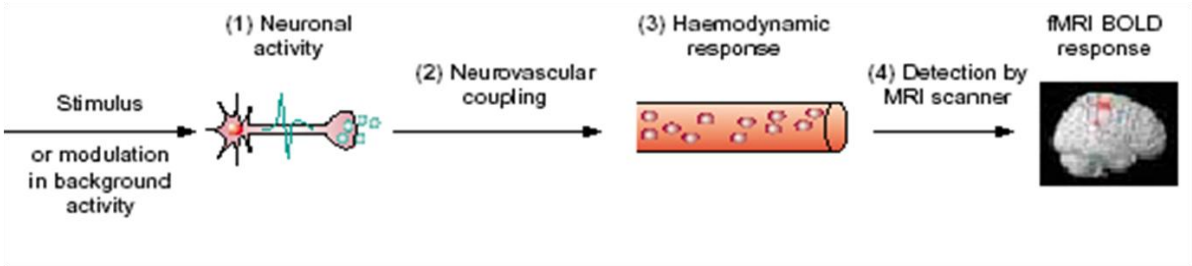

Figure 3.6 – The BOLD fMRI response is based on the neurovascular coupling mechanism and depends on the time course of the haemodynamic response. Therefore, the recorded signal is the result of different and heterogeneous effects and is an indirect measure of cerebral activity.

3.1.3 Experimental paradigms

To obtain changes in BOLD signal, the brain should undergo different "conditions". These conditions consist in performing one or more tasks and may be differentiated in conditions of interest, conditions of no interest, and rest condition, i.e. a condition in which, ideally, only basal cerebral activity is present. The key elements to consider while designing an fMRI experiment are that it should enable to refuse a null hypothesis and that task conditions should elicit an appreciable change in rCBF and therefore in the BOLD signal. In a typical application, signal changes in a series of rapidly and serially acquired brain images are correlated with the time course of a motor, sensory or cognitive probe task. Activation is defined as a region showing statistically significant changes in BOLD signal correlated with the time course of changes in

performance through the probe task (for example, cycles of movement versus rest with hand tapping). The length of time that the patient performs the task is determined by the extent of averaging of the small signal changes associated with each task change that is needed to provide statistically significant measures of correlation. In fact, over the course of an experiment, the brain is continuously active. This means that the level of oxygenation of the blood varies continuously. However, typically only a small percentage of this variation in oxygenation is actually related to the task at hand and constitutes the signal of interest. Therefore, great care must be taken when designing an fMRI experiment. The optimal experimental design maximises the possibility of finding a reliable answer to the research question posed. In other words, the optimal design maximises both statistical power and the power to draw inferences. The phases of an fMRI study may be briefly listed as follows:

- formulating the research or clinical question;
- choosing the type of study (e.g., presence of a control group, inclusion and exclusion criteria, longitudinal study, follow-up);
- defining the general features of the paradigm (e.g., block design, event-related design, number of runs per session, duration of each run);
- choosing the stimuli (type, duration, onsets) for each condition and implementing the sequence in a stimulation system (see Section 3.1.6);
- choosing the parameters of the echo-planar sequence (EPI is the most common type of sequence used in fMRI);
- training the subject;
- acquiring basic (diagnostic) sequences;
- performing the fMRI exam;
- processing the recorded data;
- examining the results of the exam.

Two different types of experimental designs used in fMRI research will be described in the following, namely block designs and event-related designs, and

their strengths and weaknesses regarding their ability to answer certain research questions will be explored.

3.1.3.1 Block designs

The block design or "boxcar" has been the first widely used experimental design in neuroimaging. In a block design, two or more conditions are alternated in blocks. Each block will have duration of a certain number of fMRI scans (corresponding to an extended period of time relative to the HRF, typically 20÷30 s) and within each block only one condition is presented (continuously or with repetitive stimuli). By making the conditions differ in only the cognitive process of interest, the fMRI signal that differentiates the conditions should represent this process. This is the so-called subtraction paradigm. Using a block design has one main advantage. The increase in fMRI signal in response to a stimulus is additive. This means that the amplitude of the BOLD signal increases when multiple stimuli are presented in rapid succession (until saturation). When blocks are alternated allowing the HRF enough time to return to baseline, a maximum amount of variability is introduced in the signal (Figure 3.7). Therefore, block designs offer considerable statistical power (Donaldson and Buckner, 2001).

The main assumption of the subtraction paradigm is the idea of pure insertion. This means that a cognitive process can be added to a set of already active cognitive processes without affecting them. If this assumption fails, the difference in the fMRI signal between two conditions that is supposed to reflect the cognitive process of interest will in reality reflect the interaction between the process of interest and the already active cognitive processes. Another problem with block designs is that within each block only one condition is presented and randomisation of stimulus types is not possible. This makes the type of stimulus

within each block very predictable. As a consequence, participants may become aware of the order of the events. It is because of these problems that it is often very hard to draw solid conclusions from fMRI experiments using block designs. So while block designs have high statistical power, they have a low power to draw inferences.

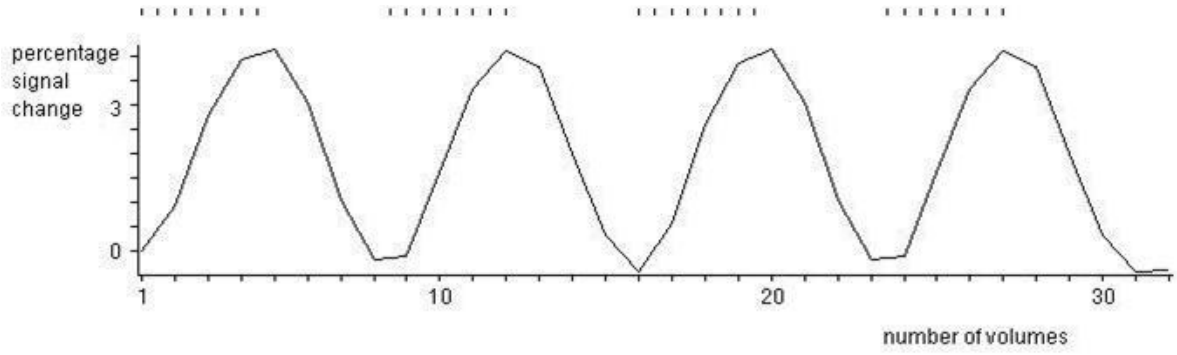

Figure 3.7 – Representation of the typical behaviour of the BOLD signal in a block design. The tick marks on the top of the figure show the stimulus onsets. In this example, 8 stimuli are presented in each task block. Each task block is alternated with rest. The rest must be sufficiently long to allow the HRF to return to baseline levels.

3.1.3.2 Event-related designs

In an event-related design the course of the HRF following each stimulus presentation is estimated. The multiple HRF's following a single type of stimulus can be averaged. This allows more real world testing, however, the statistical power of event-related designs is inherently low, because the signal change in the BOLD fMRI signal following a single stimulus presentation is small. The BOLD signal is very sensitive and neuronal activation lasting as short as tens of milliseconds still produces a measurable change in the BOLD response. This means that even stimuli of very short duration can be used in an event-related design. When two or more stimuli are presented in relatively rapid succession, the BOLD response increases roughly linearly. The approximate linearity of the BOLD signal variation in response to successive presentations of

stimuli, allows stimuli to be presented in relative quick succession in an event-related fMRI design. A follow-up issue is the question of the optimal spacing in time between the onsets of successive stimulus presentations that maximises the statistical power.

The answer to this question depends strongly on the type of event-related design and the effect of interest. When the effect of interest is a difference effect between the effects of multiple stimulus condition (for example, comparing condition A with condition B), then maximal power is obtained when the order of the stimulus conditions is randomized and the spacing in time between stimuli is minimised (as long as the assumption of linear summation of BOLD responses still holds). However, when the effect of interest is a main effect of a stimulus condition, this only holds when some measure is taken to add additional predicted variability into the BOLD signal. When stimuli of same condition are presented rapidly and closely spaced in time, the BOLD response saturates and statistical power is low. However, the power can be increased by adding predicted variability to the BOLD response. This additional predicted variability can be added either by introducing a latency jitter or by including null events. A latency jitter can be introduced by employing a variable inter stimulus interval (ISI) instead of a fixed ISI, thus varying the time between the onsets of successive stimuli. In the case of a null event, no stimulus presentation occurs. Like the introduction of a latency jitter, the inclusion of an occasional null event adds additional predicted variability to the BOLD response by allowing the HRF to partially return to baseline.

Even though the statistical power of event-related designs can be improved by the above mentioned procedures, it is still inherently low compared to the statistical power of block designs. Despite this limit, there are a number of advantages in using event-related designs. The main advantage is that they allow for randomisation of trials, thus allowing minimising potential confounds like habituation, anticipation and strategy effects. This increases the power to draw

solid conclusions (i.e., meaningful inferences) from an experiment. Another advantage of event-related designs over block designs is that they allow for removal of certain trials. For example, if a subject has to make a response to a stimulus, it can be desirable to be able to remove the HRF following stimuli associated with the wrong responses post hoc. Finally, some experimental questions cannot be answered using a block design, as those posed in odd-ball experiments, in which the response to an infrequently occurring stimulus appearing in a series of frequently occurring stimuli is the focus of the experiment.

3.1.4 Preparing fMRI data for statistical analysis

The goal of fMRI is to compare BOLD signal values in a given voxel in different conditions (e.g. rest, task, presence of specific event-types). Before application of a statistical analysis approach to detect the brain activations underlying these signal variations, data must be prepared by processing the recorded time series. Several approaches for fMRI data processing have been proposed. These approaches differ both in the order of single processing steps and in the way each step is implemented. The sequential combination of spatio-temporal image processing steps following data acquisition is referred to as the fMRI pre-processing pipeline. The pre-processing steps interact with virtually every decision made in designing and performing an fMRI experiment.

One of the challenges facing both academic researchers interested in fMRI processing pipelines and general users of the major software packages is the difficulty in identifying the current pre-processing pipeline practices in most major research groups. This information only partly exists in the academic literature and the e-mail discussion lists and user manuals of major software packages. Based on the existing literature, it is impossible to make conclusive

statements about the optimal algorithms and software implementations for any single pre-processing step, let alone entire pipelines (Strother, 2006). The main classification is between all-in-one analyses, in which raw data is completely pre-processed before statistical analysis, and a summary statistic approach, in which some pre-processing steps are by-passed and the statistical maps are subsequently registered for further higher-level data analysis.

When the analysis concerns a single subject, the pre-processing for the all-in-one analysis should include realigning the time series, correcting for slice acquisition timing, coregistering, optionally segmenting and normalising, smoothing and filtering. A different pre-processing pipeline is required when the analysis of fMRI data from a group of subjects is concerned, i.e. when data from different subjects, acquired in the same experimental conditions, are analysed all together to extend inferences to the population from which subjects were drawn. In this latter case, data from each subject must be normalised to a common stereotactic space so that corresponding anatomical regions of different subjects are superimposed on a structural template, i.e. a common anatomical framework. In a group analysis, the realigned time series, after fMRI-to-MRI transformation (calculated by first coregistering the averaged fMRI to a structural scan), may be passed straight to normalisation to create a set of subjects' fMRI scans aligned to a common coordinate system, and these scans are passed on to spatial smoothing.

However, there are a number of other possible combinations of the above steps. One example is the possibility of collecting both low-resolution structural EPI scans that match the low-resolution fMRI scans, and high-resolution MRIs in the same subject; the fMRI scans are aligned to the low-resolution structural EPI scans, which are warped to the high-resolution MRI to complete coregistration. Furthermore, image quality control checks should be performed before and after specific processing steps. A first quality control consists in looking for artefacts in the raw image data. Another critical quality issue is

image orientation, particularly absolute identification of the left and right hemispheres of the brain in an fMRI image volume. Details of the pre-processing steps are given in the following sections.

3.1.4.1 Realignment

Even small head movements during scanning can be a major problem due to the increase in residual variance and their potential correlation with the task performed, which may result in showing false positives in activation maps. Typical edge artefacts are produced in EPI scans as a consequence of uncorrected head motion and data may get completely lost if sudden movements occur. Therefore, it is important to reduce head movements with careful use of head-immobilisation techniques when placing the subject in the scanner, and by instructing him/her explicitly to remain as calm as possible. Scan duration also plays a relevant role in movement reduction. However, head motion during scanning cannot be completely eliminated.

To ensure that each voxel's time series is an accurate representation of the BOLD time series for a constant spatial location in the brain, voxels must be spatially aligned across the sequentially collected fMRI image volumes. Therefore, the primary aim of the realignment step of pre-processing is to remove movement artefacts in time series. Realignment is based on an algorithm which realigns a time series of images acquired from the same subject using a six parameters rigid-body spatial transformation (thus assuming that the shape of the brain does not change in time). It is accomplished in two steps. The first step consists in optimising the six parameters that describe a rigid-body transformation between the source image and a reference image:

$$\begin{bmatrix} x_1 \\ y_1 \\ z_1 \\ 1 \end{bmatrix} = \begin{bmatrix} m_{11} & m_{12} & m_{13} & m_{14} \\ m_{21} & m_{22} & m_{23} & m_{24} \\ m_{31} & m_{23} & m_{33} & m_{34} \\ 0 & 0 & 0 & 1 \end{bmatrix} \cdot \begin{bmatrix} x_0 \\ y_0 \\ z_0 \\ 1 \end{bmatrix} \quad (3.1)$$

All scans are realigned to the image specified as the reference. Usually, though not necessarily, the first volume acquired in the time series is used as the reference image. As an alternative, after a first realignment a mean image may be produced and all the images may be successively registered to the mean image. If multiple runs are acquired within the same scanning session, they can be realigned together. In this case, the runs are first realigned to each other, by aligning the first scan from each run to the first scan of the first run. Then, the images within each run are aligned to the first image of the run. The parameter estimation is performed this way because it is assumed that there may be systematic differences in the images between runs. A set of realignment parameters is obtained for each run at the end of the realignment step. These parameters reflect the relative orientations of the data and may subsequently be modelled as confounds within the general linear model (see Section 3.1.5.1).

A given cost function must be used to measure the similarity of each image volume in a time series to the reference volume. The cost function allows determining when an algorithm has generated sufficiently similar volumes to provide optimal estimates of the six rigid-body movement parameters. Many of the differences between realignment algorithms implemented in different software tools relate to the choice of a cost function and the optimisation strategies implemented to iterate to a global, as opposed to a local, minimum.

The second step of realignment consists in resampling the images such that they match voxel-by-voxel the reference image. An interpolation function is a combination of the original voxel values in the spatial neighbourhoods of the new locations. Different interpolation methods can be chosen to sample images in order to reslice them. The type of interpolation scheme used represents a trade-off between residual interpolation errors and speed. Higher degree

interpolation methods provide better interpolation, but they are slower because they use more neighbouring voxels.

It is well established that resampling using rigid-body transformation parameters is insufficient to remove all motion effects. Residual-movement artefacts left after standard motion correction techniques can be removed by subsequently performing a general linear model analysis using motion estimates as unwanted effects regressors. However, it is not uncommon for subjects to produce small head movements that are correlated with performing the task (particularly in motor tasks). In these cases the motion-regression approach of regressing out residual motion effects based on the estimated motion variables may not work properly because the variables are correlated with the stimulus.

A quality check should be performed on the plots of the six rigid-body motion parameters to determine the estimated range of motion in the data. Figure 3.8 shows the time course of the realignment parameters estimated on a subject performing a visual task (see Section 4.5.2). Many centres use a rule-of-thumb that suggests that data should be discarded if estimated motion is more than 1÷2 mm. The effects of a movement exceeding this limit are shown in Figure 3.9, where an erroneous motion correction resulted in false activations, well evident in axial projections.

Another source of motion-dependent inaccuracies is susceptibility artefacts caused by field inhomogeneities. These inhomogeneities are primarily determined by the relatively large change in local magnetic field strength that occurs at a boundary between materials with very different magnetic susceptibility properties, e.g., an air- or bone-tissue boundary in the brain. A number of data acquisition approaches exist to reduce this artefact, including static gradient shimming and modified pulse sequences, but appreciable image distortion typically remains in fMRI images. Geometric unwarping is needed to correct for these inhomogeneities. One method involves measuring the magnetic field inhomogeneities to create a field map for the fixed component, which is

used to modify the acquired fMRI images. Another approach involves simultaneous, direct estimation of the rigid-body transformations for motion correction, together with a geometric unwarping correction (this latter technique has been included in the SPM software package).

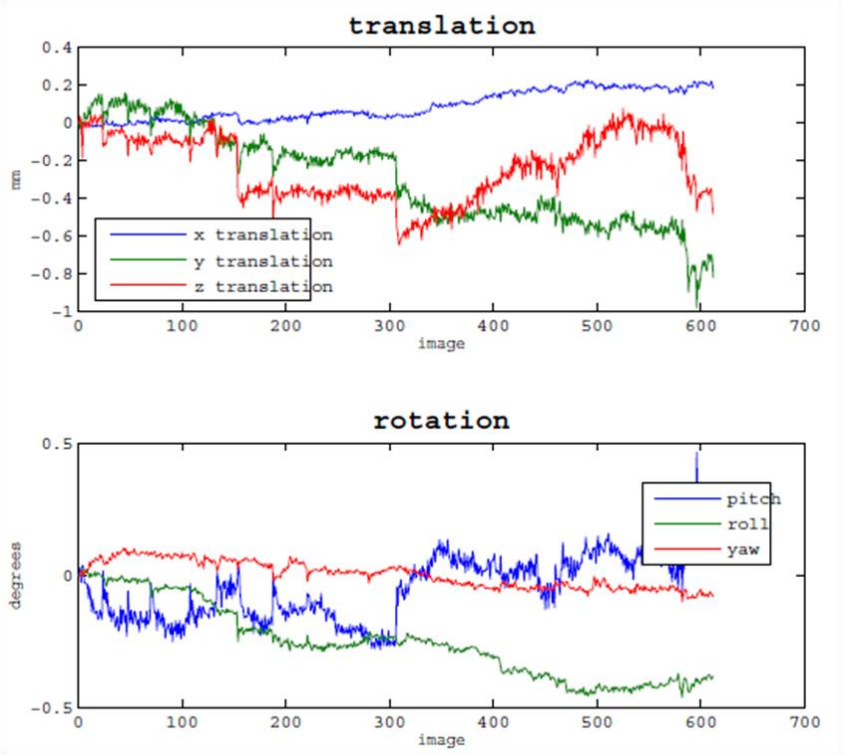

Figure 3.8 – Time course of the rigid-body motion parameters estimated on a subject performing the visual task described in Section 4.5.2. The number of EPI scans is shown in the x-axis.

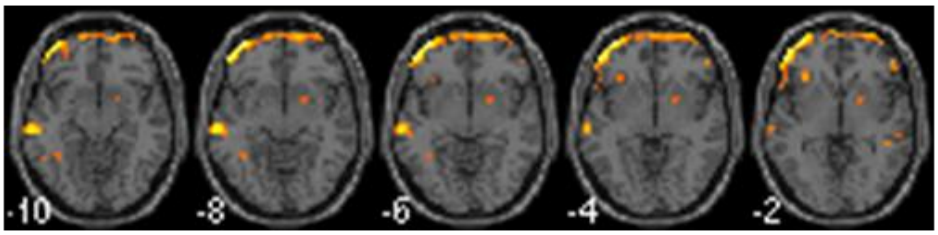

Figure 3.9 – False activations resulting from excessive movement of a subject performing the verb generation task described in Section 3.2.2.

3.1.4.2 Slice-timing correction

The slice-timing correction is intended to correct differences in slice acquisition times. The correction is necessary to make the data on each slice correspond to the same point in time. While a new volume may be collected every 2÷3 s, the individual slices are collected sequentially during this time period. For the usual ascending or descending sequential acquisitions, the last slice is collected almost one TR after the first slice (TR is the time between acquiring a slice of one volume and the same slice in the next volume.). With interleaved acquisitions (i.e., all odd slices are collected first, followed by all even slices), adjacent slices are collected a full TR/2 apart.

Slice-timing correction uses interpolation between the same slice and voxel in neighbouring volumes to estimate the signal that would have been obtained had the slices been acquired at the same time. The interpolated time point is typically chosen as the TR/2 time to minimise relative errors across each TR. The slice-timing correction routine works by lagging the time series data on each slice using sinc-interpolation (corresponding, in the time domain, to a delta function shifted in time). This results in each time series having the values that would have been obtained had the slice been acquired at the same time as the reference slice. Without correction, values of a slice acquired one second later than the reference slice will describe a haemodynamic response that will appear to have begun one second earlier than the reference.

All the approaches for realignment assume that the stack of slices comprising a volume is collected instantaneously, and that movement of the entire stack occurs across sequentially collected scans. However, slices are not acquired simultaneously and rapid movements are not accounted for by the rigid-body model. Any movement during the TR for one volume will affect the individual slices differently so that there is an interaction between movement,

the rigid-body assumption, slice-timing correction, and the type of slice acquisition sequence. A separate correction for slice-timing with temporal interpolation is provided by the major software packages, but there are no clear rules regarding whether this should be applied before or after rigid-body movement correction. There appears to be a general consensus that slice-timing correction is probably unnecessary for most block designs. A more flexible statistical model may be used instead, by including the derivatives of the HRF if timing of activation is of particular interest. Huettel et al. (Huettel et al., 2004) have proposed commonsense rules for single-event designs: slice-timing correction should precede motion correction for an interleaved slice acquisition with a long TR; with sequential acquisitions or short TRs, motion correction should be done before timing correction.

3.1.4.3 Coregistration

A structural MRI is usually collected during the same scanning session as the fMRI scans. This MRI has much higher resolution and tissue contrast than EPI scans. The first reason why it is useful to collect structural MRI is that by coregistering it to the fMRI scans, the location of a statistical increase in the fMRI signal may be accurately determined by visualising single-subject statistical maps overlaid on a high resolution anatomical scan of that same subject. A second reason is that coregistration can sometimes help with spatial normalisation. The normalisation of the high resolution anatomical scan to a standard brain often leads to better results than matching the fMRI scans to the standard brain. If the high resolution anatomical scan and the fMRI scans are first coregistered, the parameters that are used to match the anatomical scan to the standard brain can then be applied to the fMRI dataset (Frackowiak et al., 2004). Therefore, the T1-weighted scan enables to achieve a more precise

normalisation of fMRI scans to a common coordinate space defined by a structural template, combining fMRI-to-MRI and nonlinear MRI-to-template transformations. This, in turn, allows warping single-subject data-analysis results to the template's coordinate space for group analyses.

High-resolution MRI should undergo brain vs. non-brain segmentation and intensity bias correction before coregistering with fMRI. Several routines, including segmentation and classification of MRI brain voxels and some cost functions used with fMRI-to-MRI alignment, perform better if the non-brain tissues (e.g., scalp, skull) are identified and removed from MRI images. Moreover, structural MRI volumes tend to have nonuniform tissue intensities as a result of the nonuniform sensitivity profiles of the radio frequency coils used to transmit and receive the signal. Significant nonuniformities may bias the results of segmentation and registration algorithms and should be corrected. Bias correction algorithms are usually incorporated into tissue segmentation routines because bias correction interacts with tissue classification (see Section 2.1.2.1).

During spatial realignment, EPI fMRI scans are repositioned until they are in the same position as a reference EPI scan. In other words, different scans within the same modality are aligned together. However, aligning scans from different modalities together (known as spatial coregistration or as between-modality registration) requires different algorithms from realignment. While two images from the same modality will have similar intensities for each specific tissue type (e.g., water is always dark on a T1 scan), two images from different modalities will usually not have similar intensities for a given tissue type (e.g., water is dark on a T1 scan, but bright on a T2 scan). Therefore, matching intensities of the different images is not possible.

One possible approach for coregistration is using intermodal similarity functions (Frackowiak et al., 2004). First, each modality is normalised to a standard brain of the same modality. After this normalisation, one of the images is segmented into separate tissue types, each containing only the locations in the

brain with a specific intensity range. Coregistration is subsequently performed by mapping each of these segmented images onto the second image using an algorithm that minimises the squared differences.

The most common approach, however, is based on mutual information theory (Frackowiak et al., 2004). Mutual information is used as a robust cost function to be minimised by coregistration. This approach is based on the principle that even though the same tissue appears different between modalities, intensity differences between different tissues are preserved in each modality. If the intensities in each image are represented as a histogram, a joint histogram can be created, with each voxel having an intensity value (from one modality) on the *x*-axis and an intensity value (from the other modality) on the *y*-axis. Each tissue type will have a range of values on both the *x*-axis and the *y*-axis, which is different from the other tissue types in each image. Between modality registration basically tries to minimise the amount of noise in this joint histogram. While aligning the images, the noise in the joint histogram decreases. If the images are in perfect alignment, the histogram will show a "blob" for each tissue type.

In coregistration of fMRI time series to structural scans, the mean EPI scan obtained from the realignment step is used as the target (reference) image and the structural image as the source image (Figure 3.10). By proceeding in this way, the mean EPI (and, therefore, all the EPIs) remains in the native space, while it is the structural image that is coregistered (the higher-resolution image will suffer less distortion after interpolation). A visual check should be performed after coregistering.

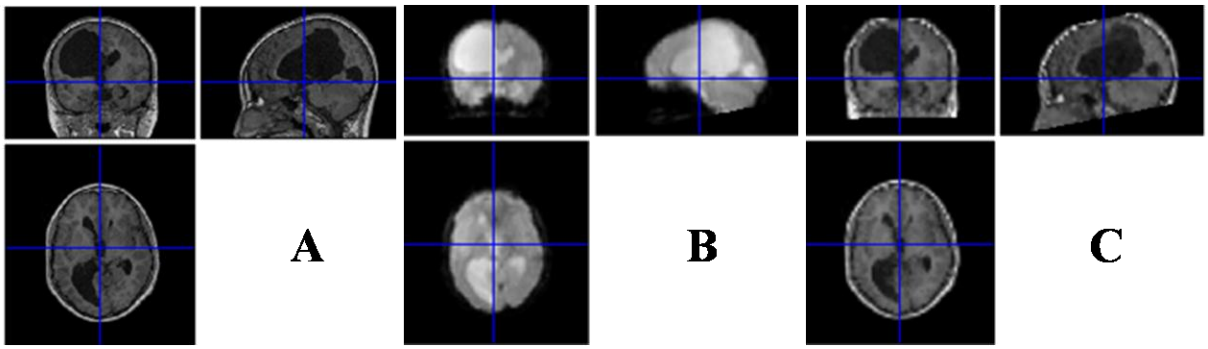

Figure 3.10 – Effects of between-modality registration. (A) T1-weighted scan of a hemiplegic patient participating in the study described in Section 4.6. (B) Mean EPI from the same subject, obtained from the realignment step of fMRI pre-processing. (C) T1 scan coregistered to the mean EPI. Coregistration was performed using mutual information.

3.1.4.4 Normalisation

As previously stated, spatially normalising the data is only a pre-requisite for inter-subject averaging or reporting in a standard space, whereas it is not needed when single-subject analyses are performed and there is no need to register the images on a labelised space.

Normalisation is described in detail in Section 2.1.2.2. As a general rule, the template should match the data being aligned as closely as possible. Therefore, leaving out coregistration completely and nonlinearly warping the average of the movement-corrected fMRI time series directly to a matched template (e.g., an EPI structural template) may minimise the effects of geometric distortion from magnetic field inhomogeneities. However, this approach may be less robust than the use of structural MRIs through coregistration, due to the lower resolution of EPIs compared to MRIs. Nevertheless, evidence seems to be accumulating that highly accurate structural warps are not necessary for functional group analyses (Strother, 2006).

3.1.4.5 Smoothing

Spatial smoothing is described in detail in Section 2.1.2.5. Smoothing may have a dramatic impact on signal detection power in fMRI and is one of the most influential pre-processing choices when compared with other steps. In fMRI the effects of interest are produced by changes in blood flow, which are predominantly expressed in low spatial frequency bands (with wavelengths in the order of several millimetres), while noise is usually present at higher frequencies. The spatial filtering step is placed before temporal filtering and regression of unwanted effects (see Sections 3.1.4.7 and 3.1.5.1, respectively) to improve variable estimates within these steps. Gaussian smoothing kernels of 1÷2 voxels FWHM are typically used.

3.1.4.6 Intensity normalisation

Intensity normalisation is the re-scaling of the intensities to a common mean intensity value. One way to perform this normalisation is within a continuous fMRI dataset. First, the mean intensity of an fMRI volume is determined. Subsequently, all voxels in that volume are re-scaled to a certain pre-determined mean intensity value. The underlying idea is that re-scaling to a common mean will get rid of global variations in intensity between volumes that are a result of scanner properties (e.g., heating). However, there is a huge problem with this approach. In case certain voxels in a volume show a strong increase in response to the task condition, intensity normalisation will re-scale voxels in the whole volume to a certain mean intensity value. However, the result is also that the voxels showing less increase in the BOLD signal in that same volume might be re-scaled to such an extent that they appear to show a

signal decrease. This is one of the reasons why intensity normalisation within a continuous fMRI dataset is usually not performed.

Global variations in intensity that are not part of the actual signal can generally be dealt with using high-pass temporal filtering (see Section 3.1.4.7). There is still the problem, though, that some sort of intensity normalisation between different fMRI datasets (e.g., obtained from different subjects) must be performed. A variety of global normalisation approaches have been developed to model and control for this variation, including grand-mean session scaling, proportional scaling, and ANCOVA. In grand mean scaling, for example, each continuous fMRI dataset is re-scaled to a pre-specified common mean for the dataset. The result is that all the different fMRI datasets have the same mean intensity value so that comparisons over and between these datasets are meaningful.

3.1.4.7 Temporal filtering

As stated above, unwanted temporal frequencies can be removed from the dataset by temporal filtering. Low-pass filtering for denoising or temporal smoothing for control and estimation of temporal autocorrelations may degrade signal detection power both in block designs and in event-related designs. However, pre-whitening (estimation and removal of temporal autocorrelation to whiten the residual noise) should be used to improve parameter estimation efficiency.

High-pass filtering allows for control of low-frequency noise trends. The noise power in the majority of fMRI time series occurs at low frequencies ($f < 0.05$ Hz) with an approximately 1/f envelope. The exact causes of this noise structure remain unclear, although it is probably some mixture of scanner drift (as the scanner heats up in the course of an exam, the signal will appear to drift)

and physiological effects as cardiac noise and respiratory noise (such as that due to resting fluctuations in arterial CO_2). Care must be taken to not attenuate the signal, which in block designs often has a relatively low fundamental frequency of around 0.02 Hz (depending on epoch period). Besides low-pass filtering in the frequency domain, removal may be effected by regressing out linear and higher-order polynomial trends as unwanted effects in a general linear model analysis (see Section 3.1.5.1). However, there is no consensus as to which high-pass filtering or detrending approach to use (Strother, 2006).

3.1.5 Statistical analysis of fMRI data

The goal of the statistical analysis is to determine what areas of the brain are significantly activated under certain task conditions. Most commonly the general linear model (GLM) is used for this statistical analysis (Friston et al., 1995). However, alternative approaches have emerged during the last few years, such as independent component analysis (ICA).

3.1.5.1 The general linear model

The statistical analysis within the GLM consists of a number of steps. First, the BOLD response must be modelled. Secondly, the parameters of this model must be estimated. Finally, it must be determined whether there is any evidence for a statistically significant increase in the BOLD signal in response to a task condition.

The basic principle of the GLM is that measured data are interpreted as the linear combination of a set of functions plus additive noise. The shapes of

the functions (regressors) are known, while their amplitudes are the parameters to estimate (Figure 3.11). Thus, the basic formula used in the GLM is:

$$Y = X \cdot B + E \tag{3.2}$$

In this formula Y is a matrix containing all the observed data with a column for each voxel and a row for each fMRI volume, X is a matrix containing a column for each predictor variable and a row for each fMRI volume and is called the design matrix, B is a matrix containing the slopes and intercepts of the linear regression vectors and is called the parameter matrix and E is a matrix with the normally distributed error terms.

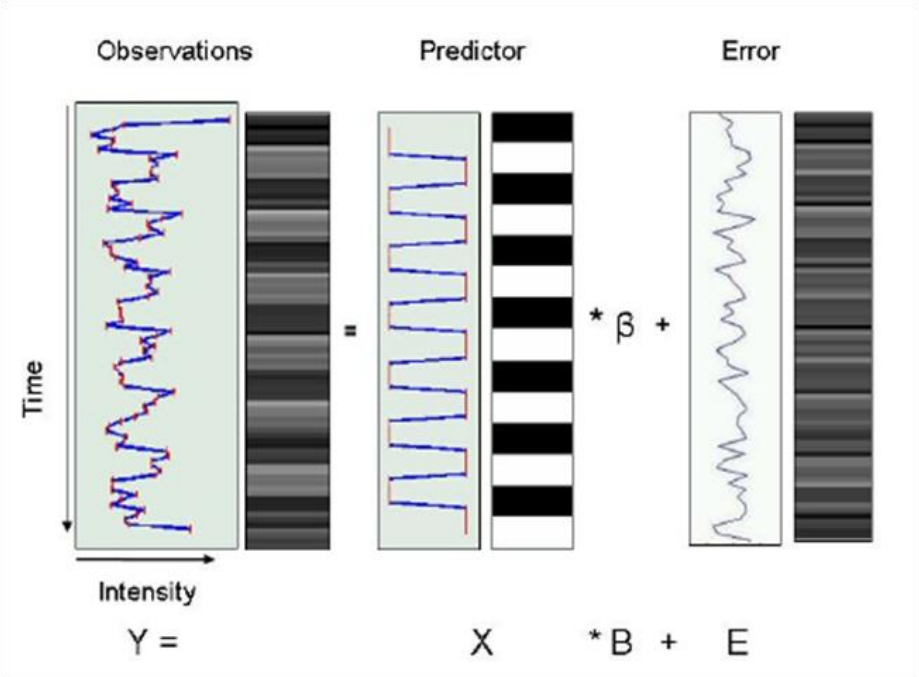

Figure 3.11 – The general linear model (GLM). The time course of signal intensity measured in a single voxel is interpreted as the linear combination of predictor variables (only one predictor is shown in the figure) weighted by a set of unknown coefficients, plus additive noise.

In the design matrix the general shape of the BOLD response over time is modelled. Therefore, it is this matrix which defines the experimental design and

the nature of hypothesis testing to be implemented. The design matrix should contain as regressors all the explanatory variables, i.e. both the stimulus functions and other known effects. The columns of the design matrix representing the stimulus functions actually result from the convolution of these functions with the HRF. Covariates like task performance and confounds like slow drifts may also be modelled in this matrix. In addition to the predictor variables, their derivatives are often modelled. The most commonly used derivatives are the temporal and dispersion derivatives. The temporal derivative allows for variations in the onset of the HRF response, while the dispersion derivative allows for variations in the width of the HRF response. Additional columns may be included in the design matrix to model effects that would not be convolved with the haemodynamic response. One such example would be the estimated movement parameters, to remove residual- movement artefacts. In other words, to obtain a strict control of movement artefacts, besides performing realignment during pre-processing, the estimated realignment parameters can be included in the statistical model. Other examples of regression parameters include reaction times, low-frequency trends, global intensity variations, and even physiological time series.

The parameter matrix must be estimated for each voxel separately, using linear regression in order to fit the model separately to the time course of each voxel. In other words, the statistical analysis of fMRI datasets is massively univariate. For each predictor variable, a parameter is obtained that optimises the fit of the overall BOLD response modelled in the column of the design matrix to the observed data for each voxel. After estimating the parameter matrix, the error matrix would ideally represent the variance in the model that is left unexplained. However, in BOLD fMRI time series the successive data points are not independent because the time it takes to acquire a single data point (TR) is shorter than the time it takes for HRF to return to baseline. Therefore, successive acquisitions partly sample the same HRF and are not independent.

This temporal autocorrelation has to be modelled to avoid inaccurate estimates of the degrees of freedom and therefore inaccurate estimates of the error variance.

After estimating parameters and error, the parameter matrix is compared to the error matrix for each voxel individually, culminating in a test (t or F) statistic to determine for each voxel separately whether a specific linear combination of the predictor variables defined in the design matrix explains a significant amount of variance in the BOLD fMRI dataset. In other words, the explained variance given by a linear combination of parameters in the parameter matrix is statistically compared to the unexplained variance in the error matrix. The result of the statistical analysis for a given linear combination of predictor variables is a map of t- or F-scores for each voxel. Similarly to VBM (see Section 2.1.2.6), a method to deal with the multiple comparisons in mass-univariate analyses should be applied (e.g., Gaussian random field theory, false discovery rate correction, minimum cluster size, region of interest analysis).

It is interesting to investigate how the statistical analysis of fMRI data with the GLM is implemented in the SPM tool. This analysis comprises specification of the design matrix, estimation of the parameters and interrogation of estimate results using contrast vectors to produce statistical parametric maps.

The design matrix for fMRI data consists of one or more run-specific partitions. These partitions are usually either one per subject or one per fMRI scanning run for that subject. Epoch and event-related responses are modelled in exactly the same way by specifying their onset times and their durations, the only distinction being the duration of the underlying input or stimulus function (event-related responses are modelled in terms of responses to instantaneous events). Mathematically, they are both modelled by convolving a series of delta or box functions (indicating the onset of an event or epoch, respectively) with a set of basis functions to give regressors that enter into the design matrix. These basis functions model the haemodynamic convolution applied by the brain to the

inputs. The delta function can be modulated by some parametric variate (this can be time or some trial-specific variate like reaction time) modelling the interaction between the trial and the variate. For factorial designs, one can later associate these experimental conditions with the appropriate levels of experimental factors.

After estimating the GLM parameters, t or F contrasts must be defined to contrast different experimental conditions. As an example, if two task conditions A and B were present, together with a rest condition, both activations for each condition (i.e. voxels significantly activated in condition A and, separately, voxels significantly activated in condition B) and differential activations (i.e. voxels significantly more activated in condition A than in condition B, or vice versa) may be tested. Furthermore, the main (i.e., joint) effect of both task conditions may be tested. Finally, a statistical threshold must be chosen taking into account the number of parametric tests (i.e., voxels) to control for the FWE.

Analyses of data from multiple subjects proceed in two stages using models at two levels. The first level models are used to implement a within-subject analysis and there will be as many first level models as there are subjects. After analysing every subject individually, a single subject T-contrast must be specified according to the inference that one wants to make (both at the single subject and at the group level). To make inferences about the population from which the subjects were drawn, a random-effects analysis (or, more properly, a mixed-effects analysis) is required. In SPM, random-effects analysis is implemented using the summary-statistic approach, where contrast images from each subject are used as summary measures of subject responses. For each contrast of interest, contrast images obtained from single subjects are entered as data into a second level model (e.g. a one sample t-test), called a second level or between-subjects analysis. This analysis assesses the significance of the response across subjects, i.e. it allows drawing of a population-level inference.

3.1.5.2 Independent component analysis of fMRI data

ICA is a statistical and computational technique for revealing hidden factors that underlie sets of random variables, measurements, or signals, by defining a generative model for the observed multivariate data. In the model, the data variables are assumed to be linear mixtures of some unknown latent variables, and the mixing system is also unknown. The latent variables are called independent components or sources and they are assumed non-Gaussian and statistically mutually independent (Hyvärinen and Oja, 2000). Sources are obtained by maximising the statistical independence of the estimated components. The way independence is defined determines the algorithms used in ICA. Typically, independent components are obtained by minimising mutual information or by maximising their non-Gaussianity. It is important to note that ICA doesn't allow estimating the number of sources that generate the measured signals.

Let us denote by $x^T=(x_1,\ldots,x_n)$ the random vector whose elements are the measured data and likewise by $s^T=(s_1,\ldots,s_n)$ the sources to estimate. The goal is to estimate the linear transform $s=Wx$ which makes the sources maximally independent according to a given function of independence $F(s_1,\ldots,s_n)$. Each component of the x vector is generated as a sum of the independent components:

$$x_i = a_{i,1}s_1 + \cdots + a_{i,k}s_k + \cdots + a_{i,n}s_n \tag{3.3}$$

that is:

$$x = As \tag{3.4}$$

Given N realisations of the random vector x, the task is to estimate both the matrix A (called the mixing matrix) and the sources s. This is done by iteratively calculating the w vectors to maximise the independence of sources $s_k=w^Tx$. The sources can then be recovered by multiplying the observed signals x by the inverse of the mixing matrix (the so-called unmixing matrix) $W=A^{-1}$.

In the field of biomedical data, applications of ICA algorithms include psychometric measurements, EEG recordings, and bioimaging. In this latter field, ICA is an alternative method to the hypothesis-driven approaches, notably to GLM, for fMRI data analysis. While the GLM is based on the knowledge of the stimulus sequence, which is convolved with the HRF to predict the measured signal, ICA is based on a data-driven approach. Therefore, ICA doesn't require *a priori* knowledge or specific assumptions on the time course of the stimuli or on the brain processes associated with the task (whether they are wanted or non-task-related processes). It is this feature that makes ICA an interesting method when this information is not available (McKeown et al., 1998).

Conventional approaches to fMRI data analysis do not allow investigating relations between cerebral regions. An activated voxel means the time course of signal intensity in that voxel is correlated to the stimulus sequence, while no inference can be drawn as to the relation between two activated voxels in different brain regions. With ICA, fMRI datasets are decomposed in spatially independent components (maps), each consisting in a set of voxels with a common time course. This allows analysing coactivated spatially remote areas. It is worthy to note that it is spatial ICA which is here described, while temporally independent components may be separated in temporal ICAs (Calhoun et al., 2005).

In ICA it is assumed that each component map, characterised by a specific spatial distribution of values (one for each voxel), represents a pattern of brain areas that, by behaving in a statistically dependent manner, affect the fMRI signal. A further hypothesis is that the component maps are spatially

independent. This means that if $p_k(C_k)$ is the probability distribution of voxel values in the *k-th* component map, then the joint probability distribution of all *n* components can be decomposed as:

$$p(C_1, \dots, C_n) = \prod_{k=1}^{n} p_k(C_k) \tag{3.5}$$

where each component map $C_k=(c_{k1}, \dots c_{kM})$ is a vector of *M* elements, one for each voxel. Finally, it is assumed that the measured data are the sum of the contributions of individual component processes in each voxel. Therefore, the component maps are composed by the voxels that more actively contribute to a given component of the observed signal, while the value measured in each voxel is modelled as the sum of the contributions of all the independent components (there may be some overlaps between component maps, i.e. different component maps can generate activations in the same brain areas). The amount of contribution of each component in a given voxel is thus given by the product of the voxel value in the respective component map and the time course associated with the map. No *a priori* assumptions are required on the time course of the various components, nor is it necessary to formulate hypotheses about the existing link between a given component and the specific processes generating it (i.e., if the component is activated by a physiological phenomenon related to the task or is rather linked to nuisance factors such as unwanted physiological signals, movement, noise or other artefacts).

To solve the problem of blind source separation, the unmixing matrix must be identified (McKeown et al., 1998). If voxel values of each component map are assumed known and are arranged in separate rows of the C_{ki} matrix, the value of the *i-th* voxel at the *j-th* volume can be expressed as a function of the mixing matrix and of component maps:

$$X_{ji} = \sum_{k=1}^{n} M_{jk} \cdot C_{ki} \tag{3.6}$$

where the mixing matrix *M* specifies the relative and time-varying contributions of each component map to the observed fMRI data. The ICA algorithm iteratively determines the unknown unmixing matrix *W*, which is a linearly scaled and permuted version of the inverse of the mixing matrix. Through the unmixing matrix, it is possible to separate observed data in independent component maps:

$$C_{ij} = \sum_{k=1}^{n} W_{ik} \cdot X_{kj} \tag{3.7}$$

where C_{ij} is the value of the *j-th* voxel in the *i-th* component map and X_{kj} is the *k-th* sample of the *j-th* voxel. The estimate of the observed data obtained by the ICA algorithm is then given by:

$$X'_{ij} = \sum_{k=1}^{n} W_{ik}^{-1} C_{kj} \tag{3.8}$$

To identify which voxels contribute most to a specific component map, z maps may be used, for which a threshold is (arbitrarily) fixed, above which voxels are considered “active”.

A common pre-processing step of ICA algorithms is aimed to reduce the size of the model by sub-sampling the data set (i.e., reducing the number of acquired volumes) and by choosing a subset of components (e.g., by using approaches such as principal component analysis). This will determine (often arbitrarily) the number of independent components considered in the model.

As already stated, being ICA a technique of blind source separation, it does not require any *a priori* information on the time course of the brain processes involved in the task. In some cases, however, this may be a limit. Especially in the analysis of data acquired in event-related experiments, it may

be useful to incorporate the information on the timing of the experimental paradigm. This information is typically used after the application of the algorithm, in order to select *a posteriori* only those components whose temporal trends are more related to the stimuli (Calhoun et al., 2005).

3.1.6 Systems for subject stimulation

As previously described, during an fMRI exam the subject undergoes a motor, cognitive or sensorial task, with endogenous or, more frequently, exogenous stimuli. Performing such an exam requires setting-up a stimulation paradigm and the scan sequence parameters. To allow for subsequent data analysis, onsets and durations of each stimulus delivered in the fMRI stimulus sequence must be specified and stimulus delivery must be synchronous with BOLD signal acquisition. Finally, subject responses may need to be acquired, together with their delays. A multidisciplinary team, composed of neuroradiologists, radiologic technicians, engineers or physicists, and other clinicians (e.g., neuropshycologists, neuropsychiatrists, neurorehabilitators, neurosurgeons, depending on the application) is typically involved in the phases of designing the task, setting-up the sequences, performing the exams, processing and analysing data. Furthermore, an appropriate MR-compatible stimuli-delivery system is required if exogenous stimuli must be administered. This system must comply with the norms ensuring safe operation in the MR environment and must be compatible with the MRI scanner model used for the exam. Patient's side signal transfer connections must be safe and should not interfere with the static magnetic field, gradients and RF coils, otherwise they would produce artefacts in the acquired images.

To start research with fMRI at Bambino Gesù Children's Hospital, a comparative assessment of stimuli-delivery systems for performing fMRI exams

on adults and children was performed before the acquisition of such a system for the Imaging Department of Palidoro. Several models exist, with different designs and characteristics. The marketed systems were compared with regard to a variety of features and configurations according to a multidisciplinary Health Technology Assessment (HTA) approach (see Nocchi et al., 2008, HTAi Meeting). Table 3.2 shows the main technical characteristics and performances of the systems.

Visual stimulation				
Stimuli-delivery device	6.4" display	15" display	Goggles	Goggles
Aspect ratio	4:3	4:3	4:3	4:3
Field of view	15°	30°	30°	30°
Screen/s technology	LCD	LCD	OLED	OLED
Resolution	640 x 480	1024 x 768	800 x 600	800 x 600
Video channels	1	1	2	2
Eye movements tracking	Optional	Optional	Optional	Optional
Auditory stimulation				
Stimuli-delivery device	Stereo headphones	Stereo headphones	Stereo headphones	Stereo headphones
Frequency band	50 Hz ÷ 20 kHz	50 Hz ÷ 20 kHz	40 Hz ÷ 40 KHz	8 Hz ÷ 35 KHz
Passive noise attenuation	16 ÷ 20 dB	16 ÷ 20 dB	30 dB	30 dB
Patient response				
Response device	N. 2 keypads (5 buttons)	N. 1 keypad (10 buttons)	Keypad, trackball or joystick	N. 2 grips (2 buttons) N. 1 keypad (4 buttons)

Table 3.2 - Technical characteristics and performances of different stimuli-delivery systems.

Visual stimulation devices have a particularly relevant role. These devices can mainly be classified in those who deliver the visual stimuli by means of a single display and those who allow stimulation with goggles. Important parameters that should be considered are the field of view, the technology of the screens and the resolution. Different designs of the visual-stimuli delivery systems affect the chances of successful implementing specific experimental

protocols. From this point of view, goggles present the advantage of avoiding distractions from the environment. Furthermore, they enable independent, stereo and 3D visual stimulation, while a drawback of goggles is the necessity of setting the correct interpupillary distance. The OLED technology provides true black and short response time. One main feature that was considered is patient's comfort during the scan session, which may remarkably affect the success of fMRI performed in children. The video system is once more the component that most differentiates the systems from this point of view. However, response devices should also be carefully considered. These devices should be easy to use when the goal is performing fMRI in children or impaired patients.

The configuration of the system used at the Imaging Department of Palidoro is shown in Figure 3.12. Some of the components are installed in the operator room, while others are located in the magnet room.

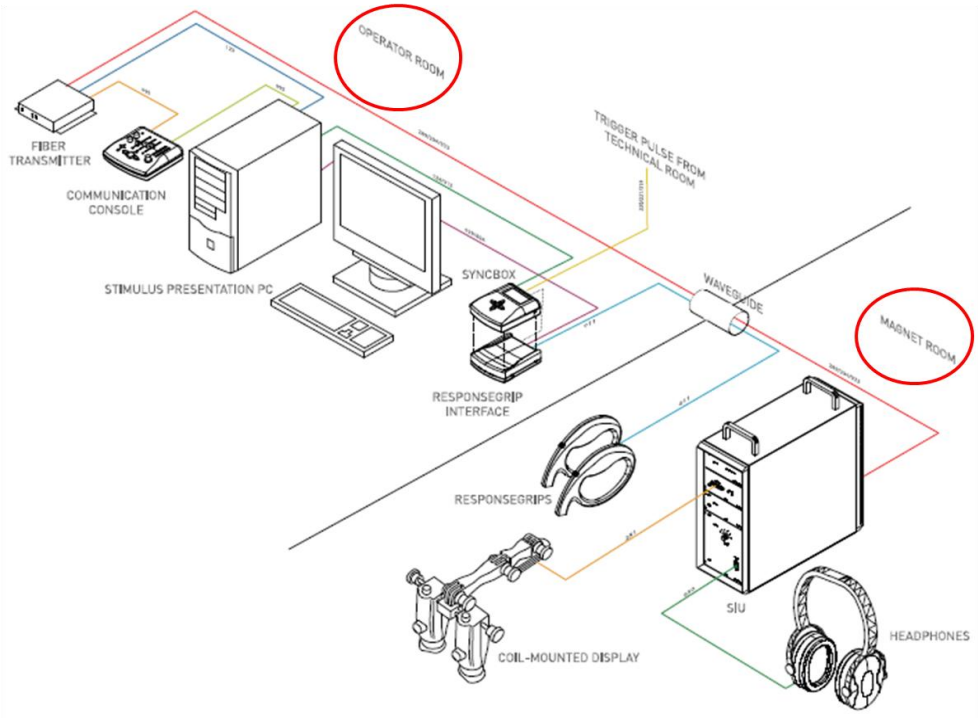

Figure 3.12 – Schematic representation of the MR-compatible stimuli-delivery system (NordicNeuroLab, Bergen, Norway) at the Imaging Department of Palidoro.

The components in the operator room include a PC with stimulus presentation software, a fiber-optic transmitter, an interface for the response device, a communication console and a synchronisation device. The components in the magnet room include an MR-compatible rack, the visual stimulation device (goggles), the auditory stimulation device (stereo headphones) ant the response device (hand grips). The MRI scanner produces a trigger pulse at the beginning of the acquisition of each volume. The synchronisation device receives the trigger pulses and enables the PC to send a synchronised stimulus to the patient. The synchronisation box also enables simulating triggers from the scanner, a useful feature for paradigm simulation.

Figure 3.13 shows the fMRI setting currently installed, together with a screenshot of the sequence editor of the STIM2 software (Compumedics Neuroscan, El Paso, Texas, USA) used to implement the stimulation paradigms.

Figure 3.13 – fMRI setting at Bambino Gesù Children's Hospital (Imaging Department of Palidoro). Both the system components in the operator room and in the magnet room are shown, together with a screenshot of the software used to implement stimulus sequences.

3.2 An example application: motor planning

Motor planning is the ability of the brain to conceive and organise a skilled, non-habitual motor act in the correct sequence from beginning to end. It is an essential part of functional life that relies on the preparation of several constituent sub-processes when the required response to a particular stimulus is known in advance. Indeed, planning is a super ordinate term that subsumes integration of incoming sensory stimuli, strategy formation, coordination and sequencing of mental functions and holding information on-line to provide accurate motor responses (Newman et al., 2003). Therefore, several brain regions are known to participate in the processes involved in planning and feedforward operations. Interest in how the brain plans and implements accurate movement has grown over the years, owing to the complex nature of movements that are pre-planned but flexible enough to adapt to environmental demands (Boyd et al., 2009; Cavina-Pratesi et al., 2006; Cunnington et al., 2003; Hesse et al., 2006; Jäncke et al., 2006; Toni et al., 2001).

3.2.1 A motor planning task

To set-up a first experimental protocol with application to movement analysis, we designed a motor planning task based on a previous work from Hanakawa (Hanakawa et al., 2008). The aim was to examine cerebral activity during planning of delayed finger tapping sequences.

Trials consist of a series of video stimuli administered to the subject (Figure 3.14). First, an instruction stimulus (IS) with a pseudo-random number between 1 and 4 is administered to the patient. This input represents the number of keys to be pressed and determines the sequence of finger tapping that the

subject must plan. The IS is followed by an interval of pseudo-random duration (13”÷18”) introducing a first delay (D1) during which the subject, who is aware of the sequence of finger tapping he/she is going to perform, must wait. The pseudo-random duration allows avoiding anticipation effects. A cue stimulus (CS) is then provided and the subject starts executing the finger tapping sequence. Finally, a further delay period (D2) of pseudo-random duration precedes the next trial. During this second interval, the subject must remember the finger from which he/she will start the next finger tapping sequence.

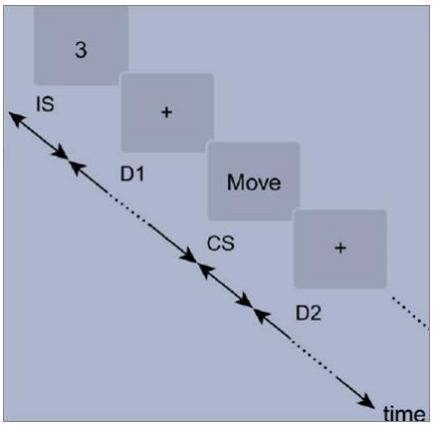

Figure 3.14 – Schematic representation of a single trial of the motor planning task (adapted from Hanakawa et al., 2008).

In this task, the sensory-motor processing is separated from the phase of movement execution. The task is based on the following assumptions about the underlying neurophysiological processes. During the D1 interval, the subject plans the sequence of movements determined by the previous movement and by the instruction stimulus. Therefore, he/she gets ready to perform the task and keeps the task instructions in memory. When the cue stimulus is presented, the subject recognises it as the “go” instruction, recovers the information about the finger tapping sequence from short-term memory and executes the sequence of movements. Finally, during the D2 interval, the subject must keep in memory the finger from which he/she will resume finger tapping (thus maintaining in

memory partial information for movement planning, which must be completed by the next instruction). The D2 interval is thus the control condition for D1 (according to the subtractive paradigm), having in common with D1 the short-term storage of the information related to last movement, but not the planning of the new movement. Therefore, the D1>D2 contrast enables to highlight the activations specific to movement planning only. The main difference between the task implemented and the one used in the study by Hanakawa, is that the latter allows for a further differentiation between executed and imagined movements.

An experimental session is composed of 6 runs lasting 4'40" each, for a total scan time of 28'00". In each run 7 trials are presented. Data where acquired with a gradient echo EPI sequence with the following parameters: 112 volumes, 28 slices per volume (slice thickness = 5 mm), field of view = 256x256 mm, reconstruction matrix = 64x64, TR = 2,500 ms, TE = 38 ms. Figure 3.15 shows the results obtained from a single subject and their comparison with the study group from Hanakawa. In Figure 3.15.A the results from the analysis of the 6 runs are presented. In the analysis of single runs, only small clusters were significantly activated and evident differences were present in activations between different runs.

3.2.2 The Tower of London task

As part of the research project in neurorehabilitation with robotic training, described in detail in Chapter 4, the possibility of using an fMRI experimental task called "Tower of London" (TOL) was considered, with the aim to assess changes in motor planning skills not explicitly related to the robotic rehabilitation protocol adopted.

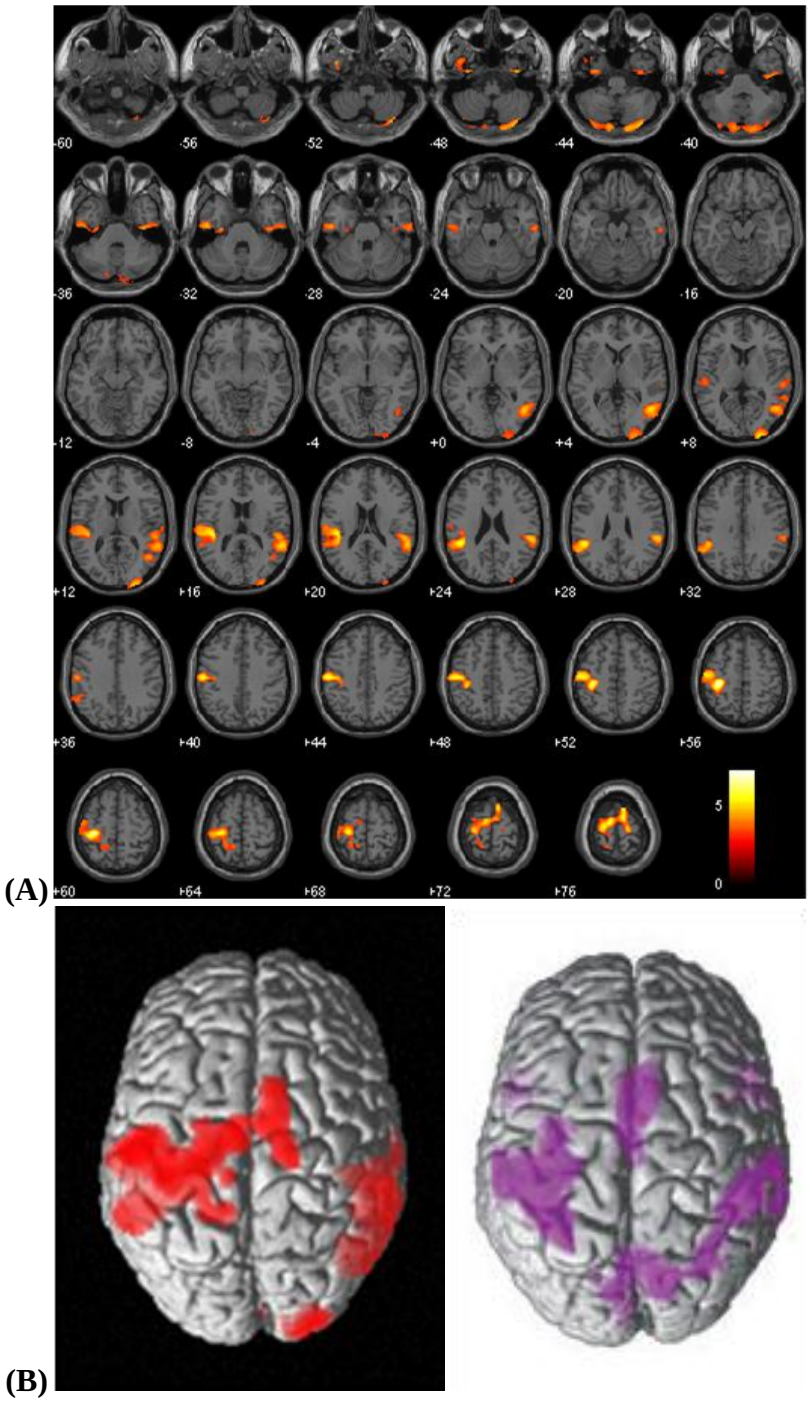

Figure 3.15 – Results of the motor planning task from a single subject. (A) t-maps of the D1 > D2 contrast ($p<0.001$, spatial threshold = 500 voxels). Activations are superimposed on the MNI single subject T1 template. The coordinates represented in the lower left corner of each axial section refer to the MNI stereotactic space. Results from the 6 runs analysed together are presented. (B) 3D rendering of the results (red blobs) compared to the results of the group study from Hanakawa et al. (purple blobs). Note that differences in activations may be attributed both to the number of examined subjects (single-subject vs. group of 13 subjects) and to differences in the study design, including number of runs and trials.

The TOL task (Shallice, 1982) is a well-known test used in applied clinical neuropsychology for the assessment of executive functions, specifically to detect deficits in planning which may occur due to a variety of medical and neuropsychiatric conditions. It requires planning and goal-management ability by asking participants to "look ahead" and map out a plan to solve the problem (Newman et al., 2003).

The task consists in planning the movement of objects (usually small balls), placed within compartments or stacked on pins (Figure 3.16). The subject must try to transform the initial configuration in the final one with the fewest possible moves, following some simple rules that constrain the movements (a single ball can be moved at a time, there must not be other balls placed on top and only compartments of adequate depth can be occupied). The task can include movement of the objects to reach the final configuration or only planning the moves.

Typically, problem difficulty is manipulated by varying the minimum number of moves. However, other parameters may influence task difficulty, including goal hierarchy (i.e. ambiguity of goal priorities, which is manipulated by varying the arrangement of the final configuration), number of optimal solution paths, and search depth (i.e., the number of sub-goal moves before the first ball is placed in its goal position). Task difficulty affects working memory, visuo-spatial and motor processes, together with planning processes. The neural network implicated in the TOL includes regions that have been associated with visuo-spatial processing (parietal cortex), and executive processing such as working memory (prefrontal regions), planning (prefrontal cortex and basal ganglia) and error detection (anterior cingulate gyrus) (Newman et al., 2009).

It is assumed that the post-traumatic child subjected to robotic rehabilitation responds, more or less consciously, with an analysis of the system (the environment that surrounds him/her and the administered task), finding in it constraints and/or laws that can be usefully exploited. Therefore, this adaptation

mechanism exploits structural constraints related to the characteristics of the robot to improve the performance (accuracy and response time) in the task. Although the team of neurorehabilitators found (in agreement with most of the literature) that following robot-mediated rehabilitation subjects improve the performance of the limb with respect to standard clinical scales, they hypothesized that these improvements may partly be related to the use of the constraints imposed by the robot to the direction with no degrees of freedom. This strategy adopted by patients could affect treatment outcomes. Therefore, the TOL task could be helpful in pursuing the aim of understanding whether or not the child is acquiring new skills related to a generalised strategy for movement.

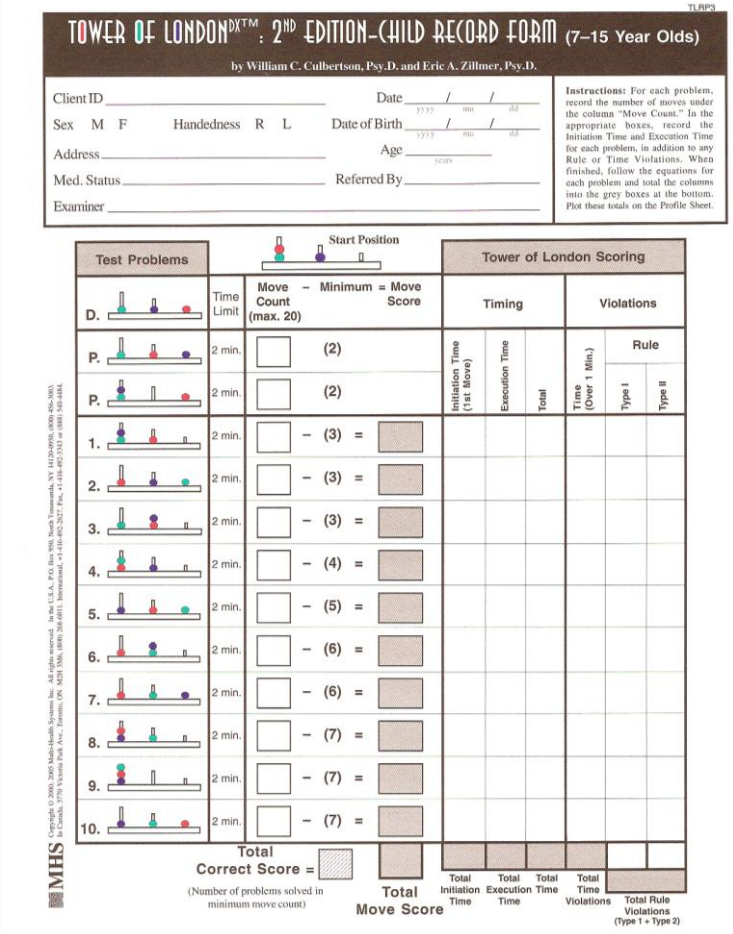

Figure 3.16 – The Tower of London task used in pediatric neuropsychology.

The main constraints in the design of the TOL paradigm for the research project at Bambino Gesù Children's Hospital were the age of patients and their condition, as pediatric hemiplegic patients typically have limited ability to concentrate and are more likely to give up performing the administered task. This has influenced the choice of task structure, difficulty of trials and frequency of presentation. 48 possible trials were identified, 12 of which may be solved in one move, 24 in two moves and the remaining 12 in three moves. The initial and final configurations are presented simultaneously by placing the initial one in the upper portion of the screen and the final one in the lower portion (Figure 3.17).

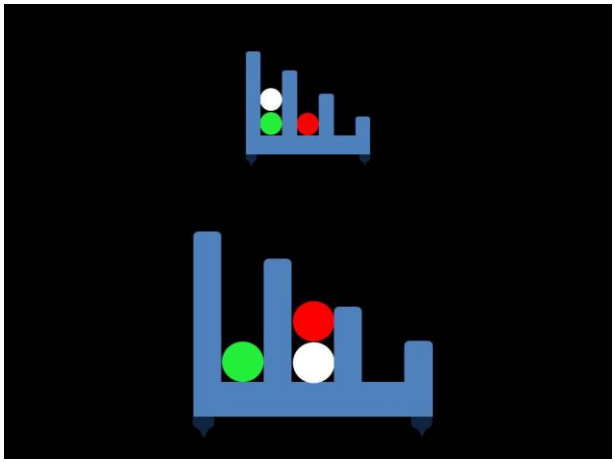

Figure 3.17 – Typical visual stimulus for the Tower of London (TOL) task. The initial and final configurations are presented simultaneously by placing the initial one in the upper portion of the screen and the final one in the lower portion. Three moves must be planned, in this example, to obtain the final configuration.

The trials are divided into 12 blocks lasting 30 seconds, each consisting of 4 trials. To limit difficulty of the task, each block is formed by a combination of trials with different minimum numbers of moves. Furthermore, to avoid habituation effects, in each block there cannot be more than two trials with the same minimum number of moves. The duration of each stimulus presentation pseudo-randomly varies between 5.5 and 8.5 seconds, while a black screen with no fixation point is presented for one second before the following stimulus

appears. Successive blocks are separated by a 30 seconds rest phase, during which the subject listens to backwards speech. This type of stimulus allows distracting the subject from the task of interest, while avoiding to produce activations generated by cognitive processes (as might happen, for example, if the subject was asked to count). The overall task duration is 12'00".

Patient's responses are acquired through a single response grip with 2 buttons. The subject must press either a button with the thumb if he/she believes that the minimum number of moves is 1 or 2, or the other button with the index finger if he/she believes that it takes at least 3 moves to reach the final configuration. The answer can be given until the beginning of the next trial. The choice of using a single hand piece is motivated by the anticipation of administering the task to hemiplegic patients, who may thus respond with their healthy limb, thus minimising the influence of the response on the analysis of motor areas contralateral to the plegic limb.

The experimental protocol was set-up in such a way to provide as much information as possible during the preliminary phase of development, in order to reach a final version of the task. The results may be analysed in two ways. The epoch structure of the task, which includes blocks of 30 seconds during which trials are presented, alternating with 30 seconds of "rest" blocks (with auditory stimulation only) enables to examine the main effect of the presentation of TOL trials, maximising the statistical power of the task. The randomisation of trials difficulty (1, 2 or 3 moves) within the blocks, as well as the random interval between successive stimuli, allows analysing the effect of trial difficulty. The results of this preliminary version of the task on a voluntary adult subject are shown in Figure 3.18. A large cluster that spans the cerebellum, the occipital lobe and the parietal lobe is evident, together with activations in the middle frontal gyrus and in the precentral gyrus.

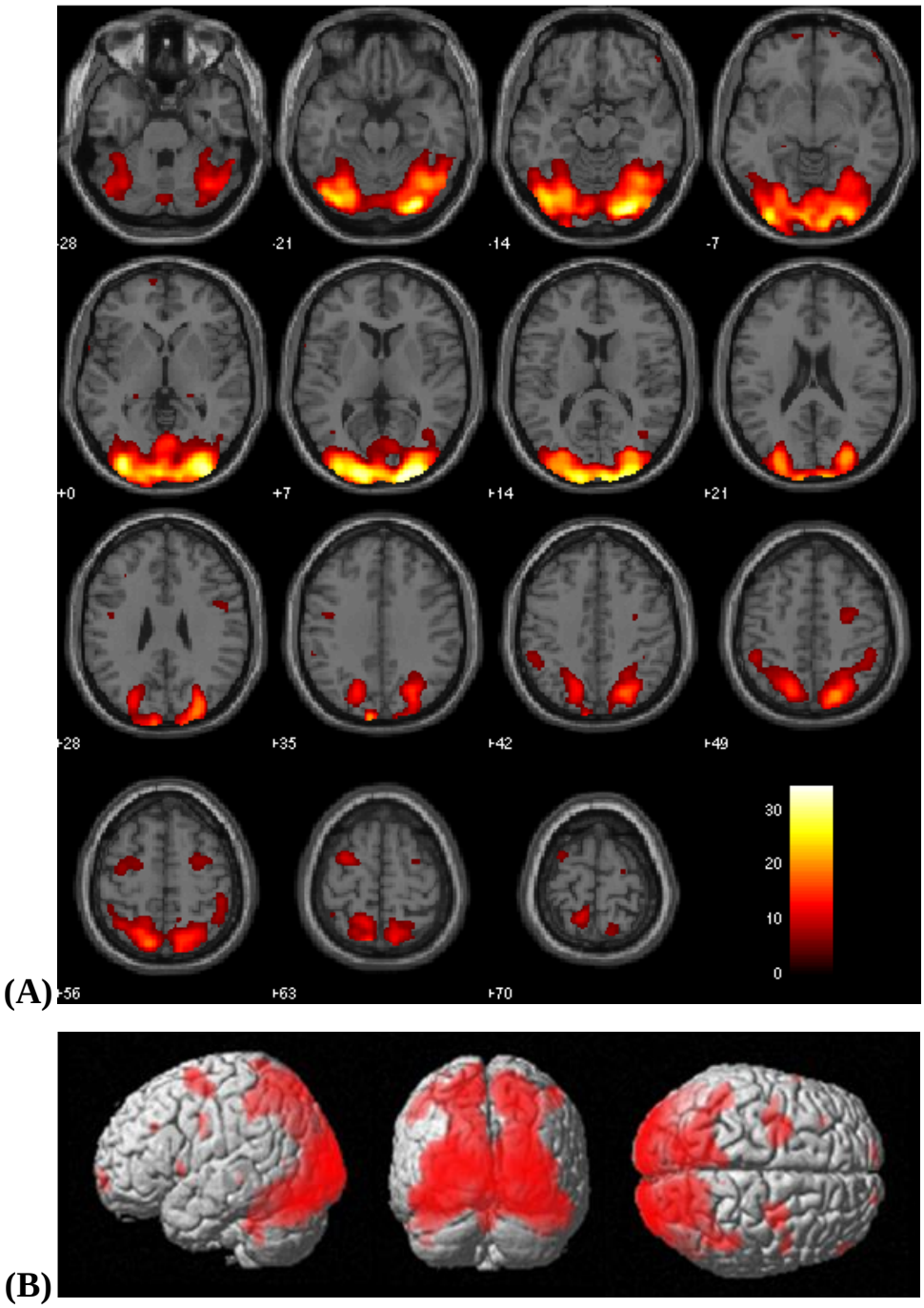

Figure 3.18 – Results of the analysis of the Tower Of London (TOL) task performed by a single subject (t-maps of task > rest contrast; $p<0.05$, FWE corrected). Activations are superimposed on the MNI single subject T1 template. (A) The coordinates represented in the lower left corner of each axial section refer to the MNI stereotactic space. (B). 3D rendering of the results shown in (A).

3.3 fMRI for the pre-surgical assessment of language function in drug-resistant epilepsy patients

fMRI is currently being applied for pre-surgical mapping of brain functions. The goal of this application is to localise cerebral functions in tissue within or near regions intended for neurosurgical resection, thus allowing surgeons to predict the likelihood of post-surgical deficits, to assess the proximity of resection to functionally active cortical regions and to spare tissue that, if injured during the surgery, would cause new clinical deficits or limit good recovery. Regions identified with motor or language tasks, or somatosensory stimulation, agree well with classically localised regions of the brain that are specialised for processing these activities. As measurements can be made on single individuals, borders between functionally and anatomically distinct regions (which can vary substantially between different people) can be defined to allow precise and safe neurosurgical planning. Direct integration of fMRI with surgical navigation tools is also possible.

However, major problems remain to be resolved. To cite only a few of the open issues, the definition of activation is based on the notion of an arbitrary measure of statistical significance, a measure determined not just by the magnitude of the signal, but also by factors irrelevant to the pathology, such as patient movement during the study, patient preparation to the fMRI task, and duration of the experiment. Another problem is the substantial variation of signal intensity between sessions and between individuals because of physiological changes and interindividual differences. The clinical interpretation of fMRI studies is also complex. For example, the functional significance of activation changes outside anatomically well-established brain regions is not often certain. Caution also needs to be exercised concerning the interpretation of the absence of activation changes. fMRI defines only the regions of brain in

which there is a statistically significant change in BOLD contrast as the applied task modulates brain activity. However, potentially widespread regions that are involved in a cognitive process, but are not changing activity significantly between the states being tested, will not be distinguished as active. It is therefore possible that injury to regions not activated with the task modulation could lead to clinically significant deficits. In addition, because percentage changes of BOLD signal are small, they are easily confounded by noise arising from patient and instrument-related factors.

Despite these limitations, fMRI may represent a helpful tool for the pre-surgical evaluation of epileptic patients (Medina et al., 2005). It may provide identification of eloquent regions by integrating anatomical and functional maps, thus allowing predicting the outcomes of surgery. In particular, the study of language using fMRI can reduce the risk of postsurgical deficits of language functions. When a lesion is located near the inferior frontal gyrus (Broca's area), the posterior third of the superior temporal gyrus (Wernicke's area), the supramarginal or angular gyrus of the dominant hemisphere for language, there is a risk of permanent deficits of language, as a result of neurosurgery. The cumulative incidence of epilepsy in children is approximately 1%. In 30÷40% of cases, drug-resistant forms of epilepsy are present, which are often eligible to be surgically treated. Surgical treatment may in fact be an efficacious therapeutic tool that may allow the prevention of deleterious effects on cognitive development that are evident in some forms of childhood epilepsy.

For such reasons, we designed an experimental protocol for the localisation of the language brain regions and the evaluation of their lateralisation. The final aim of this work was to provide clinicians with a tool to help enhance identification of eloquent areas in children and predict the outcome of surgical intervention in patients with drug-resistant epilepsy candidate to surgery. Figure 3.19 shows an activation map obtained from a language task

used during this study, superimposed on the structural MRI of a child with frontal lobe epilepsy.

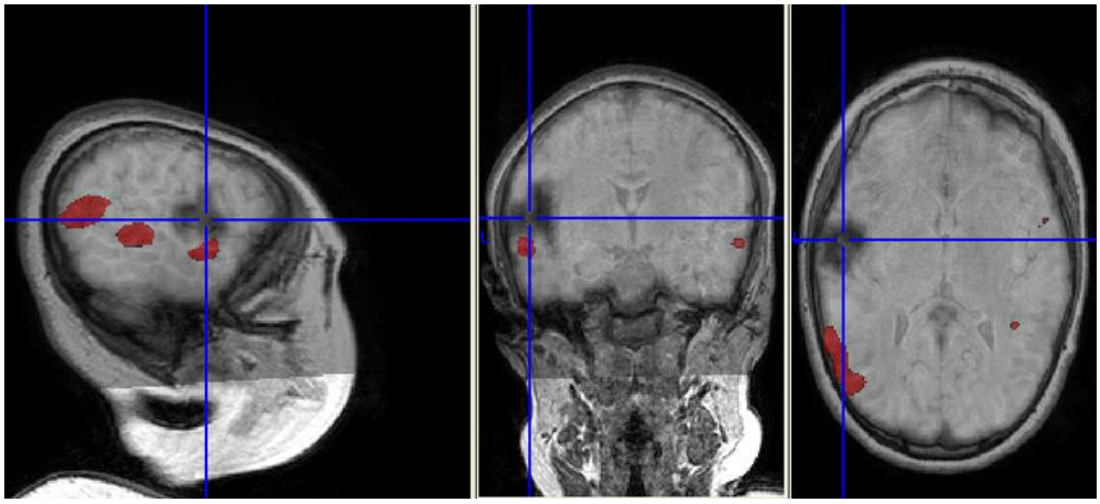

Figure 3.19 – Identification of language areas in a child with frontal lobe epilepsy. The fMRI map, showing activations in language areas, is overlaid on a structural MRI from the same subject. Images were acquired with the 1.5 T MRI scanner of the Imaging Department of Palidoro at Bambino Gesù Children's Hospital.

3.3.1 The role of the lateralisation index

Hemispheric dominance and lateralisation index (LI) are relevant aspects to assess several physiopathologic conditions and to study the organisation of cognitive functions in children. The LI describes the degree of lateralisation of cognitive functions as a result of performing a given task, which must be chosen depending on the specific function under investigation. Several studies have shown that the lateralisation of a cognitive function is of theoretical and clinical relevance. In recent years, non-invasive approaches for investigating the LI have been proposed. These methods may potentially be used in place of invasive techniques, such as cortical electrical stimulation or the Wada test (i.e. selective narcotisation of one hemisphere by the intracarotid injection of amobarbital), which for a long time have been the only available means to reliably assess

hemispheric dominance. fMRI is a particularly interesting method to non-invasively investigate LI. Several studies have shown concordant results between fMRI and standard invasive techniques in determining lateralisation.

Evaluating LI on the basis of fMRI data, however, is problematic. A first critical issue is variability both between subjects and in repeated exams on the same subject. Furthermore, LI depends on heterogeneous factors, including the administered task, the investigated cerebral regions (single ROIs, groups of ROIs, hemispheres), the way these regions are defined, the way the neuronal activity is measured (percentage variation of BOLD signal, number of voxels or sum of the statistical scores of voxels above a given threshold in the statistical parametric map), and the significance threshold chosen for the activation map from which the LI is calculated. Although several approaches have been established, the optimal method for evaluating the lateralisation of a cognitive function, which should allow for repeatable, reproducible, and objective measures, remains controversial (Jansen et al., 2006; Seghier, 2008).

Undoubtedly, the most widely studied domain is language. The left hemisphere is dominant for language in 96% of right-handed adult subjects and in 76% of left-handed ones, while a right-dominance is present in 10% of left-handed adults (Pujol et al., 1999). LI is a marker for the susceptibility to language deficits after brain lesions and stroke or caused by neurological disorders associated with development. The determination of language lateralisation is also relevant for the presurgical evaluation of patients with medically intractable epilepsy. Concordant results between fMRI and Wada test were found in determining the LI in adult epileptic patients (Liégeois et al., 2002; Szaflarski et al., 2008). Furthermore, a significant correlation was found between age and lateralisation measured with fMRI in a verbal fluency task performed by healthy children, with left lateralisation increasing with age (Holland et al., 2001). Finally, a comparison between healthy and epileptic subjects showed the absence of a significant correlation between age and

lateralisation in the latter group (Yuan et al., 2006). fMRI exams allow evaluating various aspects of language function. Listening to someone reading a text preferentially activates posterior temporal regions, verbal fluency tests preferentially activate anterior regions of the inferior frontal gyrus, repeating phrases results in activation of frontal and temporal areas, including the primary auditory cortex. As with the motor function, premotor and supplementary motor areas are involved in the initial phase of language production and therefore a surgical removal of these areas may cause a deficiency in word generation if the excision affects the dominant hemisphere.

3.3.2 An experimental protocol for identifying eloquent regions and computing the lateralisation index

To identify language areas and evaluate their lateralisation, an experimental protocol was designed, consisting of administering a set of fMRI tasks: a verb generation task, a naming task, and an auditory comprehension task (Nocchi et al., 2009, AIFM Congress). These tasks should be easy enough for pediatric and impaired patients. During the active condition of the verb generation task, names of objects are administered to the subject by means of a system for auditory stimulation and he/she is asked to generate (using subvocal speech) verbs associated with the name. During rest, tones are given to compensate for the auditory stimulation of the task condition and the subject performs a motor activity (bilateral finger tapping). It is hypothesised that executing this task involves the activation of Broca's area in the frontal lobe and of Wernicke's area in the temporal lobe. In the naming task, in response to the auditory presentation of a word that identifies a category, the subject generates (using subvocal speech) names of objects belonging to the given category, while during the rest condition he/she counts in his/her mind. It is hypothesised that

this task mainly activates Broca's area. Finally, in the comprehension task the subject listens to phrases from a fairy tale alternating with non understandable speech. The activation of Wernicke's area is expected. The above described tasks were selected for their ability to selectively cause activation of language regions. Furthermore, they are likely to be easy to perform for children and impaired subjects. Expected activation areas for the three tasks are shown in Figure 3.20.

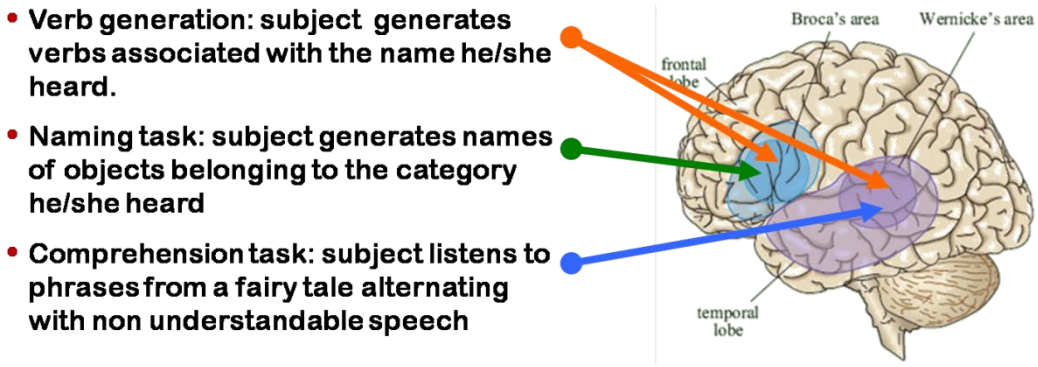

Figure 3.20 – Set of tasks used for investigating language areas. Expected activation regions are shown for each task.

EPI sequences for fMRI data acquisition with the Philips Achieva 1.5 T scanner (Philips Healthcare, Best, The Netherlands) at the Imaging Department of Palidoro were set-up with the following parameters: TR = 3.000 ms, TE = 38 ms, reconstruction matrix = 64x64, 30 slices (slice thickness = 5 mm, without gap), voxel size = 4x5x4 mm, 5 dummy scans, 100 dynamics (i.e., volume acquisitions) for the verb generation and comprehension tasks (duration = 5'15"), 120 dynamics for the naming task (duration = 6'15"). Furthermore, for each subject an anatomical scan was performed. The sequences for synchronous auditory stimulation were programmed with the STIM2 software.

23 adult healthy volunteers (13 males, 10 females, age = 26.0±7.6 years, right-handed) participated in this study. 80 fMRI runs (58 runs of the verb generation task, 11 of the naming task, and 11 runs of the comprehension task)

were administered to these subjects. The first 12 subjects underwent three times the verb generation task, with different names administered in the three runs (total duration of fMRI sequences: 15'45"). The remaining 11 subjects underwent twice the verb generation task and once the two remaining tasks (total duration of fMRI sequences: 22'00"). The three types of tasks were administered to these latter subjects in a pseudo-random order.

Data from all the tasks and subjects were pre-processed with normalisation to the MNI template to bring the activations in a stereotactic space in which coordinates are associated with anatomical regions. A 2nd-level analysis was performed to obtain group results. Figure 3.21 shows the results of the group analysis for the verb generation task. To obtain a uniform analysis, the first two runs from each subject were examined.

Algorithms for the calculation of the LI as a function of critical parameters have been applied to the statistical parametric maps obtained from pre-processing and statistical analysis. The aim was to define a set of values to use as a reference for the analysis of lateralisation in pathological patients. The maps obtained from the SPM5 version of SPM were used as inputs to a tool that we designed and implemented using MATLAB 7.0 code. This tool provides the LI as a function either of the statistical threshold or of the number (or percentage) of most statistically significant voxels taken into account.

With reference to the case of computation of the LI as a function of the statistical threshold, being $N_{LH}(T)$ and $N_{RH}(T)$ the number of voxels above the statistical threshold T of the left and right cerebral hemisphere, respectively, the LI can be obtained by comparing the number of voxels in the two hemispheres:

$$LI(T) = \frac{N_{LH}(T) - N_{RH}(T)}{N_{LH}(T) + N_{RH}(T)} \tag{3.9}$$

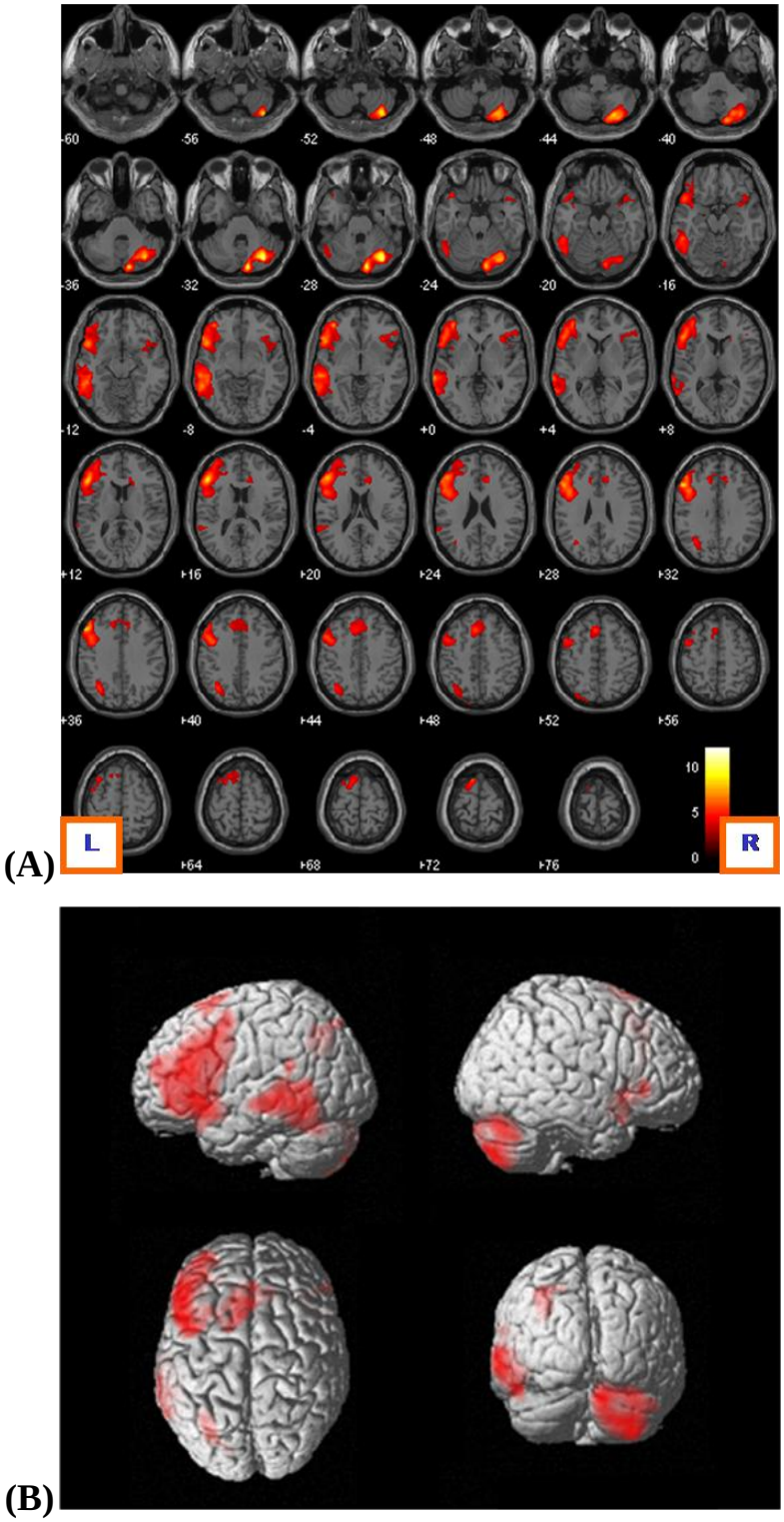

Figure 3.21 – (A) Results of the group analysis for the verb generation task (t-maps of task > rest contrast at the group level; $p<0.05$, FDR corrected). To obtain a uniform analysis, the first two runs from each subject were examined. Activations are superimposed on the MNI single subject T1 template. The coordinates represented in the lower left corner of each axial section refer to the MNI stereotactic space. (B) 3D rendering of the results shown in (A). Left lateralised activation of Broca's and Wernicke's language areas and of pre-motor area are well evident, together with contralateral activation of cerebellum.

Alternatively, denoting with t_n the t-score of the n-th voxel, the LI can be defined as:

$$LI(T) = \frac{\sum_{n=1}^{N_{LH}(T)} t_n - \sum_{n=1}^{N_{RH}(T)} t_n}{\sum_{n=1}^{N_{LH}(T)} t_n + \sum_{n=1}^{N_{RH}(T)} t_n} \quad (3.10)$$

In addition to calculating the LI to determine the dominant hemisphere, local LIs can be obtained. From a stereotactic atlas given in input, the tool allows to generate masks for specific ROIs. The regional analysis allows the evaluation of lateralisation of both an individual ROI (e.g., Broca's area, Wernicke's area) and of an arbitrary set of ROIs (e.g., allowing the calculation of the global LI of frontal and temporal areas involved in language processing). Finally, it is possible to set the margin from the inter-hemispheric fissure to omit mesial areas that could affect the accuracy of the analysis. The implemented tool is schematically represented in Figure 3.22. The tool requires the following inputs:

- statistical parametric maps for which the LI is to be determined (SPM);
- convention for axes of input maps, which can be neurological or radiological (CONV);
- computation of the LI as a function of the statistical threshold or of the number (or percentage) of voxels to take into account (METHOD);
- value of the statistical threshold T (THRESHOLD);
- number or percentage of most statistically significant voxels to take into account (MSV);
- minimum threshold, in case of analysis with MSV (MIN THRESH);
- atlas for ROI selection (ATLAS);
- region (or regions) for which the LI is to be determined (ROI);
- margin from the inter-hemispheric fissure (M).

The following outputs can be obtained:

- lateralisation index for the input maps (LI);
- lateralisation curve (LI_{Curve});
- mask for the analysis of single or multiple ROIs (MASK);
- mean and standard deviation of the LI of group analyses (LI_{Group});
- group lateralisation curve ($LI_{Curve,Group}$).

Figure 3.22 – Black box representation of the tool implemented to determine the lateralisation index.

The percentage of runs that the neuroradiologists involved in this research classified as suitable for the analysis of hemispheric lateralisation was 43.1% for the verb generation task, 45.5% for the naming task and 72.7% for the comprehension task (Table 3.3). Lower percentages were obtained for the suitability of the lateralisation analysis of Broca's area (respectively 41.4%, 36.4% and 54.5%) and of Wernicke's area (respectively 37.9%, 36.4% and 63.6%). In all valid runs, clusters of voxels with statistically significant activations ($p < 0.001$, non-corrected threshold) were found in the investigated areas. A group analysis was performed only for the verb generation task, due to the small number of subjects available for the two other tasks.

	Verb generation task	Naming task	Comprehension task
Total number of runs	58	11	11
Valid runs (hemispheric lateralisation)	25 (43.1%)	5 (45.5%)	8 (72.7%)
Valid runs (lateralisation of Broca's area)	24 (41.4%)	4 (36.4%)	6 (54.5%)
Valid runs (lateralisation of Wernicke's area)	22 (37.9%)	4 (36.4%)	7 (63.6%)

Table 3.3 – Percentages of runs classified as suitable for lateralisation analyses by the neuroradiologists of Bambino Gesù Children's Hospital.

The calculation of the LI by comparing the number of voxels above the statistical threshold and their t-scores (see eq. 3.9 and eq. 3.10) showed a critical dependence on the threshold (Figure 3.23). Similarly, there was a critical dependence on the number of voxels with the highest statistical significance taken into account (Figure 3.24).

The application of the implemented tool to the group of volunteers provided preliminary results for the identification of reference values for these parameters in the language tasks. These preliminary results need to be confirmed with a larger sample. It would also be important to repeat the measurements on a sample of healthy pediatric patients. The experimental protocol suggests the usefulness of fMRI examinations in patients with drug-resistant epilepsy candidates for surgical resection of epileptogenic lesions, both for better and more reliable identification of eloquent areas, and to evaluate the lateralisation of language function.

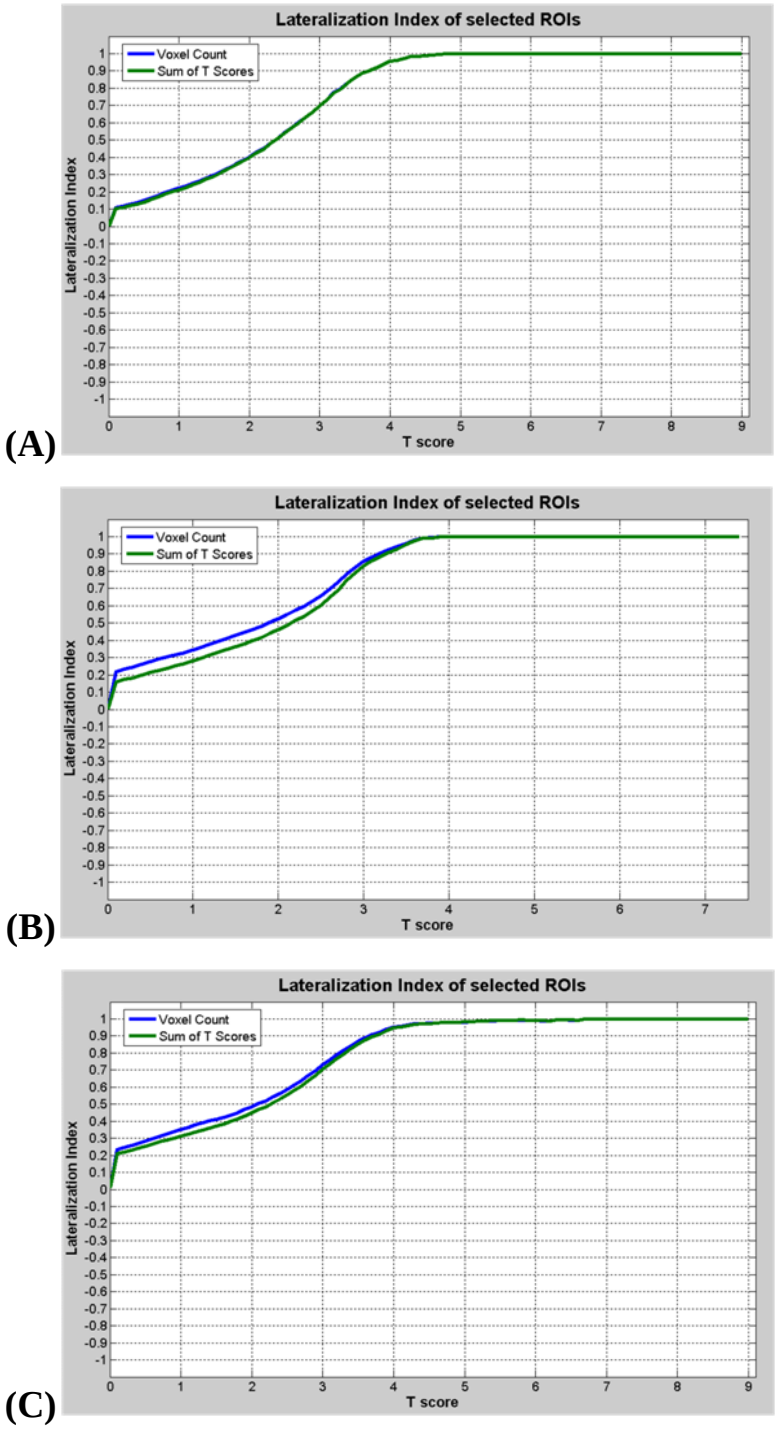

Figure 3.23 – Group results for the verb generation task. The lateralisation index obtained both by comparing the number of voxels above the statistical threshold and by comparing their t-scores is presented as a function of the statistical threshold T. (A) Lateralisation of Broca's area; (B) lateralisation of Wernicke's area; (C) hemispheric lateralisation (the contralateral contribution of cerebellum was masked out).

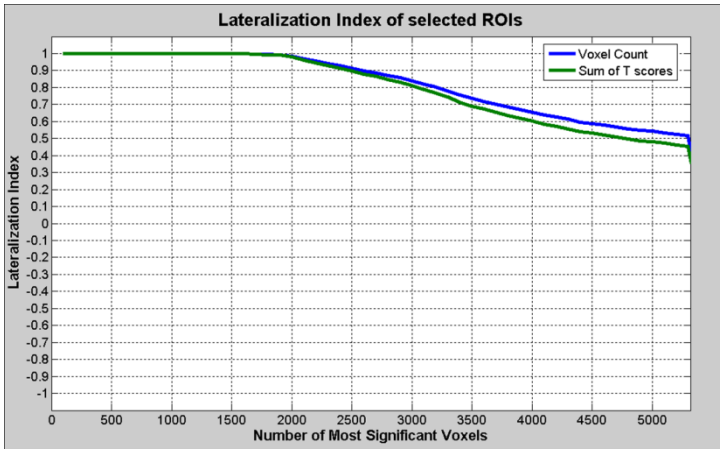

Figure 3.24 – Group results for the verb generation task. The lateralisation index obtained both by comparing the number of most significant voxels and by comparing their t-scores is presented as a function of the number of voxels taken into account. Wernicke's area lateralisation is shown.

3.3.3 EEG-fMRI

In recent years there has been a remarkable increase of interest in the multimodal approach to the study of neuroscience. This interest is justified by the advantages provided by the combined use of non-invasive functional imaging tools and traditional neurophysiological techniques. In particular, the integration of information on bioelectrical brain activity obtained from EEG with functional magnetic resonance images has allowed overcoming the inherent limitations of individual techniques (low spatial resolution of EEG and low temporal resolution of fMRI). Coupling these techniques enabled to study the correlation of haemodynamics with bioelectrical activity in different brain areas (Salek-Haddadi et al., 2003). Therefore, the generators of functional changes that underlie events can be localised in the brain using simultaneous EEG and fMRI recording.

The interest of the scientific community to this particular field of research is supported by its potential clinical applications. In this sense, one of the most relevant applications is the localisation of ictal foci and the surgical removal of tissue, which in some instances can cure epilepsy (Cunningham et al., 2008; Laufs et al., 2008). In the simplest application of EEG-fMRI, a patient lies at rest in the imaging system as images and the EEG are acquired. The EEG data are then used to define a model with which signal changes in the fMRI series are correlated. The goal is to identify regions of the brain that show signal changes immediately following each epileptic spike. This approach has clinical utility because it provides more refined localising information than is available from the EEG alone. In situations in which brain structural changes are ambiguous or absent, such a technique could have a great influence on the consideration of treatment options.

However, despite the promising results from leading centres, the full value of the methodology is still difficult to realise. Several aspects of the combined approach are still being investigated. Safety issues for combined EEG and fMRI are a concern, although they can be resolved. More difficult is optimal filtering of the EEG data obtained from the combined observations. The shifting gradients used for generating MRI images produce electromotive forces in the EEG leads, which must be filtered out. Although methods are improving, there is a risk that filters degrade the quality or otherwise bias the signal. Figure 3.25 shows how interactions of the EEG system with the magnetic field (static field, gradients and RF excitation pulses) almost completely mask the EEG signal. Artefacts may also be produced by gross movements of subject's head. Moreover, movements associated with the cardiac cycle produce another EEG artefact, the so-called ballistocardiogram (BCG) artefact. Finally, artefacts in the EEG may also be produced by the stimuli-delivery system used in fMRI exams. Of course, the EEG system may in turn produce artefacts in fMRI images.

A more fundamental concern in implementation is that many events must be averaged to give a sufficient signal, which limits applications to highly inter-ictally active epileptic foci. Of course, at the same time care must be taken to ensure that the epileptic activity is not allowed to trigger a generalised seizure in the patient, the consequences of which would create severe movement artefacts and compromise patient safety.

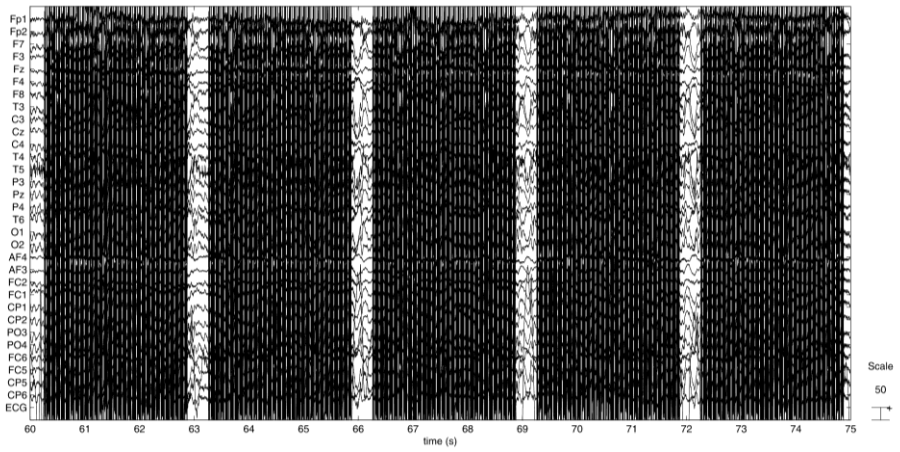

Figure 3.25 – EEG recorded simultaneously to the acquisition of fMRI images. Interactions of the EEG system with the magnetic field almost completely mask the EEG signal, particularly when field gradients are applied.

We carried out a preliminary study to set up the simultaneous EEG-fMRI acquisition technique at Bambino Gesù Children's Hospital and to optimise the quality of both EEG recordings and fMRI images (Carnì et al., 2009, AIFM Congress). 6 healthy volunteers (19.8±2.1 years) participated in the study. The experimental protocol included the recording of EEG alpha rhythm and visual evoked potentials (VEPs) with and without simultaneous fMRI acquisition. EEG was recorded using the Micromed Brain Quick 32-channel MR-compatible system (Micromed, Mogliano Veneto, Italy). An EEG cap was used, with 31 electrodes following the extended international 10-20 system and 2 further electrodes for the electrocardiographic signal. Each electrode integrates a 13 kΩ resistor to reduce induced currents. EEG data were sampled at 1,024 Hz. fMRI

images were acquired with the 1.5 T Philips Achieva scanner of the Imaging Department of Palidoro. The following parameters were used in GRE-EPI acquisition sequences: 200 dynamic scans (i.e., volumes), 29 slices per volume (slice thickness = 4 mm), field of view = 256x256 mm, reconstruction matrix = 64x64, TR = 3,000 ms, TE = 50 ms, Flip Angle = 90°.

The raw EEG data, including artefacts induced by the MR, were initially corrected with the Micromed System Plus software (Figure 3.26.A). The trigger signal sent by the MR tomograph to the EEG recording system at the beginning of each volume acquisition was used to create the model of artefact that was then applied during artefact removal. Once performed this first correction, the EEG data were further processed with the EEGLAB tool (http://sccn.ucsd.edu/eeglab/) running in MATLAB (Figure 3.26.B). A spectral analysis was performed to evaluate the quality of data at various frequencies of interest. Data acquired during visual stimulation were segmented into epochs for the analysis of VEPs.

fMRI data were processed with the SPM5 version of SPM. During pre-processing, images were realigned, normalised to the MNI standard template, and spatially filtered by means of an isotropic Gaussian filter with 8 mm FWHM kernel. The 6 rototranslational movement parameters were used as regressors in the GLM. Results of the analyses were displayed in SPMs with $p<0.05$, using the FWE threshold correction for multiple comparisons.

The spectral analysis of EEG signals and the VEPs obtained with fMRI were compared with EEG and VEPs obtained without fMRI (Figure 3.27). The quality of signals was judged adequate for clinical analysis. The fMRI image quality, assessed by comparing the amplitude of the fMRI activations with and without simultaneous EEG recording, is such that no appreciable differences were found. The results of this set up of the technique show that, by combining hardware tools with appropriate signal processing of EEG signals and fMRI

images, a substantial reduction of the MR-induced artefacts on the EEG can be obtained and the quality of fMRI images can be fully preserved.

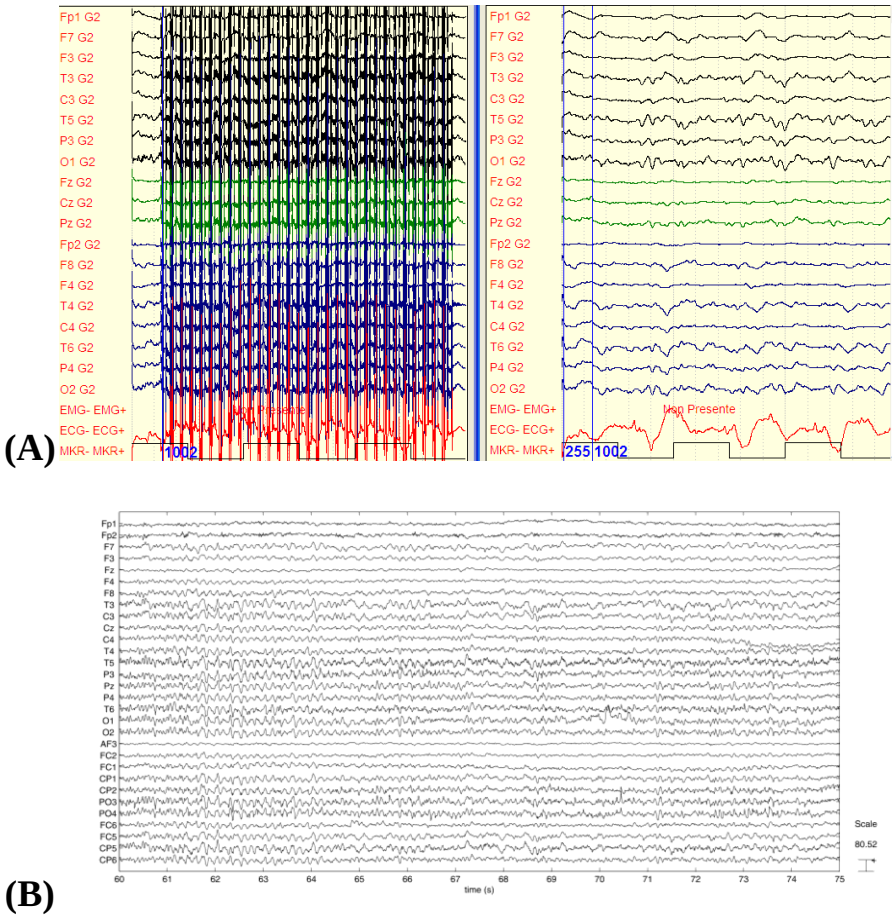

Figure 3.26 – (A) Screenshot of the Micromed System Plus software used to acquire EEG data and to apply a first correction for the MR-induced artefacts. (B) EEG data of Figure 3.25 after artefact removal and processing with the EEGLAB tool.

3.3.4 Simultaneous EEG-fMRI recording with a reduced set of electrodes

As stated above, simultaneous EEG-fMRI recording is a powerful and promising tool in brain imaging experiments, particularly in epilepsy studies.

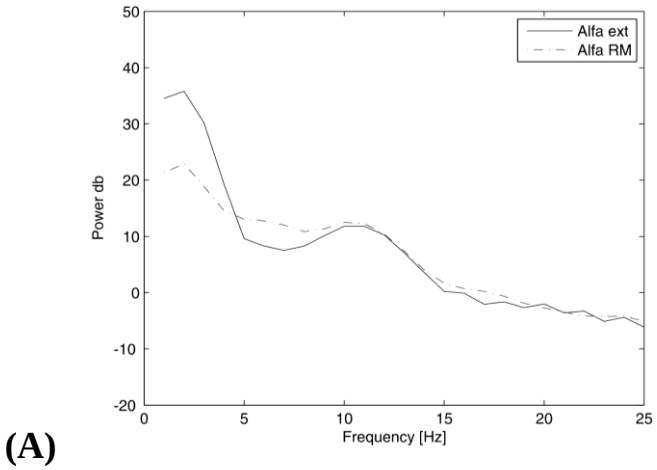

(A)

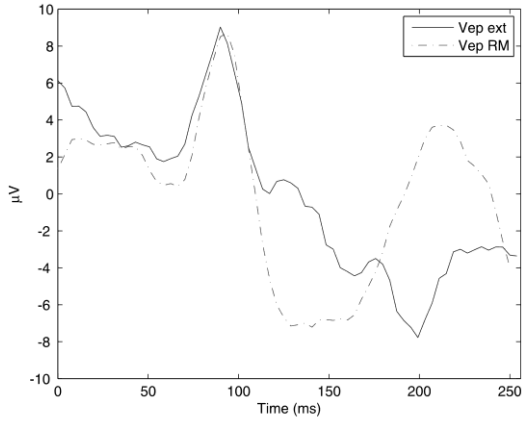

(B)

Figure 3.27 – Comparison of signals recorded with and without simultaneous fMRI acquisition. (A) Spectral analysis performed to evaluate the quality of data at various frequencies of interest (alpha rhythm). (B) VEPs (data acquired during visual stimulation were segmented into epochs). The quality of both alpha rhythm and VEPs obtained with simultaneous fMRI acquisition was judged adequate for clinical analysis by the Neurologists of Bambino Gesù Children's Hospital.

However, wearing conventional EEG caps used in EEG-fMRI recordings has some drawbacks. It is time consuming, caps are uncomfortable, and frequently, particularly in children, they do not fit the size of the head. These issues may result in increasing the residual imaging and BCG artefacts, thus compromising the quality of EEG signals. To minimise residual artefacts in EEG-fMRI acquisitions, we explored the use of a reduced set of electrodes, by testing a prototype of seven multi-lead Ag/AgCl electrodes (O1, O2, Oz, REF, GND, EKG, EOG) without cap, designed to reduce these problems (Carnì et al.,

2010). Further advantages of using a reduced set of electrodes are that it allows minimising the time needed to mount the electrodes and overcoming the problems related to fitting caps to different head sizes.

To assess the quality of the recorded EEG signals, the system was evaluated in VEPs experiments, by comparing the VEPs waveforms acquired inside and outside the MRI scanner. Three healthy subjects (2 males, age 32±4 years) participated in this study. Each electrode of the set was equipped with a 10 kΩ resistor (Lemieux et al., 1997) and the EEG leads were connected to the Brain Quick 32-channel MR-compatible EEG recording system. EEG signals were sampled at 1,024 Hz. The 1.5 T Philips Achieva scanner was used to acquire fMRI images. The stimulus sequence was implemented in the STIM2 software and delivered by the MR-compatible visual system described in Section 3.1.6.

Six stimulus sequences were administered to each subject (Table 3.4). The first three runs consisted of 180 seconds checkerboard stimulation. A 1.5 Hz reversing checkerboard with a 30° (horizontal) by 20° (vertical) field of view and central fixation point was used. The last three runs comprised 14 active blocks of 15 seconds checkerboard stimulation and 13 rest blocks (black screen with central fixation point) lasting 30 seconds each. Three series of 200 fMRI volumes were acquired in these latter runs, with the following acquisition parameters: 30 axial slices (slice thickness = 5 mm); field of view = 240x240 mm, reconstruction matrix = 64x64; TR = 3,000 ms, and TE = a 50 ms. The first two series were acquired with EEG electrodes mounted, the last one without electrodes.

The imaging artefact on the EEG data was removed offline using the averaged artefact subtraction method (Allen et al., 2000). After artefact correction, data were down-sampled to 250 Hz and then filtered at 0.5÷100 Hz. BCG artefact was reduced by means of the algorithm (Niazy et al., 2005) implemented in the FMRIB plug-in for EEGLAB. Data were then segmented in

trials of 256 ms each, based on stimulus onset. Analysis of fMRI data was performed with the SPM8 version of SPM. Data were pre-processed with motion correction, slice-timing correction, spatial normalisation, and smoothing by convolution with an 8-mm isotropic Gaussian kernel. Subsequently, statistical parametric maps were thresholded at $p<0.05$ (FWE corrected).

Run n.	Distance of the subject from the MR isocentre	EEG	fMRI	Scan duration	Trials
1	3 m	Yes	No	180 s	270
2	1 m	Yes	No	180 s	270
3	0 m (inside scanner)	Yes	No	180 s	270
4	0 m (inside scanner)	Yes	Yes	600 s	315
5	0 m (inside scanner)	Yes	Yes	600 s	315
6	0 m (inside scanner)	No	Yes	-	-

Table 3.4 – Stimulus sequences administered to each subject for the assessment of the reduced set of electrodes for EEG-fMRI recordings.

The application of the electrodes did not introduce significant distortions on structural and functional images. Indeed, BOLD maps obtained with and without EEG electrodes showed equivalent activations in the primary visual cortex (Figure 3.28). All EEG data-sets acquired in the scanner exhibit BCG artefact. Figure 3.29 displays the VEP waveforms at occipital electrodes (O2, Oz, and O1) for the three subjects. The waveforms recorded inside and outside the scanner were consistent with the typical VEPs elicited by checkerboard reversing.

Our results confirmed that high quality EEG signals can be acquired using a reduced set of electrodes (Becker et al., 2005; Karakaş et al., 2009). When the interest is in detecting if an event happens, and in localising the corresponding neuronal activations with fMRI, a reduced set of electrodes could be preferred to standard EEG caps. The use of this solution can be particularly useful in the applications of EEG-fMRI technique in children with epilepsy.

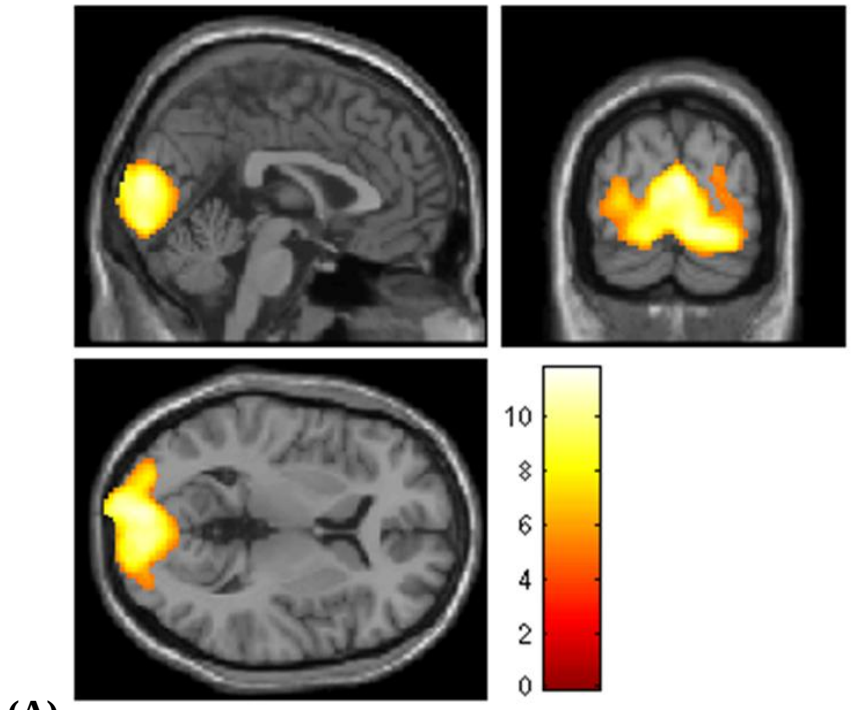

(A)

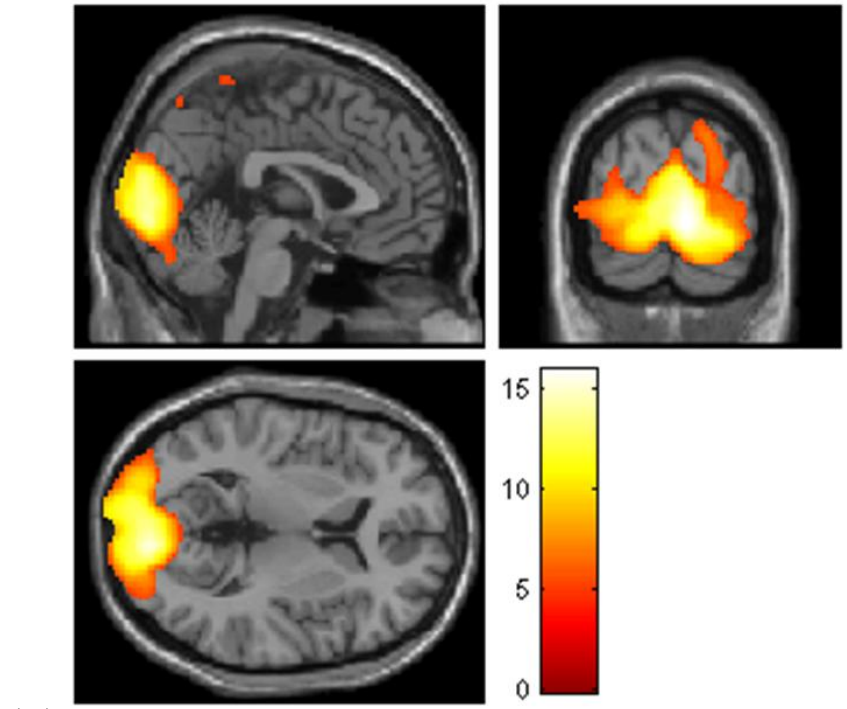

(B)

Figure 3.28 – Statistical parametric map obtained from BOLD data of one of the subjects that participated in the study ($p<0.05$, FWE corrected). Activations in occipital visual areas are well evident. Maps were obtained with (A) and without (B) simultaneous EEG recording.

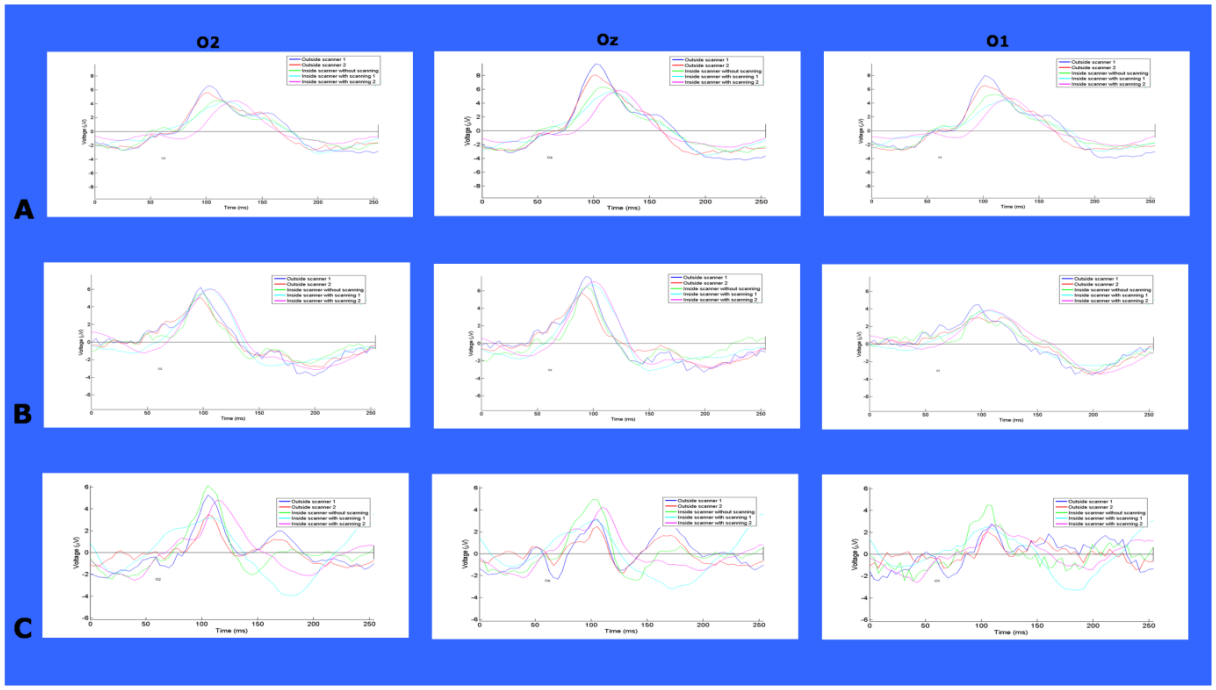

Figure 3.29 – Single-subject Visual Evoked Potentials (VEPs) for the three subjects included in the EEG-fMRI assessment study for the prototype of seven multi-lead electrodes. VEPs recorded at three positions (O2, Oz, and O1) for the five conditions tested are shown.

CHAPTER 4: Neuroimaging and robotic training in neurorehabilitation

4.1 Brain plasticity and neurorehabilitation

An issue dominating the current debate in the field of rehabilitation concerns with the nature of functional recovery after neurological injury. Adaptive reorganisation of the central nervous system is thought to be one of the fundamental mechanisms involved in recovery. The recovery of motor function with and without specific rehabilitation training has been partly attributed to functional reorganisation within the brain (Dong et al., 2007). Following cortical injury in motor and sensory regions, modifications in adjacent spared neural tissues and related areas are required to drive more normal motor control. Neuroimaging data offer converging evidence on the relationship between regional brain injury and the involvement of various cortical regions in compensatory processes (Romero et al., 2002). The underlying neurophysiological mechanisms may include changes in neuronal membrane excitability, synaptic strengthening, synaptogenesis, dendritic arborisation, fiber sprouting from surviving neurons, and recruitment of nearby and remote neuronal ensembles. Current rehabilitation models seek to stimulate functional recovery by capitalising on the inherent potential of the brain for positive reorganisation after a neurologic damage (Boyd et al., 2007).

Simple and complex movements were used in fMRI experiments to investigate motor control in normal and neurologically impaired subjects (Binkofski et al., 1999; Kollias et al., 2001; Lotze et al., 2006). Moreover, neuroimaging provides a means to quantify the dynamic reorganisation of patterns of brain activation associated with specific rehabilitative interventions and changes were described in neuronal motor network as a consequence of rehabilitation training. Nudo and Milliken (1996) suggested the importance of perilesional adaptive reorganisation and the potential modulative effects of focused, intensive rehabilitative training in facilitating the use-dependent

reorganisation. Rehabilitation therapy-induced adaptive reorganisation within putative motor networks has been investigated in adult stroke patients who received constraint-induced movement therapy (Johansen-Berg et al., 2002). The reorganisation of primary motor cortex and sensorimotor cortex after constraint-induced movement therapy was also described in children with hemiplegia (Sutcliffe et al., 2007; Cope et al., 2010). Takahashi et al. (2008) assessed the robotic treatment effects on brain reorganisation of chronic stroke patients with fMRI, founding significant volume activation variations in cerebellum, sensorimotor cortex and supplementary motor area. Nevertheless, the correlates between motor functional gains and changes in physiological signals are still a matter of debate. To best elucidate the mechanisms mediating cerebral adaptations after stroke, studies should take into account the variability among subjects in the initial level of impairments, lesions topography and size, the trajectory of behavioural gains associated with time and motor learning experience, and the intensity of rehabilitation therapy (Dobkin et al., 2005).

Several VBM studies investigated the impact of learning and practice on brain structure (Draganski et al., 2004; Gaser and Schlaug, 2003; Maguire et al., 2000; Mechelli et al., 2004). In the first of these studies (Maguire et al., 2000), VBM was used to test whether structural changes could be detected in the brain as a result of extensive experience of spatial navigation. The posterior hippocampi in a group of subjects with such an extensive experience (London taxi drivers) were significantly larger relative to those of healthy controls, while the anterior hippocampi were larger in controls than in taxi drivers. These results suggest that the posterior hippocampi expand regionally in individuals who have extensive experience of spatial navigation. An alternative hypothesis, however, would be that the difference in the hippocampal volume is associated with innate navigational expertise. Another study (Draganski et al., 2004) shed light on this issue, by demonstrating that the acquisition of new skills may indeed change neuroanatomy. Brain scans were acquired from healthy subjects before they

learnt a classic three-ball cascade juggling routine and 3 months later when they had become skilled performers. The comparison of the scans acquired before and after practice revealed an expansion in GM in bilateral mid-temporal areas and left posterior intra-parietal sulcus. These findings were specific to the training stimulus, as a group of controls showed no changes in GM over the same period. Because jugglers and controls were randomly divided by the experimenters, the results can be interpreted in terms of structural changes induced by training rather than genetic predisposition. The authors also reported a decrease in the expansion of GM once the jugglers stopped practicing for 3 months. This suggests that the effect of training on brain structure may be transient. These findings were extended by a study showing that structural changes occur in the human brain in response to second language acquisition, and that the degree of structural reorganisation depends on the age of acquisition and the proficiency attained (Mechelli et al., 2004). Increased GM volume was identified in the left inferior parietal cortex of bilinguals relative to monolinguals, with greater effects in early bilinguals than in late bilinguals. To summarise, VBM studies of healthy subjects have challenged the traditional view that the acquisition of new skills only changes the way the brain functions, by showing structural changes at the macroscopic level. These studies have also suggested that the GM changes induced by training may be transient and dependent on the age of the subjects and the performance achieved.

Altering behaviourally relevant afferent input to the central nervous system can induce plastic changes in functions and organisation of the brain cortex. Experiments requiring a sustained use of a body part in animals lead to an increase of the brain's cortical representation of that body part (Jenkins et al., 1990). Conversely, decreased input or use reduces the representational area of that body part, as occurs after amputation of a digit or somatosensory deafferentiation of an entire forelimb in monkeys (Pons et al., 1991). Recently, longitudinal studies using VBM provided evidence of structural neuroplasticity

(i.e., increases or decreases in amount of GM) resulting from changes in afferent input to the undamaged central nervous system. In line with functional neuroimaging studies, limb amputation is associated with decreased thalamic GM, a structural brain change presumably reflecting the loss of sensory input from a specific body part (Draganski et al., 2006). Furthermore, Gauthier et al. (2008) report increases in GM in sensory and motor cortical areas and in the hippocampus in adult patients with stroke after constraint therapy.

4.2 Robot-mediated therapy for motor recovery

Recently, new technologies such as robotics and virtual reality are increasingly placing side by side traditional rehabilitation treatments to assist, enhance and assess motor training. The role of these technologies within therapeutic treatment programs and their effectiveness are currently under debate (Adamovich et al., 2009; Castelli, 2011; Henderson et al., 2007; Huang and Krakauer, 2009; Prange et al., 2006). In particular, in the literature the opportunity of their association with traditional therapy (Waldner et al., 2009) and the differences between improvements in motor control and in activities of daily living were discussed (Kwakkel et al., 2008). Interactive robotic devices are relatively new tools for the professionals of rehabilitation intervention and robot-mediated therapy (RMT) has been a very active area of research in recent years, holding much promise for improved outcomes. RMT appears to promote improvement in sensorimotor as well as cognitive processes and, by means of specific tasks, it may result useful in the rehabilitation of patients affected by congenital or acquired brain injury (Krebs et al., 2008). Robotic approaches capable of functioning at sites remote from human therapists may also enable telerehabilitation (Lai et al., 2004; Winters, 2004).

RMT produces a controlled and repeatable therapy experience. An advantage over traditional techniques and clinical scales is that it allows gathering quantitative kinematics and kinetics data to estimate the patient's progress in parallel with therapeutic applications. Robotic devices can simulate a variety of tasks providing high intensity, precision and repeatability, without fatigue (Barreca. et al., 2003). They can be programmed to perform in different functional modes and may be employed both to impose novel forms of mechanical manipulation that therapists cannot emulate (Patton and Mussa-Ivaldi, 2004) and to adapt to patients' performance, assisting them as needed during a given motor task (Colombo et al., 2008). Robotic systems are capable of assisting movement in a number of different modes (Prange et al., 2006), including active non-assist mode, in which the subject does all work and the robot provides no help, and active assist mode, in which the subject attempts to move and the robot supplements this effort. These two modes are usually preferred to a passive assist mode, in which the subject relaxes while the robot performs all movements, because interventional studies suggest that greater gains are achieved when the subject actively exerts an effort (Lotze et al., 2003). In these two active modes, the subject's effort, i.e. devotion of attention and energy to movement generation, is likely similar, though active assist mode might at times require less effort than non-assist mode because a portion of movements can be passive. Active assist mode might have advantages. For example, in subjects with paresis it is likely to produce a larger range of motion, with superior multijoint coordination, than non-assist mode. As such, active assist mode likely generates greater proprioceptive feedback to the brain and sensorimotor integration than does the active non-assist mode. The quantity and character of such sensory signals reaching motor cortex are known to modulate motor cortex function and excitability, and increased afferent feedback has been considered useful for improving motor learning (Kaelin-Lang et al., 2002; Rossini and Dal Forno, 2004; Takahashi et al., 2008), a conclusion that is

underscored by the rich structural and functional connections between primary sensory and motor cortices.

Many different robotic devices have been proposed for upper limb rehabilitation (Kan et al., 2011) and several clinical studies regarding the effectiveness of RMT for the paretic upper limb after stroke in adult population have shown statistically significant improvements of arm motor function, with reduction of motor impairment and increase of motor power during both acute and chronic phases of recovery (Fasoli et al., 2003; Fasoli et al, 2004; Ferraro et al., 2003; Kahn et al., 2006; Krebs et al., 1999; Lo et al., 2010; Lum et al., 2002; MacClellan et al, 2005; Reinkensmeyer et al., 2004). However, only recently has RMT been used in pediatric settings and the Movement Analysis and Robotics Laboratory (MARLab) of Bambino Gesù Children's Hospital is the first organisation worldwide having included robotic instrumentation in clinical protocols (Frascarelli et al., 2009, J Rehabil Med). To this end, the InMotion2 robot (Interactive Motion Technologies, Cambridge, Massachusetts, USA), a commercial version of the MIT-Manus device, has been customised by the neurorehabilitators to extend its application to pediatric patients. The results obtained at the MARLab support previous positive findings on the application of upper limb RMT in children with cerebral palsy (Fasoli et al., 2008) and extend them to children with traumatic brain injury, thus providing evidence that short-term, goal-directed robotic therapy can significantly improve both coordination and function of the exercised limb segments (Frascarelli et al., 2009, Eur J Phys Rehabil Med).

Recent evidence suggests that the contribution of new technologies to clinical practice is currently limited to the provision of intensive and repetitive movements (Brochard et al., 2010). This aspect is indeed very important in neurorehabilitation, as animal studies have shown that high dosage per unit time seems to increase synaptic density (Luke et al., 2004; Remple et al., 2001). Therefore, a recurring theme is that interventions emphasizing intense, active

repetitive movement are of high value in restoring motor function by increasing strength, accuracy and functional use (Wolf et al., 2006). However, robotic therapy also offers new opportunities to study both motor control and motor learning processes by means of repeatable training and measurement (Casadio et al., 2009). Furthermore, salient task practice (Carr and Shepherd, 1987; Proteau et al., 1994), training in novel environments triggering high motivation (Nudo and Friel, 1999) and enhanced visual, auditory, and/or haptic feedback (Masia et al., 2011; Sallnas et al., 2000; Winstein et al., 1999) are some of the features of virtual reality and robotic treatment that deserve further investigation, given the key influence that attention and sensory events have on motor learning in the normal and neurologically impaired states. Moreover, limited evidence has been provided on the neural networks involved and on their reorganisation related to training. To summarise, the potential of robotic devices in neurorehabilitation is not yet completely investigated.

4.2.1 The MIT-Manus robotic device

As previously stated, the MARLab is equipped with an InMotion2 robot, a version of the MIT-Manus device (Figure 4.1). This is a planar two degrees-of-freedom robot, specifically designed for upper extremity neurological rehabilitation (Krebs et al, 1998; Hogan et al., 1995), which administrates an intensive and goal-oriented treatment with visual and haptic feedback. The neurorehabilitation workstation is mounted on a custom-made adjustable table and chair, which allows the chair to be rotated 360° and translated 0.5 m toward a tabletop. During therapy, subjects are seated with the trunk strapped by a 5-point seatbelt to limit forward trunk compensation, and their paretic arm is placed in a hand holder attached to the robot end-effector. Exercises to be performed are displayed with a dedicated computer screen placed in front of the

child, which provides online visual feedback of target location and of hand movement. A physiotherapist is present at all times to provide verbal instructions and to ensure proper positioning of the child. Because InMotion2 is an end-effector based robot, no modifications were required to allow its use by small children except for modifying the chair size and the hand-holder to fit smaller hands.

InMotion2 can move or perturb the movement of a patient's upper limb. It can provide graded assistance, dynamically adapting to each patient's ability. Active assistance and correction lessens as the patient improves, while active resistance may be increased. Like other robots for rehabilitation, InMotion2 is configured for safe, stable and compliant operation in close physical contact with humans. This is achieved using impedance control. Its computer control system modulates the way the robot reacts to mechanical perturbation from a patient and ensures a gentle compliant behaviour. The device was designed to have a low intrinsic endpoint impedance (i.e., to be highly backdrivable), with a low and nearly-isotropic inertia and friction. Furthermore, the robot can provide precise and continuous real-time recording of key variables of motion, including position, velocity, and applied forces. Position and velocity are sampled at 200 Hz, with accuracies of 0.1 mm and 1.5 mm/s respectively.

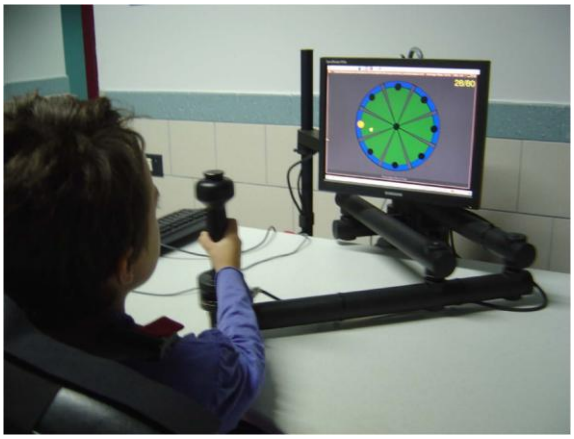

Figure 4.1 – Upper limb robotic training setting at the MARLab of Bambino Gesù Children's Hospital.

The two degrees-of-freedom module for elbow and forearm motion consists of a SCARA (selective compliance assembly robot arm) mechanism driven by brushless motors rated at 7.86 Nm of continuous stall torque with 16-bit resolvers for position and velocity measurements. Redundant velocity sensing is provided by dc-tachometers with a sensitivity of 1.75 V/rad/s. Torque sensors on the motor shafts are rated at 22.6 Nm with a torsional stiffness of 2,302 Nm/rad. Position sensing is provided by built-in precision potentiometers (0.9 kΩ/rad). The actuators include tachometers with a rated 0.07 V/rad/sec sensitivity. The robot control architecture is implemented in a standard personal computer (Krebs et al., 1998).

4.3 Congenital and acquired hemiparesis in children

Cerebral palsy is a well-recognised neurodevelopmental condition beginning in early childhood and persisting through the lifespan. It is defined as "a group of disorders of the development of movement and posture causing activity limitation that are attributed to non-progressive disturbance that occurred in the developing foetal or infant brain. The motor disorders of cerebral palsy are often accompanied by disturbance of sensation, cognition, communication, perception, and/or behaviour, and seizure disorder" (Bax et al., 2005). It is the most common cause of physical disability in childhood, occurring between 2 and 3 per 1,000 live births. Hemiparetic forms, characterised by a clinical pattern of unilateral motor and sensory impairment, constitute the most frequent expression of cerebral palsy (more than 38% of cases). However hemiparesis is not exclusive to cerebral palsy. If the damage to a part of the brain originating hemiparesis occurs before, during, or soon after birth, it is known as congenital hemiparesis. If it occurs later in childhood (up to age 3), it is called acquired hemiparesis. Typically, the upper limb is more

involved than the lower one, with impairments of spasticity, sensation, and reduced strength. Reaching, grasping, releasing, and manipulating objects is often compromised, resulting in a significant reduction of the effective use of the arm and hand in the daily activities. Children with hemiparesis usually have the intellectual capacity to attend regular school; however, impaired arm function restricts their participation in educational, leisure, and later vocational roles. Note that hemiplegia is the total paralysis of the arm, leg, and trunk on one side of the body and is more severe than hemiparesis (however, the two terms are frequently used as synonyms).

There are many models of intervention targeting deficits in upper limb function that aim to reduce activity limitations for children with hemiparesis. In a recent review, four main interventions were identified: intramuscular botulinum toxin A combined with upper-limb training; constraint-induced movement therapy; hand-arm bimanual intensive training and neurodevelopmental therapy. The review demonstrated that no one treatment approach seems to be superior. However, injections of botulinum toxin A provide a supplementary benefit to a variety of upper limb-training approaches (Sakzewski et al., 2009). Recently, a possible new rehabilitative approach has been proposed (Sgandurra et al., 2011; Small et al., 2010), based on action observation (see also Section 4.5.1). This approach is based on the discovery of mirror neurons in the ventral premotor cortex and in the inferior parietal lobule of the monkey (di Pellegrino et al., 1992; Gallese et al., 1996). Mirror neurons are a class of visuomotor neurons discharging both when a monkey performs a goal-directed motor act (e.g. grasping an object) and when it observes another individual performing the same or a similar motor act. A comparable mirror systems was later identified in humans (Rizzolatti et al., 2009).

4.4 Neuroimaging and robotic training: rationale and relevance of the research

Exploring the impact of RMT on the recovery of upper limb deficit in children with hemiparesis may open up new scenarios for functional recovery in these patients. RMT cannot be routinely used in rehabilitation centres because of its complexity and cost, thus it is essential to provide evidence of its usefulness. Solid evaluation tools are required to test the effectiveness of innovative rehabilitation interventions such as RMT on motor learning after brain damage or disease. The clinical evaluations of motor recovery during rehabilitation are usually based on functional scales. When RMT is applied, accurate measurements of movement variables can also be gathered by the robot. However, an incomplete understanding of the biological bases for recovery has led in the past to the use of intuitive and unsubstantiated approaches to rehabilitation (Yagura et al., 2006).

Neuroimaging techniques have the potential to reveal patterns of neural activation after brain injury and to investigate directly which rehabilitation interventions stimulate neuroplastic changes. Therefore, by giving insight on brain reorganisation related to training, non-invasive neuroimaging techniques represent a powerful tool that may guide the development of evidence-based rehabilitation interventions. Research conducted over the last decade has greatly improved the understanding of how neuronal circuits are shaped by experience and learning. However, little is known about how the brain actually recovers from and compensates for neurologic damage with specific rehabilitative approaches. Functional recovery after brain damage or disease is dependent on the neuroplastic capability of the not affected brain. Importantly, it appears that beneficial neuroplastic changes are stimulated only by certain forms of behavioural interventions (Nudo et al., 1996; Plautz et al., 2000). It is also worth

noticing that few studies have been conducted on patients in developmental age, when there is a bigger window for neuronal plasticity and the expected functional recovery could be better, while several studies proved that brain damages in early phases of cerebral development result in a worse prognosis with respect to adult age.

Studies combining the use of robotic devices for rehabilitation and MRI in children with brain injury are sparse. To fill this gap, a research project was started aiming at using neuroimaging data to explore the efficacy of RMT on children with brain damage with the final goal of improving clinical practice. The research is based on an ongoing collaboration among the BioLab[3] Laboratory, the MARLab and the Imaging Research Unit of Bambino Gesù Children's Hospital.

By studying the performances of hemiparetic children in a longitudinal design, the research aims at applying neuroimaging techniques (VBM and fMRI) to analyse anatomical and functional cerebral plasticity underlying the recovery of upper limb motor performance induced by rehabilitation treatment. This explorative study may prove useful in underlining the reorganisation of cerebral activations related to functional recovery and in identifying possible patterns for the recovery of motor performance associated to changes in brain structure. Furthermore, the research may contribute to assess potential cognitive reorganisations of motor planning and motor control, through the analysis of brain functional activations induced by specific tasks. The evidence that will be gathered will lead to a better understanding of neuropsychological effects in terms of motor and praxic functions in children with hemiparesis. Moreover, the research may enable us to verify whether or not recent evidence on cerebral structural modifications in adult patients induced by specific rehabilitation techniques is confirmed in a pediatric population. Indeed, the hypothesis was made in this research that structural neuroplasticity might be induced also in children with congenital or acquired hemiparesis following rehabilitation

protocols. As to the analysis of these potential neuroanatomical modifications, we assumed an increase of the GM content in somatosensory and motor areas of the brain, that will be studied through a longitudinal VBM analysis.

A key objective of the research is to ascertain the effectiveness of RMT protocols in children affected by congenital or acquired hemiparesis and to elucidate its role in the rehabilitation planning with respect to traditional rehabilitation programs. It will be possible to confirm the applicability of RMT in children and to objectively prove, by means of the anatomical and functional modifications shown by neuroimaging techniques, whether or not it is more effective than traditional physiotherapy.

The potential utility of this approach is to learn more about the efficacy of a specific training strategy with respect to evaluations performed with functional scales only. Changes in specific ROIs of the brain may serve as an assay for predicting behavioural gains for a given type and duration of rehabilitation intervention. In this case, the approach of monitoring brain-behaviour correlates during treatment would allow customising rehabilitative programs to optimise motor recovery. Therefore, the final aim of the research project is to identify integrated evaluation protocols to obtain specific indications on the most effective rehabilitation therapy for children with hemiparesis based on clinical evidence. Results yelded by this research may lead to the development of both standardised and personalised training protocols combining RMT and traditional rehabilitation approaches for the recovery of upper limb in children with hemiparesis, according to the criteria of evidence-based rehabilitation. These protocols would improve patients' outcomes as relates to the quality of the upper limb functional control, integration of the plegic side in the motor activation patterns, and autonomy in daily life activities.

A valuable aspect of the project is its multimodal and multidisciplinary approach characterised by the use of several assessment modalities (clinical scales, movement measurements, structural and functional neuroimaging) and

technologies (robot for rehabilitative training, MR-scanner for acquisition of structural and functional images). An additional strength is the population of this study. The literature dealing with similar topics is mainly focused on recovery of adult patients affected by acquired brain injury. Conversely, only patients in developmental age are included in this research project. In this vein, this study analyses neuronal plasticity as effect of standardised rehabilitation training during a critical period of brain maturation, when cerebral circuits may be more easily shaped by experiences and training. This could give us new insight on neuronal mechanisms related with recovery of function after brain damage in developmental age. The methodology and the instruments used in this research might be extended and adapted to the treatment of other neuro-motor disorders.

The experimental protocol was approved by the Ethical Committee of Bambino Gesù Children's Hospital. Children's parents or a legal representative provide their written informed consent to participate in the study. They are informed that children would be participating in a research project and would thus be randomly assigned to receive a traditional rehabilitation therapy or RMT, administered by a trained therapist. The informed consent module for healthy volunteers is shown in Figure 4.2.

4.5 Preliminary fMRI study on healthy adults

4.5.1 Introduction to the preliminary study

To implement an assessment protocol for comparing neuronal activity before and after intensive robotic training in children with hemiparesis, an fMRI task was set up and preliminary tested on healthy adult subjects (Grisolia et al., 2010, SIAMOC Congress; Grisolia et al., 2011, EACD Meeting).

Bambino Gesù
OSPEDALE PEDIATRICO

Tecniche avanzate di neuroimaging nello studio della plasticità cerebrale indotta da riabilitazione robot-mediata in bambini con emiparesi/WP10

SCHEDA INFORMATIVA E DICHIARAZIONE DI ASSENSO
per gli adolescenti e gli adulti volontari sani

1. OSPEDALE PEDIATRICO BAMBINO GESÙ

SCHEDA INFORMATIVA RELATIVA ALLO STUDIO:

Tecniche avanzate di neuroimaging nello studio della plasticità cerebrale indotta da riabilitazione robot-mediata in bambini con emiparesi

In questo Ospedale è in programma una ricerca medico-scientifica dal titolo **"Studio di neuroimaging della riorganizzazione cerebrale indotta dalla terapia con robot in ragazzi con emiparesi"** (WP10). Questa ricerca si svolge esclusivamente in questo Ospedale.

Che cosa si propone la ricerca

Lo studio ha come obiettivo generale accertare attraverso la risonanza magnetica funzionale l'efficacia della riabilitazione robotica in bambini e ragazzi emiparetici in confronto alla terapia riabilitativa tradizionale. In particolare, con la ricerca che qui presentiamo, si intendono ottenere dati relativi alla riorganizzazione cerebrale indotta dalla terapia con robot.

Cosa comporta la tua partecipazione alla ricerca

In una fase preliminare della ricerca è opportuno verificare che il protocollo di Risonanza Magnetica funzionale creato sia adeguato per lo studio di neuroimaging già brevemente descritto. Per far questo effettueremo, su individui volontari sani, sia adulti che bambini, un singolo esame di Risonanza Magnetica funzionale.

La RM funzionale è un esame in grado di visualizzare con buona risoluzione anche temporale (pochi secondi) un aumento del flusso sanguigno in determinate regioni cerebrali, e con ciò l'attivazione funzionale di determinate regioni cerebrali.

Nel caso tu decida di partecipare allo studio, a te, come volontario sano, sarà richiesto di eseguire un esame di Risonanza Magnetica funzionale durante il quale ti sarà chiesto di stare fermo, guardare dei video e rispondere ad un quesito, che ti sarà opportunamente illustrato prima dell'esame.

La partecipazione alla sperimentazione non comporta per te alcun aggravio di spese.

Bambino Gesù
OSPEDALE PEDIATRICO

Tecniche avanzate di neuroimaging nello studio della plasticità cerebrale indotta da riabilitazione robot-mediata in bambini con emiparesi/WP10

Quali sono i rischi derivanti dalla partecipazione alla ricerca

La risonanza magnetica non è dolorosa e non utilizza radiazioni ionizzanti.

Prima di essere sottoposto all'indagine ti verranno poste una serie di domande alle quali dovrai rispondere. Tali domande hanno lo scopo di prevenire eventuali danni causati dall'esposizione al forte campo magnetico prodotto dalla macchina di Risonanza Magnetica. Per esempio dovrà essere accertata la presenza di pace-maker cardiaco, pompe di infusione interne, neurostimolatori, protesi all'orecchio interno che possono subire danneggiamenti sotto l'azione del campo magnetico.
Analogamente possono costituire controindicazione all'esame la presenza di schegge metalliche all'interno del corpo e in particolare in vicinanza degli occhi, clip metalliche a seguito di interventi chirurgici al cervello o al cuore. È bene segnalare l'eventuale stato di gravidanza, specie se nel primo trimestre.

Prima di effettuare le sequenze di RM funzionale saranno effettuate delle sequenze anatomiche che saranno visionate da un medico radiologo.

Interruzione della ricerca

La tua adesione a questo programma di ricerca è completamente volontaria e potrà essere ritirata in qualsiasi momento.

Riservatezza dei dati personali

L'OPBG e il promotore Dott. Enrico Castelli, che ha commissionato lo studio che ti è stato descritto, ciascuno per gli ambiti di propria competenza e ai sensi del Decreto Legislativo 30 giugno 2003 n.196 in materia di protezione dei dati personali, tratteranno i tuoi dati, in particolare quelli sulla salute ed eventuali altri dati relativi alla tua origine, esclusivamente in funzione della realizzazione dello studio.
A tal fine i dati indicati saranno raccolti dall'OPBG e trasmessi al Promotore e alle persone o società esterne che agiscono per loro conto, tra le quali: "Sapienza" Università di Roma – Dipartimento di Meccanica e Aeronautica e Università degli Studi Roma Tre – Dipartimento di Elettronica Applicata.

Ti informiamo, inoltre, che il trattamento dei dati personali raccolti nel corso dello studio dal tuo medico è indispensabile allo svolgimento dello studio stesso: il rifiuto di conferirli non ti consentirà di parteciparvi.

Bambino Gesù
OSPEDALE PEDIATRICO

I dati, trattati mediante strumenti anche elettronici, saranno diffusi solo in forma rigorosamente anonima, ad esempio attraverso pubblicazioni scientifiche, statistiche e convegni scientifici. La tua partecipazione allo studio implica che, in conformità alla normativa sulle sperimentazioni cliniche dei medicinali, il personale dello Sponsor o delle società esterne che eseguono per conto dello stesso il monitoraggio e la verifica lo studio, il Comitato Etico e le autorità sanitarie italiane e straniere potranno conoscere i dati che ti riguardano, contenuti anche nella documentazione clinica originale, con modalità tali da garantire la riservatezza della tua identità.

Potrai esercitare i diritti di cui all'art. 7 del Codice in materia di protezione dei Dati Personali (es. accedere ai tuoi dati personali, integrarli, aggiornarli, rettificarli, opporsi al loro trattamento per motivi legittimi, ecc.) rivolgendoti direttamente al centro di sperimentazione o al Promotore.

Informazioni circa i risultati della ricerca

Se lo richiederai, alla fine dello studio potranno esserti comunicati i risultati ottenuti in generale e, in particolare, quelli che ti riguardano.

Ulteriori informazioni

Per ulteriori informazioni e comunicazioni durante la ricerca sarà a disposizione il seguente personale:

Dott. Enrico Castelli 06.6859.[omissis]

Dott. Simone Gazzellini 06. 6859. [omissis]

Dott.ssa Carmela Grisolia 06.6859. [omissis]

Dott. Federico Nocchi 06.6859. [omissis]

Dott. Maurizio Petrarca 06.6859. [omissis]

Il protocollo dello studio che ti è stato proposto è stato redatto in conformità alle Norme di Buona Pratica Clinica della Unione Europea e alla Dichiarazione di Helsinki, ed è stato approvato dal Comitato Etico per la Sperimentazione Clinica di questo Ospedale.

Potrai segnalare qualsiasi fatto che riterrai opportuno evidenziare, relativamente alla ricerca che ti riguarda, al Comitato Etico per la Sperimentazione del Farmaco di questo Ospedale. La segnalazione dovrà essere inoltrata all'attenzione del Presidente del Comitato Etico per la Sperimentazione clinica; Ospedale Pediatrico Bambino Gesù, Piazza S. Onofrio 4, 00165 Roma

Bambino Gesù
OSPEDALE PEDIATRICO

Tecniche avanzate di neuroimaging nello studio della plasticità cerebrale indotta da riabilitazione robot-mediata in bambini con emiparesi/WP10

2. DICHIARAZIONE DI ASSENSO

Io sottoscritto: _____

dichiaro di aver ricevuto dal Dottor _____

esaurienti spiegazioni in merito alla richiesta di partecipazione alla ricerca in oggetto, secondo quanto riportato nella scheda informativa qui allegata, copia della quale mi è stata prima d'ora consegnata.

Data ……ora …….

Dichiaro altresì di aver potuto discutere tali spiegazioni, porre tutte le domande che ho ritenuto necessarie e di aver ricevuto risposte soddisfacenti, come pure di aver avuto la possibilità di informarmi in merito ai particolari dello studio con persona di mia fiducia.

Accetto dunque liberamente di partecipare alla ricerca, avendo compreso completamente il significato della richiesta e i rischi e benefici che possono derivare da questa partecipazione.

Sono stato informato/a, inoltre, del mio diritto ad avere libero accesso alla documentazione (farmaco-terapeutica, clinico-scientifica, assicurativa) relativa alla ricerca ed alla valutazione espressa dal Comitato Etico per la Sperimentazione del Farmaco.

_____ _____
Data/ora Firma del medico che ha informato il paziente

_____ _____
Data/ora Firma per assenso del paziente

_____ _____
Data/ora Firma per assenso del genitore del minore

Figure 4.2 – Version for healthy volunteers of the informed consent module.

In this study, a visual fMRI task was used, able to elicit the activation of a neuronal network related to upper limb motor training with the MIT-Manus device. The task was designed to identify the cerebral activity patterns associated with processing (observation, analysis and representation) of human and abstract object movements similar to those implicated in robotic treatment. Human movements are presented as an arm performing a motor gesture similar to that carried out by patients during robotic training, whereas abstract object movements are presented as a dot moving along rectilinear trajectories and closely represent the visual feedback provided by the MIT-Manus device.

The selection of an appropriate fMRI protocol represents a particularly relevant issue in studies involving children (O'Shaughnessy et al., 2008). While designing an fMRI task intended to be administered to children with hemiparesis, it may be a good strategy to minimise subjects' motion, since movements of both the healthy and the paretic upper limb in these patients may result in excessive head motions that could completely compromise the exam. Therefore, visual fMRI tasks may be preferred to motor ones when impaired children are involved. With regard to this aspect, it has been shown that the neural network activated in humans in consequence of the observation of an action overlaps with that involved during the execution of the same action (Buccino et al., 2001; Jeannerod, 2001; Rizzolatti and Craighero, 2004). Furthermore, recent clinical trials proved that action observation used as treatment for the upper limb rehabilitation in chronic stroke patients improves functional abilities measured by clinical scales (Ertelt et al., 2007; Franceschini et al., 2010) and induces cortical reorganisation revealed by enlarged fMRI activation in the bilateral ventral premotor cortex, bilateral superior temporal gyrus, supplementary motor area and contralateral supramarginal gyrus (Ertelt et al., 2007). However, an open question regards the necessity of functional biological plausibility and intentionality of the stimulus (Buccino et al., 2004; Costantini et al., 2005; Engel et al., 2008).

Therefore, one of the aims of the fMRI task was to verify commonalities and differences in the brain networks able to process human upper limb gestures and abstract object movements. This analysis could be useful to test the effectiveness of the abstract feedback associated with the robotic training and to assess the brain ability to assign the same intentionality to both biological (arm gestures) and non-biological (abstract object) movements.

The preliminary study was carried out on a sample of 22 healthy right-handed volunteers (8 males, age 25.6±4.3 years, min = 19.2, max = 36.0). The inclusion criteria were: 18÷39 years of age; right-handedness; no current or previous motor and neurological disorders; subjects had not previously received any kind of rehabilitation protocol or robotic training. A clinical evaluation was performed in each participant, prior to scanning, by a skilled physician. Informed consent was obtained from all subjects.

4.5.2 Experimental design

The selected fMRI task consisted in the administration of a video requiring the recognition of human arm planar movements and rectilinear trajectories of a dot, both in one of 8 possible directions, presented in a random order. The motion stimuli were followed by a representation of the video screen presented to the subjects during the rehabilitation training with the MIT-Manus robot. A randomly positioned fixed dot (the target point), allowed the subjects to compare the direction of the received motion stimulus (arm planar movement or dot planar trajectory) with that of the target point (Figure 4.3). Since a behavioural feedback was necessary to control for subjects' performance during scanning, participants were asked to mentally count the number of congruencies of the target position with whatever kind of motion stimulus, i.e. to count the number of trials in which the target point was positioned in the same direction of

the previously presented arm movement or dot trajectory (Figure 4.3). The use of a visual task enabled to avoid voluntary movements during the fMRI session. For the same reason, any kind of motor feedback from the subjects (e.g.: pushing a response button in a keypad) was avoided.

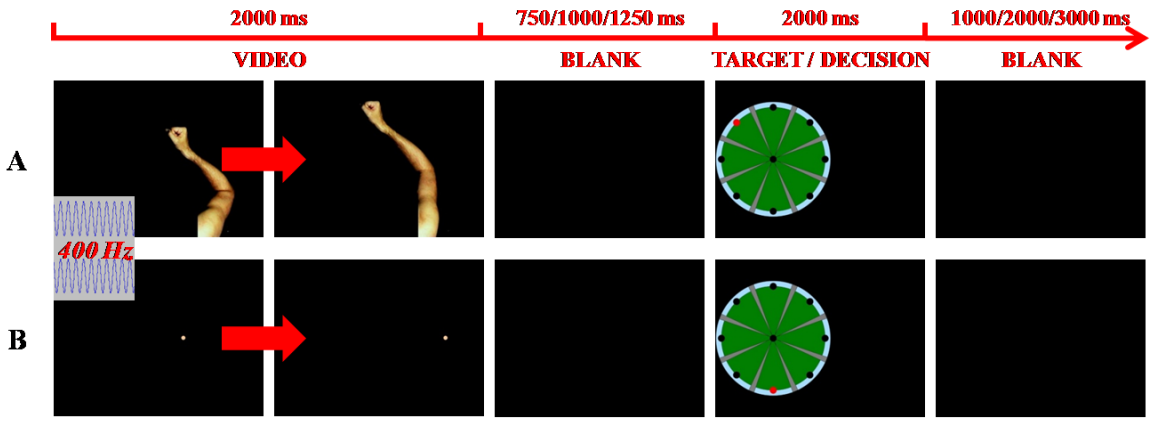

Figure 4.3 – Schematic representation of the fMRI task. Human arm planar movements (A) and rectilinear trajectories of a dot (B), are followed by a representation of the video screen presented to the subjects during the rehabilitation training with the MIT-Manus robotic device, with a randomly positioned colored dot. Subjects are asked to compare the direction of each motion stimulus with the position of the target point. A congruent (A) and an incongruent (B) trial are shown.

We hypothesized that, during the presentation of the arm movement, the subject must process the observed movement, assess the congruence between direction of the arm movement and position of the target point, and make a decision. During the presentation of the dot trajectory, the subject must process the trajectory, assess the congruence between direction of the dot and position of the target point, and make a decision. According to this hypothesis, these two conditions only differ in the analysis of the anthropomorphic movement, which is absent in the case of dot trajectory presentation.

Arm movements from a healthy adult subject were video recorded during the execution of a MIT-Manus training session (planar point-to-point reaching task) and processed in order to implement the stimulation sequence. Both right and left arm movements were used as video stimuli in anticipation of the

subsequent administration of the task to hemiparetic patients. An audible beep was given to the subjects at the beginning of each trial (i.e., when an arm movement or a dot trajectory started). A time interval of random duration (750, 1,000, or 1,250 ms), during which subjects saw a blank screen, followed the motion stimulus and preceded the presentation of the target. A second variable time interval (1,000, 2,000, or 3,000 ms) was introduced following the target and before the onset of the successive motion stimulus (Figure 4.3).

Four runs were performed by each subject. Each run consisted of 54 trials. All motions (right arm movements, left arm movements, dot trajectories) occurred with the same frequency in each run. Taking the 4 runs together, each movement direction was presented the same number of times and an equal number of congruent and incongruent trials occurred. To avoid possible ambiguities related to the interpretation of the human arm movements, the angular mismatch between the movement direction and the position of the target was greater than or equal to 90° both for arm movements and dot trajectories. At the end of each run, subjects were asked for the number of congruent trials of that specific run.

A 15’ session with the InMotion2 robot was administered to each subject 1 hour before the MRI exam. This very short session consisted in planar point-to-point reaching movements towards targets presented on the monitor of the InMotion2 workstation and was aimed at making the subjects aware of the goal of the stimuli displayed during the fMRI exam. This preliminary robotic session is part of the instructions given to subjects prior to scanning. Subsequently, all subjects received a set of trials of the fMRI task to verify their ability to perform it.

4.5.2.1 MRI data acquisition

All scans were performed on the 1.5 T Philips Achieva MRI scanner of the Imaging Department of Palidoro, equipped with a 8-channels Sense head coil. The imaging protocol for each subject consisted of a 3D T1-weighted anatomical scan acquired as structural reference and of 4 T2*-weighted EPI sequences. The following parameters were used in EPI scans: TR = 2,500 ms, TE = 46 ms, flip angle = 90°, field of view = 256x140x256 mm, reconstruction matrix = 64x64 (pixel size = 4x4 mm), 28 axial slices (slice thickness = 5 mm, without gap), 6 dummy scans, 153 dynamic scans for each sequence (duration: 6'22"). The total scan time for the protocol was 31'45". The visual and auditory stimulus sequences were implemented in the STIM2 software and delivered by the NordicNeuroLab MR-compatible stimulation system.

4.5.2.2 fMRI data analysis

Analysis of fMRI data was performed with the SPM8 version of SPM running in MATLAB version 7.9.0.529 (R2009b) (The Mathworks, Natick, Massachusetts, USA). Data from each subject were pre-processed with motion correction, normalisation to the standard Montréal Neurological Institute (MNI) template and spatial smoothing by convolution with a 8-mm FWHM isotropic Gaussian kernel.

Statistical analysis was performed in a 2-stage, mixed-effect, procedure using the general linear model approach for event-related fMRI designs. In the 1st-level, individual subject analysis, 6 regressors were used in each run to model the BOLD response for each of 6 event types. The events were defined as observation of an arm movement (AM), observation of a dot trajectory (DT),

presentation of a congruent target point following an AM (AMCT), presentation of a congruent target point following a DT (DTCT), and presentation of incongruent target points following AMs or DTs (AMIT and DTIT, respectively). Estimates of the 6 head movement parameters obtained from the realignment stage of pre-processing were included as additional regressors. Contrasts between regressors were then obtained for each subject (Table 4.1).

Contrast†	AM	DT	AMCT	DTCT	AMIT	DTIT	M1	M2	M3	M4	M5	M6
AM	1	0	0	0	0	0	0	0	0	0	0	0
DT	0	1	0	0	0	0	0	0	0	0	0	0
AM>DT	1	-2	0	0	0	0	0	0	0	0	0	0
DT>AM	-1	2	0	0	0	0	0	0	0	0	0	0
AMT	0	0	1	0	1	0	0	0	0	0	0	0
DTT	0	0	0	1	0	1	0	0	0	0	0	0
AMT>DTT	0	0	1	-2	1	-2	0	0	0	0	0	0
DTT>AMT	0	0	-1	2	-1	2	0	0	0	0	0	0
CT>IT	0	0	1	1	-1	-1	0	0	0	0	0	0
IT>CT	0	0	-1	-1	1	1	0	0	0	0	0	0
AMCT	0	0	1	0	0	0	0	0	0	0	0	0
AMIT	0	0	0	0	1	0	0	0	0	0	0	0
DTCT	0	0	0	1	0	0	0	0	0	0	0	0
DTIT	0	0	0	0	0	1	0	0	0	0	0	0
AMCT>AMIT	0	0	1	0	-1	0	0	0	0	0	0	0
AMIT>AMCT	0	0	-1	0	1	0	0	0	0	0	0	0
DTCT>DTIT	0	0	0	1	0	-1	0	0	0	0	0	0
DTIC>DTCT	0	0	0	-1	0	1	0	0	0	0	0	0

Table 4.1 – Contrast vectors used in the preliminary fMRI study on healthy adults. †**AM** = arm movement; **DT** = dot trajectory; **AMT** = presentation of the target following an AM; **DTT** = presentation of the target following a DT; **CT** = presentation of a congruent target; **IT** = presentation of an incongruent target; **AMCT** = presentation of a congruent target following an AM; **AMIT** = presentation of an incongruent target following an AM; **DTCT** = presentation of a congruent target following a DT; **DTIT** = presentation of an incongruent target following a DT.

The results from the 1st-level analysis were entered into a one-sample t-test for the 2nd-level analysis, thus enabling inferences based on the contrasts to be extended to the population from which the subjects were drawn (Friston et al., 1999). All statistical parametric maps were thresholded at $p<0.001$ at the voxel-level (uncorrected) and only clusters surviving a FWE corrected threshold

of $p<0.05$ were considered significant (Forman et al., 1995). A conjunction analysis of AM vs. implicit baseline (IB) and DT vs. IB contrasts was performed to identify areas activated in both conditions. The t-maps of these contrasts at the group level were thresholded, binarised, and multiplied voxelwise with each other (Nichols et al., 2005). The analysis of congruence between the observed arm movement or dot trajectory and the position of the target point implies retrieval from memory of the previously observed movement and imagery of the movement toward the target, which, for the sake of clearness, were referred to as "representation of arm movements" (AMT) and "representation of dot trajectories" (DTT). A second conjunction analysis was performed for these "representations".

4.5.3 Results

4.5.3.1 Subjects' performance

At the end of each fMRI run, subjects were asked for the number of congruent trials of that specific run. Percentage errors where less than 12% for each run in each subject. This low percentage error was assumed to be a sufficient and objective proof of subjects' continued participation in the task. Therefore, no subject nor run was excluded from the group analysis due to low task performance.

4.5.3.2 Observation of arm movements and cue trajectories

When the observation of AMs was compared to the IB, a significant bilateral activation was found in occipital lobe (primary, secondary and

associative visual cortex, Brodmann Areas - BA - 17, 18, 19), parietal lobe (superior parietal lobules, BA 5, 7; supramarginal gyrus, BA 40; angular gyrus, BA 39; postcentral gyrus, BA 3, 1, 2; precuneus, BA 7 medial; paracentral lobule, BA 3, 1, 2, 5 medial), temporal lobe (middle and inferior temporal gyrus, fusiform gyrus, BA 20, 21, 22, 37), several areas of the frontal lobe (precentral gyrus-primary motor area, BA 4; supplementary motor area, BA 6; medial frontal gyrus, BA 8, 9; superior frontal gyrus, BA 4, 6, 8; middle frontal gyrus, BA 9; inferior frontal gyrus, BA 44, 46, 47), limbic lobe (cingulate gyrus, BA 31; hippocampus and parahippocampal gyrus, BA 27, 30), and insula (BA 13). Furthermore, activations were found in a large portion of the cerebellum (vermis, anterior and posterior cortex) and in the thalamus.

The comparison of DTs observation with the IB revealed a large pattern of activations overlapping with the above described network. Consequently, conjunction analysis identified significant activations in all the regions mentioned above, with medial frontal gyrus activated only in the left hemisphere and a right lateralisation of cingulate gyrus and parahippocampal gyrus (Figure 4.4).

The differential analysis between AM and DT conditions (AM > DT) showed significant differences in occipital lobe, temporal lobe and cerebellum (Table 4.2). These differences, which appear in commonly activated regions, are due to a greater extent and intensity of the activations related to the observation of AMs. Finally, the reverse contrast (DT > AM) highlighted only small clusters of voxels in occipital and temporal regions, attributable to more intense focal activations.

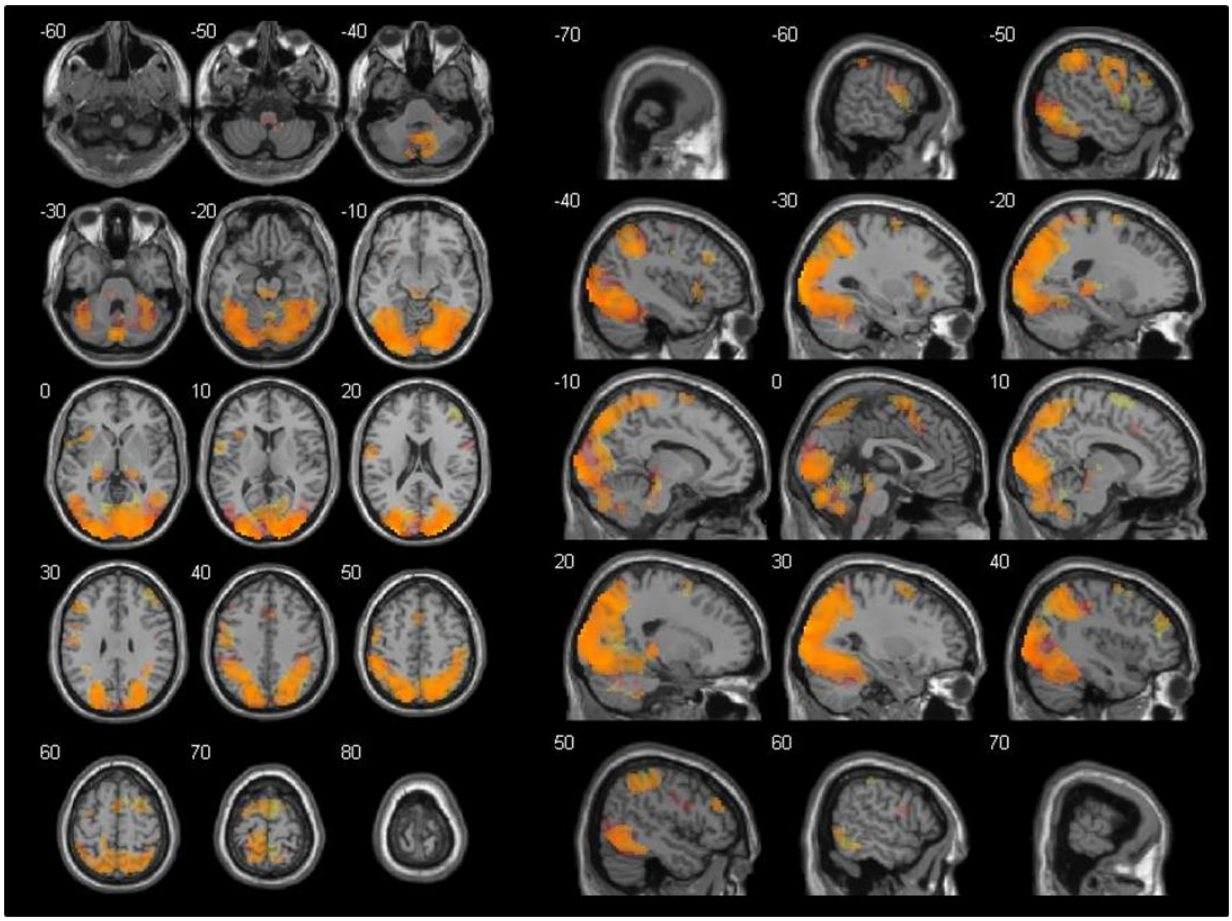

Figure 4.4 – Cerebral regions involved in both the observation of arm movements and dot trajectories (orange) as revealed by conjunction analysis. The t-maps of AM > IB and DT > IB contrasts at the group level were thresholded ($p<0.05$ at cluster-level, FWE corrected), binarised, and multiplied voxelwise with each other to identify common areas of activation. Areas activated only when arm movements where presented are shown in red, while areas activated only when dot trajectories where presented are shown in yellow. Activations are superimposed on the MNI single subject T1 template. The coordinates represented in the upper left corner of each section refer to the MNI stereotactic space.

4.5.3.3 Representations of arm movements and cue trajectories and congruence analysis

In each trial, following the presentation of the target, subjects were required to analyse the congruence between the observed arm movement or dot trajectory and the position of the target point. A network of activations was found when the representation of arm movements (AMT) was compared to the IB. Regions with significant activations included the occipital lobe (primary, secondary and associative visual cortex, BA 17, 18, 19), the parietal lobe (superior parietal lobules, BA 5, 7; right supramarginal gyrus, BA 40; angular gyrus, BA 39; postcentral gyrus, BA 3, 1, 2; precuneus, BA 7 medial; paracentral lobule, BA 3, 1, 2, 5 medial), the temporal lobe (superior, middle and inferior temporal gyrus, fusiform gyrus, BA 20, 21, 22, 37, 38), the frontal lobe (left precentral gyrus-primary motor area, BA 4; right supplementary motor area, BA 6; medial frontal gyrus, BA 8, 9; superior frontal gyrus, BA 4, 6, 8; middle frontal gyrus, BA 9; inferior frontal gyrus, BA 46, 47), the limbic lobe (hippocampus, parahippocampal gyrus, BA 27, 30), insula, cerebellum, basal ganglia (caudate, left putamen), and thalamus.

Similarly to the case of movement observation, a well overlapping pattern of activations was found when comparing the representation of dot trajectories (DTT) to the IB, so that all the above cited regions were present in the conjunction analysis of the two contrasts (Figure 4.5).

The presentation of the target following arm movements was compared with the presentation of the target following dot trajectories, showing significant differences in the superior parietal cortex and in the precuneus (AMT > DTT, Table 4.2). The reverse contrast (DTT > AMT) revealed a large cluster of voxels in occipital lobe, temporal lobe and cerebellum, with a similar pattern to that obtained with the AM > DT contrast.

When comparing the presentation of congruent and incongruent targets (CT > IT, Table 4.2), significant differences were found in the right occipital lobe (secondary and associative visual cortex, BA 18, 19), left parietal (postcentral gyrus, BA 3), right temporal (inferior temporal gyrus and fusiform gyrus, BA 37, 34), left frontal (orbital cortex, BA 47; precentral gyrus-primary motor area, BA 4; supplementary motor area, BA 6; olfactory cortex, BA 25), and right limbic lobe (parahippocampal gyrus and amygdala). Significant activations were also found in cerebellum, caudate, putamen and in the thalamus.

AMs mainly contributed to this result, as evident from the analysis of component contrasts. In particular, the AMCT > AMIT contrast revealed significant differences in the right occipital lobe (associative visual cortex, BA 19), left parietal (postcentral gyrus, BA 3), right temporal lobe (inferior temporal gyrus, BA 37), bilateral frontal lobe (supplementary motor area, BA 6; precentral gyrus-primary motor area, BA 4; middle and inferior frontal gyrus, BA 46, 10), and bilateral limbic lobe (cingulate cortex, BA 24, 31); vice versa, no cluster survived a $p<0.10$ FWE corrected threshold when the DTCT > DTIT contrast was applied.

In the reverse contrast (IT > CT) no cluster survived the corrected threshold. However, when component contrasts were analysed, while no cluster survived a $p<0.10$ FWE threshold in the AMIT > AMCT contrast, the DTIT > DTCT contrast revealed significant activations in the left occipital cortex (primary, secondary and associative visual cortex, BA 17, 18, 19).

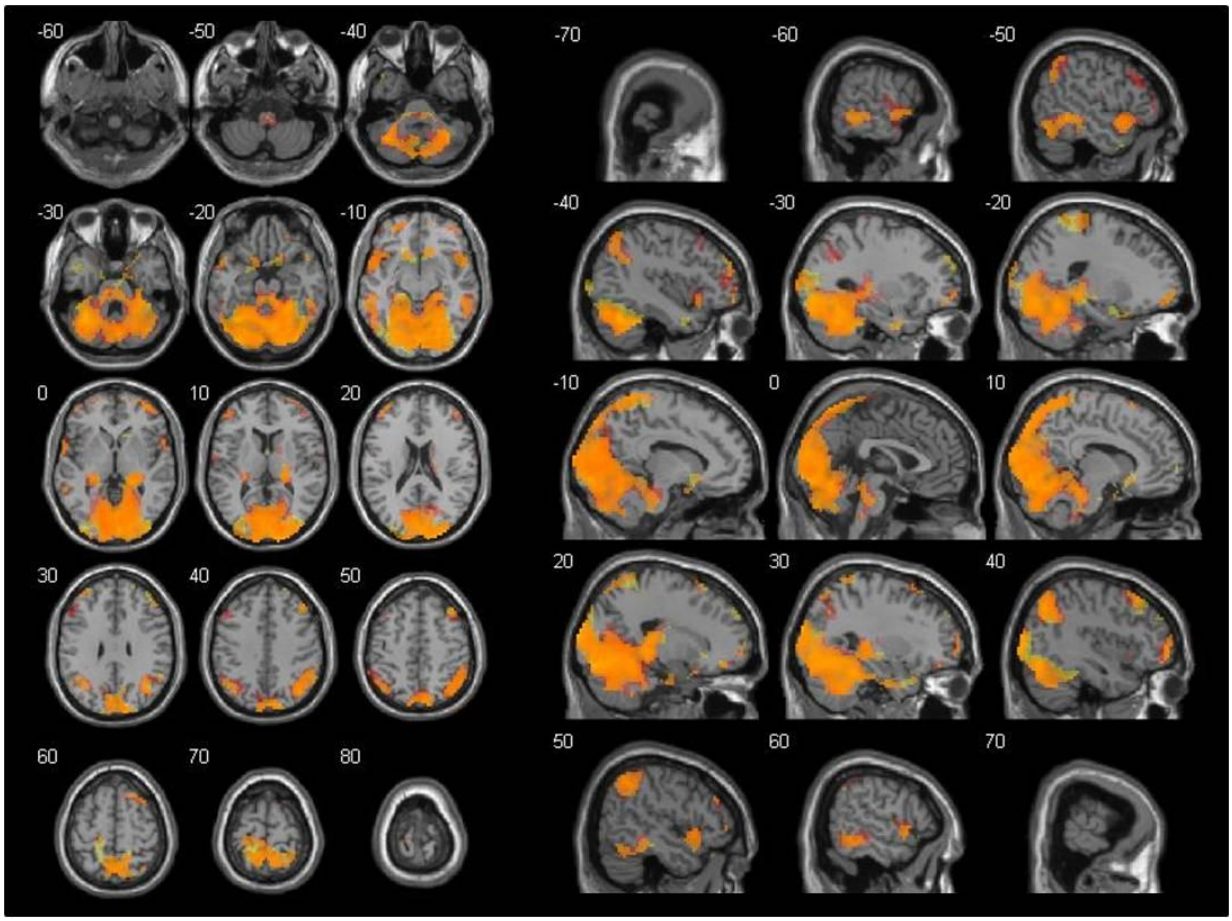

Figure 4.5 – Cerebral regions involved in both the representation of arm movements and dot trajectories (orange) as revealed by conjunction analysis. The t-maps of AMT > IB and DTT > IB contrasts at the group level were thresholded ($p<0.05$ at cluster-level, FWE corrected), binarised, and multiplied voxelwise with each other to identify common areas of activation. Areas activated only for arm movements representation are shown in red, while areas activated only for dot trajectories representation are shown in yellow. Activations are superimposed on the MNI single subject T1 template. The coordinates represented in the upper left corner of each section refer to the MNI stereotactic space.

Contrast †	Significant clusters	Brodmann areas	Size (voxels)	p	T	MNI coordinates		
						x	y	z
AM > DT	Occipital_Mid_L, Fusiform_R, Calcarine_L, Fusiform_L, Occipital_Inf_R, Cuneus_R, Occipital_Inf_L, Occipital_Mid_R, Cuneus_L, Occipital_Sup_L, Lingual_L, Cerebelum_6_R, Occipital_Sup_R, Temporal_Mid_R, Cerebelum_6_L, Cerebelum_Crus1_L, Lingual_R, Temporal_Mid_L, Calcarine_R, Temporal_Inf_R, Cerebelum_Crus1_R, Temporal_Inf_L, Cerebelum_4_5_R, Parietal_Sup_R	19, 18, 37, 17, 39, 36, 20, 23	4008	0.000	14.65	-42	-88	4
DT > AM	Temporal_Mid_R, Temporal_Sup_R, Rolandic_Oper_R, SupraMarginal_R, Postcentral_R, Heschl_R	21, 22, 42, 43, 41, 40	167	0.000	6.21	57	-16	13
	Temporal_Inf_L, Temporal_Mid_L	37, 21, 22	54	0.061*	5.53	-54	-55	-11
	Angular_R, Parietal_Inf_R, Occipital_Mid_R, Occipital_Sup_R, Parietal_Sup_R	7, 40, 19, 39	88	0.009	4.84	36	-64	43
AMT > DTT	Precuneus_R, Precuneus_L, Parietal_Sup_R, Parietal_Sup_L	7	114	0.003	5.19	-6	-70	55
DTT > AMT	Occipital_Mid_L, Fusiform_R, Fusiform_L, Occipital_Mid_R, Occipital_Inf_R, Occipital_Inf_L, Occipital_Sup_R, Lingual_L, Cerebelum_6_R, Occipital_Sup_L, Lingual_R, Cerebelum_6_L, Cerebelum_Crus1_L, Cuneus_L, Cuneus_R, Calcarine_L, Temporal_Mid_R, Temporal_Mid_L, Temporal_Inf_R, Cerebelum_4_5_R, Cerebelum_Crus1_R	19, 18, 37, 39, 17, 7	1830	0.000	10.72	-42	-88	1

Contrast †	Significant clusters	Brodmann areas	Size (voxels)	p	T	MNI coordinates		
						x	y	z
CT > IT	Caudate_R, Thalamus_L, Thalamus_R	---	184	0.000	6.93	12	5	16
	Postcentral_L, Precentral_L	4, 3, 6	57	0.069*	6.41	-51	-10	46
	Cerebelum_6_R, Fusiform_R, Lingual_R, Cerebelum_Crus1_R, Temporal_Inf_R	18, 19, 37	252	0.000	5.59	33	-58	-23
	Putamen_R, Amygdala_R, Olfactory_R, ParaHippocampal_R, Rectus_R, Frontal_Sup_Orb_R	34, 25, 47	80	0.021	5.35	15	8	-23
AMCT > AMIT	Frontal_Mid_R, Frontal_Inf_Tri_R	46, 10	76	0.021	6.67	45	47	4
	Postcentral_L, Precentral_L	4, 3, 6	55	0.069*	6.20	-51	-10	46
	Cerebelum_6_R, Fusiform_R, Cerebelum_Crus1_R, Temporal_Inf_R	37, 19	91	0.010	4.52	33	-58	-23
	Cingulum_Mid_L, Supp_Motor_Area_R, Supp_Motor_Area_L, Cingulum_Mid_R	24, 6, 31	74	0.024	4.00	0	-4	64
DTCT > DTIT	---	---	---	---	---	---	---	---
IT > CT	---	---	---	---	---	---	---	---
AMIT > AMCT	---	---	---	---	---	---	---	---
DTIT > DTCT	Occipital_Sup_L, Calcarine_L, Cuneus_L, Occipital_Mid_L, Lingual_L	18, 17, 19	189	0.000	7.24	-12	-100	10

Table 4.2 – Differential activations between conditions. For each contrast, all significant clusters ($p<0.05$ at cluster-level, FWE corrected) are shown. The anatomical areas defined in the Automatic Anatomical Labeling (AAL) atlas (Tzourio-Mazoyer et al., 2002) and Brodmann areas are listed for each cluster, ordered by decreasing number of voxels. T-scores and MNI coordinates refer to the voxel with the peak value. Clusters with $0.05 \leq p < 0.10$ are also reported (marked with a star); these clusters were considered marginally significant. †**AM** = arm movement; **DT** = dot trajectory; **AMT** = presentation of the target following an AM; **DTT** = presentation of the target following a DT; **CT** = presentation of a congruent target; **IT** = presentation of an incongruent target; **AMCT** = presentation of a congruent target following an AM; **AMIT** = presentation of an incongruent target following an AM; **DTCT** = presentation of a congruent target following a DT; **DTIT** = presentation of an incongruent target following a DT.

4.5.4 Discussion of the results

An fMRI experiment was used to investigate the brain regions involved in the execution of a task which simulates the visual feedback of a training session with the MIT-Manus robotic device. The task requires upper limb motor gesture recognition and activation of the cognitive representations of arm movements and dot trajectories, both presented on a screen.

The results showed a significant bilateral activation during perception and recognition of arm movements, and depict a caudo-rostral pathway for movement processing: visual perception (primary, secondary and associative visual cortex), sensory integration, subsequent recognition of arm movement and attention shifting (posterior parietal cortex), spatial input processing (inferior parietal cortex: supramarginal gyrus), re-mapping on the somatosensory and motor cortex (postcentral gyrus, precentral gyrus, supplementary motor area), storage in memory (hippocampus and parahippocampal gyrus, temporal areas, dorso-lateral pre-frontal cortex), motor control and motor learning (cerebellum, hippocampus and parahippocampal gyrus). Such results are consistent with previous studies (Boyd et al., 2009; Cunnington et al., 2003; Goodyear and Douglas, 2009; Hanakawa et al., 2008; Juncke et al., 2006) and point out that the neural correlates of the movement are a brain property that emerges from a complex cortical-subcortical network. A similar pattern was observed when dot trajectories were presented, showing a wide overlapping of areas significantly activated during arm movement and dot trajectory processing, as revealed by a conjunction analysis. The larger activations in occipital and temporal lobes in arm movement presentation with respect to dot trajectory trials, revealed by the AM > DT subtractive analysis, may be ascribed to visuo-perceptual differences among the two conditions; the wider cerebellar involvement in AM reveals the contribution of such structure in

motor activities (e.g. control and learning); interestingly, no difference was found in the motor and pre-motor areas.

In each trial, following the presentation of the target point, subjects were required to analyse the congruence between the observed arm movement or dot trajectory and the position of the target. This implies retrieval from memory of the observed movement and imagery of the movement toward the target (both for human arm motor gesture, AMT, and dot trajectory, DTT). Similarly to the case of movement observation, a wide overlapping of activated areas was also found with regard to movement retrieval and imagery. The active *loci* correspond to those found during AM observation, with the minor differences described in Section 4.5.3. This result was again confirmed by a conjunction analysis. However, more intense parietal cortical activity (superior parietal lobule) was found for AMT than for DTT, probably due to the more complex reconstruction of the corresponding mental image. In the reverse contrast (DTT > AMT), the differential activations involved occipital and temporal lobes and the cerebellum, which are the same areas that were more activated during AM observation than during DT observation.

Previous studies claimed the necessity of biological plausibility of observed movements in order to elicit their corresponding motor cortex activation (Buccino et al., 2004; Costantini et al., 2005). However, this issue is still under debate, since other works reported that observing upper limb movements carried out by humanoid robotic devices may generate the same fMRI pattern activated by the observation of a human arm (Engel et al., 2008; Gazzola et al., 2007; Press et al., 2005). Therefore, a possible explanation of the results provided by this preliminary study, would be that the observation of dot trajectories (abstract movements corresponding to the visual feedback in the MIT-Manus training) activates the same brain areas involved in the processing (recognition, retrieval, and imagery) of the human arm motor gesture. In that case, these data would support the hypothesis that the artificial feedback is

processed in a similar manner of the natural motor gesture. Hence, these results would enforce the idea that the re-mapping of motor inputs on the neural motor pathway does not necessarily require a complete biological plausibility. Probably, a key role in the procedures of re-mapping input and output representations of movements may be played by intentionality, i.e. the attribution of goal-orientedness to motor gestures or dot movements. From this point of view, the contribution of the visual feedback provided during rehabilitation with MIT-Manus to neural recovery is reinforced.

The interpretation according to which the reconstruction of dot trajectories requires the reconstruction of the corresponding motor gestures, seems to be supported by the fact that significant areas in the DTT > AMT comparison overlap (with smaller extension and lower intensity) with those in which activations are stronger during arm movement presentation than during dot trajectory observation (AM > DT; Table 4.2). These data would suggest that when participants were seeing the target, and hence had to make the decision on the congruity of the dot trajectory previously seen, they mentally reconstructed the motor gesture which subtends such trajectory. That claim is proved by the overlap of brain activity during dot trajectory representation and arm movement observation. However, a possible objection could be that such result may also be related to the characteristics of the experimental design. In the event-related task that was implemented in this study, the presentations of AM and DT trials were randomised and this could have facilitated a strategy based on the recall of the corresponding motor gesture even in case of dot trajectory presentation. In other words, the dissociation between the processing of arm movements and abstract object trajectories cannot be fully discarded since its absence in the results could be due to the characteristics of the task, which, similarly to what happens during robotic training, may induce the assimilation of strategies for upper limb movement and dot trajectory processing.

Results on congruent versus incongruent trials revealed more intense neural activity in a few cortical areas in case of congruent conditions. *Post hoc* analyses demonstrated that such effect should be ascribed to the AM condition. Indeed, in this condition we found greater activity in a network including bilateral cingulate cortex, right inferior and middle frontal gyrus which are involved in the go-signal and in the decision control (Chevrier et al., 2007; Kemmotsu et al., 2005; Kübler et al., 2006), supplementary motor area and, with a marginal significance, left primary motor and sensorimotor areas which are involved in perception of limb movements and motor imagery (Hanakawa et al., 2008; Naito, 2004). These differences could depend on the task demand characteristics, namely on the fact that participants were asked to count the number of overall congruent conditions. For that reason, congruent information was more relevant for decision with respect to the incongruent one, and participants may have repeated and reinforced the mental reconstruction of the congruent gesture to avoid mistakes.

The role played by the knowledge of results provided by the feedback during robotic training deserves further consideration. In the fMRI task used in this study, the target point was shown after the end of movement observation and it wasn't superimposed on the motor gesture or dot trajectory. Literature on motor learning suggests that a delayed feedback (i.e. a feedback provided at the end of the action), similar to the one used in this study, increases the processing of the features of performance and promotes a more stable learning than an instantaneous feedback, like the one provided during the MIT-Manus training (Swinnen et al., 1990). Therefore, while this study addresses the issue of the biological or non-biological plausibility of the feedback, the effectiveness of the nature of the feedback during robotic therapy (continuous or delayed) remains an open question.

In conclusion, results from healthy adult subjects support the hypothesis of the appropriateness of the visual feedback provided to patients during robotic

treatment. The selected fMRI task contributes to highlight the potential of fMRI in improving the understanding of motor processes and may result useful in detecting the neuronal plasticity that could be associated with robotic treatment. What is expected is a reorganisation of the described areas after the administration of intensive robotic training. However, due to the nature of the task, this study does not take into account some relevant contributions which affect motor control such as motor learning related to the haptic feedback and the aspects of motor execution provided by robotic training.

4.6 Upper limb robot-mediated therapy and neuroimaging in children with hemiparesis

4.6.1 Design of the study

Thirty pediatric patients will take part in the longitudinal study. Children are randomly assigned to one of two groups of 15 patients. The first group receives RMT treatment, while the second group receives physiotherapy comparable for frequency and intensity with RMT. Both therapies involve one hour daily sessions and last for 4 weeks.

4.6.1.1 Inclusion criteria

Recruited children must meet the following inclusion criteria: congenital or acquired, mild to moderate upper extremity hemiparesis; age between 6 and 12 years; time interval from the acute event > 6 months; clinically stable and able to participate in a robotic therapy program; modified Ashworth scale ≤ 3

for each upper limb segment; passive range of motion > 120° for shoulder flexion and abduction, < 90° for elbow flexion, and > 150° for elbow extension; absence of visual acuity deficits or visual field defects; cognitive level within the normal range, borderline or mild mental retardation (as measured by the Wechsler Intelligence Scale for Children - III); attention strategies, executive functions and language abilities must be adequate to understand and to perform the required tasks. Patients undergoing pharmacological treatment for muscle spasticity (e.g., botulinum toxin) or who had previously been treated with RMT are excluded from the study.

4.6.1.2 Subjects assessment

All patients are assessed, at the enrolment and completion of the rehabilitation treatment, according to protocols based on standardised clinical scales, measurements provided by the InMotion2 robotic device, behavioural tasks, and MRI exam.

The clinical evaluations include (Frascarelli et al., 2009, Eur J Phys Rehabil Med; Frascarelli et al., 2009, J Rehabil Med) the modified Ashworth scale (to rate muscle spasticity), the passive range of motion measurement of shoulder, elbow and wrist, the Melbourne assessment of unilateral upper limb (to measure unilateral upper extremity quality of movement in children), the Fugl-Meyer assessment of upper extremity function (to measure upper limb motor functionality in daily life activities), and the Parent's Questionnaire (to evaluate acceptability and estimate how the child uses his weaker arm in daily life activities).

Robot measures include average speed (i.e., value of the end-point velocity), maximum lateral deviation (i.e., the leftward and rightward lateral deviations from the straight line that connects the initial position to the target),

and average of the jerk (i.e., the average amplitude of the rate of change of acceleration divided by the average speed) over the duration of the movement. The latter parameter is a measure of movement smoothness, which is the result of the physiologic control of movement (Chang et al., 2004) and was proven to be an useful index for the characterisation of the quality of patient's motor performance (Frascarelli et al., 2009, Eur J Phys Rehabil Med). A movement is assumed to begin when speed becomes greater than 10 mm/s for more than 100 ms and is assumed to end when the position of the handle is within 1 cm radius from the target for more than 100 ms.

Furthermore, a neuropsychological assessment is performed, consisting in the evaluation of the following tasks: the Tower of London task (for motor planning and execution), the Benton test (for visuo-spatial abilities), Wisc-III cubes (for visuo-spatial and prassic abilities), the CPT-II (Conners' Continuous Performance Test II, for sustained attention), and the subtest for visuo-spatial relationships of the TVPS (Test of Visual Perceptual Skills).

Finally, the neuroimaging assessment is performed by means of the neuroimaging protocol described in Section 4.6.1.4. Besides being used during the fMRI exam, the task described in Section 4.5.2 is also administered by means of a desktop PC to measure to the subjects' performance (accuracy of responses and reaction times).

4.6.1.3 Rehabilitative training

The RMT with the InMotion2 robot, administered to a group of 15 children, consists in 4 weeks of one hour daily sessions of a visually-guided, goal-directed planar reaching task. Eight targets are equally spaced around a centre target and visual feedback of both target and robot handle locations are provided on a computer screen in front of the child. The task requires each

subject to attempt to move from the centre position to a target and then return to the centre (Frascarelli et al., 2009, Eur J Phys Rehabil Med). Target locations are randomised with each of the eight possible positions presented an equal number of times. The goal is to increase the child's attention by avoiding mnemonic schemes of target presentation. Each robotic session is composed of one active batch at the beginning and one at the end of the session (consisting in 80 point-to-point reaching movements each) and by four robot-assisted batches (320 point-to-point reaching movements each). The active mode implies that the robot provides no assistance during the task, so that the child must move the low inertia, low friction robotic arm to the target.

Similarly to RMT, traditional rehabilitation is administered to a group of 15 children and consists in 4 weeks of one hour daily sessions of intensive training. Given that the goal of the research is to compare the effectiveness of RMT to the most effective traditional rehabilitation program for each patient, subject-specific upper limb training programs are planned, consisting in reaching and grasping tasks administered by a physiotherapist.

4.6.1.4 Neuroimaging assessment protocol

As stated above, at the enrolment and completion of the rehabilitation treatment subjects undergo an MRI exam to objectively investigate the therapy-induced (i.e., pre-treatment vs. post-treatment) anatomical and functional neuroplasticity. Preliminary diagnostic exams are performed at the enrolment in a separate MRI session. All scans are performed on the 1.5 T scanner of the Imaging Department of Palidoro at Bambino Gesù Children's Hospital.

A 3D T1-weighted anatomical scan covering the entire head is acquired for VBM analyses. The following parameters are used: TR = 25.0 ms; TE = 4.60

ms; flip angle = 30°; field of view 240x160x240; reconstruction matrix = 256x160x256; voxel size = 0.94x1.00x0.94 mm.

The analysis of functional plasticity is focussed on the study of fMRI data gathered through the administration of specific experimental tasks. A concern sometimes raised in relation to rehabilitation is that gains achieved during therapy incompletely generalise to the range of demands faced in real-world tasks. Findings from a previous study (Takahashi et al., 2008) suggest that treatment-induced cortical reorganisation can be specific to the practiced task. In other words, given that therapy-related gains are achieved on the basis of brain plasticity (Hodics et al., 2006), a highly standardised therapy such as RMT may induce a cortical reorganisation associated to the specific content of treatment but, in the absence of generalisation, not to a separate motor task that was not part of therapy. Therefore, several tasks have been proposed for this study to assess functional improvements in both motor output and higher level cognitive aspects of action performance, such as motor planning and control.

In a hand motor task, patients are asked to perform simple hand movements. This task allows evaluating the broad impact, if any, of upper limb RMT to planning, control and execution of fingers movements. Two T2*-weighted EPI sequences are acquired, with the imaging parameters described in Section 4.5.2.1 and with 120 dynamic scans for each sequence (duration: 5’15”). In the first sequence, the subject is asked to repeatedly open and close the healthy hand in a 30” task block, alternating with 30” rest. The second sequence is the same as the first one, but the movement must be performed with the paretic hand.

In the movement congruence task described in Section 4.5.2, a series of video recordings of movements of the upper limb during the RMT training session with the InMotion2 robot are presented to patients, together with a representation of the corresponding visual feedback provided by the robot. This

visual task allows evaluating the impact of therapy on the cerebral activity patterns associated with observation, analysis and representation of movements.

Finally, a computerised version of the Tower of London task (described in Section 3.2.2) was proposed to evaluate the effect of the therapy, if any, on executive functions. However, the hypothesis of using this further task was discarded to avoid excessive scan time.

The total scan time for the MRI protocol with the T1 sequence, the hand motor task (2 runs) and the movement congruence task (4 runs) is 42'15". All the visual and auditory stimulus sequences for the fMRI tasks were implemented in the STIM2 software. The NordicNeuroLab MR-compatible stimulation system is used to deliver synchronous exogenous stimuli. Visual stimuli are delivered with MR-compatible goggles, which are a suitable tool for administering stimuli to children inside an MRI scanner, since they present the advantage of avoiding distractions from the environment and of allowing a quick vision correction. Subjects are specifically trained for the tasks before each fMRI exam.

4.6.2 Preliminary results

Only very preliminary results are presented for this study, due to the effort required by the training protocol (lasting 4 weeks for each subject), which requires dedicated rehabilitators.

VBM analyses cannot provide reliable inferences unless sufficiently large groups of patients are analysed (Nocchi et al., 2008, IFMBE Proceedings; Nocchi et al., 2008, OHBM Meeting). Therefore, no result on anatomical plasticity will be presented. Study-specific *a priori* probability maps and a customised T1 template will be created at completion of enrolment. Subsequently, individual images will be processed and a statistical analysis will

be carried out. Furthermore, the evaluation of global GM changes will be performed, together with the analysis of regional GM volumes and of the correlations between GM and clinical parameters.

As for fMRI, it is well evident from Figure 4.6, showing results of the hand motor task performed by a single subject with the healthy hand, that abnormalities in brains of hemiparetic children can lead to difficulties in interpreting the activation maps.

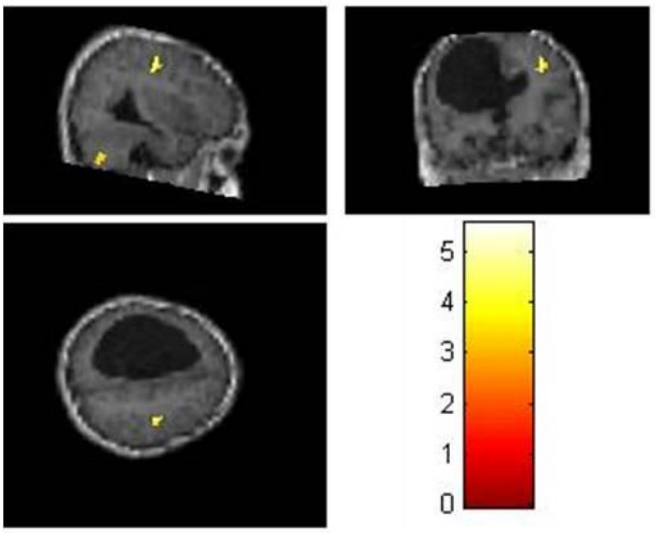

Figure 4.6 – Statistical parametric map for the hand motor task performed by a single subject with the healthy (left) hand (t-test without correction for multiple comparisons, $p<0.001$ at voxel-level, $T = 3.17$).

Figure 4.7 compares head rotation estimates for the hand motor task to the same estimates for the movement congruence task, thus illustrating how excessive head movement can represent a serious problem when the task requires movements of an impaired child. This should make it clear why, to study higher cognitive motor functions, a visual task was preferred to a motor task and motor responses from the subject were avoided. Therefore, as with all fMRI studies of movement in patients with significant motor deficits, the results need to be interpreted with caution given the occurrence of occasional movements (Takahashi et al., 2008).

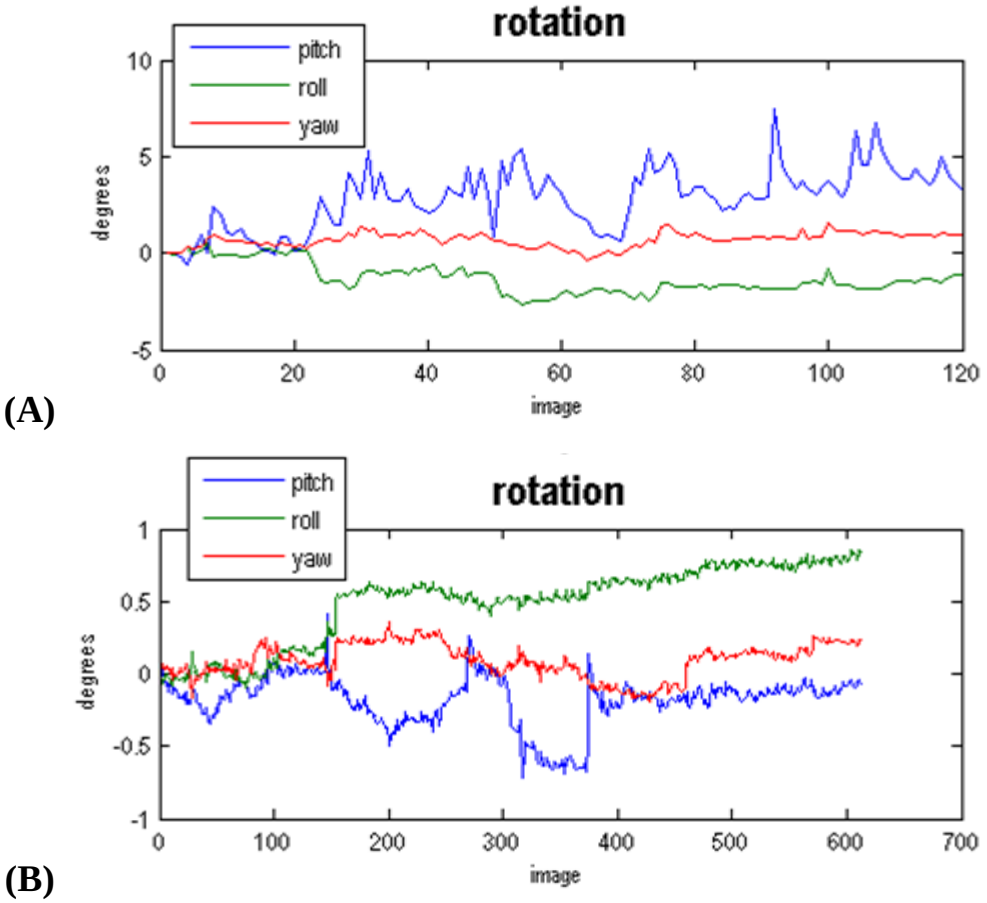

Figure 4.7 – Estimate of head rotations during (A) the hand motor task performed by a hemiparetic patient with the healthy hand and (B) the movement congruence task performed by the same subject. A large rotation of patient's head is estimated for the hand motor task, in which the subject is required to move either the healthy or the impaired hand.

Pre- and post-training activations for the hand motor task with the paretic limb are compared in Figure 4.8. Only the post-training map shows activations that can be ascribed to the contralateral pre-central gyrus and to the basal ganglia.

Contrasts between regressors for the movement congruence task administered to hemiparetic children are listed in Table 4.3. With respect to the analysis described in Section 4.5.2.2, to allow a separate analysis for both the healthy and the paretic limb, the AM regressor was split in a regressor for the observation of a left arm movement (LAM) and a regressor for the observation

of a right arm movement (RAM). Similarly, the event types "presentation of a congruent target point following an arm movement" and "presentation of an incongruent target point following an arm movement" were split in the corresponding events types for the left and right arm and represented by the LAMCT, RAMCT, LAMIT, and RAMIT regressors, respectively.

Results of the movement congruence task for the observation and representation of right arm movements by a child with right hemiparesis are shown in Figure 4.9. Although results show that, following RMT, significant activations can be found, in hemiparetic patients, in brain regions that are involved in movement function, further research is needed to confirm these very preliminary findings.

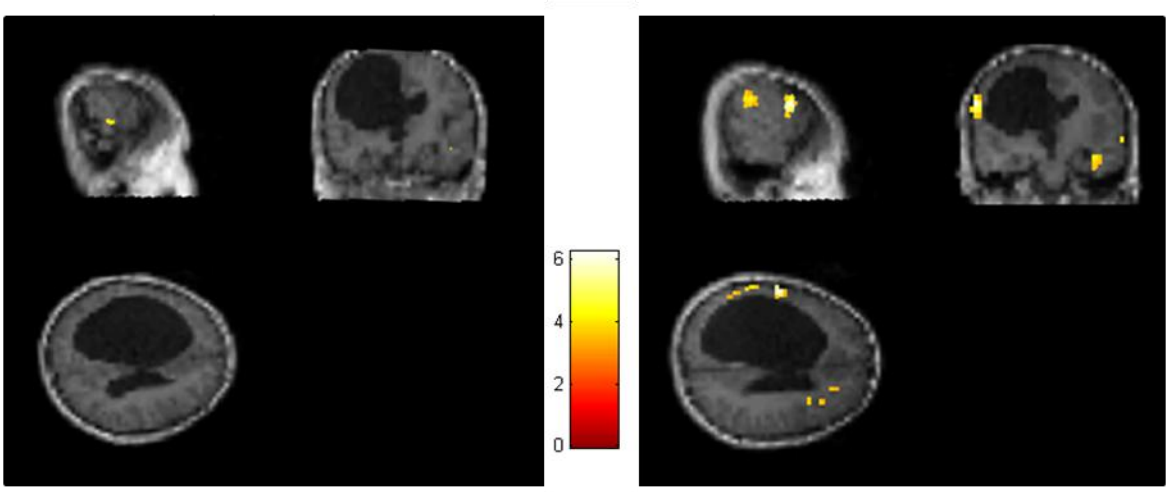

(A) **(B)**

Figure 4.8 – Statistical parametric maps for the hand motor task performed by a single subject with the impaired (right) hand (t-test without correction for multiple comparisons, $p<0.001$ at voxel-level, $T = 3.17$). (A) Pre-training scan; (B) post-training scan. Only the post-training SPM shows activations that can be ascribed to the motor area contralateral to the paretic limb.

Contrast†	LAM	RAM	DT	LAMCT	RAMCT	DTCT	LAMIT	RAMIT	DTIT	M1	M2	M3	M4	M5	M6
AM	1	1	0	0	0	0	0	0	0	0	0	0	0	0	0
DT	0	0	1	0	0	0	0	0	0	0	0	0	0	0	0
LAM	1	0	0	0	0	0	0	0	0	0	0	0	0	0	0
RAM	0	1	0	0	0	0	0	0	0	0	0	0	0	0	0
AM > DT	1	1	-2	0	0	0	0	0	0	0	0	0	0	0	0
DT > AM	-1	-1	2	0	0	0	0	0	0	0	0	0	0	0	0
LAM > DT	1	0	-1	0	0	0	0	0	0	0	0	0	0	0	0
RAM > DT	0	1	-1	0	0	0	0	0	0	0	0	0	0	0	0
AMT	0	0	0	1	1	0	1	1	0	0	0	0	0	0	0
DTT	0	0	0	0	0	1	0	0	1	0	0	0	0	0	0
LAMT	0	0	0	1	0	0	1	0	0	0	0	0	0	0	0
RAMT	0	0	0	0	1	0	0	1	0	0	0	0	0	0	0
AMT > DTT	0	0	0	1	1	-2	1	1	-2	0	0	0	0	0	0
DTT > AMT	0	0	0	-1	-1	2	-1	-1	2	0	0	0	0	0	0
LAMT > DTT	0	0	0	1	0	-1	1	0	-1	0	0	0	0	0	0
RAMT > DTT	0	0	0	0	1	-1	0	1	-1	0	0	0	0	0	0
CT > IT	0	0	0	1	1	1	-1	-1	-1	0	0	0	0	0	0
IT > CT	0	0	0	-1	-1	-1	1	1	1	0	0	0	0	0	0
AMCT	0	0	0	1	1	0	0	0	0	0	0	0	0	0	0
AMIT	0	0	0	0	0	0	1	1	0	0	0	0	0	0	0
DTCT	0	0	0	0	0	1	0	0	0	0	0	0	0	0	0
DTIT	0	0	0	0	0	0	0	0	1	0	0	0	0	0	0
LAMCT	0	0	0	1	0	0	0	0	0	0	0	0	0	0	0
LAMIT	0	0	0	0	0	0	1	0	0	0	0	0	0	0	0
RAMCT	0	0	0	0	1	0	0	0	0	0	0	0	0	0	0
RAMIT	0	0	0	0	0	0	0	1	0	0	0	0	0	0	0
AMCT > AMIT	0	0	0	1	1	0	-1	-1	0	0	0	0	0	0	0
AMIT > AMCT	0	0	0	-1	-1	0	1	1	0	0	0	0	0	0	0
DTCT > DTIT	0	0	0	0	0	1	0	0	-1	0	0	0	0	0	0
DTIT > DTCT	0	0	0	0	0	-1	0	0	1	0	0	0	0	0	0
LAMCT > LAMIT	0	0	0	1	0	0	-1	0	0	0	0	0	0	0	0
LAMIT > LAMCT	0	0	0	-1	0	0	1	0	0	0	0	0	0	0	0
RAMCT > RAMIT	0	0	0	0	1	0	0	-1	0	0	0	0	0	0	0
RAMIT > RAMCT	0	0	0	0	-1	0	0	1	0	0	0	0	0	0	0

Table 4.3 – Contrast vectors used in the movement congruence visual task. †**AM** = arm movement; **DT** = dot trajectory; **LAM** = left arm movement; **RAM** = right arm movement; **AMT** = presentation of the target following an AM; **DTT** = presentation of the target following a DT; **LAMT** = presentation of the target following a LAM; **RAMT** = presentation of the target following a RAM; **CT** = presentation of a congruent target; **IT** = presentation of an incongruent target; **AMCT** = presentation of a congruent target following an AM; **AMIT** = presentation of an incongruent target following an AM; **DTCT** = presentation of a congruent target following a DT; **DTIT** = presentation of an incongruent target following a DT; **LAMCT** = presentation of a congruent target following a LAM; **LAMIT** = presentation of an incongruent target following a LAM; **RAMCT** = presentation of a congruent target following a RAM; **RAMIT** = presentation of an incongruent target following a LAM.

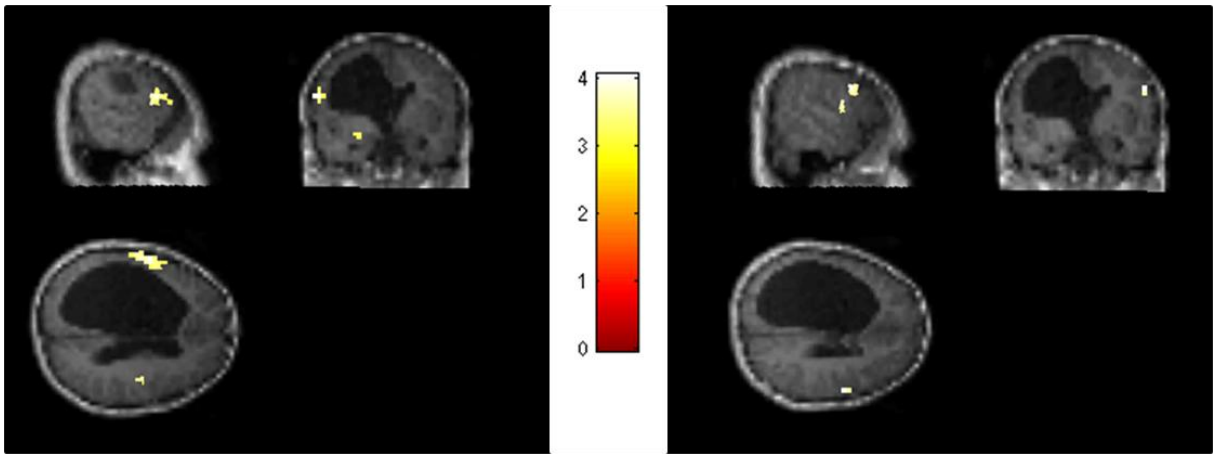

(A) **(B)**

Figure 4.9 – Statistical parametric maps for the movement congruence task performed by a patient with right hemiparesis (t-test without correction for multiple comparisons, $p<0.001$ at voxel-level, $T = 3.11$). (A) Observation of right arm movements; (B) representation of right arm movements and congruence analysis (see Section 4.5 for a detailed description of the task). The analogous pre-training SPMs did not show significant activations in corresponding brain areas.

CONCLUSIONS

Two MR neuroimaging techniques were applied in the present work: VBM was used to investigate the anatomical correlates of pathologic conditions in adolescent patients, while fMRI was mainly applied to study brain function in healthy adult subjects in order to set up experimental protocols for subsequent application in pediatric patients. Investigations in the field of computational neuroimaging at Bambino Gesù Children's Hospital only started in the last few years. Experience was limited to diffusion tensor imaging (DTI) and no study with VBM, nor with fMRI had been carried out acquiring and processing data at the hospital.

The methodological issue of the number of subjects that should be included in VBM studies was addressed. A simulation analysis was carried out to investigate the effects of including outliers (i.e., subjects that have different anatomical characteristics from the group to which they belong) and to assess to what extent the identified inter-group neuroanatomical differences can be considered reliable when analysing small samples with VBM. The study was aimed at providing the clinicians with a support tool for driving the recruiting process which, particularly in pediatric trials, may take several months or even years. The results yielded by the simulations confirm that the number of subjects is a critical aspect to consider while designing a VBM study and that outliers may lead to erroneous inferences in VBM analyses performed on small groups of subjects.

VBM was applied to a clinical study in a group of adolescent patients with anorexia nervosa restrictive type (AN-r). The purpose of the study was to investigate global and local structural grey matter (GM) alterations in a sample of patients with a short illness history. The analyses revealed a significant global GM volume decrease in the AN-r patients; furthermore, a significant region-

specific early decrease in GM was highlighted in brain regions known to participate in mental processes related to the disease, suggesting that there might be a region-specific GM vulnerability that could play a role in the pathophysiology of AN-r and explain the presence of a distorted body image in these patients.

fMRI may be a helpful tool in localising cerebral functions in tissue within or near regions intended for neurosurgical resection of epileptic foci in drug-resistant forms of childhood epilepsy. To identify brain language areas and evaluate their lateralisation, an experimental protocol was designed, consisting in a set of fMRI tasks for pediatric patients, and in a tool for the assessment of functional lateralisation. Although preliminary results on healthy adults need to be confirmed on a large sample of healthy pediatric subjects, they suggest the usefulness of the fMRI experimental protocol, both for a reliable identification of eloquent areas, and to evaluate the lateralisation of language function.

The results of the preliminary study carried out to set up the simultaneous EEG-fMRI acquisition technique show that the quality of acquired EEG signals can be adequate for clinical analysis and the quality of fMRI images can be fully preserved. However, wearing the standard EEG caps used for EEG-fMRI recordings may be particularly problematic in children. Therefore, the use of a reduced set of electrodes was explored. Results suggest that this approach could be useful when the main interest is in detecting when an epileptic spike happens and in localising the corresponding ictal *foci* with fMRI.

A research was described, aiming at exploring the effectiveness of motor RMT protocols on the recovery of upper limb deficits in children affected by congenital or acquired hemiparesis. VBM and fMRI are used in a longitudinal design to detect potential anatomical and functional cerebral plasticity induced by rehabilitation training (both with RMT and traditional therapy). The final goal of this research is to identify integrated evaluation protocols in order to obtain indications on the most effective rehabilitation therapy for children with

hemiparesis based on clinical evidence. Only very preliminary results could be obtained, due to the effort required by the training protocol. However, a preliminary study was performed on healthy adult subjects. An fMRI task was used to investigate the neuronal activation patterns associated with processing of both human upper limb and abstract object movements similar to those implicated in robotic training and to assess the brain's ability to assimilate abstract movements to motor gestures. Results support the hypothesis of appropriateness of the non-biological visual feedback provided to patients during robotic rehabilitation. The fMRI task contributes to highlight the potential of fMRI in improving the understanding of motor processes. However, due to the nature of the task, this study does not take into account some relevant contributions which affect motor control such as motor learning related to the haptic feedback and the aspects of motor execution provided by robotic training.

In conclusion, the research done has allowed exploring several approaches to study brain anatomy and function and to apply them in different fields of pediatric neuroimaging.

LIST OF ABBREVIATIONS

- AAL: automatic anatomical labelling
- AM: arm movement
- AMCT: presentation of a congruent target following an arm movement
- AMIT: presentation of an incongruent target following an arm movement
- AMT: presentation of the target following an arm movement
- AN: anorexia nervosa
- AN-b/p: anorexia nervosa binge/purging type
- ANCOVA: analysis of covariance
- AN-r: anorexia nervosa restrictive type
- BA: Brodmann area
- BCG: ballistocardiogram artefact
- BMI: body mass index
- BOLD: blood oxygen level dependent signal/contrast
- CDI: Children's Depression Inventory
- $CMRO_2$: cerebral metabolic rate of oxygen extraction
- CS: control subjects (Chapter 2)
- CS: cue stimulus (Chapter 3)
- CSF: cerebrospinal fluid
- CT: Computed Tomography (Chapter 1)
- CT: presentation of a congruent target (Chapter 4)
- DCT: discrete cosine transform
- DT: dot trajectory
- DTCT: presentation of a congruent target following a dot trajectory
- DTI: diffusion tensor imaging
- DTIT: presentation of an incongruent target following a dot trajectory
- DTT: presentation of the target following a dot trajectory
- DWI: diffusion-weighted imaging
- EAT: Eating Attitudes Test

- ED: eating disorders
- EEG: electroencephalography
- EPI: echo planar imaging
- ERP: event-related potential
- FWE: family-wise error
- FDR: false discovery rate
- FID: free induction decay
- fMRI: functional magnetic resonance imaging
- FWHM: full-width at half maximum
- GLM: general linear model
- GM: grey matter
- GRE: gradient echo
- HP: haloperidol patients
- HRF: haemodynamic response function
- IB: implicit baseline
- ICA: independent component analysis
- ICBM: International Consortium for Brain Mapping
- IR: Inversion-recovery
- IS: instruction stimulus
- IT: presentation of an incongruent target
- LAM = left arm movement
- LAMCT = presentation of a congruent target following a left arm movement
- LAMIT = presentation of an incongruent target following a left arm movement
- LAMT = presentation of the target following a left arm movement
- LI: lateralisation index
- MEG: magnetoencefalography
- MNI: Montréal Neurological Institute
- MPRAGE: magnetisation prepared rapid acquisition gradient echo
- MRI: magnetic resonance imaging
- MSR: most significant region
- NHP: non-haloperidol patients

- NM: nuclear medicine
- NMR: nuclear magnetic resonance
- PET: positron-emission tomography
- RAM = right arm movement
- RAMCT = presentation of a congruent target following a right arm movement
- RAMIT = presentation of an incongruent target following a right arm movement
- RAMT = presentation of the target following a right arm movement
- rCBF: regional cerebral blood flow
- RF: radio frequency
- RMT: robot-mediated therapy
- ROI: region-of-interest
- SE: spin echo
- SNR: signal to noise ratio
- SPECT: single-photon-emission computed tomography
- SPM: Statistical Parametric Mapping
- TE: echo time
- TI: inversion time
- TIV: total intracranial volume
- TMS: transcranial magnetic stimulation
- TOL: Tower of London task
- TR: repetition time
- VBM: voxel-based morphometry
- VEP: visual evoked potential
- WM: white matter

REFERENCES

1. Adamovich SV, Fluet GG, Tunik E, Merians AS - *Sensorimotor training in virtual reality: a review.* - NeuroRehabilitation 2009;25:29-44.
2. Allen PJ, Josephs O, Turner R - *A method for removing artefact from continuous EEG recorded during functional MRI* - NeuroImage 2000;12(2):230-9.
3. Ashburner J - *A fast diffeomorphic image registration algorithm* - NeuroImage 2007;38(1):95-113.
4. Ashburner J - *Computational anatomy with the SPM software.* - Magnetic Resonance Imaging 2009;27:1163-1174.
5. Ashburner J, Friston KJ - *Nonlinear spatial normalization using basis functions.* - Human Brain Mapping 1999;7(4):254-266.
6. Ashburner J, Friston KJ - *Voxel-Based Morphometry - The Methods* - NeuroImage 2000;11:805-821.
7. Ashburner J, Friston KJ - *Unified Segmentation.* - NeuroImage 2005;26:839-851.
8. Ashburner J, Neelin P, Collins DL, Evans AC, Friston KJ - *Incorporating prior knowledge into image registration.* – NeuroImage 1997;6:344-352.
9. Barreca S, Wolf SL, Fasoli S, Bohannon R - *Treatment intervention for the paretic upper limb of stroke survivors: a critical review.* - Neuorehabil Neural Repair 2003;17:220-6.
10. Basser PJ, Pierpaoli C - *Microstructural and physiological features of tissues elucidated by quantitative-diffusion-tensor MRI.* - J Magn Reson B 1996;111:209-219.
11. Bax M, Goldstein M, Rosenbaum P, Leviton A, Paneth N, Dan B, Jacobsson B, Damiano D; Executive Committee for the Definition of Cerebral Palsy. - *Proposed definition and classification of cerebral palsy, April 2005.* - Dev Med Child Neurol 2005;47(8):571-6.
12. Becker R, Ritter P, Moosmann M, Villringer A - *Visual Evoked Potentials Recovered From fMRI Scan Periods* - Human Brain Mapping 2005;26:221-230.
13. Belliveau JW, Kennedy DN, McKinstry RC, Buchbinder BR, Weisskoff RM, Cohen MS, Vevea JM, Brady TJ, Rosen BR - *Functional mapping of the human visual cortex by magnetic resonance imaging.* - Science 1991;254(5032):716-719.

14. Binkofski F, Buccino G, Posse S, Seitz RJ, Rizzolatti G, Freund H - *A fronto-parietal circuit for object manipulation in man: evidence from an fMRI-study*. - Eur J Neurosci 1999;11:3276-3286.

15. Bookstein FL - *"Voxel-based morphometry" should not be used with imperfectly registered images.* - Neuroimage 2001;14(6):1454-62.

16. Boyd LA, Vidoni ED, Daly JJ - *Answering the call: the influence of neuroimaging and electrophysiological evidence on rehabilitation.* - Phys Ther. 2007;87(6):684-703.

17. Boyd LA, Vidoni ED, Siengsukon CF, Wessel BD - *Manipulating time-to-plan alters patterns of brain activation during the Fitts' task* - Experimental Brain Research 2009;194(4):527-539.

18. Brochard S, Robertson J, Médée B, Rémy-Néris O - *What's new in new technologies for upper extremity rehabilitation?* - Curr Opin Neurol 2010;23:683-687.

19. Buccino G, Binkofski F, Fink GR, Fadiga L, Fogassi L, Gallese V, Seitz RJ, Zilles K, Rizzolatti G, Freund HJ - *Action observation activates premotor and parietal areas in a somatotopic manner: an fMRI study*. - Eur J Neurosci 2001;13:400-404.

20. Buccino G, Lui F, Canessa N, Patteri I, Lagravinese G, Benuzzi F, Porro CA, Rizzolatti G - *Neural circuits involved in the recognition of actions performed by nonconspecifics: an fMRI study.* - J Cogn Neurosc 2004;16:114-126.

21. Calhoun VD, Adali T, Stevens MC, Kiehl KA, Pekare JJ - *Semi-blind ICA of fMRI: a method for utilizing hypothesis-derived time courses in a spatial ICA analysis* - NeuroImage 2005;25:527-538.

22. Carnì M, Genovese E, Bufalari S, Franchin T, Nocchi F, Cannatà V - *Acquisizione simultanea di segnali EEG ed immagini fMRI: qualità dei dati* - VI Congresso Nazionale dell'Associazione Italiana di Fisica Medica (Reggio Emilia, 16-19 settembre 2009); Vol. 1; Pagg. 126-128.

23. Carnì M, Genovese E, Nocchi F, Bufalari S, Franchin T, Montes M, Cannatà V - *Simultaneous EEG-fMRI recording with a reduced set of electrodes* - 16th Annual Meeting of the Organization for Human Brain Mapping (Barcelona, Spain, June 6-10, 2010).

24. Carr JH, Shepherd RB: eds. Movement Science. - *Foundations for physical therapy in rehabilitation.* - Aspen Publishers, Rockville, MD; 1987.

25. Casadio M, Giannoni P, Masia L, Morasso P, Sandini G, Sanguineti V, Squeri V, Vergaro E - *Robot therapy of the upper limb in stroke patients: preliminary experiences for the principle-based use of this technology.* - Funct Neurol 2009;24:195-202.

26. Castelli E - *Robotic movement therapy in cerebral palsy.* - Dev Med Child Neurol 2011;53:481.
27. Castro-Fornieles J, Bargalló N, Lázaro L, Andrés S, Falcon C, Plana MT, Junqué C - *A cross-sectional and follow-up voxel-based morphometric MRI study in adolescent anorexia nervosa.* - Journal of Psychiatry Research 2009;43:331-340.
28. Cavanna AE, Trimble MR - *The precuneus: a review of its functional anatomy and behavioural correlates.* - Brain 2006;129:564-583.
29. Cavina Pratesi C, Valyear KF, Culham JC, Köhler S, Obhi SS, Marzi CA, Goodale MA - *Dissociating Arbitrary Stimulus-Response Mapping from Movement Planning during Preparatory Period: Evidence from Event-Related Functional Magnetic Resonance Imaging* - The Journal of Neuroscience 2006;26(10):2704-2713.
30. Chang J , Wu T, Wu W, Su F - *Kinematical measure for spastic reaching in children with cerebral palsy.* - Clinical Biomechanics 2004;20(4):381-388.
31. Chevrier AD, Noseworthy MD, Schachar R - *Dissociation of response inhibition and performance monitoring in the stop signal task using event-related fMRI.* - Hum Brain Mapp 2007;28:1347-1358.
32. Chowdhury U, Gordon I, Lask B, Watkins B, Watt H, Christie D - *Early-onset anorexia nervosa: is there evidence of limbic system imbalance?* - International Journal of Eating Disorders 2003;33:388-386.
33. Colombo R, Pisano F, Micera S, Mazzone A, Delconte C, Carrozza MC, Dario P, Minuco G - *Assessing mechanisms of recovery during robot-aided neurorehabilitation of the upper limb.* - Neurorehabil Neural Repair 2008;22(1):50-63.
34. Cope SM, Liu XC, Verber MD, Cayo C, Rao S, Tassone JC - *Upper limb function and brain reorganization after constraint-induced movement therapy in children with hemiplegia.* - Dev Neurorehabil 2010;13:19-30.
35. Costantini M, Galati G, Ferretti A, Caulo M, Tartaro A, Romani GL, Aglioti SM - *Neural systems underlying observation of humanly impossible movements: an FMRI study.* - Cereb Cortex 2005;15:1761-1767.
36. Cunningham CJ, Zaamout Mel-F, Goodyear B, Federico P - *Simultaneous EEG-fMRI in human epilepsy* - Can J Neurol Sci 2008;35(4):420-35.
37. Cunnington R, Windischberger C, Deecke L, Moserc E - *The preparation and readiness for voluntary movement: a high-field event-related fMRI study of the Bereitschafts-BOLD response* - NeuroImage 2003;20:404-412.
38. Dale AM, Fischl B, Sereno MI - *Cortical surface-based analysis. I: segmentation and surface reconstruction.* - Neuroimage 1999;9:179-194.

39. di Pellegrino G, Fadiga L, Fogassi L, Gallese V, Rizzolatti G - *Understanding motor events: a neurophysiological study.* - Exp Brain Res. 1992;91(1):176-80.

40. Dobkin BH - *Rehabilitation and functional neuroimaging dose response trajectories for clinical trials.* - Neurorehabil Neural Repair 2005;19:276-282.

41. Dolan RJ, Mitchell J, Wakeling A - *Structural brain changes in patients with anorexia nervosa.* - Psychological Medicine 1988;18:349-53.

42. Donaldson DL, Buckner - *Effective paradigm design.* – In Jezzard P, Matthews PM, and Smith SM (Eds.), Functional MRI: An introduction to methods (pp. 177-195). New York: Oxford University Press Inc., 2001.

43. Dong Y, Winstein CJ, Albistegui-DuBois R, Dobkin BH - *Evolution of fMRI Activation in the Perilesional Primary Motor Cortex and Cerebellum With Rehabilitation Training-Related Motor Gains After Stroke: A Pilot Study.* - Neurorehabilitation and Neural Repair 2007;21:412-28.

44. Doraiswamy PM, Krishnan KR, Figiel GS, Husain MM, Boyko OB, Rockwell WJ, Ellinwood EHJ - *A brain magnetic resonance imaging study of pituitary gland morphology in anorexia nervosa and bulimia.* - Biological Psychiatry 1990;28:110-116.

45. Draganski B, Bhatiad KP - *Brain structure in movement disorders: a neuroimaging perspective* - Current Opinion in Neurology 2010;23:413-419.

46. Draganski B, Gaser C, Busch V, Schuierer G, Bogdahn U, May A - *Neuroplasticity: changes in grey matter induced by training.* - Nature 2004;427:311-2.

47. Draganski B, Moser T, Lummel N, Ganssbauer S, Bogdahn U, Haas F, May A - *Decrease of thalamic gray matter following limb amputation.* – Neuroimage 2006;31:951-957.

48. Engel A, Burke M, Fiehler K, Bien S, Rosler F - *How moving objects become animated: The human mirror neuron system assimilates non-biological movement patterns.* - Soc Neurosci 2008;3:368-387.

49. Ertelt D, Small S, Solodkin A, Dettmers C, McNamara A, Binkofski F, Buccino G - *Action observation has a positive impact on rehabilitation of motor deficits after stroke.* - Neuroimage 2007;36(Suppl 2):164-173.

50. Fasoli SE, Fragala-Pinkham M, Hughes R, Hogan N, Krebs HI, Stein J - *Upper limb robotic therapy for children with hemiplegia.* - Am J Phys Med Rehabil 2008;87:929-936.

51. Fasoli SE, Krebs HI, Stein J, Frontera WR, Hogan N - *Effects of robotic therapy on motor impairment and recovery in chronic stroke.* - Arch Phys Med Rehabil 2003;84(4):477-82.
52. Fasoli SE, Krebs HI, Stein J, Frontera WR, Hughes R, Hogan N - *Robotic therapy for chronic motor impairments after stroke: Follow-up results.* - Archives of Physical Medicine and Rehabilitation 2004;85(7):1106-1111.
53. Ferraro M, Palazzolo JJ, Krol J, Krebs HI, Hogan N, Volpe BT - *Robot-aided sensorimotor arm training improves outcome in patients with chronic stroke.* – Neurology 2003;61(11):1604-7.
54. First MB, Gibbon M, Spitzer RL, Williams JBW, Smith Benjamin L - *Structured Clinical Interview for DSM-IV Axis II Disorders.* - Washington, DC: American Psychiatric Association, 1997.
55. Forman SD, Cohen JD, Fitzgerald M, Eddy WF, Mintun MA, Noll DC - *Improved assessment of significant activation in functional magnetic resonance imaging (fMRI): Use of a cluster-size threshold.* - Magn Reson Med 1995;33:636-647.
56. Frackowiak RSJ, Friston KJ, Frith C, Dolan R, Price CJ, Zeki S, Ashburner J, and Penny WD - *Human brain function 2nd ed.* - San Diego: Academic Press, 2004.
57. Franceschini M, Agosti M, Cantagallo A, Sale P, Mancuso M, Buccino G - *Mirror neurons: action observation treatment as a tool in stroke rehabilitation.* - Eur J Phys Rehabil Med 2010;46:517-523.
58. Frascarelli F, Masia L, Di Rosa G, Cappa P, Petrarca M, Castelli E, Krebs HI - *The impact of robotic rehabilitation in children with acquired or congenital movement disorders.* - Eur J Phys Rehabil Med 2009;45:135-141.
59. Frascarelli F, Masia L, Di Rosa G, Petrarca M, Cappa P, Castelli E - *Robot-mediated and clinical scales evaluation after upper limb Botulinum Toxin type A injection in hemiparetic children* - J Rehabil Med 2009:41(12):988-94.
60. Friston KJ, Ashburner J, Frith C, Poline JB, Heather JD, Frackowiak RSJ - *Spatial Registration and Normalization of Images.* - Human Brain Mapping 1995;2:165-189.
61. Friston KJ, Holmes AP, Worsley KJ. - *How many subjects constitute a study?* - Neuroimage 1999;10:1-5.
62. Friston KJ, Holmes AP, Worsley KJ, Poline JP, Frith CD, Frackowiak RSJ - *Statistical parametric maps in functional imaging: A general linear approach.* - Human Brain Mapping 1995;2:189-210.

63. Gallese V, Fadiga L, Fogassi L, Rizzolatti G - *Action recognition in the premotor cortex.* – Brain 1996;119(Pt 2):593-609.

64. Garner DM, Olmsted MP, Bohr Y, Garfinkel PE - *The eating attitudes test: psychometric features and clinical correlates.* - Psychological Medicine 1982;12:871-8.

65. Gaser C, Schlaug G - *Brain structures differ between musicians and non-musicians.* - J Neurosci 2003;23:9240-9245.

66. Gaudio S, Franchin T, Nocchi F, Genovese E, Cannatà V, Longo D, Vicari S, Fariello G - *Region-Specific Gray Matter Decrease in Adolescents with Anorexia Nervosa* - XIV World Congress of Psychiatry (Praga, Czech Republic, September 20-25, 2008).

67. Gaudio S, Nocchi F, Franchin T, Genovese E, Cannatà V, Longo D, Fariello G - *Gray matter changes in adolescents with Anorexia Nervosa restrictive type: a Voxel-Based Morphometry study* - The World Journal of Biological Psychiatry 2009;10(Suppl. 1):115.

68. Gaudio S, Nocchi F, Franchin T, Genovese E, Cannatà V, Longo D, Fariello G - *Gray matter decrease distribution in the early stages of anorexia nervosa restrictive type in adolescents Psychiatry Research: Neuroimaging* - Psychiatry Res. 2011;191(1):24-30.

69. Gauthier LV, Taub E, Perkins C, Ortmann M, Mark VW, Uswatte G - *Remodeling the brain: plastic structural brain changes produced by different motor therapies after stroke.* - Stroke 2008;39(5):1520-5.

70. Gazzola V, Rizzolatti G, Wicker B, Keysers C - *The anthropomorphic brain: the mirror neuron system responds to human and robotic actions.* - NeuroImage 2007;35:1674-1684.

71. Gilbert AR, Keshavan MS, Diwadkar V, Nutche J, MacMaster F, Easter PC, Buhagiar CJ, Rosenberg DR - *Gray matter differences between paediatric obsessive-compulsive disorder patients and high-risk siblings: A preliminary voxel-based morphometry study.* - Neuroscience Letters 2008;435:45-50.

72. Giordano GD, Renzetti P, Parodi RC, Foppiani L, Zandrino F, Giordano G, Sardanelli F - *Volume measurement with magnetic resonance imaging of hippocampus-amygdala formation in patients with anorexia nervosa.* - Journal of Endocrinological Investigation 2001;24:510-514.

73. Giuliani NR, Calhoun VD, Pearlson GD, FrancisA, Buchanan RW - *Voxel-based morphometry versus region of interest: a comparison of two methods for analyzing gray matter differences in schizophrenia* - Schizophrenia Research 2005;74:135-147.

74. Golden NH, Ashtari M, Kohn MR, Patel M, Jacobson MS, Fletcher A, Shenker IR - *Reversibility of cerebral ventricular enlargement in anorexia*

nervosa, demonstrated by quantitative magnetic resonance imaging. - Journal of Pediatrics 1996;128:296-301.

75. Good CD, Johnsrude IS, Ashburner J, Henson RN, Friston KJ, Frackowiak RS - *A voxel-based morphometric study of ageing in 465 normal adult human brains.* - NeuroImage 2001;14:21-36.

76. Goodyear BG, Douglas EA - *Decreasing task-related brain activity over repeated functional MRI scans and sessions with no change in performance: implications for serial investigations.* - Exp Brain Res 2009;192:231-239.

77. Grisolia C, Gazzellini S, Nocchi F, Petrarca M, Cannatà V, Cappa P, D'Alessio T, Castelli E - *An ad hoc fMRI protocol to detect changes in neural activity after an intensive robotic rehabilitative protocol in children with hemiplegia: preliminary application to healthy adult volunteers.* - 23rd Annual Meeting of the European Academy of Childwood Disability (Roma, June 8-11, 2011).

78. Grisolia C, Nocchi F, Gazzellini S, Petrarca M, Cannatà V, Cappa P, Castelli E - *Neuroimaging study of cerebral reorganization induced by robot mediated therapy in children with hemiparesis: protocol development* - XI Congresso Nazionale SIAMOC (Ferrara, 4-7 ottobre 2010).

79. Hanakawa T, Dimyan MA, Hallett M - *Motor Planning, Imagery, and Execution in the Distributed Motor Network: A Time-Course Study with Functional MRI* - Cerebral Cortex 2008;18:2775-2788.

80. Harris EC, Barraclough B - *Excess mortality of mental disorder.* - The British Journal of Psychiatry 1998;173:11-53.

81. Henderson A, Korner-Bitensky N, Levin M - *Virtual reality in stroke rehabilitation: a systematic review of its effectiveness for upper limb motor recovery.* - Top Stroke Rehabil 2007;14:52-61.

82. Hesse MD, Thiel CM, Stephan KE, Fink GR - *The left parietal cortex and motor intention: an event-related functional magnetic resonance imaging study* - Neuroscience 2006;140:1209-1221.

83. Hodics T, Cohen LG, Cramer SC - *Functional imaging of intervention effects in stroke motor rehabilitation.* - Arch Phys Med Rehabil 2006;87(12 Suppl 2):S36-42.

84. Hogan N, Krebs HI, Sharon A, Charnnarong J - *Interactive robotic therapist.* - U.S.Patent. 5, 466, 213, 1995.

85. Holland SK, Plante E, Weber Byars A, Strawsburg RH, Schmithorst VJ, Ball WSJ - *Normal fMRI Brain Activation Patterns in Children Performing a Verb Generation Task* - NeuroImage 2001;14:837-843.

86. Huang VS, Krakauer JW - *Robotic neurorehabilitation: a computational motor learning perspective.* - J Neuroeng Rehabil 2009;6:5.

87. Huettel SA, Song AW, McCarthy G - *Functional Magnetic Resonance Imaging.* - Sinauer Assoc., Sunderland, MA, USA, 2004.

88. Hyvärinen A, Oja E - *Independent component analysis: algorithms and applications* - Neural Networks 2000;13:411-430.

89. Jansen A, Menke R, Sommer J, Förster AF, Bruchmann S, Hempleman J, Weber B, Knecht S - *The assessment of hemispheric lateralization in functional MRI: Robustness and reproducibility* - NeuroImage 2006;33:204-217.

90. Jáuregui-Lobera I - *Neuroimaging in eating disorders* - Neuropsychiatric Disease and Treatment 2011;7:577-584.

91. Jäncke L, Lutz K, Koeneke S - *Converging evidence of ERD/ERS and BOLD responses in motor control research* - Progress in Brain Research 2006;159:261-271.

92. Jeannerod M - *Neural simulation of action: a unifying mechanism for motor cognition.* - Neuroimage 2001;14:S103-9.

93. Jenkins WM, Merzenich MM, Ochs MT, Allard T, Guic-Robles E - *Functional reorganization of primary somatosensory cortex in adult owl monkeys after behaviorally controlled tactile stimulation.* - J Neurophysiol. 1990;63:82-104.

94. Johansen-Berg H, Dawes H, Guy C, Smith SM, Wade DT, Matthews PM - *Correlation between motor improvements and altered fMRI activity after rehabilitative therapy.* – Brain 2002;125:2731-2742.

95. Kaelin-Lang A, Luft AR, Sawaki L, Burstein AH, Sohn YH, Cohen LG - *Modulation of human corticomotor excitability by somatosensory input.* - J Physiol 2002;540(Pt 2):623-33.

96. Kahn LE, Zygman ML, Rymer WZ, Reinkensmeyer DJ - *Robot-assisted reaching exercise promotes arm movement recovery in chronic hemiparetic stroke: a randomized controlled pilot study.* - J Neuroeng Rehabil 2006;3:12.

97. Kan P, Huq R, Hoey J, Goetschalckx R, Mihailidis A - *The development of an adaptive upper-limb stroke rehabilitation robotic system.* - J Neuroeng Rehabil 2011;8:33.

98. Karakaş HM, Karakaş S, Ozkan Ceylan A, Tali ET - *Recording event-related activity under hostile magnetic resonance environment: Is multimodal EEG/ERP-MRI recording possible?* - International Journal of Psychophysiology 2009;73:123-132.

99. Katzman DK, Lambe EK, Mikulis DJ, Ridgley JN, Goldbloom SD, Zipursky RB - *Cerebral gray matter and white matter volume deficits in adolescent girls with anorexia nervosa.* - Journal of Pediatrics 1996;129:794-803.

100. Katzman DK, Zipursky RB, Lambe EK, Mikulis DJ - *A longitudinal magnetic resonance imaging study of brain changes in adolescents with anorexia nervosa.* - Archives of Pediatrics and Adolescent Medicine 1997;151:793-797.

101. Keller SS, Wilke M, Wieshmann UC, Sluming VA, Roberts N - *Comparison of standard and optimized voxel-based Morphometry for analysis of brain changes associated with temporal lobe epilepsy.* - NeuroImage 2004;23:860-868.

102. Kemmotsu N, Villalobos ME, Gaffrey MS, Courchesne E, Müller RA - *Activity and functional connectivity of inferior frontal cortex associated with response conflict.* - Brain Res Cogn Brain Res 2005;24:335-342.

103. Kohlmeyer K, Lehmkuhl G, Poutska F - *Computed tomography of anorexia nervosa.* - American Journal of Neuroradiology 1983;4:437-438.

104. Kohn MR, Ashtari M, Golden NH, Schebendach J, Patel M, Jacobson MS, Shenker IR - *Structural brain changes and malnutrition in anorexia nervosa.* - Annals of New York Academy Science 1997;817:398-399.

105. Kojima S, Nagai N, Nakabeppu Y, Muranaga T, Deguchi D, Nakajo M, Masuda A, Nozoe S, Naruo T - *Comparison of regional cerebral blood flow in patients with anorexia nervosa before and after weight gain*. - Psychiatry Research 2005;140:251-258.

106. Kollias SS, Alkadhi H, Jaermann T, Crelier G, Hepp-Reymond MC - *Identification of multiple nonprimary motor cortical areas with simple movements.* - Brain Research Reviews 2001;36:185-195.

107. Kovacs M - *The Children's Depression Inventory (CDI).* - Firenze: Organizzazioni Speciali Firenze, 1988.

108. Krebs HI, Hogan N, Aisen ML, Volpe BT - *Robot-aided neurorehabilitation.* - IEEE Trans Rehabil Eng 1998;6:75-87.

109. Krebs HI, Hogan N, Volpe BT, Aisen ML, Edelstein L, Diels C - *Overview of clinical trials with MIT-MANUS: a robot-aided neuro-rehabilitation facility.* - Technol Health Care 1999;7: 419-23.

110. Krebs HI, Mernoff S, Fasoli SE, Hughes R, Stein J, Hogan N - *Transport of the arm and manipulation of objects in chronic stroke: a pilot study* - NeuroRehabilitation 2008;23:81-87.

111. Krieg JC, Pirke KM, Lauer C, Backmund H - *Endocrine, metabolic, and cranial computed tomographic findings in AN.* - Biological Psychiatry 1988;23:377-387.

112. Kuzniecky RI, Jackson GD - *Magnetic Resonance in Epilepsy (Second Edition)* - Elsevier, 2005.

113. Kübler A, Dixon V, Garavan H - *Automaticity and reestablishment of executive control-an fMRI study.* - J Cogn Neurosci 2006;18:1331-1342.

114. Kwakkel G, Kollen BJ, Krebs HI - *Effects of robot-assisted therapy on upper limb recovery after stroke: a systematic review.* - Neurorehabil Neural Repair 2008;22:111-121.

115. Lai JC, Woo J, Hui E, Chan WM - *Telerehabilitation – a new model for community-based stroke rehabilitation.* - J Telemed Telecare 2004;10:199-205.

116. Lambe EK, Katzman DK, Mikulis DJ, Kennedy SH, Zipursky RB - *Cerebral gray matter volume deficits after weight recovery from anorexia nervosa.* - Archives of General Psychiatry 1997;54:537-542.

117. Laufs H, Daunizeau J, Carmichael DW, and Kleinschmidt A - *Recent advances in recording electrophysiological data simultaneously with magnetic resonance imaging* - NeuroImage 2008;40(2):515-28.

118. Le Bihan D, Mangin JF, Poupon C, Clark CA, Pappata S, Molko N, Chabriat H - *Diffusion Tensor Imaging: Concepts and Applications* - Journal of Magnetic Resonance Imaging 2001;13:534-546.

119. Lemieux L, Allen PJ, Franconi F, Symms MR, Fish DR - *Recording of EEG during fMRI experiments: Patient safety* - Magnetic Resonance in Medicine 1997;38(6):943-952.

120. Liégeois F, Connelly A, Salmond CH, Gadian DG, Vargha-Khadem F, Baldeweg T - *A Direct Test for Lateralization of Language Activation using fMRI: Comparison with Invasive Assessments in Children with Epilepsy* - NeuroImage 2002;17:1861-1867.

121. Lo AL, Guarino PD, Richards LG, Haselkorn JK, Wittenberg GF, Federman DG, Ringer RJ, Wagner TH, Krebs HI, Volpe BT, Bever CT Jr, Bravata DM, Duncan PW, Corn BH, Maffucci AD, Nadeau SE, Conroy SS, Powell JM, Huang GD, Peduzzi P - *Robot-assisted therapy for long-term upper-limb impairment after stroke.* - The New England Journal of Medicine 2010;362(19):1772-83.

122. Logothetis NK - *What we can do and what we cannot do with fMRI* – Nature 2008;453.

123. Longo D, Gaudio S, Franchin T, Nocchi F, Genovese E, Cannatà V, Delfino L, Vicari S, Fariello G - *Anorexia Nervosa: a Voxel Based*

Morphometry (VBM) Study in Adolescents with the Restrictive Type - IX Congresso Nazionale di Neuroradiologia Pediatrica (Catania, 12-14 giugno 2008).

124. Lotze M, Braun C, Birbaumer N, Anders S, Cohen L - *Motor learning elicited by voluntary drive.* - Brain 2003;126:866-72.
125. Lotze M, Markert J, Sauseng P, Hoppe J, Plewnia C, Gerloff C - *The role of multiple contralesional motor areas for complex hand movements after internal capsular lesion.* - J Neurosci 2006;26:6096-6102.
126. Lucas AR, Crowson CS, O'Fallon WM, Melton LJ III. - *The ups and downs of Anorexia Nervosa.* - International Journal of Eating Disorders 1999;26:397-405.
127. Luke LM, Allred RP, Jones TA - *Unilateral ischemic sensorimotor cortical damage induces contralesional synaptogenesis and enhances skilled reaching with the ipsilateral forelimb in adult male rats.* - Synapse 2004;54:187-199.
128. Lum PS, Burgar CG, Shor PC, Majmundar M, Van der Loos M - *Robot-assisted movement training compared with conventional therapy techniques for the rehabilitation of upper-limb motor function after stroke.* - Arch Phys Med Rehabil 2002;83:952-9.
129. MacClellan LR, Bradham DD, Whitall J, Volpe B, Wilson PD, Ohlhoff J, Meister C, Hogan N, Krebs HI, Bever CT Jr - *Robotic upper-limb neurorehabilitation in chronic stroke patients.* - Journal of Rehabilitation Research and Development 2005;42(6):717-722.
130. Maguire EA, Gadian DG, Johnsrude IS, Good CD, Ashburner J, Frackowiak RSJ, Frith CD - *Navigation-related structural change in the hippocampi of taxi drivers.* - Proc Natl Acad Sci USA 2000;97:4398-4403.
131. Masia L, Frascarelli F, Morasso P, Di Rosa G, Petrarca M, Castelli E, Cappa P - *Reduced short term adaptation to robot generated dynamic environment in children affected by Cerebral Palsy.* - J Neuroeng Rehabil 2011;8:28.
132. Matthews PM, Honey GD, Bullmore ET - *Applications of fMRI in translational medicine and clinical practice* - Nature Reviews Neuroscience 2006;7:732-744.
133. McKeown MJ, Makeig S, Brown GG, Jung TP, Kindermann SS, Bell AJ, Sejnowski TJ - *Analysis of fMRI Data by Blind Separation Into Independent Spatial Components* - Human Brain Mapping 1998;6:160-188.
134. Mechelli A, Crinion JT, Noppeney U, O'Doherty J, Ashburner J, Frackowiak RSJ, Price CJ - *Neurolinguistics: structural plasticity in the bilingual brain.* - Nature 2004;431:757.

135. Mechelli A, Price CJ, Friston KJ, Ashburner J - *Voxel-Based Morphometry of the Human Brain: Methods and Applications.* - Current Medical Imaging Reviews 2005;1:105-113.

136. Medina LS, Bernal B, Dunoyer C, Cervantes L, Pacheco MRE, Jayakar P, Morrison G, Ragheb J, Altman NR - *Seizure Disorders: Functional MR Imaging for Diagnostic Evaluation and Surgical Treatment - Prospective Study* - Radiology 2005;236:247-253.

137. Mori S, Zhang J - *Principles of Diffusion Tensor Imaging and Its Applications to Basic Neuroscience Research* - Neuron 2006;51:527-539.

138. Mühlau M, Gaser C, Ilg R, Conrad B, Leibl C, Cebulla MH, Backmund H, Gerlinghoff M, Lommer P, Schnebel A, Wohlschläger AM, Zimmer C, Nunnemann S - *Gray matter decrease of the anterior cingulate cortex in anorexia nervosa.* - American Journal of Psychiatry 2007;164:1850-1857.

139. Naito E. - *Sensing limb movements in the motor cortex: how humans sense limb movement.* - Neuroscientist 2004;10:73-82.

140. Naruo T, Nakabeppu Y, Deguchi D, Nagai N, Tsutsui J, Nakajo M, Nozoe S - *Decreases in blood perfusion of the anterior cingulate gyri in Anorexia Nervosa Restricters assessed by SPECT image analysis.* - BMC Psychiatry 2001;1:2.

141. Newman SD, Carpenter PA, Varma S, Just MA - *Frontal and parietal participation in problem solving in the Tower of London: fMRI and computational modeling of planning and high-level perception* - Neuropsychologia 2003;41:1668-1682.

142. Newman SD, Greco JA, Lee D - *An fMRI study of the Tower of London: A look at problem structure differences* - Brain Research 2009;1286:123-132.

143. Niazy RK, Beckmann CF, Iannetti GD, Brady JM, Smith SM - *Removal of FMRI environment artefacts from EEG data using optimal basis sets* – NeuroImage 2005;28(3):720-37.

144. Nichols T, Brett M, Andersson J, Wagner T, Poline JB - *Valid conjunction inference with the minimum statistic.* - Neuroimage 2005;25:653-660.

145. Nocchi F, Franchin T, Genovese E, Bufalari S, Carnì M, Cannatà V - *Determinazione dell'indice di lateralizzazione mediante Risonanza Magnetica funzionale per la valutazione prechirurgica del linguaggio in pazienti con epilessia farmaco-resistente* – Atti del VI Congresso Nazionale dell'Associazione Italiana di Fisica Medica 2009;1:195-198.

146. Nocchi F, Franchin T, Genovese E, Longo D, Fariello G, Cannatà V - *Analysis of Outliers Effects in Voxel-Based Morphometry by means of Virtual Phantoms* - IFMBE Proceedings 2008;20(8):540-543.

147. Nocchi F, Franchin T, Genovese E, Longo D, Fariello G, Cannatà V - *Comparison of small clinical samples with Voxel-Based Morphometry: a quantitative approach to the analysis of outliers effects by means of virtual phantoms* - 14th Annual meeting of the Organization for Human Brain Mapping (Melbourne, Australia, June 15-19, 2008).

148. Nocchi F, Genovese E, Ritrovato M, Franchin T, Cannatà V, Capussotto C, Derrico P - *Multidisciplinary Health Technology Assessment of a stimuli-delivery system for functional Magnetic Resonance Imaging (fMRI)* - V Annual Meeting of the Health Technology Assessment International Society (Montréal, Canada, July 6-9, 2008).

149. Nudo RJ, Friel KM - *Cortical plasticity after stroke: implications for rehabilitation.* - Rev Neurol (Paris) 1999;155:713-717.

150. Nudo RJ, Milliken GW - *Reorganization of movement representations in primary motor cortex following focal ischemic infarcts in adult squirrel monkeys.* - J Neurophysiol 1996;75:2144-2149.

151. Nudo RJ, Wise BM, SiFuentes F, Milliken GW - *Neural substrates for the effects of rehabilitative training on motor recovery after ischemic infarct. –* Science 1996;272:1791-1794.

152. O'Shaughnessy ES, Berl MM, Moore EN, Gaillard WD - *Pediatric Functional Magnetic Resonance Imaging (fMRI): Issues and Applications.* - J Child Neurol 2008;23:791-801.

153. Ogawa S, Lee TM, Nayak AS, and Glynn P - *Oxygenation-sensitive contrast in magnetic resonance image of rodent brain at high magnetic fields* - Magnetic Resonance in Medicine 1990;14(1):68-78.

154. Patton JL, Mussa-Ivaldi FA - *Robot-assisted adaptive training: custom force fields for teaching movement patterns.* - IEEE Trans Biomed Eng 2004;51(4):636-46.

155. Plautz EJ, Milliken GW, Nudo RJ - *Effects of repetitive motor training on movement representations in adult squirrel monkeys: role of use versus learning.* - Neurobiology of Learning and Memory 2000;74:27-55.

156. Pons TP, Garraghty PE, Ommaya AK, Kaas JH, Taub E, Mishkin M - *Massive cortical reorganization after sensory deafferentation in adult macaques.* – Science 1991;252:1857-1860.

157. Prange GB, Jannink MJ, Groothuis-Oudshoorn CG, Hermens HJ, Ijzerman MJ - *Systematic review of the effect of robot-aided therapy on recovery of the hemiparetic arm after stroke.* - J Rehabil Res Dev 2006;43:171-184.

158. Press C, Bird G, Flach R, Heyes C - *Robotic movement elicits automatic imitation.* - Cogn Brain Res 2005;25:632-640.

159. Proteau L, Blandin Y, Alain C, Dorion A - *The effects of the amount and variability of practice on the learning of a multi-segmented motor task.* - Acta Psych 1994;85:61-74.

160. Pujol J, Deus J, Losilla JM, Capdevila A - *Cerebral lateralization of language in normal left-handed people studied by functional MRI.* - Neurology 1999;52:1038-1043.

161. Rachakonda S, Egolf E, Correa N, Calhoun V - *Group ICA of fMRI Toolbox (GIFT) Manual* - http://mialab.mrn.org/software/gift/

162. Reinkensmeyer D, Emken J, Cramer S - *Robotics, motor learning, and neurologic recovery.* - Annu Rev Biomed Eng 2004;6:497-525.

163. Remple MS, Bruneau RM, VandenBerg PM, Goertzen C, Kleim JA - *Sensitivity of cortical movement representations to motor experience: evidence that skill learning but not strength training induces cortical reorganization.* - Behav Brain Res 2001;123:133-141.

164. Ritrovato M, Genovese E, Nocchi F, Franchin T, Fariello G, Longo D, Delfino L, Cannatà V – *Confronto tra diverse modalità di applicazione della bias correction a immagini morfologiche utilizzate per studi di VBM con software SPM2* – V Congresso Nazionale dell'Associazione Italiana di Fisica Medica (Lucca, 17-20 settembre 2007).

165. Rizzolatti G, Craighero L - *The mirror-neuron system.* - Annu Rev Neurosci 2004;27:169-192.

166. Rizzolatti G, Fogassi L, Gallese V - *The Mirror Neuron System: A Motor-Based Mechanism for Action and Intention Understanding.* - In The Cognitive Neuroscience IV. Edited by: Gazzaniga M. The MIT Press, Cambridge USA 2009;625-640.

167. Romero SG, Manly CF, Grafman J - *Investigating cognitive neuroplasticity in single cases: lessons learned from applying functional neuroimaging techniques to the traditional neuropsychological case study framework.* – Neurocase 2002;8:355-368.

168. Rossini PM, Dal Forno G - *Integrated technology for evaluation of brain function and neural plasticity.* - Phys Med Rehabil Clin N Am. 2004;15(1):263-306.

169. Sachdev P, Mondraty N, Wen W, Gulliford K - *Brains of anorexia nervosa patients process self-images differently from non-self-images: An fMRI study.* - Neuropsychologia 2008;46:2161-2168.

170. Sakzewski L, Ziviani J, Boyd R - *Systematic review and meta-analysis of therapeutic management of upper-limb dysfunction in children with congenital hemiplegia.* – Pediatrics 2009;123(6):e1111-22.

171. Salek-Haddadi A, Friston KJ, Lemieux L, Fish DR - *Studying spontaneous EEG activity with fMRI.* - Brain Research Reviews 2003;43:110-133.

172. Sallnas EL, Rassmus-Gruhn K, Sjosstrom C - *Supporting presence in collaborative environments by haptic force feedback.* - ACM Trans Computer-Human Interact 2000;7:461-467.

173. Salmond CH, Ashburner J, Vargha-Khadem F, Connelly A, Gadian DG, and Friston KJ - *Distributional Assumptions in Voxel-Based Morphometry.* - NeuroImage 2002;17:1027-1030.

174. Seghier ML - *Laterality index in functional MRI: methodological issues.* - Magnetic Resonance Imaging 2008;26:594-601.

175. Senjem ML, Gunter JL, Shiung MM, Petersen RC, Jack CRJ - *Comparison of Different Methodological Implementations of Voxel-Based Morphometry in Neurodegenerative Disease.* - NeuroImage 2005;26: 600-608.

176. Sgandurra G, Ferrari A, Cossu G, Guzzetta A, Biagi L, Tosetti M, Fogassi L, Cioni G - *Upper limb children action-observation training (UP-CAT): a randomised controlled trial in Hemiplegic Cerebral Palsy.* - BMC Neurol 2011;11:80.

177. Shallice T - *Specific impairments of planning* - Philosophical Transactions of the Royal Society of London. Series B, Biological Sciences 1982;298(1089):199-209.

178. Small SL, Buccino G, Solodkin A - *The Mirror Neuron System and Treatment of Stroke.* - Dev Psychobiol (Epub 24 Nov 2010).

179. Strother SC - *Evaluating fMRI preprocessing pipelines.* - IEEE Eng Med Biol Mag. 2006;25(2):27-41.

180. Sutcliffe TL, Gaetz WC, Logan WJ, Cheyne DO, Fehlings DL - *Cortical reorganization after modified constraint-induced movement therapy in pediatric hemiplegic cerebral palsy.* - J Child Neurol 2007;22:1281-1287.

181. Swayze VW II, Andersen A, Andreasen NC, Arndt S, Sato Y, Ziebell S - *Brain tissue volume segmentation in patients with anorexia nervosa before and after weight normalisation.* - International Journal of Eating Disorders 2003;33:33-44.

182. Swayze VW II, Andersen A, Arndt S, Rajarethinam R, Fleming F, Sato Y, Andreasen NC - *Reversibility of brain tissue loss in anorexia nervosa assessed with a computerized Talairach 3-D proportional grid.* - Psychological Medicine 1996;26:381-390.

183. Swinnen SP, Schmidt RA, Nicholson DE, Shapiro DC - *Information feedback for skill acquisition: Instantaneous knowledge of results degrades learning.* - J Exp Psychol Learn Mem Cogn 1990;16:706-716.

184. Szaflarski JP, Holland SK, Jacola LM, Lindsell C, Privitera MD, Szaflarski M - *Comprehensive presurgical functional MRI language evaluation in adult patients with epilepsy* - Epilepsy & Behavior 2008;12:74-83.

185. Takahashi CD, Der-Yeghiaian L, Le V, Motiwala RR, Cramer SC - *Robot-based hand motor therapy after stroke.* - Brain 2008;131:425-37.

186. Takano A, Shiga T, Kitagawa N, Koyama T, Katoh C, Tsukamoto E, Tamaki N - *Abnormal neuronal network in anorexia nervosa studied with I-123-IMP SPECT.* - Psychiatry Research 2001;107:45-50.

187. Thacker NA - *Tutorial: A Critical Analysis of Voxel Based Morphometry.* - Imaging Science and Biomedical Engineering, University of Manchester. - TiNA Memo No. 11, 2003.

188. Toni I, Thoenissen D, Zilles K - *Movement Preparation and Motor Intention* - NeuroImage 2001;14:S110-S117.

189. Torrey EF - *Schizophrenia and the inferior parietal lobule.* - Schizophrenia Research 2007;97:215-225.

190. Tzourio-Mazoyer N, Landeau B, Papathanassiou D, Crivello F, Etard O, Delcroix N, Mazoyer B, Joliot M - *Automated anatomical labeling of activations in SPM using a macroscopic anatomical parcellation of the MNI MRI single-subject brain.* - Neuroimage 2002;15:273-289.

191. Vogt BA, Finch DM, Olson CR - *Functional heterogeneity in cingulate cortex: the anterior executive and posterior evaluative regions.* - Cerebral Cortex 1992;2:435-443.

192. Wagner A, Greer P, Bailer UF, Frank GK, Henry SE, Putnam K, Meltzer CC, Ziolko SK, Hoge J, McConaha C, Kaye WH - *Normal brain tissue volumes after long-term recovery in anorexia and bulimia nervosa.* - Biological Psychiatry 2006;59:291-293.

193. Waldner A, Tomelleri C, Hesse S - *Transfer of scientific concepts to clinical practice: recent robot-assisted training studies.* - Funct Neurol 2009;24:173-177.

194. White NB, Alkire MT, Haier RJ - *A voxel-based morphometric study of non-demented adults with Down syndrome.* - NeuroImage 2003;20:393-403.

195. Whitwell JL - *Voxel-Based Morphometry: An Automated Technique for Assessing Structural Changes in the Brain* - The Journal of Neuroscience 2009;29(31):9661-9664.

196. Winstein CJ, Merians AL, Sullivan KJ - *Motor learning after unilateral brain damage.* - Neuropsych 1999;37:975-987.

197. Winters JM - *A telehomecare model for optimizing rehabilitation outcomes.* - Telemed J E Health 2004;10:200-12.

198. Wolf SL, Winstein CJ, Miller JP, Taub E, Uswatte G, Morris D, Giuliani C, Light KE, Nichols-Larsen D - *Effect of constraint-induced movement therapy on upper extremity function 3 to 9 months after stroke: the EXCITE randomized clinical trial.* – JAMA 2006;296(17):2095-104.

199. Yagura H, Hatakenaka M, Miyai I - *Does therapeutic facilitation add to locomotor outcome of body weight–supported treadmill training in nonambulatory patients with stroke? A randomized controlled trial.* - Arch Phys Med Rehabil. 2006;87:529-535.

200. Yuan W, Szaflarski JP, Schmithorst VJ, Schapiro M, Byars AW, Strawsburg RH, Holland SK - *FMRI Shows Atypical Language Lateralization in Epilepsy Patients* - Epilepsia 2006;47(3):593-600.